PDZD8 and its role in intellectual disability

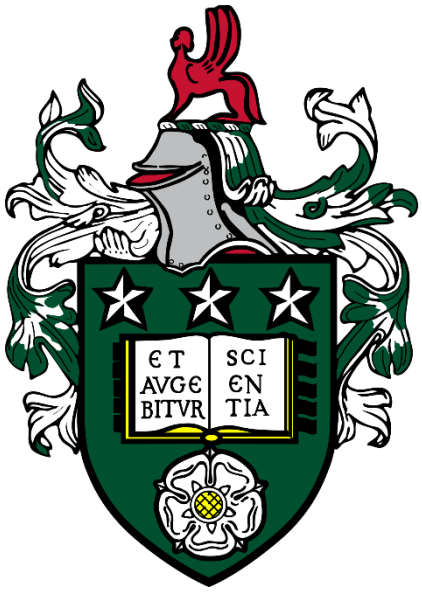

Andreea Daniela Panţiru

Submitted in accordance with the requirements for the degree of Doctor in Philosophy

University of Leeds

School of Biomedical Sciences

January 2023

The candidate confirms that the work submitted is her own, except where work which has formed part of jointly authored publications has been included. The contribution of the candidate and the other authors to this work has been explicitly indicated below. The candidate confirms that appropriate credit has been given within the thesis where reference has been made to the work of others.

Results chapter 1 and 2 contain work published in the following paper: **'PDZD8 Disruption Causes Cognitive Impairment in Humans, Mice and Fruit Flies'** (2022), *Biological Psychiatry***;** Al-Amri, A. H., Armstrong, P., Amici, M., Ligneul, C., Rouse, J., El-Asrag, M. E., **Pantiru, A. D.,** Vancollie, V. E., Ng, H. W., Ogbeta, J. A., Goodchild, K., Ellegood, J., Lelliott, C. J., Mullins, J. G. L., Bretman, A., Al-Ali, R., Beetz, C., Al-Gazali, L., Al Shamsi, A., Lerch, J. P., Mellor, J. R., Al Sayegh, A., Ali, M., Inglehearn, C. F. and Clapcote, S. J.

Data attributable to me: qRT-PCR, western blots and data analysis for all experiments included in this thesis; Clemence Ligneul: performed MRI experiments; Paul Armstrong: Barnes maze, elevated plus maze, open field; Valerie Vancollie: body measurements data from Sanger Institute; and Tom Wainright: technical assistance.

Acknowledgements

This research has been carried out by a team which has included Dr Jamie Johnston and Dr Steven Clapcote. My own contributions, fully and explicitly indicated in the thesis have been: western blots, qRT-PCR, immunohistochemistry, metabolic cage experiments, developing and using the motion sensor device, light-dark box, marble burying, forced swim test, fear conditioning, social interaction paradigms, olfactory discrimination, acute and chronic cranial window surgeries, anesthetized and awake calcium imaging, sniffing experiments and all data processing and analysis done for this thesis. The other member of the group and their contributions have been as follows: Arianna Fozatto for helping with the brown fat experiment, Ami Aspinall and Elizabeth Lee for helping with the Golgi experiments, Dr Paul Armstrong for Barnes maze, elevated plus maze, open field. Data obtained from our collaborators and their contributions have been mentioned on the previous page.

I would like to acknowledge the University of Leeds for their financial support. It has been an honour to be the recipient of the Emma and Leslie Reid Scholarship and to undertake this research project.

An immense thank you to my PhD supervisors, Dr Jamie Johnston, and Dr Steven Clapcote. Your support and guidance throughout this project have been invaluable. Dr Jamie Johnston in particular who has been instrumental in my development as a scientist. Thank you to all academics who helped me get to this stage, especially Prof Susan Deuchars and Prof Jim Deuchars, for their invaluable counsel.

It has been an amazing experience working in this lab especially thanks to Marilyn, Mark, Emma, Merve, Emily. I will miss our group therapy sessions! Thank you, Cedric, Paul, and Clare, for your advice and help with my experiments. Thank you Nela and Jen your friendship and support. Special thanks to my best friend Carina who has been always there for me.

An immense thank you to my family for their continuous support.

I would like to dedicate this thesis to my mom, I wish you were still here.

Abstract

Intellectual disability is the most common childhood neurodevelopmental disorder that affects learning ability, impairs cognitive functioning, and is defined by an intelligence quotient below 70. Four children from two unrelated families were diagnosed with intellectual disability, developmental delay, macrocephaly, and other autistic features caused by a specific mutation in **PDZ domain containing protein 8 (*PDZD8*)** gene. Pdzd8 is an endoplasmic reticulum-mitochondria tethering protein which regulates calcium dynamics in mammalian neurons and has not previously been associated with any human disease. As *PDZD8* mutation is a novel mutation linked to intellectual disability, a mouse model with a mutation in *Pdzd8* was used to characterise the disruption of Pdzd8 from a molecular, behavioural, and neural activity perspective. *Pdzd8* mutant mice displayed changes in the relative brain volume, decreased neurogenesis, and increased spine density. On a molecular level, *Pdzd8* mice exhibited an increase in mRNA expression in multiple genes linked to cerebral development, neurogenesis, mitochondria function, endoplasmic reticulum stress and Pdzd8 interactors. From a behavioural perspective, *Pdzd8* mice presented hyperactivity, repetitive behaviours, decreased anxiety, impaired long-term memory, altered associative learning, and distorted social discrimination. *In vivo* imaging of neuronal dynamics revealed altered spontaneous excitatory activity compared to wild type controls. Overall, the myriad of changes observed in *Pdzd8* mice, from molecular and structural abnormalities to neuronal and behavioural impairments, strongly characterize deficits observed in intellectual disability and autism spectrum disorders.

Table of Contents

List of figures

List of tables

I. Introduction

1.1 Intellectual disability

Intellectual disability (ID) disorders are a heterogenous group of disorders classified by an impairment in cognitive abilities that generally emerges in childhood, as characterised by the Diagnostic and Statistical Manual of Mental Disorders (DSM-5) (American Psychiatric Association, 2013). According to DSM-5 an ID diagnosis requires the satisfaction of three criteria: a deficit in intellectual functioning confirmed by intelligent quotient testing, deficits in adaptive functioning of an individual and the onset of these deficits in childhood (American Psychiatric Association, 2013). ID is thought to be the predominant neurodevelopmental disorder, with a prevalence of 1 – 3% of the world population. ID constitutes a tremendous socio-economical cost, with an estimation of $1 million of additional cost per person with ID (Honeycutt *et al.*, 2004); therefore, it represents one of the biggest medical and social challenges in our society. The heterogeneity of ID is reflected in the wide range of causative factors, from environmental influences to chromosomal alterations and single gene mutations. This chapter will cover an overview of the causes ID as well the consequences of this disorder, from both a cellular and behavioural perspective, with a focus on animal model research.

1.1.1 Aetiology of ID

ID is a condition fundamentally characterised by an intelligent quotient below 70 often presenting with severe adaptive limitations (World Health Organization, 1992; American Psychiatric Association, 2013). ID can occur on its own but, is more often accompanied by behavioural disturbances, malformations, neurological impairments, and other neurodevelopmental disorders such as autism spectrum disorders (ASD). ASD comprise of

a group of disorders including autistic disorder, Asperger syndrome, pervasive developmental disorder not otherwise specified and Rett syndrome (RTT). ID and ASD are highly heterogenous conditions but are often found together in patients. Approximately 70% of individuals with ASD have ID, although the severity level can differ significantly, whereas, only about 10 % of patients with ID display core symptoms of ASD (Chiurazzi *et al.*, 2020; American Psychiatric Association, 2013).

Environmental factors. ID presents a highly heterogeneous aetiology, with both environmental and genetic factors contributing to it. Environmental factors, for example, intrauterine exposure to alcohol, maternal infections such as rubella and HIV, or hazardous exposure to chemicals, and ultraviolet radiation have been shown to lead to ID, with approximately 40% of cases presenting an early environmental aetiology (O'Leary *et al.*, 2013).

Genetic factors. With advancement in genetic and molecular technologies, it is now thought that more than 50% of ID cases have a genetic component, such as aneuploidies, copy number variants, or single gene mutations (Vissers, Gilissen and Veltman, 2016).

Chromosomal aberrations, such as extra chromosomes, are associated with ID. Karyotyping is a test to assess chromosomes to identify various genetic disorders, and can identify aneuploidies in ID, such as Down's syndrome (trisomy 21), Edwards' syndrome (trisomy 18) or Patau syndrome (trisomy 13). Cognitive impairment is present in all these aneuploidies and Down's syndrome is one of the most common forms of ID (Vissers, Gilissen and Veltman, 2016).

Copy number variants (CNV) are segments of DNA larger than 1 kilobase (kb), which appear as duplications or deletions compared to a reference genome (Coe *et al.*, 2014). Numerous CNV have been involved in ID, such as locus 16p11.2, which is a region of approximately ~600 kb on chromosome 16, position 11.2, including almost 30 genes (Rein and Yan, 2020). Both deletions and duplications of this region have been linked to ID, ASD, as well as attention deficit hyperactivity disorder (ADHD) and other motor or developmental delay (D'Angelo *et al.*, 2016). Mouse models of either duplication or deletion of 16p11.2 gene locus display symptoms of ID seen in patients, such as cognitive deficits (Coe *et al.*, 2014).

Abnormalities in more than 1,000 genes have been so far linked to ID, many of these displaying a significant overlap with other neurodevelopmental disorders such as ASD (Kochinke *et al.*, 2016). Some of the most studied single gene mutations in relation to ID and ASD include *SHANK3, SYNGAP1, FMR1, MECP2* and *neuroligins (NLGN1, NLGN3, NLGN4)* (Golden, Buxbaum and De Rubeis, 2018). There are multiple *SHANK* genes, including *SHANK1, SHANK2* and *SHANK3.* Mutation in the *SHANK3* gene, such as point mutation or deletion of 22q13.3 cause Phelan-McDermid syndrome, which is a highly debilitating neurodevelopmental disorder commonly presenting cognitive impairments in patients (Uchino and Waga, 2013). *SHANK3* encodes for SHANK3 (SH and multiple ankyrin repeat domain protein 3), a scaffolding protein which is essential in the formation of synapses and neuronal physiology (Golden, Buxbaum and De Rubeis, 2018). A meta-analysis has recently shown that mutations in SHANK genes are present in about 1% of the patients that display ID and ASD (Leblond *et al.*, 2014). The *SYNGAP1* gene encodes for SynGAP (synaptic Ras GTPase-activating protein), a signalling protein important in the maturation of synapses and synaptic transmission (Jeyabalan and Clement, 2016). *SYNGAP1* gene

mutations lead to an autosomal dominant form of encephalopathy (generalized epilepsy), which presents itself with mild to severe ID and ASD. The *FMR1* gene encodes for fragile X mental retardation protein (FMRP), an RNA-binding protein with functions important in synapse development. A repeat region, a trinucleotide sequence CGG, is present in the non-coding region of the gene. A higher number of repeats (> 200) is associated with an absence of FRMP, causing fragile X syndrome (FXS), the most recurrent monogenic form of inherited ID (Bagni *et al.*, 2012). *MECP2* gene, encoding methyl CpG binding protein 2 (MeCP2), leads to RTT, which is characterized by an initial period of normal development and a subsequent deterioration of motor and cognitive skills, with ID and often ASD comorbidity. One of the functions of the MeCP2 protein is the maintenance of synapses between neurons (Lombardi, Baker and Zoghbi, 2015; Golden, Buxbaum and De Rubeis, 2018). Mutations in the *neuroligin* genes *NLGN1, NLGN3* and *NLGN4* and *neurexin* gene *NRXN1, NRXN2* and *NRXN3* involved in synaptic communication and synapse formation have also been associated with ID and ASD (Srivastava and Schwartz, 2014).

The aetiology of ID is heterogenous, and the causative factors are likely to interact with each other. However, a lot of valuable information has been revealed by studying rodent models of genetic mutations. The following sections will cover the consequences of mutations in ID-related genes in terms of their effects on the central nervous system (CNS) and behaviour in animal models.

1.1.2 Behavioural phenotypes of ID and their brain circuitry

Behavioural abnormalities are common in children with ID regardless of the underlying aetiology (American Psychiatric Association, 2013). Some of the behavioural phenotypes observed in ID include deficits in social interaction, learning and memory. Mouse models of

ID are used to understand role of CNS in these behavioural phenotypes to facilitate the development of potential therapeutic strategies for ID. However, due to the complexity of ID and the heterogeneity of its symptoms many brain areas have been involved in this disorder, such as prefrontal cortex (PFC), olfactory bulb, basal ganglia, thalamus, hippocampus, amygdala, and cerebellum. Briefly, the structure and function of these brain regions will be introduced (Text Box 1, Fig. 1).

Brain region	**Description**
Prefrontal cortex (PFC)	The PFC is a phylogenetically divergent structure located in the anterior portion of the frontal lobe. The PFC is highly developed in primates and it plays a crucial role in executive control, such as planning, problem solving, as well as cognitive functions. The PFC can be divided into multiple regions, such as the medial PFC (mPFC), the orbitofrontal cortex, the ventrolateral PFC, and the dorsolateral PFC. The mPFC is further contains the anterior cingulate cortex, the prelimbic cortex and the infralimbic cortex, key areas which underlie emotional regulations and memory (Sigurdsson and Duvarci, 2016).
Olfactory bulb	The olfactory bulb is a hub for processing olfactory information located in the anterior aspect of the forebrain. The olfactory bulb contains spherical structures called glomeruli, where odorant-related information is received from the sensory epithelium of the nose and then processed, before relaying it to the primary olfactory cortex, in the temporal lobe (Chen and Hong, 2018).
Basal ganglia	Basal ganglia refer to a group subcortical nuclei, locate in the temporal lobe mainly involved in motor control (Kim, Lim and Kaang, 2016). Basal ganglia are usually divided into three types of nuclei: input, intrinsic and output. Striatum forms the input nuclei, where information from various cortical regions is

	received, and it is further divided into caudate nucleus, putamen and nucleus accumbens. The internal segment of the globus pallidus and the substantia nigra pars reticulata are the output nuclei of the basal ganglia, which transfer motor-related information to the thalamus. The intrinsic nuclei facilitate communication between the input and output regions, and contain the external segment of the globus pallidus, the substantia nigra pars compacta and the subthalamic nucleus (Kim, Lim and Kaang, 2016).
Thalamus	The thalamus is a brain regions located in the diencephalon and it is mainly known as a relay centre for most of the incoming sensory and motor information. The thalamus then sends projections to multiple cortical areas, including the PFC (Gandhi and Lee, 2021).
Hippocampus	The hippocampus is a brain structure located in the medial temporal lobe and is crucial part of the limbic systems. The hippocampus is essential for spatial navigation, and several types of learning and memory. It contains multiple subfields: the dentate gyrus, cornu ammonis (CA) 1-3. The dentate gyrus receives most of the inputs from the entorhinal cortex, and the hippocampus sends numerous projections to cortical areas (Sigurdsson and Duvarci, 2016).
Amygdala	The amygdala is an almond-shaped region of the brain locate deep in the medial temporal lobe. The amygdala is a key part of the limbic system, highly involved in the regulation of emotions, especially processing of fearful and threatening stimuli. The amygdala is a categorized into three main divisions, with the lateral, basolateral and the central amygdala (Duvarci and Pare, 2014).
Cerebellum	The cerebellum is a major structure of the hindbrain, located next to the brainstem. The cerebellum's main functions include

	maintaining posture and balance, as well as coordinating voluntary movements. Structurally, it is divided into three lobes – anterior, posterior, and flocculonodular, which receive balance-related information from auditory and visual systems (Kim, Lim and Kaang, 2016).

Text Box 1. Brain regions involved in ID – general description.

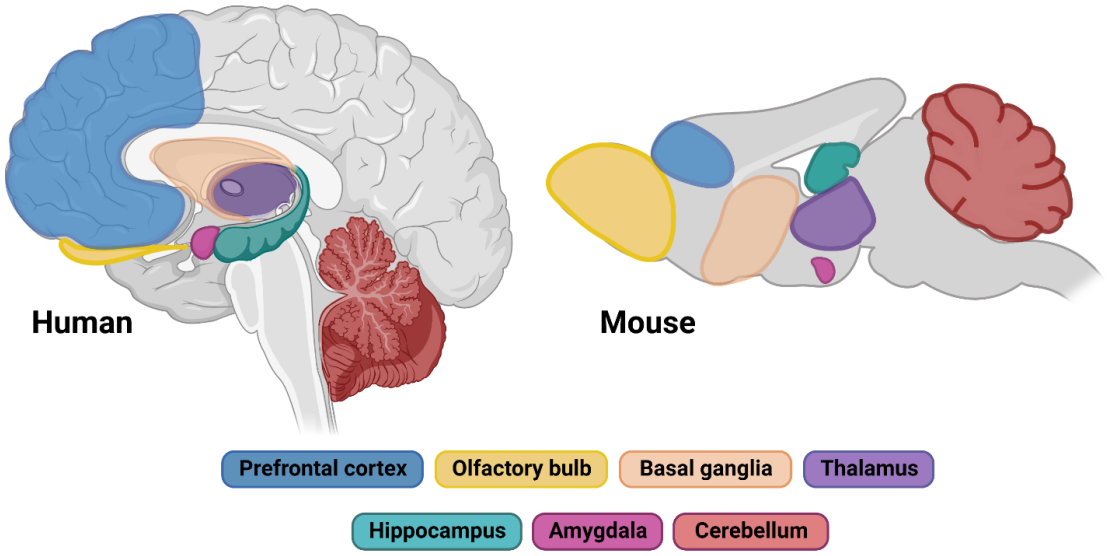

Figure 1. Brain regions involved in ID. Schematic representation of the human brain regions involved in ID and their mouse equivalents: prefrontal cortex (blue), somatosensory cortex (green), olfactory bulb (yellow), basal ganglia (orange), thalamus (purple), hippocampus (turquoise), amygdala (pink), cerebellum (red), Figure created with *BioRender.com.*

The brain structures and functions mentioned (Text Box 1, Fig. 1) were previously implicated in ID (Golden, Buxbaum and De Rubeis, 2018; Verma et al., 2019). Altered brain structure and function can lead to changes in behavioural output. The main behavioural deficits observed in ID – social interaction, repetitive behaviours, learning and memory – will be discussed in the following section.

Social interaction. Social behaviour refers to any mode of communication or interaction between animals. Such exchanges between conspecifics could be fighting, mating or parenting. These types of interactions are displayed by all sexually reproducing animal species and are crucial for survival, health and reproduction (Wei, Talwar and Lin, 2021). However, impairment in social interactions is detrimental to animal survival and this is often a characteristic of neuropsychiatric and neurodevelopmental disorders, such as ID and ASD (Chen and Hong, 2018; Fernández, Mollinedo-Gajate and Peñagarikano, 2018).

Neural circuitry of social interaction. Social interaction comprises of detection of a conspecific, approach, and investigation, all of which involve multiple regions of the brain and a complex circuitry. Social experience in primates is predominantly dependent on vision, however in mice it relies on olfaction, which will be the focus of this section. Olfactory cues, such as urine, are essential in mice for detecting a social target (Wei, Talwar, and Lin, 2021). For example, introducing socially-relevant odours to wild-type (WT) mice is able to lead to normal social interaction, such as investigatory behaviour, on its own despite the lack of visual cues to indicate the presence of a conspecific (Ryan *et al.*, 2008). The olfactory pathway (Fig. 2) starts with olfactory sensory neurons, in the main olfactory epithelium, which detect olfactory cues. This information is transmitted to the olfactory bulb, which distribute the signal to various subcortical and cortical regions, such as olfactory tubercle (the most ventral part of the striatum), anterior olfactory nucleus, piriform cortex, entorhinal cortex, and amygdala (Fig. 2) (Chen and Hong, 2018; Wei, Talwar and Lin, 2021). It is noteworthy that unlike other sensory pathways, the olfactory system transmits information to cortical areas without a thalamic relay. For example, information from the entorhinal cortex is received by the hippocampus, which in turn connects to the mPFC. The piriform

cortex transmits information to the orbitofrontal cortex, which then communicates with the mPFC. Additionally, information from the olfactory bulb is also transmitted to the amygdala, which also has reciprocal connections to the mPFC (Fig. 2) (Gangopadhyay *et al.*, 2021). Recently it was shown that the basolateral amygdala projections to the dorsomedial PFC are involved in reduction of social interaction behaviours and increased anxiety when activated by optogenetics using channelrhodopsin-2. Conversely, halorhodopsin-mediated inhibition of these projections resulted in increased social interaction and reduced anxiety (Felix-Ortiz *et al.*, 2016). The dorsomedial PFC, also known as the frontal association cortex or the secondary motor area, is a hub for integrating sensory information (Barthas and Kwan, 2017). This encodes complex social information necessary to modulate social behaviours (Gangopadhyay *et al.*, 2021; Lee *et al.*, 2016). Through microendoscopic calcium imaging in awake rodents which are socially interacting with each other, it was recently shown that not only do mice exhibit increased dorsomedial PFC activity during social behaviours, but also synchronicity in brain activity was observed between the animals which was dependent on the social interactions (Kingsbury *et al.*, 2019).

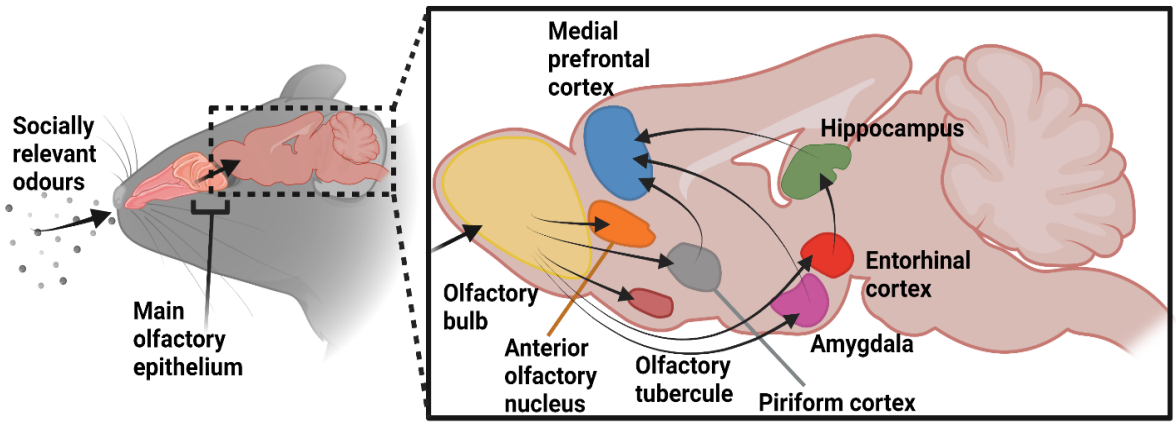

Figure 2. Neural circuitry of social interaction. Simplified schematic representation of key mouse brain areas involved in social interaction. Socially relevant odours are detected by neurons in the main olfactory epithelium, which synapse in the olfactory bulb. The olfactory bulb transmits odour-related information to multiple brain areas: anterior olfactory nucleus, olfactory tubercule, piriform cortex, amygdala, entorhinal cortex. The olfactory tubercule, amygdala, and hippocampus further communicate odour-related information to the medial prefrontal cortex. Figure created with *BioRender.com.*

Social interaction in mouse models of ID disorders. As social interaction is essential for survival and mating, many behavioural paradigms have been developed to assess this type of behaviour in rodents. For example, the social preference test is used to assess social motivation, social novelty preference is used to investigate social memory / recognition, while hierarchy is assessed by a social dominance test (Wei, Talwar and Lin, 2021; Chen and Hong, 2018). Mice expressing a 16p11.2 deletion exhibit ID- and ASD-like symptoms and abnormalities in neural activity in the mPFC (Wang *et al.*, 2018). In a social approach test to assess interaction, 16p11.2 mice displayed deficits in social interaction with an age and sex-matched mouse, compared to WT controls. Experimental elevation of the activity of the mPFC pyramidal neurons in 16p11.2 mice, using Gq-coupled designer receptors exclusively activated by designer drugs (Gq-DREADD), alleviated deficits in social investigation time and number of social interactions, social interaction parameters becoming comparable to WT controls (Wang *et al.*, 2018).

PTEN is another gene associated with ID and ASD (Cummings *et al.,* 2021). In a mouse model of *PTEN* mutation, in which *PTEN* is knocked-out (KO) specifically in inhibitory GABA (γ-aminobutyric acid) interneurons, social interaction with juvenile mice was diminished, while social interaction-evoked electroencephalogram signals were abnormal and inhibitory neuronal activity in the PFC was elevated. Enhanced GABAergic activity thus seems to be beneficial in models of ASD. Remarkably, transplantation of medial ganglionic

eminence interneurons from WT embryos into the PFC of neonatal *PTEN* KO mice seemed to rescue the social deficits previously observed in *Pten* mutants (Southwell *et al.*, 2020).

In *SHANK3* KO mouse model with either a homozygous or a heterozygous deletion, social impairments were observed only in juvenile mice, but not in adults, in a juvenile social interaction paradigm (Yang *et al.*, 2012). The three-chamber sociability test assesses social interaction preference between a mouse and an inanimate object, and then the initial mouse and a novel mouse. WT mice tend to display a preference for interaction with the mouse versus the object and with the novel mouse versus the initial one (Wei, Talwar and Lin, 2021). Mice that contain a mutation in *FMR1* gene were observed to interact more with the mouse compared to the object, similar to WT controls. However, when a novel mouse was placed in the apparatus, *FMR1* mutant mice displayed decreased social interaction with the novel mouse compared with the WT mice tested (Tian *et al.*, 2017). Mice with double KO of *SHANK1* and *SHANK3* also showed impairment on the three-chamber social interaction test (Mossa *et al.*, 2021). Mutant mice were more interested in investigating the object versus the stranger mouse and showed a preference for the already familiar mouse when a novel mouse was introduced (Mossa *et al.*, 2021).

Overall, deficits in social interaction can be observed across a variety of mouse models of ID supporting the clinical phenotype seen in humans (Chen and Hong, 2018; Fernández, Mollinedo-Gajate and Peñagarikano, 2018).

Restricted repetitive behaviours. Repetitive behaviours can be observed in children with obsessive-compulsive disorder (OCD) or neurodevelopmental disorders, such as ASD and ID (Wilkes and Lewis, 2018). Restrictive repetitive behaviours (RRB) consist of a sequence of behaviour that is repeated at a relatively high rate, without a specific purpose and which

displays little variation in the pattern. Generally, RRB can be detrimental, as they can hinder daily life functioning and can even lead to self-injury. There are a wide variety of RRB, from simple motor movements, such as flapping hands, to compulsions and ritualistic behaviours (Wilkes and Lewis, 2018). RRB are generally divided into lower and higher order behaviours. Lower order RRB comprise of more simple motor behaviours, whereas ritualistic behaviour, obsessions, and opposition to change are classified as higher order RRB. In animal models, lower order stereotyped behaviours are better described in the literature as they are more obvious and easier to assess in rodents (Kim, Lim and Kaang, 2016). Lower order behaviours in rodents are highly variable, and include behaviours such as excessive self-grooming, repetitive burying, rearing, jumping, circling, and locomotor hyperactivity. Higher order behaviours display a higher degree of complexity and seem to be associated with alterations in executive functions. Behaviours such as cognitive rigidity and inability to change are assessed by more complex behavioural paradigms, such as reversal learning and extinction testing (Gandhi and Lee, 2021).

Neurobiology and mechanisms of RRB. Signalling mechanisms such as glutamatergic, GABAergic, and dopaminergic systems across a variety of brain regions are postulated to be involved in RRB. The PFC, orbitofrontal cortex, basal ganglia, striatum, cerebellum, and the projections between these regions have all been implicated in stereotypic behaviours. However, the cortico – basal ganglia – thalamic pathway (Fig. 3), which is involved in motor activities, has been extensively implicated in stereotypical behaviours (Gandhi and Lee, 2021). Even in humans, the occurrence of repetitive behaviours has been directly correlated with an increased basal ganglia volume (Wilkes and Lewis, 2018). Glutamatergic cortical projections innervate the striatum, which leads to movement activation (direct pathway) and

movement inhibition (indirect pathway). In the direct pathway, dopamine-1 receptor expressing neurons in the striatum send GABAergic projection to the substantia nigra pars reticulata and internal globus pallidus, which result in reduced inhibition of the thalamus and subsequent glutamatergic activation of the motor cortex and movement initiation (Kim, Lim and Kaang, 2016). The indirect pathway, dopamine-2 receptor – striatal neurons inhibit the external globus pallidus, which in turn inhibit the subthalamic nucleus. The subthalamic nucleus activates the substantia nigra pars reticulata and the internal globus pallidus via glutamatergic projections which in turn further inhibit the thalamus (Kim, Lim and Kaang, 2016). Additionally, the PFC projects to substantia nigra pars compacta, which provides dopaminergic input to the striatum. The substantia nigra pars compacta stimulates dopamine-1 receptor expressing neurons, activating the direct pathway, and inhibits dopamine-2

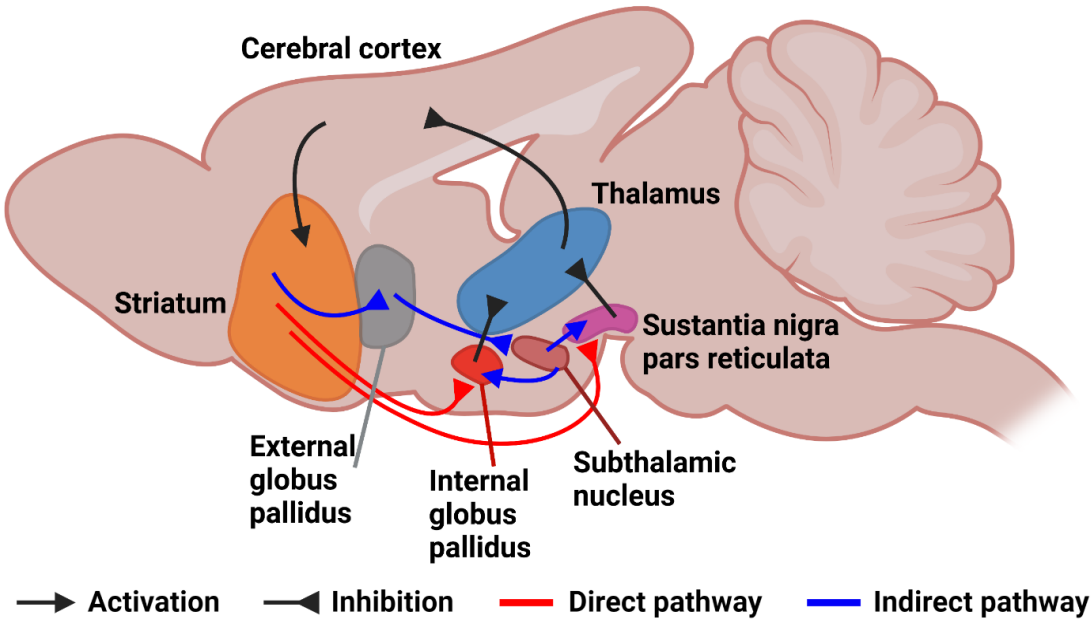

Figure 3. Direct and indirect pathway of basal ganglia. Simplified schematic diagram of basal ganglia direct and indirect pathways. Inputs form the cerebral cortex to the striatum active the direct (red) and indirect (blue) pathways, which lead to inhibition (inverted arrows) or activation (arrows) of the thalamus. Figure created with *BioRender.com.*

receptor striatal neurons, supressing the indirect pathway (Kim, Lim and Kaang, 2016). Recently, it was also shown that corticostriatal dysfunction in a *SAPAP3* KO mouse model of OCD was correlated with increased neuronal postsynaptic responses in the striatum that originated in the frontal association cortex (Corbit *et al.*, 2019).

RRB in mouse models of ID disorders. Excitation – inhibition balance is crucial for proper brain functioning and alterations to this balance have been implicated in ID disorders (Text Box 2) (Nelson and Valakh, 2015). An imbalance in excitation and inhibition seems to contribute to RRB as well, such that enhanced excitation, hyperexcitability or reduced inhibition have been shown to cause or worsen repetitive behaviours (Kim, Lim and Kaang, 2016). Heightened excitatory activity via NMDA (N-methyl-D-aspartate) receptor (NMDAR) agonist applied to basal ganglia motor circuits generated repetitive behaviours in mice. Application of NMDA antagonists such as MK-801 or memantine to block glutamatergic signalling between the cortex and the striatum has been shown to reduce RRB in mice (Gandhi and Lee, 2021). Conversely, systemic application of an NMDA antagonist has been shown to induce repetitive behaviours, such as increased self-grooming. In the PFC, NMDAR are present on inhibitory neurons, which might lead to hyperexcitation of motor pathways due to a lack of inhibition from the GABAergic neurons (Gandhi and Lee, 2021). Alterations in glutamatergic signalling via metabotropic receptors, such as metabotropic glutamate receptor 5, in the cortex and striatum have also been implicated in repetitive behaviours, and application of the metabotropic glutamate receptor 5 antagonist MPEP alleviated repetitive behaviours in rodents. MPEP administration in an *Fmr1* KO mouse model significantly reduced marble burying and prevented excessive self-grooming *Shank3* mutant mouse model of ASD (Dölen *et al.*, 2007; Wang *et al.*, 2016). Additionally, enhancing

GABAergic signalling in the cortex and basal ganglia reduced stereotypical behaviours, such as marble burying and circling (Kim, Lim and Kaang, 2016). Overall, a signalling imbalance in the excitation and inhibition seems to play an important role in RRB in mouse models of ID and ASD.

Excitation – inhibition theory. This paradigm of excitation – inhibition disproportionality was suggested in 2003 by Rubenstein and Merzenich. This idea was formed on the basis that the heightened excitatory drive in the cortex often seen in ASD is a result of an increase in the excitation to inhibition ratio of neuronal activity (Rubenstein and Merzenich, 2003). However, in the following years, a decrease in the excitation to inhibition ratio was also linked to ASD. Nevertheless, an imbalance in excitation – inhibition is a prevalent theory in neurodevelopmental disorders as both clinical and pre-clinical studies report changes excitation and / or inhibition in models of ID and ASD (Port, Oberman and Roberts, 2019; Canitano and Palumbi, 2021). The origin of this imbalance between excitation and inhibition displays heterogeneity. Mutations in genes linked to neurogenesis or spinogenesis, which cause ID and ASD, have been previously shown lead to an excitation – inhibition imbalance. Changes in excitation and inhibition could arise from higher excitatory glutamatergic neuronal signalling or a reduction in inhibition, due to lower GABAergic signalling. Impairment excitatory and inhibitory neurotransmission properties and the receptors involved in neurotransmission, such as NMDAR, have been observed in multiple mouse models of ID and ASD across various brain regions (Canitano and Palumbi, 2021).

Text Box 2. Excitation and inhibition theory in ASD and ID.

Learning and memory. Survival of most animals species relies on their ability to learn and adapt to their environment. Learning and memory are closely linked processes. Learning represents the acquisition of new skills or knowledge, while memory refers to how the brain stores and retrieves this information at later time points (Golden, Buxbaum and De Rubeis, 2018). Learning and memory are complex processes, and deficits in both have been associated with ID in humans and rodents (Li, Long and Yang, 2015).

A multitude of behavioural paradigms have been developed to assess different aspects memory – short-term and long-term memory – and different types of learning – spatial or

associative learning – in mice (Verma *et al.*, 2019; Sigurdsson and Duvarci, 2016). Short-term memory is defined as the ability to retain a small amount of information for a short period of time and it can be investigated in mice by performing a Y maze spontaneous alternation test. Long-term memory refers to the ability of transferring information from short-term memory into long-term storage, which can be accessed in the future, and it can be assessed in mice using a Barnes maze paradigm (Verma *et al.*, 2019; Vicari, Costanzo and Menghini, 2016). Spatial learning and memory refer to the capacity of recording and recalling information regarding the position of an object or event in the environment, which is essential for orientation, and can be tested in mice using Barnes maze (Banker *et al.*, 2021). Associative learning is a different type of learning which describes the ability to make connections between two distinct and unrelated stimuli and classical fear conditioning tests are commonly used to understand associative learning, such as context dependent associative learning (Yavas, Gonzalez and Fanselow, 2019).

Neural circuitry of learning and memory. The complexity of learning and memory is mirrored in the intricacy of the neural mechanisms which underlie these processes. Many brain areas have been implicated in multiple aspect of learning and memory. However, the dynamics between the hippocampus, amygdala, and the PFC are essential for the ability to learn and recall (Fig. 4) (Dixsaut and Gräff, 2021). The hippocampus has been extensively associated with spatial information and memory, especially the dorsal regions, while the ventral portion has been mainly linked to emotion regulation, such as anxiety (Fig. 4) (Sigurdsson and Duvarci, 2016). Initially, it was thought that only the hippocampus is involved in early learning phases, encoding of short-term memories and retrieval, while the mPFC has been widely associated with the consolidation of long-term memories (Li, Long

and Yang, 2015). However, recent data indicate that inputs from the hippocampus and the basolateral amygdala to the prefrontal cortex rapidly create a prefrontal representation during the initial learning period, suggesting a role for the mPFC during early learning phases in context-dependent fear conditioning (Kitamura *et al.*, 2017). This prefrontal neural ensemble becomes strengthened in time making it essential for distant contextual memory, while the hippocampal memory depiction is weakened (Kitamura *et al.*, 2017).

Both monosynaptic connections and multisynaptic routes allow for communication between the hippocampus and mPFC during associative and contextual learning and memory (Fig. 4) (Li, Long and Yang, 2015; Sigurdsson and Duvarci, 2016). The CA1 region of the hippocampus and subiculum sends direct projection to the mPFC, with the ventral CA1 contacting the prelimbic mPFC, while the dorsal CA1 projects to the retrosplenial region of the cingulate cortex. Chemogenetic inhibition of CA1 projection neurons to the cingulate cortex, which were active during learning and memory acquisition, caused deficits in remote memory retrieval, while recent memory retrieval was unaffected (Kol *et al.*, 2020). Monosynaptic projections from the mPFC to the hippocampus have also been identified (Rajasethupathy *et al.*, 2015). Taking advantage optogenetics to investigate hippocampal context-dependent memory exposed a direct mPFC – hippocampus link, where retrieval of memories was dependent on cingulate cortex projections to the hippocampus (Rajasethupathy *et al.*, 2015).

There are multiple brain regions that could enable indirect communication between the hippocampus and mPFC, such as nucleus accumbens, ventral tegmental area, thalamic nuclei, and amygdala (Fig. 4) (Li, Long and Yang, 2015; Dixsaut and Gräff, 2021). The hippocampus sends excitatory projections to the nucleus accumbens, which in turn sends

inhibitory projections to the ventral tegmental area. The ventral tegmental area contains reciprocal projection with numerous brain regions, including nucleus accumbens, basolateral amygdala, mPFC (Fig. 4) (Li, Long and Yang, 2015; Díaz, Caffino and Fumagalli, 2021). Both infralimbic and prelimbic regions of the mPFC are linked to the ventral tegmental area via monosynaptic connections. In turn, the ventral tegmental area sends dopaminergic projections to the hippocampus (Díaz, Caffino and Fumagalli, 2021). These projections have been previously postulated to regulate learning and memory formation (Nazari-Serenjeh, Rezayof and Zarrindast, 2011).

Both the hippocampus and mPFC have reciprocal projections to the basolateral amygdala (Fig. 4) (Sigurdsson and Duvarci, 2016; Dixsaut and Gräff, 2021). The amygdala has been extensively implicated in associative and emotional learning, especially in learned fear (Duvarci and Pare, 2014). The hippocampus contains dual-projection neurons, which project to both mPFC and basolateral amygdala. These neurons were shown to be to be important in coordinating fear related memory retrieval (Ishikawa and Nakamura, 2006; Kim and Cho, 2017).

Lastly, thalamic nuclei are thought to be involved in facilitating emotional memory formation and regulations due to their vast connections with both the hippocampus and the mPFC (Dixsaut and Gräff, 2021). For example, nucleus reuniens of the thalamus receives inputs from the mPFC, and then sends projections to the hippocampus (Fig. 4). The mPFC sends axons to the nucleus reuniens, which have been shown to play a role in decreasing fear-induced behaviour, known as fear extinction, which is important in the management emotional responses (Ramanathan *et al.*, 2018).

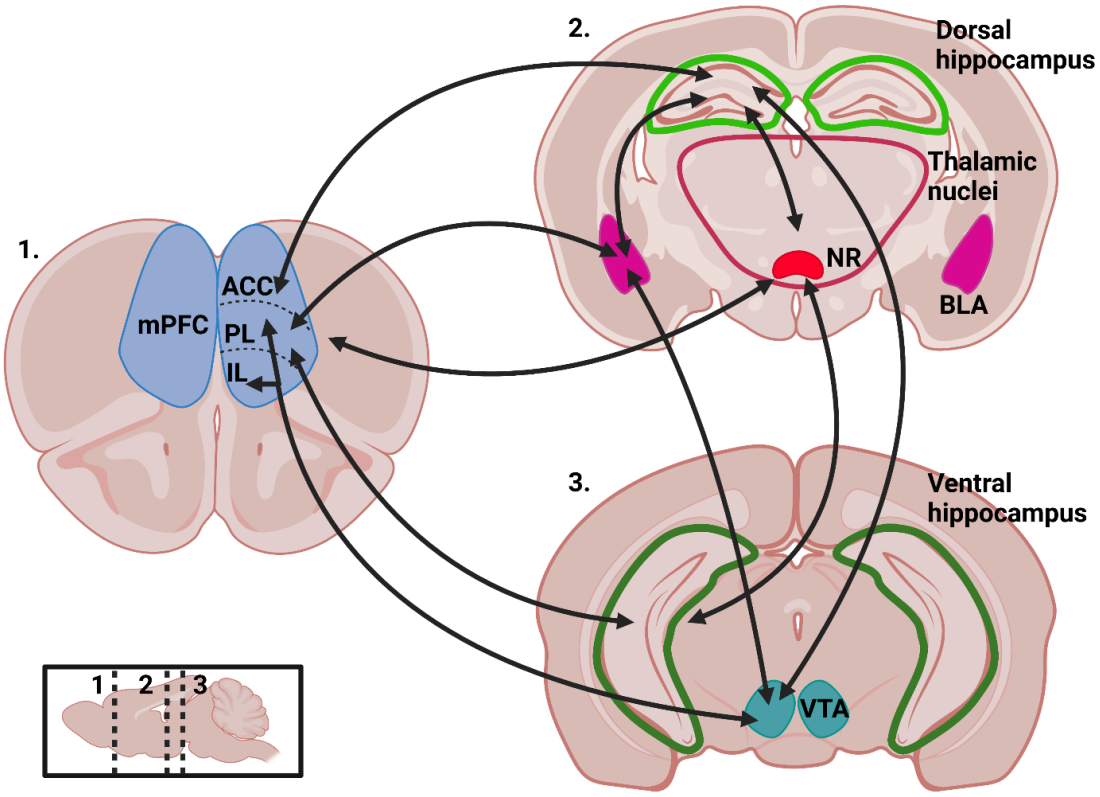

Figure 4. Learning and memory brain connectivity. Simplified schematic representation of the brain regions involved in memory and learning and their connectivity. Sagittal view of the brain (bottom left) with coronal brain planes represented (dotted lines): prefrontal cortex (1), dorsal hippocampus (2), ventral hippocampus (3). ACC – anterior cingulate cortex, PL – prelimbic, IL – infralimbic, mPFC – medial prefrontal cortex, NR – nucleus reuniens, BLA – basolateral amygdala, VTA – ventral tegmental area. Figure created with *BioRender.com.*

Learning and memory in mouse models of ID disorders. Cognitive dysfunction and deficits in adaptive functioning are amongst the main characteristics of ID (American Psychiatric Association, 2013), and both symptoms largely depend on intact learning and memory mechanisms. Abnormalities at the level of hippocampus, amygdala and mPFC or the connectivity between these regions have been identified across ID mouse models (Golden, Buxbaum and De Rubeis, 2018; Verma *et al.*, 2019).

In a *Fmr1* KO mouse model of ID, contextual fear memory retrieval was impaired, even though learning acquisition was intact (Li *et al.*, 2020). The memory retrieval impairment was a result of an alteration in the ensemble of neurons activated during contextual encoding. Interestingly, providing environmental enrichment was able to rescue this deficit, while inhibiting the hippocampal cells active during enrichment prevented efficient retrieval (Li *et al.*, 2020).

A mouse model with a truncated *SHANK3* gene, caused by a nonsense mutation R1117X, was previously associated with dysregulation in the cortical dynamics as a result of a reduction in the inhibitory drive (Ali *et al.*, 2021). *SHANK3* mutant mice underwent trace fear conditioning, which involves the addition of a time interval during associative learning. Trace fear conditioning is thought to depend on the normal functioning of the mPFC (Han *et al.*, 2003). R1117X mutants displayed reduced freezing behaviour during trace fear conditioning, not during normal fear conditioning, supporting the impairment seen at the cortical level (Ali *et al.*, 2021). However, when cortical inhibitory activity was virally enhanced, the deficit in trace fear learning was improved (Ali *et al.*, 2021), highlighting the contributions of excitation – inhibition imbalance in ID (Text box 2).

Impairments in the hippocampal – basolateral amygdala projections were also linked to ID (Zhang *et al.*, 2015). Mutations in *Il1rapl1* gene, which encodes for a member of a IL1/Toll receptor family thought to be present at excitatory synapses, were previously showed to cause ID. *Il1rapl1* mutants were found to have abnormal excitation – inhibition balance, as a result of decreased excitatory drive at the hippocampal – amygadalar projections (Zhang *et al.*, 2015). This network imbalance was associated with a reduction in freezing behaviour during a context-dependent fear conditioning paradigm. However, optical stimulation of

hippocampal – basolateral amygdala synapses results in normal contextual fear levels in mutant mice (Zhang *et al.*, 2015).

PFC – hippocampal functional connectivity was assessed in a trisomic Ts65Dn Down syndrome model of ID (Alemany-González *et al.*, 2020). Neurons fire action potentials at various frequencies and these oscillations can be reliably recorded. Inter-regional synchrony of this oscillatory activity is now known to happen during particular behaviour, such as learning (Sigurdsson and Duvarci, 2016). Simultaneous electrode recordings form the PFC and hippocampus in a Down syndrome mutant line revealed hyper-synchronicity of these two regions in various states, such as wakefulness, sleep, and memory (Alemany-González *et al.*, 2020). In a learning and memory task, mutant mice displayed impairments in memory retrieval, which was associated with disrupted neural signals between PFC and hippocampus. Treatment with green tea was sufficient to ameliorate the deficits observed in memory retrieval. Interestingly, green tea was shown to enhance cognitive abilities in children with Down syndrome (Alemany-González *et al.*, 2020).

Overall, the neural circuitry which underlie learning and memory mechanisms seems to be affected in ID. However, therapeutic approaches against impairments in these networks seem to be effective in reducing ID symptomatology across a variety of ID mouse models (Li *et al.*, 2020; Alemany-González *et al.*, 2020; Ali *et al.*, 2021; Zhang *et al.*, 2015; Al-Amri *et al.*, 2022).

1.1.3 ID: from circuits to neurons

The array of behavioural deficits observed in ID, such as altered social interaction, repetitive actions, learning and memory impairments, thus far, have been attributed largely due to discrepancies in brain network activity and neural connectivity between brain regions. However, changes at cellular and molecular level have also been shown to contribute to ID aetiology and symptomatology. The following section will focus on the role synaptic and dendritic plasticity, and neurogenesis in mouse models of ID.

Synaptic plasticity. The CNS is comprised of neurons with highly specialized morphologies and connections which are the building blocks of the neural circuits that underlie human cognition and behaviour. The processing and transmission of information is carried out in the form of electrical signals between neurons, at specialized locations known as synapse. Synapses are neuronal junctions which mediate the communication between neurons and are generally comprised of a presynaptic terminal (axon), a synaptic cleft (~25 nm), and the postsynaptic compartment (dendrites, spines) (Fig. 5). In response to action potentials, the presynaptic neuron release vesicles packed with neurotransmitter, which diffuse across the synaptic cleft and bind to receptors on the postsynaptic membrane, allowing for the signals to be further propagated (Fig. 5) (Ho, Lee and Martin, 2011). Synapses are highly dynamic structures which modify their morphology in response to stimuli (Fig. 5). Strengthening or weakening of synapses underlie the two processes of long-term potentiation (LTP) and long-term depression (LTD), which are thought to be the cellular basis of learning and memory, o a process known as synaptic plasticity. Synaptic plasticity changes entail both functional changes, such as increased synaptic input and changes in release probability, and structural

changes, such as insertion of receptors and formation of spines (Fig. 5) (Ho, Lee and Martin, 2011).

Synaptic plasticity occurs throughout the lifespan. However, after birth the brain goes through a 'critical period of plasticity' as it is exposed to many new stimuli, which lead to a significant increase in the connections formed between neurons (Reh *et al.*, 2020). This enables juveniles to learn new information rapidly. This period of heightened plasticity during development is highly susceptible to changes, such that neuronal disturbances during this period could affect later development (Lacagnina *et al.*, 2019; Ho, Lee and Martin, 2011; Reh *et al.*, 2020). Such neuronal disturbances have been observed in mouse models of ID, with a large body of literature revealing structural and functional abnormalities in synaptic plasticity across various developmental stages.

LTP and LTD. Multiple lines of evidence suggest that LTP and LTD are perturbed in several brain areas, across various mouse models of ID, with different mutant models generating distinct deficits in LTP and LTD. Heterozygous and homozygous *SHANK3* mutant mice displayed reduced glutamatergic transmission and impaired LTP in the hippocampus compared with WT controls, with a more severe deficit in homozygotes mice (Yang *et al.*, 2012). A *SYNGAP1* mutant mouse model displayed altered LTP in layer 2/3 of the somatosensory cortex (Llamosas *et al.*, 2021).

In a *FMR1* KO mouse model, LTP in the anterior cingulate cortex was shown to be significantly reduced compared with WT controls; however, administration of metabotropic glutamate receptor 5 antagonist ameliorated the deficits on plasticity seen in the *FMR1* KO model (Chen *et al.*, 2014). In a rat model of *FMR1* KO, were exon 4 is deleted, LTP induced by theta-burst stimulation protocol was diminished in rats with this mutation compared to

WT controls (Tian *et al.*, 2017). Further electrophysiological analysis revealed that LTD induced by a low frequency stimulation protocol is also weakened in hippocampal slices from *FMR1* KO rats (Tian *et al.*, 2017). Developmental changes to LTP have also been involved in mouse models of ID. For example, age-dependent effects were observed in the mPFC of *FMR1* KO mice (Martin *et al.*, 2016). Electrophysiological recordings displayed deficits in LTP only in 12 month old mice, but not in slices from 2 month old mice; acute pharmacological application of metabotropic glutamate receptor 5 antagonist rescued LTP changes seen in the aged animals (Martin *et al.*, 2016).

Both in *NLGN1* a conditional KO (cKO) mice and a triple *NLGN1, NLGN2,* and *NLGN3* cKO mice*,* NMDAR-mediated excitatory postsynaptic currents and NMDAR-dependent LTP in hippocampal CA1 slices were fully blocked, but basal synaptic function was unaffected (Jiang *et al.*, 2017). In quadruple *NLGN1-4* cKO mice, in the CA1 region of the hippocampus, NMDAR-mediated transmission was reduced and LTP was completely abolished, but these were restored by experimental expression of *NLGN1* (Wu *et al.*, 2019). In contrast, a single KO of *NLGN3* was not sufficient to impair LTP in hippocampal slices from mice (Muellerleile *et al.*, 2022).

CACNG2 encodes stargazin (voltage-dependent calcium channel gamma subunit 2), a member of transmembrane AMPA (α-amino-3-hydroxyl-5-methyl-4-isoxazole-propionic acid) receptor regulatory proteins (TARP). Mice with knock-in of *CACNG2* mutations (V143L) implicated in ID displayed reduced excitatory synaptic transmission and LTP in CA1 basal pyramidal neurons, but not in apical CA1 synapses (Caldeira *et al.*, 2022). Another gene that was recently implicated in ASD and ID is *NSUN2,* which encodes a protein that regulates protein synthesis by directly affecting RNA methylation. In hippocampal slices

from mice with an *NSUN2* loss-of-function mutation NMDAR-dependent LTP was significantly reduced compared with WT controls (George, Bashir and Hussain, 2022). Despite variability in the ID / ASD mouse models and the brain regions investigated and other experimental conditions, there is a consensus that synaptic plasticity seems to be impaired in ID disorders (Srivastava and Schwartz, 2014; Verma *et al.*, 2019).

Dendritic spines. Dendritic spines are one of the major components of synaptic plasticity. Spines are small protrusions (0.1 – 0.5 μm in length) on dendrites which receive most of the excitatory input in the brain. The advent of two-photon laser scanning microscopy (2P-LSM) has advanced the study of the morphology and functional role of these protrusions (Kasai *et al.*, 2021; Verma *et al.*, 2019). On a molecular level, each spine contains a postsynaptic density, AMPAR, and NMDAR. *In vivo* imaging techniques portray dendritic spines as extremely dynamic structures, with a morphology highly linked with synaptic plasticity, such that an increased density and size have been linked with LTP, while a decreased density and size have been associated with LTD (Fig. 5) (Lai, Franke and Gan, 2012; Hruska *et al.*, 2018). As dendritic spines are tightly correlated with synaptic plasticity, they have been investigated in relation to neurodevelopmental disorders. Changes in spine density, size and shape have all been implicated in ID (Kasai *et al.*, 2021; Zieger and Choquet, 2021; Verma *et al.*, 2019).

In post-mortem brain tissue from patients with ID, Golgi staining revealed dendritic spine loss and an abundance of immature spines (long and thin) in cortical neurons (Kaufmann and Moser, 2000). These findings have been replicated in various mouse models of ID. In a *CACNG2* V143L mutant mouse model, a significant decrease in mature spines was recorded in CA1 region of the hippocampus, although the total density of spines was WT controls

(Caldeira *et al.*, 2022). Mature spines typically have a mushroom and stubby-like morphology, but in *CACNG2* – V143L mice, the majority of spines presented a branched, thin and filipodia-like morphology with a decrease in the postsynaptic density length, suggesting an impairment in the maturation of dendritic spines. The increase in immature spines correlated with LTP deficits exhibited by these mice (Caldeira *et al.*, 2022). In young mice with double KO of *SHANK1* and *SHANK3,* Golgi staining revealed that spine density and the number of branches in the hippocampus and cortex were significantly reduced (Mossa *et al.*, 2021).

In hippocampal slices from *NLGN1-4* quadruple cKO only about 20% of spines on secondary dendritic branches showed spine growth following LTP induction in the CA1 subfield, compared with 70% of spines in the WT hippocampal slices (Wu *et al.*, 2019). However, this deficits was rescued by experimental expression of *NLGN1* (Wu *et al.*, 2019).

Mice with KO of X-linked ID-implicated genes *RAB39B,* an encoding RAS GTPase important in the development and the structure of AMPAR, were characterized by an increase in the neuronal excitability and the proportion of immature spines (Mignogna *et al.*, 2021). Spines were assessed at specific timepoints correlating with different stages of hippocampal development: postnatal day 20 (P20) – spinogenesis, P30 – synaptic pruning, and P45 – spine maintenance (Fiala *et al.*, 1998; Paolicelli *et al.*, 2011; Lendvai *et al.*, 2000). Hippocampal spines in *RAB39B* KO mice showed differences in density and morphology at P30 and P45 compared with WT mice, with the majority of spines displaying an immature morphology (Mignogna *et al.*, 2021). This suggests that RAB39B might not be essential for spinogenesis, only for synaptic pruning and spine maintenance (Mignogna *et al.*, 2021). However, experimental expression of either RAB39B or GluA2 subunit in hippocampal slices from

RAB39B KO mice was observed to rescue the reorganization and induced spine maturation (Mignogna *et al.*, 2021).

Overall, a decrease in spine density or maturity has been observed across various models of ID (Kasai *et al.*, 2021; Zieger and Choquet, 2021). Normal functioning of dendritic spines is essential for synaptic plasticity, and perturbations in these protrusions, especially during development, might contribute to the learning and memory deficits observed in mouse models of ID.

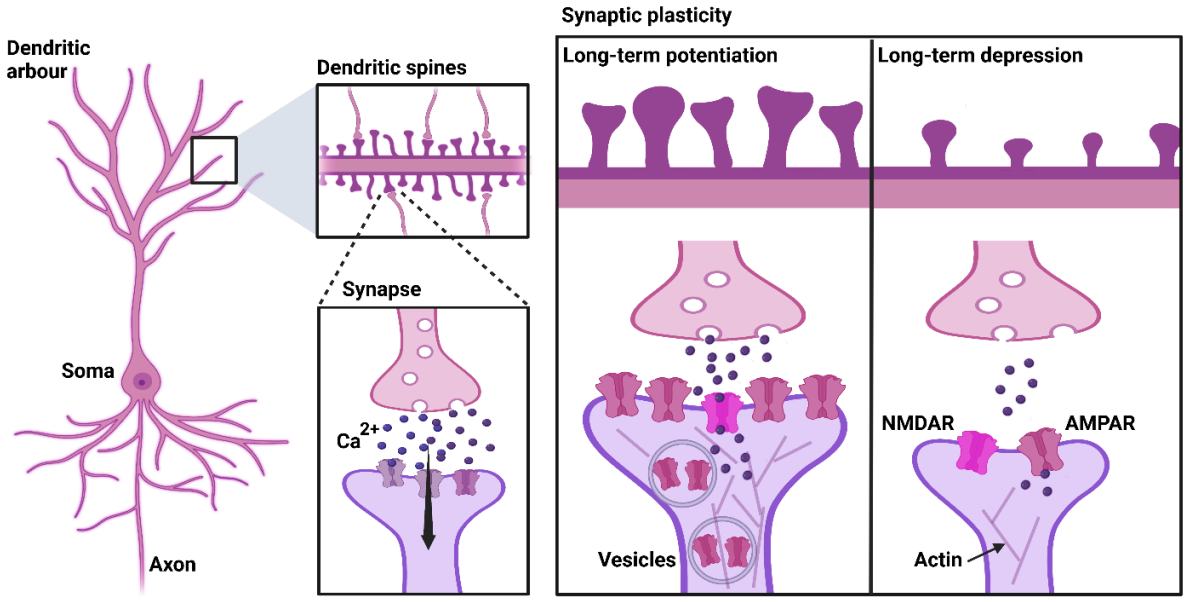

Figure 5. Neuronal communication and synaptic plasticity. Schematic representation of neuronal communication and the two main processes which underlie synaptic plasticity: long-term potentiation and long-term depression. Long-term potentiation leads to increase in number of spines, spine growth, increased receptor number (AMPAR, NMDAR) and actin filaments. Long-term depression leads to decrease in number of spines, spine shrinkage, reduced receptor number (AMPAR, NMDAR) and actin filaments. Ca^{2+} – calcium, NMDAR – N-methyl-D-aspartate receptor, AMPAR - α-amino-3-hydroxyl-5-methyl-4-isoxazole-propionic acid. Figure created with *BioRender.com.*

Neurogenesis. Neurogenesis is a process by which new neurons are formed from neural stem cells which proliferate and differentiate into neurons during development or in the mature CNS (Gage, 2000). It is important to note the controversial nature of neurogenesis in the mature CNS. Despite some research pointing to adult neurogenesis, even in humans (Moreno-Jiménez *et al.*, 2019), there are still many questions as to whether this occurs in the adult brain (Leal-Galicia *et al.*, 2021).Nonetheless, there are two main zones in the mammalian brain where new neurons are generated, the walls of the lateral ventricle and the subgranular zone of the hippocampus. Neural stem cells from the lateral ventricle travel via the rostral migratory route to provide new neurons in the olfactory bulb, whilst in the hippocampus the neural stem cells in the subgranular zone of the dentate gyrus are responsible for producing new granule cells (Gage, 2000; Alvarez-Buylla and Garcıa-Verdugo, 2002; Ming and Song, 2011). Increased adult neurogenesis is thought to be associated with learning, exercise, and enriched environments in rodents (Jurkowski *et al.,* 2020). However, impairment in adult neurogenesis has been linked to a number of neuropsychiatric and neurodevelopmental disorders, including ASD and ID.

Various mutations implicated in ID have been linked to altered neurogenesis. For example, in humans, a homozygous mutation in the *IMPA1* (inositol monophosphatase 1) gene leads to severe ID (Figueiredo *et al.*, 2021). Induced pluripotent stem cells obtained from patients with *IMPA1* mutation were used to produce hippocampal dentate gyrus neurons. These neurons lacked IMPA1 and presented severe abnormalities in neurogenesis, including increased apoptosis and altered proliferation and differentiation, compared to controls (Figueiredo *et al.*, 2021).

Multiple mouse models of ID have also displayed abnormalities in adult neurogenesis. An *RPS6KA3* mutant mouse model of the Coffin-Lowry syndrome, which is characterized by ID and facial dysmorphism, displayed altered adult hippocampal neurogenesis and impaired spatial memory. Doublecortin staining following multiple spatial memory tasks revealed reduced recruitment of neural precursor cells from the dentate gyrus in *RPS6KA3* mutants compared to WT controls, suggesting a potential role in the cognitive dysfunction seen in Coffin-Lowry syndrome (Castillon *et al.*, 2018). Adult born neurons were shown to exhibit limited survival abilities in a *PAK3* mutant mouse model of X-linked ID (Castillon *et al.*, 2020). *PAK3* mutants also displayed alternations in the learning-associated recruitment of newly generated neurons as shown by decreased doublecortin staining following a spatial memory behavioural paradigm (Castillon *et al.*, 2020). In mice deficient in the X-linked ID gene *OPHN1,* encoding oligophrenin-1, a Rho GTPase activating protein important in synaptic function, a substantial reduction in adult new-born neurons in the dentate gyrus was revealed by BrdU (5'-bromo-2'-deoxyuridine) staining. Administration of a clinically approved Rho-associated protein kinase, known as fasudil, improved neurogenesis and long-term survival of new-born neurons (Allegra *et al.*, 2017). As the underlying cause for ID is still largely unknown, deficits in neurogenesis could constitute an important factor contributing to cognitive dysfunction and pharmacological treatment may partially correct some of the deficits.

1.1.4 Mitochondria and endoplasmic reticulum

Alongside behavioural and cognitive deficits characteristic for ID and associated disorders, metabolic conditions are often seen in neurodevelopmental conditions. Impairments in the molecular machinery and proper functioning of mitochondria or other associated organelles,

such as endoplasmic reticulum, are linked to metabolic disorders and are commonly found in ID and ASD (Klein et al., 2021).

Mitochondria – structure and function. Intact energy metabolism and oxygen supply in the brain are essential for the healthy functioning of brain processes, such as neurogenesis, neurotransmission, and synaptic plasticity. Mitochondria are dynamic organelles, which are involved in the production of adenosine triphosphate (ATP), the main energy transfer molecule in cells. Structurally, mitochondria contain a double outer and inner membrane, and have their own small circular genome, known as mitochondrial DNA. This mitochondrial DNA is inherited solely from the mother and is thought to be highly susceptible to mutations due to a low reliability of the mitochondrial DNA polymerase activity (Song *et al.*, 2005; Giacomello *et al.*, 2020).

Mitochondria are very effective at metabolizing oxygen to make ATP. Most neuronal ATP is produced by mitochondrial oxidative phosphorylation (Giacomello *et al.*, 2020). The inner membrane contains some structures called cristae, where the oxidative phosphorylation takes place. The cristae contain the five mitochondrial respiratory chain complexes, responsible for generating ATP, while simultaneously, free radicals, such as reactive oxygen and nitrogen, are synthetized (Giacomello *et al.*, 2020). Irregularities in mitochondria, mitochondria respiratory chain complexes or ATP synthesis could lead to a reduction in the generation of ATP and / or more free radicals, which can cause oxidative stress and damage to cells (Valenti *et al.*, 2014).

Mitochondria are motile and travel along microtubules to areas of the cells where there is a high metabolic demand. Mitochondria can be found in all neuronal cell compartments, such as axons, dendritic shafts, presynaptic terminals, and even dendritic spines (Cardanho-

Ramos, Faria-Pereira and Morais, 2020). Two key processes occur in mitochondria: fission and fusion, essential for regulating mitochondria morphology important for mitochondrial support function and prevention of damage (Giacomello *et al.*, 2020). Fission is mediated by two main proteins, dynamin-related protein 1 and fission 1 protein. Fission is thought to be important for mitochondrial division during cell growth and in response to mitochondrial damage. Recently, it was shown that two types of fission exist; midzone fission happens during cell growth, while peripheral fission takes place to get rid of damaged mitochondria (Kleele *et al.*, 2021). Fusion is mediated by proteins, such as mitofusin 1, mitofusin 2, and optic atrophy 1. Fusion seems to be essential for cell survival, mitochondria motility within neurons, as well as transferring enzymes, metabolites, and mitochondria gene products between mitochondria (Giacomello *et al.*, 2020).

Mitochondria and ID. Most mitochondrial-related disorders arise from impairments in the mtDNA or the mitochondrial oxidative phosphorylation machinery. Mitochondria dysfunction and mitochondrial oxidative stress have been linked to multiple disorders that lead to ID. For example, ASD-related disorders such as autism, RTT and FXS, have all been linked to changes in mitochondria morphology, such as vacuolization of mitochondria, as well as dysfunction in mitochondria respiratory chain complexes and increased oxidative stress (Valenti *et al.*, 2014). Recently, ID-associated mutations in *ZBTB11,* encoding the zinc-finger and BTB domain containing 11 (ZBTB11) transcription factor, have been shown to play a role in mitochondrial function (Wilson *et al.*, 2020). ZBTB11 was shown to interact with nuclear respiratory factor 2, thereby promoting the biosynthesis of one of the MRC complexes. Mutations in *ZBTB11* impair the assembly of MRC complexes, mitochondrial respiration and caused cell death (Wilson *et al.*, 2020).

Both mitochondrial DNA replication and mitochondrial oxidative phosphorylation system are reliant on mitochondrial DNA transcription, which is dependent of mitochondrial RNA polymerase (Giacomello *et al.*, 2020). Recently, it was shown that mutations in mitochondrial RNA polymerase are linked to neurological symptoms (Oláhová *et al.*, 2021). Defects in the mitochondrial DNA transcription machinery were associated with ID in eight patients with various genetic mutations in the mitochondrial RNA polymerase (Oláhová *et al.*, 2021).

Endoplasmic reticulum – structure and function. The endoplasmic reticulum (ER) is membrane-bound subcellular organelle, which is composed of highly dynamic sheet-like membrane structures with nanoscale holes and clustered tubules (Schroeder *et al.*, 2019; Schwarz and Blower, 2016). The ER is a very important organelle, involved in protein synthesis, post-translational modification, folding and transport of proteins, as well as Ca^{2+} (calcium) homeostasis and signalling. Dysregulations in the homeostatic functioning or the morphology of ER leads to a process called ER stress, which causes unfolding or misfolding of proteins (Schwarz and Blower, 2016). Upon ER stress, unfolded protein response is initialized to diminish the damaged triggered by issues in protein folding. ER-associated degradation is a quality control mechanism of the ER to ensure that all proteins not properly assembled or folded are degraded. However, constant, and extreme ER stress ultimately lead to cell death (Schwarz and Blower, 2016)

Endoplasmic reticulum and ID. Chronic ER stress has been implicated in neuronal disorders mainly involving neurodegeneration, while defects in molecules involved in ER-associated degradation have been shown to cause neurological symptoms, such as cognitive impairment. N-glycanase 1 (NGLY1) is an enzyme that has a role in the degradation of misfolded proteins of the ER (Caglayan *et al.*, 2015). A frameshift mutation in *NGLY1*, which reduces the ability

of neurons to respond to ER stress on account of an aggregation of misfolded proteins, has been shown to cause ID along with neuromotor deficits in humans (Caglayan *et al.*, 2015).

Overall, these data highlight dysregulation of both the function and the morphology of mitochondria and ER, as another factor contributing to the aetiology of ID.

1.2 PDZ domain-containing protein 8 (*PDZD8*)

ID and ASD are caused by a wide range of genetic mutations. Recently, we identified a novel gene liked to ID. We found that syndromic ID with autism-like symptoms in two independent families from the Arabian Peninsula was caused by the presence of homozygous premature termination codons in the *PDZD8* gene, which encodes for the PDZ domain-containing protein 8 (Al-Amri *et al.*, 2022). PDZD8 is a 1,154 amino acids (aa) ER transmembrane (TM) protein (UniProtKB: Q8NEN9). PDZD8 is linked to the ER membrane by an N-terminal TM helical domain (2-24 aa), which is followed by a synaptogamin-like mitochondrial lipid-binding (SMP) domain (91-294 aa), a PSD95/D1gA/ZO-1-like (PDZ) domain (366-449 aa), a proline-rich region (551-626 aa), a phorbol-ester/diacylglycerol-binding (C1) domain (840-891 aa), and a coiled-coil (CC) domain (1,028-1,063 aa; Fig. 6) ('UniProt,' 2021; Shirane *et al.*, 2020; Elbaz-Alon *et al.*, 2020). In this chapter I will cover the research currently published on the role of PDZD8 in humans and animal models.

1.2.1 Pdzd8: an endoplasmic reticulum – mitochondria tether

Mitochondria-ER contact sites. Recently, Pdzd8 was shown to function as a tethering protein, facilitating the formation of mitochondria-ER contact sites (MERCs) (Hirabayashi *et al.*, 2017). Contact sites between two membranes are regions of close apposition, which enables communication between organelles within a cell. MERCs were initially discovered in the 1950s using electron microscopy (Bernhard and Rouiller, 1956), and have been widely

researched since then. MERCs range between 10-80 nm in size and their molecular composition greatly impacts their role within a cell. These tethering complexes have been involved in multiple cellular homeostatic functions, such as Ca^{2+} homeostasis, lipid metabolism, ER stress, and mitochondria quality control (Giacomello *et al.*, 2020; Wu, Carvalho and Voeltz, 2018; Wilson and Metzakopian, 2021). There are several tethering complexes that bridge the mitochondria to the ER. For example, the first structure detected between ER and mitochondria is a known as 1,4,5-triphosphate receptor – deglycase – glucose related protein 75 – voltage-dependent anion channel (an outer mitochondrial membrane protein). This tethering complex facilitates ER-mitochondria Ca^{2+} transmission and loss of deglycase or glucose related protein 75 prevents Ca^{2+} flow into the mitochondria (Giacomello *et al.*, 2020; Wilson and Metzakopian, 2021).

ER-mitochondria encounter structures (ERMES) are also tethering complexes between the ER and mitochondria in budding yeast (*Saccharomyces cerevisiae*). Three of these ERMES protein structures (Mmm1, Mdm12, and Mdm34) contain a SMP domain. Not long ago, Pdzd8 was identified as the mammalian paralogue of an ERMES protein, as the SMP domain of Pdzd8 is functionally homologous to that of Mmm1 (Hirabayashi *et al.*, 2017; Wideman *et al.*, 2018). Electron microscopy 3D reconstruction of HeLa cells lacking Pdzd8 revealed a significant reduction in MERCs found per mitochondria surface area compared to control HeLa cells, suggesting that Pdzd8 is involved for MERCs formation (Hirabayashi *et al.*, 2017). Localization of Pdzd8 to the ER membrane was further confirmed by multiple studies (Elbaz-Alon *et al.*, 2020; Gao *et al.*, 2022; Guillén-Samander, Bian and De Camilli, 2019; Hewitt *et al.*, 2020).

Ca^{2+} homeostasis. MERCs are involved in maintaining Ca^{2+} homeostasis. Ca^{2+} is an important second messenger involved in fundamental cellular pathways and biochemical reactions. The ER is known to be a crucial source of cytosolic Ca^{2+}. Ca^{2+} from the ER is thought to leave through the 1,4,5-triphosphate receptors and ryanodine receptors and transferred to the mitochondria via voltage-dependent anion channels (Fig. 6) (Wilson and Metzakopian, 2021). Subsequently, Ca^{2+} uptake into the mitochondria is managed by the mitochondria Ca^{2+} uniporter, a Ca^{2+} channel present on the mitochondrial inner membrane. Low concentrations of cytosolic Ca^{2+} are required for Ca^{2+} signalling and other cellular processes to take place, and usually the cytosolic Ca^{2+} concentration is less than 100 nM. However, a much higher concentration of Ca^{2+} is required to open the mitochondrial Ca^{2+} uniporter, between 1 – 5 μM depending on the composition of the channel. Only when the ER comes in close contact with the mitochondria, the cytoplasmic Ca^{2+} concentration rise enough to enable opening of the mitochondria Ca^{2+} uniporter, thus allowing Ca^{2+} to be taken up by the mitochondria (Moltedo, Remondelli and Amodio, 2019; Wilson and Metzakopian, 2021).

Ca^{2+} imaging experiments have shown that electric stimulation triggers Ca^{2+} release from the ER that is taken up by the mitochondria in excitatory neurons *in vitro* (Hirabayashi *et al.*, 2017). However, when *Pdzd8* is knocked down in these neurons, there is a significant decrease in the Ca^{2+} entering the mitochondria. Consequently, synaptic stimulation, which caused intracellular Ca^{2+} release, led to an overall increase cytosolic Ca^{2+} concentration and heightened dendritic Ca^{2+} transients (Hirabayashi *et al.*, 2017; O'Hare *et al.*, 2021). This implies that Pdzd8 acts as a functional tether between mitochondria and the ER which

facilitates Ca^{2+} transfer between the two organelles. However, neither a Pdzd8 binding site on mitochondria nor a mitochondrial binding site of Pdzd8 have been found.

Ca^{2+} plays a critical role in synaptic activation and plasticity and the ER is the main intracellular storage site for Ca^{2+}, which sequesters most of the Ca^{2+} in neurons and spans across the dendritic arbour (Takechi, Eilers and Konnerth, 1998; Schwarz and Blower, 2016). Additionally, the ER releases Ca^{2+} in an activity-dependent manner, which substantially intensifies the impact of Ca^{2+} influx from the extracellular space, and suggests that the Ca^{2+} from the ER could potentially affect synaptic plasticity by altering Ca^{2+} concentration in dendrites (Hirabayashi *et al.*, 2017; O'Hare *et al.*, 2021; Takechi, Eilers and Konnerth, 1998; Schwarz and Blower, 2016). This indicates that Pdzd8 might facilitate plasticity due to its role in intracellular Ca^{2+} buffering. Using cell specific *Pdzd8* deficient mice, it was revealed during awake imaging session *in vivo* that heightened intracellular calcium release has a role in promoting plasticity in hippocampal pyramidal neurons dendrites (O'Hare *et al.*, 2021). Given the important roles mitochondrial Ca^{2+} has in ATP synthesis and dendritic Ca^{2+} in neurotransmission and synaptic plasticity, Pdzd8 deficiency is likely to affect these processes.

Lipid transfer: Pdzd8 – Protrudin – Rab7 interaction. One of the major lipid storage sites is the ER, which, together with the mitochondria, is highly involved in lipid metabolism. MERCs enable and play an essential role in many lipid metabolism cascades, as well as being key facilitators of lipid transport between the ER and mitochondria (Moltedo, Remondelli and Amodio, 2019). For example, an important lipid metabolic pathway involves the exchange of phospholipids, such as phosphatidylserine and phosphatidylethanolamine, between the ER and the mitochondria. Phosphatidylserine is produced in the ER, but to

generate other phospholipids, such as phosphatidylethanolamine, it is transported to the mitochondrial inner membrane via MERCs, where phosphatidylserine decarboxylase makes it into phosphatidylethanolamine. Phosphatidylethanolamine is an important component of membranes, and it is shuttled back to the ER where it is further processed into other molecules. Phosphatidylserine decarboxylase is only present in the mitochondria, making MERCs essential in this lipid metabolic cascade (Moltedo, Remondelli and Amodio, 2019).

Additionally, the ER forms membrane contacting site with other organelles such as endosomes. Endosomes are dynamic organelles with roles in signalling, sorting and trafficking proteins and lipids across subcellular compartments of the secretory and endocytic pathways (Raiborg, Wenzel and Stenmark, 2015). For example, components that are endocytosed in a cell are known as early endosomes. A fraction of early endosomes further mature in late endosomes and then lysosomes, which are essential for the degradation of the endocytosed material. The transformation from late endosomes to lysosomes is continuous and often referred to as endolysosomes (Raiborg, Wenzel and Stenmark, 2015).

Membrane contact sites between the ER and late endosomes are known to be crucial for endosomal motility and this is thought to rely upon lipid transfer. Only recently has the process behind the lipid transfer from the ER to endosomes begun to be understood (Raiborg, Wenzel and Stenmark, 2015). For example, lipids can be transported via lipid transport proteins, which act as membrane contact sites. These proteins exhibit elements which contain the lipids in a hydrophobic cavity after extracting them from a membrane. The SMP domain in *Pdzd8* is often expressed in lipid transport proteins, as it is part of the TULIP (tubular lipid binding protein), a class of proteins essential for lipid signalling and trafficking of lipids (Shirane *et al.*, 2020; Raiborg, Wenzel and Stenmark, 2015). Additionally, affinity

purification mass spectrometry and complementary proximity-based labelling technology, used for determining protein-protein interactions, has found that Pdzd8 is in close proximity with endolysosomes (Liu *et al.*, 2018).

Protrudin. One protein that bridges the ER to endolysosomes is protrudin. Mutations in *ZFYVE27* encoding protrudin can influence ER morphology and are linked to hereditary spastic paraplegia (Raiborg, Wenzel and Stenmark, 2015; Mannan *et al.*, 2006). To better understand the role of protrudin in endosome maturation, proteomics analysis was conducted, which revealed that Pdzd8 is associated with protrudin, and the TM domain of Pdzd8 is crucial for this interaction as well as for ER localization (Shirane *et al.*, 2020; Elbaz-Alon *et al.*, 2020). Further investigation revealed that membrane contacts sites between ER and endolysosomes are enhanced when Pdzd8 is present in cells compared to when this is reduced via siRNA-mediated depletion. The presence of protrudin and Pdzd8 had a cooperative effect on facilitating contacts between ER and endolysosomes. Pdzd8 and protrudin also assist in the tethering of the ER to the mitochondria (Shirane *et al.*, 2020; Hirabayashi *et al.*, 2017). However, Pdzd8 and protrudin seem to be more important for the development of membrane contact sites between ER and endolysosomes than ER and mitochondria, as cells not expressing either protein have a stronger impact on ER – endolysosomes contacts than ER – mitochondria ones (Shirane *et al.*, 2020).

Lipid transfer is one of the main activities of membrane contact sites. As Pdzd8 was found to promote the generation of connections between the ER and other organelles, it is possible that it might have a role in lipid transfer. Indeed, liposome Forster resonance energy transfer (FRET) used to measure lipid transfer activity revealed that Pdzd8 extracts phospholipids such as, phosphatidic acid, phosphatidylserine, and phosphatidylethanolamine, as well as

cholesterol, but with a lower efficacy (Shirane *et al.*, 2020). Lipid transfer involves removal and incorporation of lipids from one membrane to another, but Pdzd8 was only involved in the removal of lipids via its SMP domain, as it is unable to deliver lipids to acceptor liposomes (Shirane *et al.*, 2020; Gao *et al.*, 2022). This lipid trafficking ability of Pdzd8 was observed *in vivo* too, as *Pdzd8*-deficient neurons displayed decreased co-localization between endolysosomes and phospholipids, such as phosphatidylserine (Shirane *et al.*, 2020).

The Pdzd8 and protrudin system also seems to be involved in neuronal development. Lack of Pdzd8 and protrudin result in morphological abnormalities, identified by a shortening in the size of the axons and bigger somatodendritic arbours of primary mouse neurons (Shirane *et al.*, 2020). As axonal malformations were observed, co-localization of Tau1 and α-tubulin were employed as a measure of investigating axonal health. Reduction in Pdzd8 and protrudin resulted in increased separation of Tau1 and α-tubulin, which is indicative of axonal deterioration (Shirane *et al.*, 2020). The changes in cellular morphology caused by a reduction in both Pdzd8 and protrudin suggest that these two proteins have a neuronal protective role. Additionally, protrudin has been implicated in the facilitation of anterograde transport of endolysosomes (Gao *et al.*, 2022). This protrudin-mediated transport at membrane contact sites was also shown to be important for neurite outgrowth (Raiborg, Wenzel and Stenmark, 2015). Pdzd8's interaction with protrudin and its role in lipid transfer suggest a functional role in neuronal growth. Reducing *Pdzd8* expression via shRNA in cells resulted in decreased neuronal growth factor and neuronal growth factor-dependent neurite expansion, whilst expressing *Pdzd8* in these cells prevented cellular deficits from occurring. However, neurite growth abnormalities were not prevented when *Pdzd8* containing a

mutation in the SMP domain was expressed in these cells, implying that the lipid transfer capacity of PDZD8 is required for neurite outgrowth (Gao *et al.*, 2022).

Rab7. In the absence of Pdzd8 and protrudin, endolysosomes display irregularities, such as enlargement and changes in ultrastructure, in mouse primary neurons (Shirane *et al.*, 2020). Enlarged endolysosomes were also observed in cells expressing lipid transfer-deficient *Pdzd8* with mutation in the SMP domain, suggesting a role of *Pdzd8* in the morphology and maturation of endolysosomes (Gao *et al.*, 2022). However, there are many other proteins known to have significant role in endosomal maturation, which might interact with Pdzd8 as well. Rab (Ras-related protein) GTPases are key players in the maturation of endosomes; these proteins function as molecular controls that are bound to GTP when active and are inactivated via GTP hydrolysis to GDP. Specifically, mutations in *RAB7*, encoding Rab7 protein involved in anchoring endosomes and mitochondria, have been linked to Charcot Marie-Tooth type 2B neuropathy (Verhoeven *et al.*, 2003; Houlden *et al.*, 2004). Rab7 was shown to be important for the generation and maturation of late endosomes and serves in their motility (Wong, Ysselstein and Krainc, 2018; Raiborg, Wenzel and Stenmark, 2015). Live imaging of cells displayed co-localization of Pdzd8 and Rab7 at ER. Overexpression of Rab7 resulted in enriched Pdzd8 at the ER. Increased presence of Pdzd8 was linked only to Rab7 in the GTP-bound state, suggesting that Pdzd8 recruitment to the ER is dependent on the activated state of Rab7 (Elbaz-Alon *et al.*, 2020; Gao *et al.*, 2022). Using electron microscopy, GTP-bound Rab7 was found to be heightened at contacts between ER and endolysosomes (Guillén-Samander, Bian and De Camilli, 2019). Further analysis showed that there is a triple interaction between Pdzd8, protrudin and Rab7, as shown by presence of all three proteins at ER and late endosomes. Pdzd8 is connected with protrudin and Rab7 via

different domains. Deletion of various Pdzd8 domains revealed that Pdzd8 comes in contact with late endosomes through communication with Rab7 via the C1 and CC domains, whereas anchoring to protrudin takes places via TM-mediated domain connections (Elbaz-Alon *et al.*, 2020; Gao *et al.*, 2022; Guillén-Samander, Bian and De Camilli, 2019; Khan *et al.*, 2021). Pdzd8 that lacks the TM domain failed to target the ER membrane, indicating that the TM domain is responsible for securing it to the ER (Elbaz-Alon *et al.*, 2020; Guillén-Samander, Bian and De Camilli, 2019; Shirane *et al.*, 2020; Gao *et al.*, 2022). Electron microscopy analysis of Pdzd8 – Rab7 connections at the ER revealed ER – endosome contact sites, as well as MERCs, as mitochondria were closely associated with Rab7 – endosome in *Pdzd8*-expressing cells (Elbaz-Alon *et al.*, 2020; Gao *et al.*, 2022).

The interaction of Pdzd8 with Rab7 and localization to ER – LE contacts spans multiple species. Recently it was shown that Pdzd8 interacts with the ER via Rab7 in *Caenorhabditis elegans* (*C. elegans*) (Jeyasimman *et al.*, 2021). Pdzd8 together with another SMP molecule, testis-expressed protein 2, was shown to prevent death in *C. elegans* via their lipid trafficking ability, by preventing build-up of phosphatidylinositol 4,5-biphosphate in late endosomes, which has been involved in endosomal anomalies (Jeyasimman *et al.*, 2021). Overall, these findings bring a better understanding of the function Pdzd8 by exposing a role of Pdzd8 in two distinct contact sites, ER – endosomes and MERCs, via interactions with protrudin and Rab7.

Mitophagy. Regulating mitochondrial accumulation and degradation is another function of MERCs. By knockdown of the *Pdzd8* orthologue *CG10362* in *Drosophila melanogaster*, it was found that flies lacking Pdzd8 display higher life expectancy and locomotor activity, as well as inhibited deterioration in locomotion, which is associated with age, in behavioural

paradigms such as the climbing assay, compared to WT flies (Hewitt *et al.*, 2020). These abnormalities resulted due to less contacts between ER and mitochondria in the Pdzd8 mutant flies. Enhancing mitochondria and ER contact sites led to ambulatory defects, while diminishing Pdzd8 levels with mitochondrial toxins prevented ambulatory and life expectancy deficits. The protective role of Pdzd8 inhibition was also observed in a fly model of Alzheimer's disease (Hewitt *et al.*, 2020). One explanation of the protective role of Pdzd8 reduction could be a quality control enhancement in mitochondria, which is thought to be essential for normal neuronal development. Mitophagy, which represents the degradation of aberrant mitochondria material, was enhanced in the axons of aged flies lacking Pdzd8 compared to WT flies. Surprisingly, knockdown of *Pdzd8* did not affect mitophagy in larval neurons (Hewitt *et al.*, 2020). These results imply that Pdzd8 depletion displays a protective role in aged neurons potentially by increasing mitophagy.

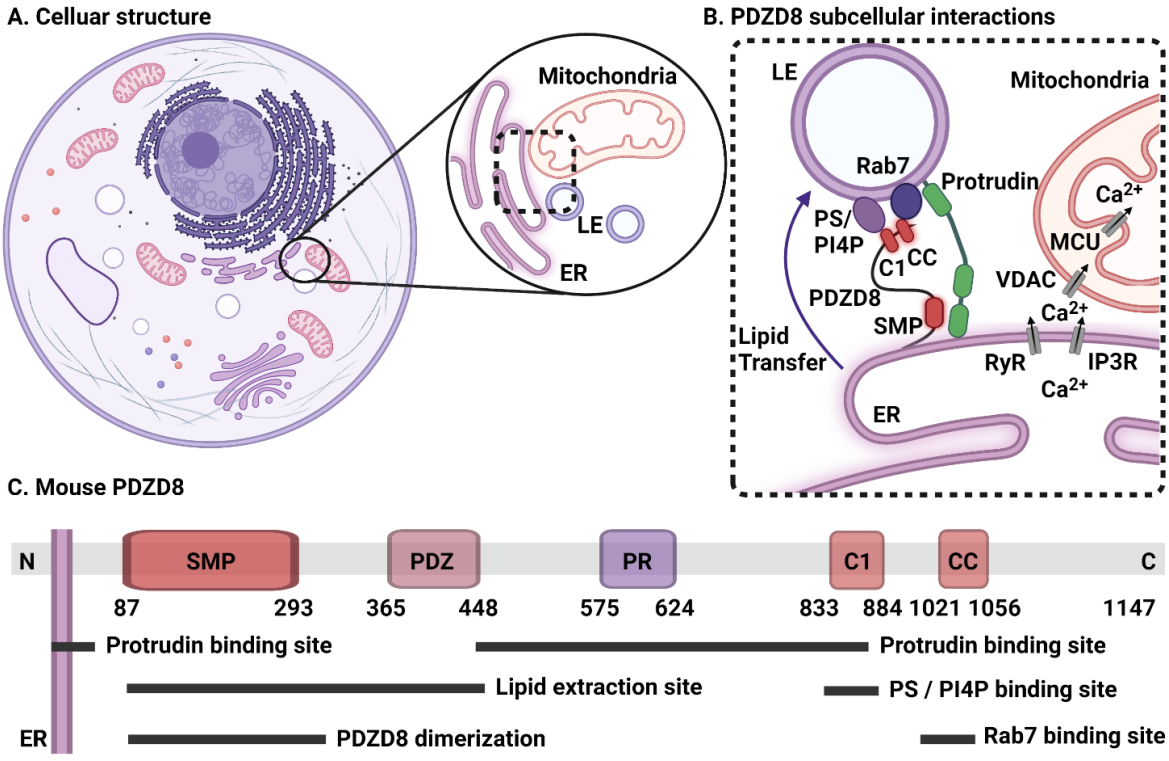

Figure 6. **Pdzd8: an ER tethering protein.** Schematic representation of a cell with its subcellular components; zoomed in, the ER – mitochondria and ER – LE connections (A). The dotted square in (A) is expanded to highlight the Pdzd8 subcellular interactions. Pdzd8 mediates lipid transfer between the ER and LE, by contacting the ER via its SMP domain and forming a complex with protrudin and Rab7 to contact LE. Pdzd8 forms connections to LE via the C1 domain with PS or PI4P or via the CC domain with Rab7. Pdzd8 also tethers the ER to the mitochondria, promoting buffering of Ca^{2+} from the ER via IP3R and RyR to the mitochondria via VDAC and MCU receptors (B). Representation of the mouse Pdzd8 protein with the SMP, PDZ, PR, C1 and CC domains, and binding sites for Pdzd8 interactors, indicated by black horizontal lines (C). ER – endoplasmic reticulum, LE – late endosome, SMP - synaptogamin-like mitochondrial lipid-binding domain, Rab7 – Ras-related protein 7, C1 – phorbol-ester/diacylglycerol-binding domain, CC – coiled-coil, PS – phosphatidylserine, PI4P – phosphadityliosotio-4-phosphate, IP3R – 1,4,5-triphosphate receptor, RyR – ryanodine receptors, VDAC – voltage dependant anion channel, MCU – mitochondria calcium uniporter, PDZ – PSD95/DigA/ZO-1-like, PR – proline-rich domain, N – N-terminus, C – C-terminus. Figure created with *BioRender.com*.

1.2.2 *PDZD8* mutation in humans

On a molecular level, Pdzd8 is crucial for maintaining cellular homeostasis by tethering the ER to the mitochondria. However, the function of PDZD8 in humans was unknown until recently. This year we published a paper showing that homozygous mutations in the *PDZD8* gene result syndromic ID (Al-Amri *et al.*, 2022). We identified two families (Family 1 and 2; Fig. 7, Table 2), in which siblings born from consanguineous parents (first cousins) display ID with autistic and dysmorphic characteristics and have mutations in the *PDZD8* gene (OMIM #620021). Genetic testing uncovered that all children with syndromic ID had a homozygous mutation in *PDZD8*, whereas individuals with a heterozygous mutation were unaffected by ID (Table 2) (Al-Amri *et al.*, 2022). The syndromic ID observed potentially resulted from an autosomal recessive inheritance of an allelic mutation as shown by the pedigree analysis (Al-Amri *et al.*, 2022). Homozygosity mapping and whole-exon sequencing revealed that both *PDZD8* mutations identified, p.(S733*) in Family 1 and p.(Y298*) in Family 2 (Fig. 7, Table 2), lead to premature termination codons. Premature

termination codons are loss of function mutations, and the mRNA is generally destroyed by nonsense-mediated mRNA decay (Supek, Lehner and Lindeboom, 2021). However, truncated PDZD8 proteins could be generated if the mRNA is not degraded (Fig. 7). These incomplete proteins would lose the ability to interact with protrudin, phosphatidylserine, Rab7, and late endosomes, as they would be missing a section form the C-terminal region (Fig. 7) (Shirane *et al.*, 2020; Gao *et al.*, 2022; Elbaz-Alon *et al.*, 2020; Hirabayashi *et al.*, 2017), essential for the proper functioning of PDZD8. To our knowledge, this is the first time mutations in *PDZD8* have been associated with a disorder in humans.

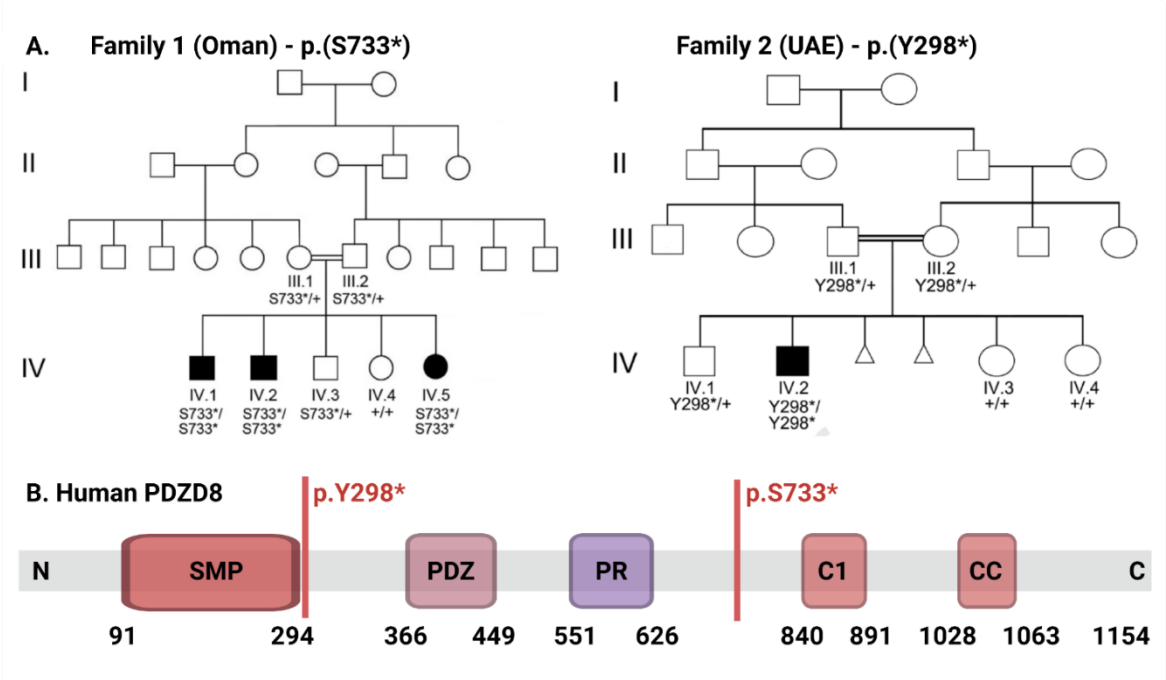

Figure 7. ***PDZD8* mutations in humans linked to syndromic ID and autism-like symptoms.** The two families identified with mutations in the *PDZD8* gene, as represented by four-generation pedigrees. Family 1 has three siblings with ID with homozygous mutation p.(S733*) in *PDZD8*. Family 2 presents one sibling with ID with homozygous mutation p.(Y298*) in *PDZD8*. The affected children are represented by filled boxes and progeny that died in utero are displayed as triangles (A). Diagram of human PDZD8 protein with the location of the mutations (red vertical lines) identified in the affected individuals (B). SMP - synaptogamin-like mitochondrial lipid-binding domain, C1 – phorbol-ester/diacylglycerol-binding domain, CC – coiled-coil, PDZ – PSD95/D1gA/ZO-1-like, PR – proline-rich domain, N – N-terminus, C – C-terminus. Adapted from Al-Amari *et al.* (2022). Figure created with *BioRender.com*.

	Family 1			Family 2
Affected individual	A.IV.1	A.IV.2	A.IV.5	B.IV.2
Genotype	p.(S733*)/p.(S733*)	p.(S733*)/p.(S733*)	p.(S733*)/p.(S733*)	p.(Y298*)/p.(Y298*)
Consanguinity	✓	✓	✓	✓
Ethnic origin	Omani	Omani	Omani	Emirati
Sex	male	male	female	male
Age (years)	30	25	17	7
Developmental delay	✓	✓	✓	✓
Intellectual disability	✓ (severe)	✓ (moderate)	✓ (severe)	✓ (moderate)
Autistic features	✓	✓ (mild)	✓	✓ (mild)
Facial dysmorphism	✓	✓	✓	✓
Orbital hypertelorism	✓	✓	✓	✓
Myopia	no	no	✓	✓
Myopathy	✓	✓ (mild)	✓	no
Epilepsy	no	✓	✓	no
Congenital heart defects	no	no	✓	no
Marfanoid habitus	✓	no	✓	no
Other behavioral problems	no	✓ (OCD)	✓ (ADHD, insomnia)	✓ (ADHD)
Brain scans findings	ND	ND	Hypoplasia of splenium of corpus callosum	normal
Other findings	no	no	amblyopia, scoliosis	astigmatism, bilateral ptosis

Table 1. Characteristics of the individuals affected by PDZD8 mutations. Adapted from Al-Amari et al. (2022).

1.3 Project aims

My project aimed to understand the role of Pdzd8 in intellectual disability using mice as a model organism. A multimodal approach was taken to probe for the consequences of Pdzd8 mutation. Based on the symptomatic profile of the children identified with *PDZD8* mutations, a variety of molecular, cellular, and behavioural techniques were employed to assess ID and ASD phenotypes in mice harbouring a mutation in *Pdzd8* gene.

II. Methods

2.1 Ethics statement

All animals used in the following experiments were housed in the animal facility at University of Leeds. The housing conditions are in strict accordance with the recommendations of the European and UK guidelines for the welfare of experimental animals. The three Rs (reduction, replacement and refinement) were applied throughout all experimental procedures, which were approved by the University of Leeds under the following Home Office project licences: PBA51A138 and PP9382954.

2.2 Mouse lines

Three different mouse lines were used. Thy1-GCaMP6s mice (C57BL/6J-Tg(Thy1-GCaMP6s)GP4.3Dkim/J) (JAX stock #024275) were used, which express under the thymus cell antigen-1 (Thy1) promoter a genetically enhanced calcium indicator (GCaMP6s) in a subset of excitatory neurons (Fig. 8) (Dana *et al.*, 2014). GCaMP6s consists of a fusion between 3 key domains: enhanced green fluorescent protein (EGFP), fused with calmodulin

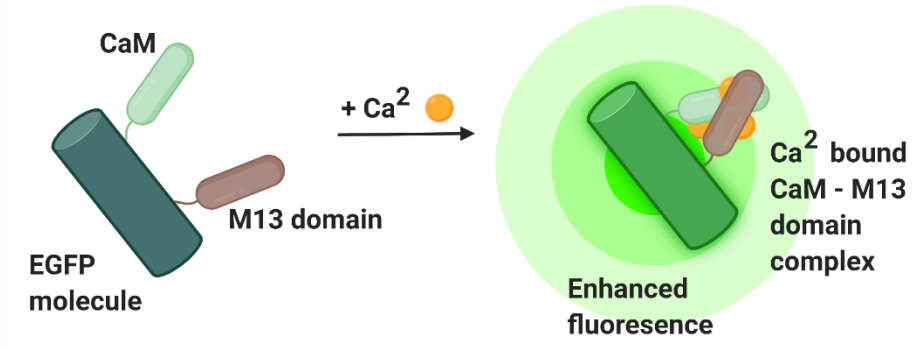

Figure 8. GCaMP. Schematic representation of a GCaMP6 construct. CaM and M13 domain of the myosin light chain are bound to a EGFP molecule. The presence of Ca^{2+} changes the conformation of the CaM and the M13 domain, which leads to enhanced fluorescence of the EGFP molecule. EGFP -enhanced green fluorescent protein, CaM – calmodulin, M13 – M13 domain of myosin light chain. Figure created with *BioRender.com.*

(CaM) at the C-terminus and with the M13 domain of the myosin light chain at the N-terminus (Fig. 8). The EGFP domain is circularly permuted such that, in the presence of Ca^{2+}, there is a conformational change in the CaM domain, which then binds to the M13 domain, resulting in an increase in fluorescence intensity (Fig. 8).

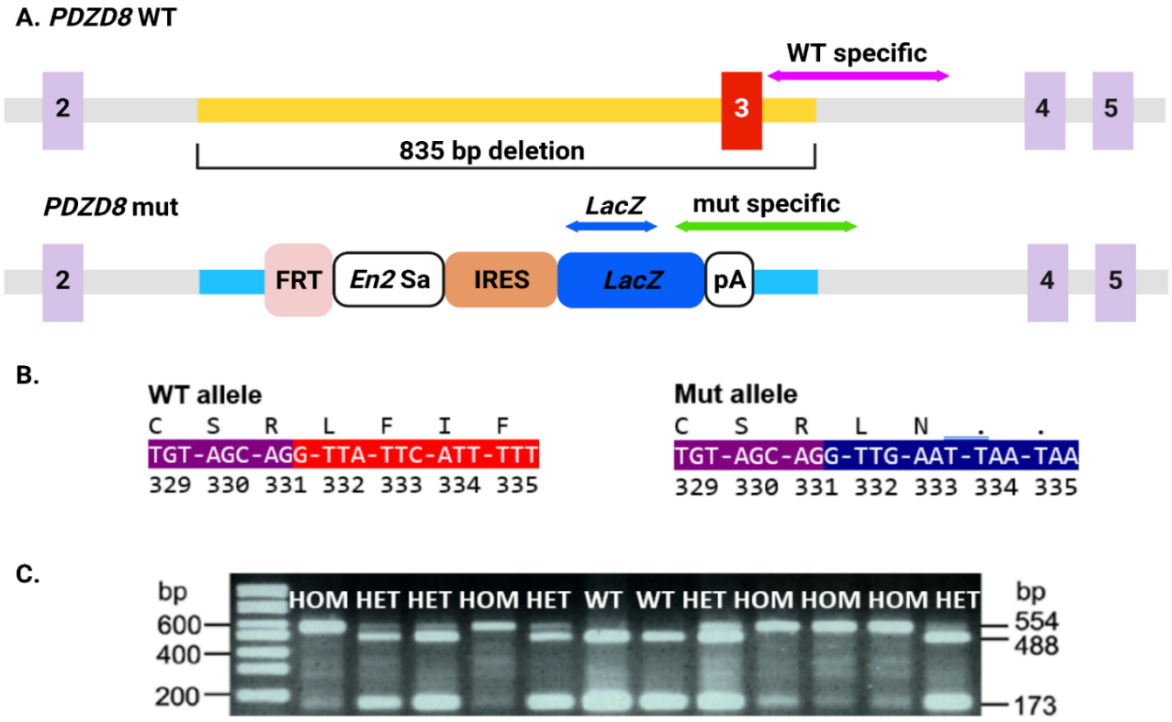

Figure 9. *Pdzd8* constructs and genotyping. *Pdzd8* WT allele displaying exon 3 (red) and the 835 bp sequence (yellow) that is deleted in the *Pdzd8* mutant allele; the magenta arrow indicates the location of the PCR assay (A, top). *Pdzd8* mutant allele construct in which a *lacZ* expression cassette replaced the 835 bp sequence containing exon 3; the arrow indicates the *Pdzd8* mutant-specific (green) and the *lacZ*-specific (blue) PCR assays (A, bottom). Frameshift mutation that results in a shift from F333 and I334 in WT (left) to N333 and *334 in the *Pdzd8* mutant; exon 2 (purple), exon 3 (red), exon 4 (blue) (B). Genotyping PCR results showing WT-specific (488 bp) and mutant-specific (554 bp) bands. The 173 bp fragment is the product of the WT specific forward primer and the *Pdzd8*-specific reverse primer. FRT – flippase recognition target, *En2* Sa – mouse engrailed-2 intron including splice acceptor, IRES – internal ribosome entry site of encephalomyocarditis virus (ECMV), *lacZ* – E. coli *lacZ* gene encoding β-galactosidase, pA – Simian virus 40 (SV40) polyadenylation signal, F – phenylalanine, I – isoleucine, N – aspargine, * – stop codon, bp – base pairs, mut – mutant, WT – wild type, HET – heterozygous, HOM – homozygous. Adapted from Al-Amari *et al.* (2022). Figure created with *BioRender.com.*

Pdzd8 mutant mice (C57BL/6NTac-*PDZD8*$^{tm1b(EUCOMM)Wtsi}$) are the result of an 835-bp sequence (including exon 3) substitution with a *LacZ* expression cassette, causing a frameshift mutation that replaces phenylalanine (F) and isoleucine (I) at position 333 and 334 to aspargine (N) and a stop codon (p.F333Nfs1*) (Fig. 9A, B) (Al-Amri *et al.*, 2022). Heterozygous mice were crossed to generate *Pdzd8* homozygous mice. *Pdzd8* homozygous mice, referred to as *Pdzd8*, were used in all experiments unless mentioned otherwise. All animal used in the following experiments were between 2-4 months old.

Pdzd8 x Thy1-GCaMP6 mice were obtained by crossing *Pdzd8* and Thy1-GCaMP6s mice to enable the expression of the calcium indicator in the *Pdzd8* homozygous mice. Polymerase chain reaction (PCR)-based assays were performed on all the mice used to determine their genotype (Fig. 9C, Table 3).

Mouseline	Forward primer	Reverse primer
PDZD8 KO	AGA AGG CAC ATG GCT GAA TA	CCA GTC AGA GAC CAT GAG AAA
PDZD8 WT	GTC TGT TCT GCT TGC TTT TCA	TTG AAC TGT TTC TCC AGC ATC
Thy1-GCaMP6s	CAT CAG TGC AGC AGA GCT TC	CAG CGT ATC CAC ATA GCG TA

Table 2. Mouse line primer pairs.

2.3 Molecular analysis

2.3.1 Quantitative reverse transcriptase polymerase chain reaction (qRT-PCR)

Technique. The development of polymerise chain reaction (PCR) modernized molecular biology, and Kary Mullis received a Nobel Prize for its discovery in 1992 (Rahman *et al.*, 2013). PCR is a method used to amplify or make multiple copies of a stretch of DNA to be studied in detail. The discoveries of reverse transcriptase and that fluorescent tags can be used to monitor PCR, led to the invention of quantitative reverse transcriptase PCR (qRT-PCR), which allows for real time measurement of messenger RNA (Rahman *et al.*, 2013).

The first step in qRT-PCR is RNA extraction from the tissue samples. Treatment with DNase, which digest DNA, is used to remove DNA contamination. Reverse transcriptase is then used to make complementary DNA (cDNA). Oligo(dT) primers are added, which bind to the polyA tail of the RNA. Reverse transcriptase then binds to the Olio(dT) and synthesises the cDNA by adding dNTPs (deoxynucleotide triphosphates), which are added into the reaction. The cDNA is used for the PCR reaction (Fig. 10A). The reaction is controlled by temperature. A higher temperature is used to separate the DNA strands, followed by a lower temperature where specific primers anneal and the strand is extended (Fig. 10B) (Rahman *et al.*, 2013).

In classical PCR the process is interrupted and the products are run on a gel, with no way of measuring the relative quantity of cDNA. In qRT-PCR the reaction is measured continuously, in real time, by using a fluorescent dye, such as SYBR green. SYBR green has enhanced fluorescence when it is attached to double stranded DNA (dsDNA), and a low fluorescence when attached to single stranded DNA. As the amplification of the product progresses, the fluorescence becomes gradually brighter, which is used in real time to quantify the product (Fig. 10B) (Joshi and Deshpande, 2010; Rahman *et al.*, 2013). To ensure the specificity of the reaction, the melting curve is checked. This displayed the separation of dsDNA into single stranded DNA as the temperature of the reaction rises. The melting temperature of DNA is dependent on the length and nucleic acid composition. If the fluorescence seen is due to the product of interest only one melting curve peak will be observed.

Quantifying the amount of product of interest in a PCR is done against a reference gene, such as β-actin (*Actb)*. An arbitrary threshold, known as the cycle threshold (Ct), is set. Ct represents the number of cycles at which the fluorescence generated by the PCR product is distinct from the background noise. The $2^{-\Delta\Delta Ct}$ method is one way to calculate the relative

fold change in gene expression of qRT-PCR samples. The formula considers the difference between the Ct of a gene of interest and the reference gene (ΔCt), and then the difference between the ΔCt of the samples and the average ΔCt of the reference gene. Finally, to calculate the fold change in gene expression the power of negative 2 of ΔΔCt is calculated.

Protocol. Messenger RNA (mRNA) was extracted using an RNAqueous™ Total RNA Isolation kit (Thermo Scientific) from whole brains of *Pdzd8* homozygous and heterozygous mice and WT controls (n=5 / genotype) (Al-Amri *et al.*, 2022). In brief, mouse brains were weighed and homogenised using lysis buffer (10 µl / mg). Lysate was further diluted with lysis buffer and centrifuged at 13,000 RPM for 3 minutes. Supernatant was discarded and same amount of 64% ethanol was added. The lysate was added to a spin column in a collection tube and centrifuged at 13,000 RPM for 1.5 minutes. Wash solution 1 and 2/3 were consecutively added and each was centrifuged at 13,000 RPM for 1 minute. The spin column was then placed in a new collection tube and elution buffer was added and centrifuged at 13,000 RPM for 30 seconds twice. A Nanodrop 2000 spectrophotometer (Thermo Scientific) was used to measure the concentration of the mRNA. Subsequently, cDNA was synthesised using a SuperScript™ III Reverse transcriptase kit (Thermo Scientific). Briefly, an initial master mix solution containing 1 µg of mRNA per sample, Oligo(dT), dNTPs and RNase free water was heated to 65°C for 5 minutes. A secondary master mix containing First-Strand Buffer, 0.1 M DTT, RNase OUT inhibitor, SuperScript III RT and the initial master mix was incubated at 50°C for 30 minutes; the reaction was then inactivated by heating the solution to 70°C for 15 minutes. The cDNA (1:100) was then used as a template for amplification in PCR. The qRT-PCR master mix contained 4 µl cDNA, 6.25 µl 2x SYBR green, 1.25 µl forward and reverse primer mix (primers were designed with Primer-BLAST; Table 4) and

1µl of RNase free water per sample. The cDNA was amplified using the following program in a QuantStudio3Real-Time PCR System (Applied Biosystems): 10 minutes at 95 °C, 15 seconds at 95 °C and 1 minute at 60 °C repeated 40 times, then 5 seconds at 60 °C (Al-Amri *et al.*, 2022).

Genes	Forward primer	Reverse primer
HRTP	TGCTGACCTGCTGGATTACAT	TTTATGTCCCCCGTTGACTGAT
B2M	CTGGTGCTTGTCTCACTGACC	CGTAGCAGTTCAGTATGTTCGG
Cyc1	ACGCATGGGTCTCAAGATGT	GTCACTTGGGTGGCCGATAA
MFN2	CCAGCTAGAAACTTCTCCTCTGTT	AGGGACATCTCGCCAGTTTA
MFN1	CAGAAAGCATAAAGCTCAGGGG	GACTGCGAGATACACTCCTCAA
DNML1	CCCGGAGACCTCTCATTCTG	TTCCATGTGGCAGGGTCATT
FIS1	CTGTGGAGGATCTGAAGAATTTTG	AACCAGGCACCAGGCATATT
OPA1	TGAGGCCCTTCTCTTGTTAGGT	CTTTTCTTTGTCTGACACCTTCCT
DDIT3	ACCTGAGGAGAGAGTGTTCCAG	ACACCGTCTCCAAGGTGAAAG
HSPA5	CGTGTGTGTGAGACCAGAAC	GCCACCACAGTGAACTTCATCA
ATF4	CAGACACCGGCAAGGAGGAT	AAGAGCTCATCTGGCATGGT
ZFYVE27	AGGGGACGGTGTTCGATACTT	AGTACCACGCACCCTCGTT
RAB7	CAAAACCCTCGACAGCTGGA	TCTTTGTGGCCACTTGTCTGT
DCX	GTAACGACCAAGACGCAAATG	GTGCTTCCGCAGACTTCCA
PDZD8 exon1/2	CTGCCCAGTTACAAGATCAGGTTTA	TTTAAGCCGGCCTTCAGTAAGT
PDZD8 exon 4/5	TCAACTGATGGGTATGCTGGG	CGATGTGATTTTCACACCTCC
PDZD8 exon 3	TTGAGCTGAGCAGTGGTGTT	AGACGAAGTGTAAGTCCGACA
LACZ	ATGGGTAACAGTCTTGGCGG	AATCAGCGACTGATCCACCC
AKT3	GTTAATGGCGGAGAGCTGTT	AGCAGAGACAATTTCTGCACCA
MTOR	GGCCATCCGGGAATTTCTGT	TGACGTGTTCATGACCCAAA
CCND2	CCCACACTGATGTGGATTGTC	CAGACTTGGATCCGGCGTTA
CALB1	AGAAGGCTGGATTGGAGCTATC	GTGGGTAAGACGTGAGCCA
PCP2	CCAGGAAGGCTTCTTCAACCT	TTTCTGGGTTCTGGCCTGG

Table 3. qRT-PCR primers. Reference genes: HPRT, B2M, and Cyc1. All primers were designed with Primer-BLAST.

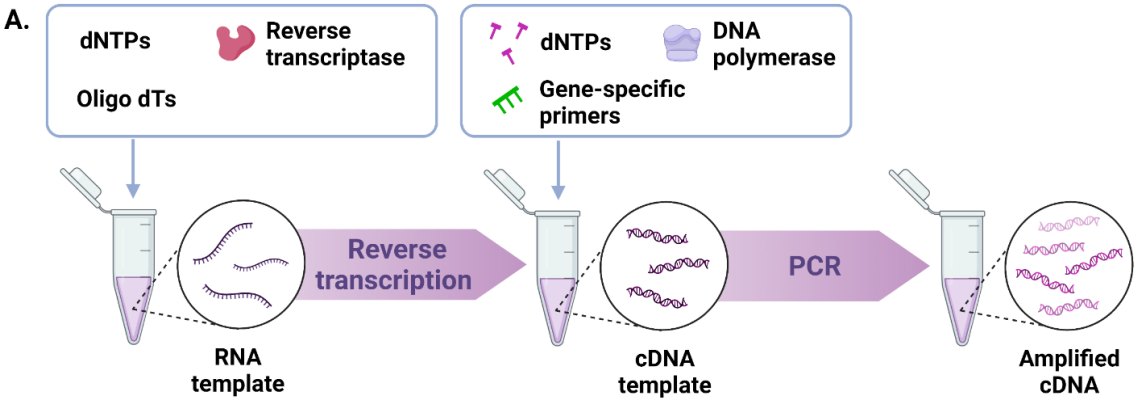
A.
dNTPs
Reverse transcriptase
Oligo dTs
dNTPs
DNA polymerase
Gene-specific primers
Reverse transcription
PCR
RNA template
cDNA template
Amplified cDNA

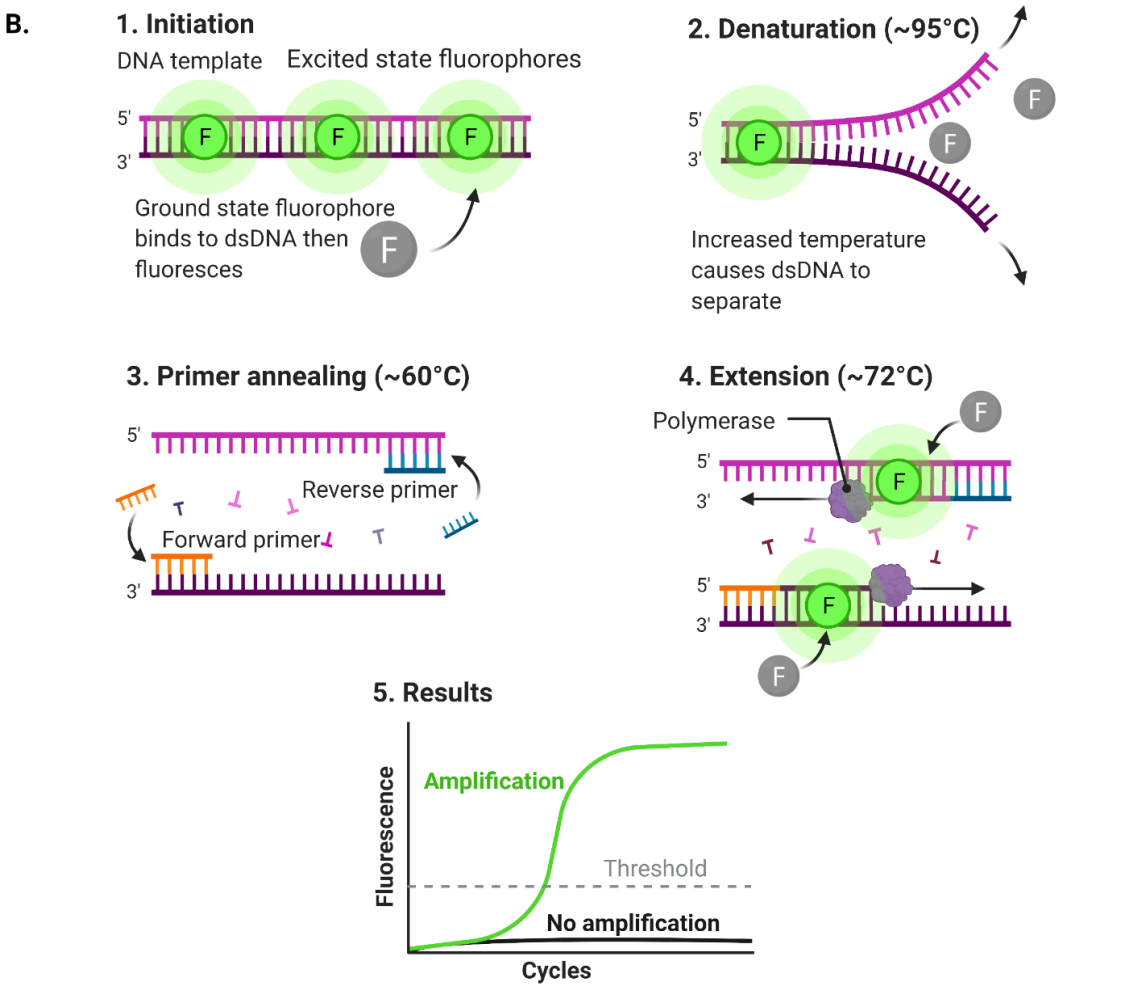
B.
1. Initiation
DNA template
Excited state fluorophores
5'
3'
F
Ground state fluorophore binds to dsDNA then fluoresces
2. Denaturation (~95°C)
Increased temperature causes dsDNA to separate
3. Primer annealing (~60°C)
Reverse primer
Forward primer
4. Extension (~72°C)
Polymerase
5. Results
Fluorescence
Amplification
Threshold
No amplification
Cycles

Figure 10. qRT-PCR diagram. Oligo dTs, dNTPs and reverse transcriptase are added to mRNA in order to make cDNA, from which the product of interest is subsequently amplified, by adding gene specific primers, dNTPs and DNA polymerase (A). The PCR reaction has multiple phases: initiation (1), denaturation (2), annealing (3) and extension (4). Initially, the fluorescent tag binds to dsDNA. The temperature is increased to separate the DNA strands, and then lowered so the forward and reverse primers can anneal to the ssDNA fragments. DNA polymerase then binds to the primers and adds nucleotides to form a new dsDNA fragment, to which the fluorescent tag binds as well. This is repeated multiple times and with each cycle the amount of the product doubles, as so does the fluorescence (B). Figure adapted from "Fluorescent dye-based real time PCR" and "Two step RT-PCR" by *BioRender.com* (2022). Retrieved from http://app.biorender.com/biorender-templates.

2.3.2 Western Blotting

Technique. Western blotting (Fig. 11) is a commonly used technique for detecting and analysing protein levels, initially described in early 1980s (Burnette, 1981; Towbin, Staehelin and Gordon, 1979). Western blotting includes multiple steps: sample preparation (Fig. 11A), gel electrophoresis (Fig. 11B), membrane transfer (Fig. 11C) and antibody staining and detection (Fig. 11D). Sample preparation includes homogenization of the tissue sample, the addition of lysis buffer to lyse the cells, and an inhibitor to avoid protein degradation. The protein concentration is measured using a assay. To enable access of the antibody, it is necessary to denature (unfold) the protein by adding the anionic detergent sodium dodecyl (SDS) and boiling the mixture at 95 – 100 °C (Mahmood and Yang, 2012).

Gel electrophoresis is then applied to separate the proteins based on size by applying a voltage which moves the negatively charged proteins through the gel towards the positively charged side. This method is known as SDS – PAGE (polyacrylamide gel electrophoresis), as polyacrylamide gels are used and SDS is added, which makes the proteins become negatively charged and allows separation of proteins by molecular weight. Western blotting gels contain two distinct sections, a stacking part, and a resolving part. The stacking part on

the top of the gel has a lower concentration of acrylamide and more acidic pH, permitting the proteins to align. The resolving part has a more basic pH and a higher concentration of acrylamide, which is important for the separation of the proteins, with smaller proteins moving faster through the gel (Mahmood and Yang, 2012).

The membrane transfer process involves transferring the proteins from the gel to a solid membrane. An electrical field is applied which causes the proteins to migrate towards the positive side where the membrane is. There are different types of membranes that can be used, such as nitrocellulose, polyvinylidene difluoride (PVDF) or nylon. PVDF and nylon are more stable but tend to display higher background, while nitrocellulose has low background, however it contains larger pores which is not suitable for low molecular weight proteins (Mahmood and Yang, 2012).

The final step of western blotting is antibody staining and detection. To prevent unspecific binding the membrane is usually blocked before staining by immersion in blocking buffer, such as milk or bovine serum albumin. Staining consists of adding a primary antibody that recognizes the protein of interest, and a secondary antibody which contains a reporter for visualization. Horseradish peroxidase-conjugated secondary antibodies are commonly used in western blotting, although there are multiple ways to label secondaries, for example, fluorophores, biotinylation or gold-conjugated. Horseradish peroxidase is commonly used as it has high substrate specificity (low background), it is stable and cheap. Horseradish peroxidase is used in combination with chemiluminescent substances, such as luminol peroxide. Horseradish peroxidase catalyses the oxidation of luminol, which results in the generation of light, which permits visualization of the protein of interest (Mahmood and Yang, 2012).

Protocol. Briefly, protein extraction was performed by homogenizing the frozen brain tissue (-80°C) from *Pdzd8* homozygous and heterozygous mice and WT controls (n=5 / genotype) in lysis buffer, followed by a centrifugation step (15 minutes, 12000 G, at 4°C). Protein concentration was quantified using a Book Hidex Sense Microplate reader with protein standards. Protein lysates were subsequently prepared for western blotting at a concentration of 20 µg / sample by diluting samples in water and sample buffer according to the protein concentration. Heat was applied (95 °C for 5 minutes) to denature the proteins. Protein samples and a ladder were loaded onto a gel (8 or 10%) in a tank filled with running buffer. SDS-PAGE was run for approximately 1.5 hour at 100-130 V to separate the proteins. Proteins were then transferred to a nitrocellulose membrane in transfer buffer for 2 hours at constant current (0.75 Amps). No-Stain Protein Labelling reagent (Invitrogen) was used to check that the protein transfer was successful. Subsequently, the membrane was incubated with antibodies as follows: 2 hours blocking in 5 % milk, incubation with the primary antibody (Pdzd8 1:500, β-actin 1:1000) over night at 4°C, and incubation with a secondary antibody the following day (horseradish peroxidase-conjugated mouse / rabbit) to allow visualization of the protein of interest. Clarity western ECL substrate peroxide solution and luminol enhancer solution (1:1 ratio) was used to visualize the proteins with an iBright imaging system (Al-Amri *et al.*, 2022).

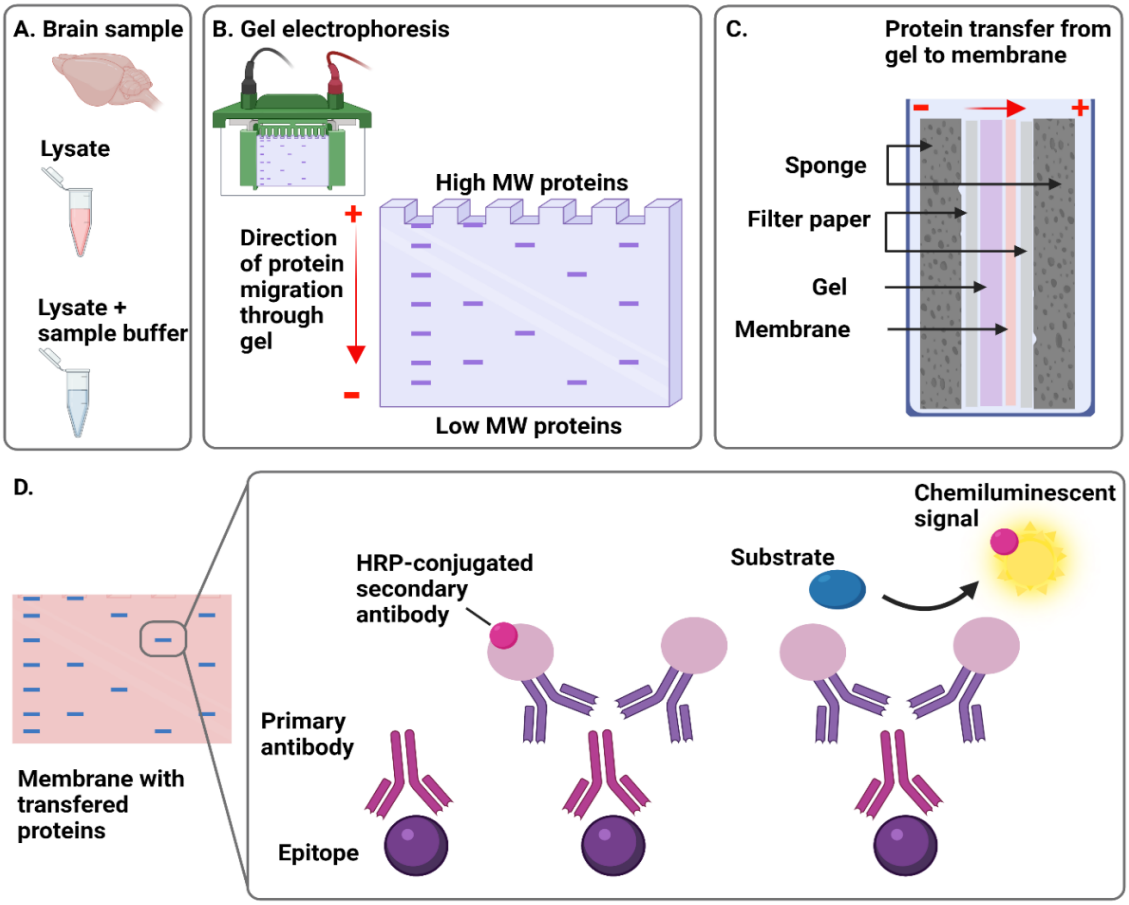

Figure 11. Western blotting diagram. First step – brain tissue homogenization and addition of lysis buffer (A). Second step of – application of gel electrophoresis to separate the proteins based on size (B). Third step– the gel and a membrane are enclosed in a cassette containing sponges and filter paper, and a voltage is applied to transfer the protein from the gel to the membrane (C). Fourth step – primary antibody that recognises the protein of interest is applied; a horseradish peroxidase-conjugated secondary antibody is applied, which is able to bind a substrate and generate light (D). HRP – horse radish peroxidase, MW – molecular weight. Figure created with *BioRender.com*.

2.4 Immunohistochemistry and brain imaging

2.4.1 *LacZ* staining

Technique. Two methods of *LacZ* (β-galactosidase) staining were performed: immunofluorescence (Fig 12) and immunohistochemical. Immunofluorescence allows detection of a target of interest by using fluorophores. As with most immunohistochemistry assays, it takes advantage of antibodies which can directly bind to specific antigens on the targeted cell or tissue. These are known as primary antibodies. A secondary antibody which contains a fluorophore is then added. This allows for visualization of the target of interest under fluorescence microscopy. Prior to antibody staining the tissue is fixed, for example with aldehyde, in order to preserve the integrity of the sample. Immunohistochemical detection of *LacZ* works by taking advantage of an artificial substrate, X-gal, which turns blue when it is cleaved by β-galactosidase, allowing for detection of all cells containing *LacZ.*

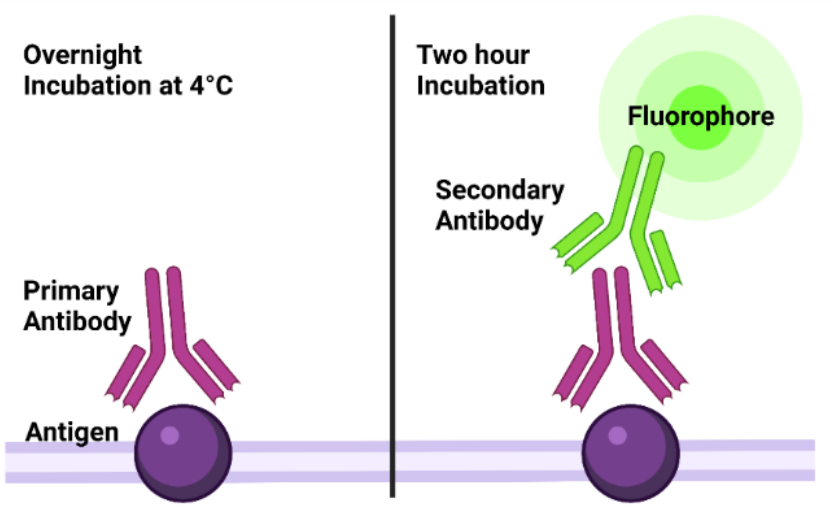

Figure 12. Immunofluorescence staining. Schematic diagram of immunohistochemistry staining: a primary antibody is used to recognize the protein of interest, and a secondary antibody with a fluorescent tag, which binds to the primary antibody, is used to visualize the protein of interest. Figure created with *BioRender.com*

Protocol. Pdzd8 and WT mice were anaesthetized with pentobarbital (60 mg / kg) via intraperitoneal injection. The heart was exposed, and a needle connected to a peristaltic pump was inserted into the left ventricle, whilst cutting the superior vena cava. Mice were perfused with 1 x phosphate buffer saline (PBS), and then fixed with 4 % paraformaldehyde. Subsequently, the brain was dissected and post-fixed overnight at 4 °C in 4 % paraformaldehyde. Sequential sagittal vibratome sections (100 µm) were collected in 0.1 M phosphate buffer (PB). Immunofluorescence staining was performed as follows: primary antibody (anti-β-galactosidase, 1:100 dilution; Thermo Fisher A-11132) was diluted in 0.02 % PBS triton and incubated with the tissue samples overnight at 4 °C. The primary antibody was washed 3 x 10 minutes in 1 x PBS. Secondary antibody (donkey-anti rabbit Alexa-488, 1:1000 dilution) was added at room temperature for 2 hours, and then washed for 3 x 10 minutes in 1 x PBS. Immunohistochemical staining was performed as follows: tissues sections were submerged in a solution of X-gal (1:20) diluted in iron buffer (Roche 11828673001) and incubated at 37 °C for 30 minutes. Sections were washed 3 x 10 minutes in 1 x PBS. Brain sections were mounted and visualized using an AxioScan Zeiss Slide Scanner (x20 objective).

2.4.2 Golgi staining

Technique. The Golgi staining method allows for visualization of the entire architecture of stained neurons. Golgi staining was discovered by accident (Golgi, 1873), and it randomly stains neurons black, including the cell body, axon, dendrites and spines. As it results in a sparse labelling of neurons, it is ideal for detailed morphological analysis. The initial staining method has been revised, and Golgi-Cox staining is now more commonly used (Cox, 1891). Golgi-Cox staining takes advantage of chromium salts which bind randomly to proteins when

the tissues in impregnated with the solution. In combination with mercuric sulphide, black deposits are formed. It is not understood why this method only stains a small subset of neurons or why those particular neurons are stained. However, this allows better visualization of single neurons (Zaqout and Kaindl, 2016).

Protocol. Golgi-Cox impregnation (FD Rapid GolgiStain Kit, NeuroTechnologies) was used to study the morphology of dendritic spines in *Pdzd8* and WT mice. Briefly, mice were anesthetized with isoflurane and then decapitated. Brains were extracted and the right brain hemisphere was submerged in 4 ml of impregnation solution (pre-mixed Solution A and B, 24 hours before) for 7 days at RT in the dark. The brain tissue was then placed in Solution C for another 3 days at RT in the dark. Coronal sections (100 µm) were taken and washed in 0.1 M PB, placed in developing solution (Solution D, Solution E and water 1:1:2) for 10 minutes, and then washed 3 times in 0.1 M PB. Sections were mounted on gelatine-coated slides and dehydrated through a series of ethanol washes (50 %, 75%, 95%, 100%; each 4 minutes). Lastly, sections were cleared using HistoClear for 10 minutes before sealing them with a coverslip and visualized using an AxioScan Zeiss Slide Scanner (x20 objective). Dendritic spine analysis was performed on frontal association cortex (mPFC), olfactory bulb, hippocampus (CA1 and dentate gyrus) and subthalamic nucleus. Dendritic spines were counted over a 10 µm length form secondar and /tertiary dendrites (at least 2 dendrites from different neurons from each brain section; ~16-25 dendrites per mouse, except for subthalamic nucleus) using Zeiss ZEN analysis software.

2.4.3 EdU staining

Technique. EdU (5-ethynyl-2'-deoxyuridine) has become a common method for assessing cell proliferation in the CNS (Salic and Mitchison, 2008). EdU is a nucleoside analogue of

thymidine which is incorporated into DNA during synthesis. The detection EdU is based on a click reaction (Fig. 13). EdU contains an alkyne terminal group which reacts with a fluorescent-azide (or a biotinylated-azide) in the presence of copper. EdU has advantages over other assays to detect DNA synthesis, such as BrdU (5-bromo-2'-deoxyuridine), where DNA has to be denatured to allow the BrdU to be detected. In contrast, the azide molecule is very small, which allows it to penetrate the tissues easily and access the EdU incorporated into the DNA, preventing any damage to the sample which can happen if the DNA is denatured. This results in a much faster protocol and more reproducible results (Salic and Mitchison, 2008).

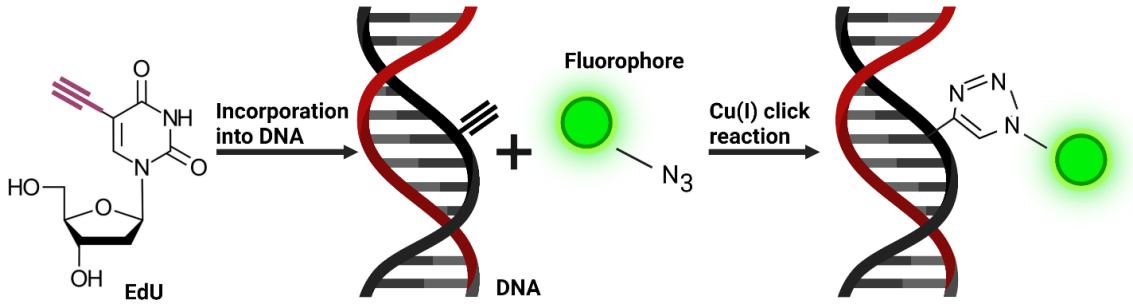

Figure 13. EdU mechanism. EdU molecule, which contains the alkyne group (purple) is incorporated into the DNA. An azide molecule is added, which in the presence of copper (Cu(I)) is linked to the alkyne group. The azide molecule contains a fluorophore which is then used to detect neurogenesis. Figure created with *BioRender.com.*

Protocol. Pdzd8 and WT mice (n = 5 / group) were given one dose of EdU (50 mg / kg intraperitoneal) and then perfused in 1 x PBS and fixed in 4 % paraformaldehyde 7 days later. Coronal brain sections (150 µm) from the hippocampus and the olfactory bulb were taken and wash in 1 x PBS for 10 minutes. Subsequently, sections were incubated in 0.2 % 1 x PBS Triton for 15 minutes, followed by 3 x 10 minute washes in 1 x PBS and 2 x 10 minute washes in 0.1 M TRIS buffer. The following: 2 M TRIS, 5 mM $CuSO_4$, 1 mM biotinylated azide in dH_2O were added to the sections and then 0.5 M ascorbic acid was added to start the

EdU reaction incubation (30 min RT in the dark). Sections were then washed once for 10 minutes in 0.1 M TRIS buffer and twice for 10 minutes in 1 x PBS. Streptavidin 555 (1:1000) was incubated in 0.1 % 1 x PBS Triton for 2 hours at RT and then washed 10 minutes three times in 1 x PBS. Lastly, brain sections were mounted onto slides and a AxioScan Zeiss Slide Scanner (x20 objective) was used to obtain images. Image analysis was performed in Cellpose (Stringer and Pachitariu, 2022), an anatomical segmentation algorithm written in python. The nucleus model from Cellpose was used, which is trained to detect nuclei, making it suitable for identifying EdU puncta. Cellpose outputs a mask with all the regions of interest detected – all EdU puncta for each individual brain section. Total EdU puncta per section were calculated and normalized by surface area. The olfactory bulb was divided into 2 regions: granule cell layer and extra granule cell layer, while the hippocampus was examined as a whole due to the lower number of EdU cells detected.

2.4.4 Structural magnetic resonance imaging

Technique. Structural magnetic resonance imaging is a non-intrusive technique of assessing brain anatomy and pathology, as opposed to functional magnetic resonance imaging which detects brain activity. Brain images obtained with magnetic resonance imaging are taken sequentially and can be used to generate volumetric analysis of the whole brain or specific regions.

Protocol. *Pdzd8* (n=32; 10 males and 22 females) and WT (n=17; 7 males and 10 females) were perfused (described above) with 10 U / ml heparin and 2 mM gadoterate meglumine in 0.1 M PBS and then fixed with 2 mM gadoterate meglumine in 4 % paraformaldehyde. The brains contained within the skulls were placed in 2 mM gadoterate meglumine in 4 % paraformaldehyde at 4 °C overnight. The brains were stored in 2 mM gadoterate meglumine

and 0.002 % sodium azide in 0.1 M PBS for at least one month. These brains were sent to the Welcome Centre for Integrative Neuroimaging in Bristol, where the structural magnetic resonance imaging was performed as described in (Al-Amri *et al.*, 2022). Briefly, multi-channel 7 Tesla scanner (Agilent Technologies) was used obtain the brain scans. Volumetric analysis was computed taking advantage of a pre-existing magnetic resonance imaging atlas and variations in brain regions were calculated by normalization to the absolute brain volume as described by the formula (individual absolute volume region / individual absolute volume whole brain * mean absolute volume whole brain) (Al-Amri *et al.*, 2022).

2.5 Behavioural analysis

An array of behavioural tests, probing for memory, learning, anxiety, social interaction and locomotor activity, were conducted to assess whether *Pdzd8* mutant mice exhibit a behavioural phenotype similar to what was seen in humans with *Pdzd8* mutation, such as intellectual disability and autistic features.

2.5.1 Fear conditioning

Pavlovian fear conditioning is a well-established technique for investigating associative learning. This learning paradigm represents the coupling of an event (for example, a tone), known as the conditioned stimulus, with an aversive event (for example, a foot shock), known as the unconditioned stimulus. Even one conditioned stimulus – unconditioned stimulus pairing was shown to be sufficient to elicit a fear response to the conditioned stimulus alone, displayed by increased freezing behaviour in mice (Kalish, 1954; Maren and Fanselow, 1996).

On Day 1, *Pdzd8* (n=17) and WT (n=8) mice underwent fear conditioning (Fig. 14). Each mouse was placed in a fear conditioning chamber, and the paradigm consisted of a 2 minute habituation period, followed by the presentation of a tone (36000 Hz, 80 dB) for 30 seconds, which co-terminated with a 1 mA foot shock for 2 seconds. Mice were tested for two different types of associative learning: context-dependent and cue-dependent. Context-dependent fear conditioning is thought to be hippocampal dependent only, whereas cue-dependent conditioning also involves the amygdala. On Day 2, mice were assessed for context-dependent associative learning, which consisted of the animals being placed for 5 minutes in the same environment in which they were conditioned the day before (Fig. 14). On Day 3, mice were assessed for cue-dependent learning (Fig. 14). The conditioning chamber was altered (colour of the floor and wall patterns, dim lighting conditions and a lemon odour was added) and the CS (auditory tone) was presented for 3 minutes, following a 3 minute habituation period. All three trials were video recorded and freezing behaviour was tracked using ANY-maze video tracking software (Stoelting, Dublin, Ireland). Data were presented as percentage of freezing during each trial. Context-dependent freezing levels were

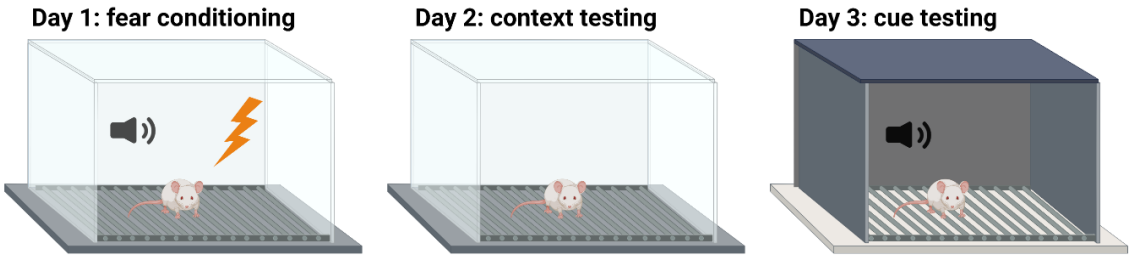

Figure 14. Fear conditioning paradigm. Schematic diagram of the fear conditioning chamber and protocol. On Day 1 the mouse was fear conditioned by pairing a tone with a foot shock. On Day 2 the mouse underwent context testing, by placing it in the same environment in which it was conditioned. On Day 3 the cue-dependent conditioning took place, by placing the mouse in an altered environment and re-exposing it to the tone presented on Day 1. Figure created with *BioRender.com.*

normalized to the 2 minutes habituation period from day 1, while cue-dependent freezing levels were normalized to the habituation period prior to the cue presentation.

2.5.2 Forced swim test

The forced swim test was devised to evaluate the efficiency of anti-depressant drugs by assessing escape-related mobility behaviour in mice (Porsolt *et al.*, 1978). The forced swim test is a commonly used paradigm to measure depressive-like behaviours in rodents (Fig. 15). *Pdzd8* mice (n=17; 8 males and 9 females) and WT controls (n=8; 4 males and 4 females) were placed in a tank filled with water (3 L, 25 °C) for 6 minutes. The first 2 minutes were considered a habituation period, data from the last 4 minutes were analysed. Immobility, freezing behaviour and distance travelled were tracked via video recording using ANY-maze software.

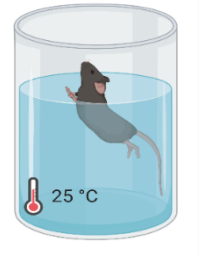

Figure 15. Forced swim test. Schematic representation of the forced swim test A mouse was placed in a tank of water and while its behaviour was being monitored. Figure created with *BioRender.com.*

2.5.3 Light-dark box

Mice show a preference for exploring dim lit areas over brightly illuminated areas, due to an innate aversion towards lighter areas. Based on this concept, the light-dark box test (Fig. 16) was is used as a measure of anxiolytic behaviour in mice (Bourin and Hascoët, 2003), and was employed to measure anxiety and exploratory behaviour in *Pdzd8* mice (n=8) and WT controls (n=8). The testing arena consisted of a square box (40 x 40 cm) divided into 2 equally sized chambers, with an entry point in between the two areas. One compartment is completely covered in black, to mimic dark / safe conditions (the dark side), and the other compartment

is brightly illuminated to mimic aversive conditions (the light side). The mice were placed in the middle of the arena next to the entry point to the dark side and were allowed to explore for 10 minutes. The 10 minutes testing session was video recorded, and ANY-maze software was used to track animals' behaviour. Data were presented as the number light side entries, the time spent in the light side, latency to enter the light side and the distance travelled by the mice.

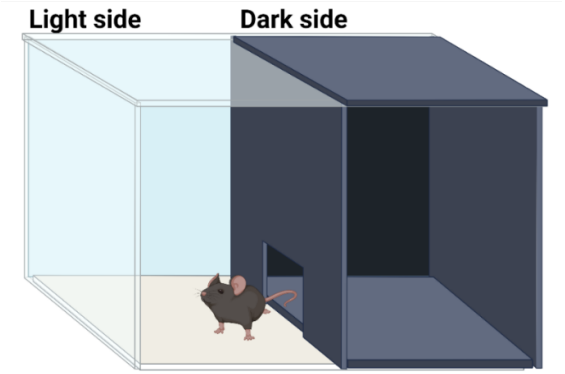

Figure 16. Light-dark box. Schematic representation of the light-dark box. The box contains two equal compartments: a light side (aversive) and a dark side (safe). The activity of the mouse in the light side is tracked. Figure created with *BioRender.com.*

2.5.4 Marble burying

Object burying is thought to be a relevant way of measuring obsessive – compulsive – like behaviour in mice (Dixit, Sahu and Mishra, 2020; Thomas *et al.*, 2009). Marble burying (Fig. 17), an acute test used to screen for repetitive behaviours, was used in *Pdzd8* mice (n=8) and WT controls (n=8). Individually ventilated cages (391 x 199 x 160 mm) were prepared with a thick layer of bedding (4 cm), on which 20 marbles were placed in 5 rows. Mice were individually placed in a cage with marbles for 1 hour, with no food and water. Photographs were taken before and after to assess marble burying. Marbles were considered buried if at least 2/3 of the marble was covered by bedding. Marble burying was manually scored by three different experimenters blinded to the genotype of the mice.

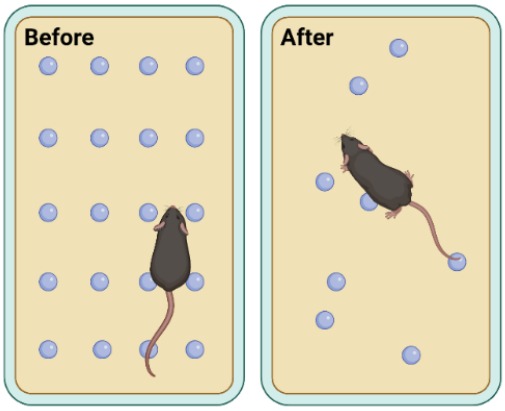

Figure 17. Marble burying test. Schematic diagram of the marble burying test. Mice are placed in a cage with 20 marbles distributed on the bedding. A photo is taken before and after the experiment. The 'after' photograph was used to count the number of marbles that were buried. Figure created with *BioRender.com*.

2.5.5 Open field

The open field test (Fig. 18) is used as a measure of locomotor – exploratory behaviour, as well as anxiolytic behaviour (Walsh and Cummins, 1976). *Pdzd8* (n=22; 10 males and 12 females) and WT (n=27; 13 males and 14 females) mice were individually placed in a square arena (40 x 40 cm; 1,600 cm^2) and continuously video-monitored for the duration of an hour (Al-Amri *et al.*, 2022). The innermost part of the arena is thought to be an anxiogenic area, and generally mice prefer to remain in the zone next to the walls of the arena, which is considered safer. ANY-maze software was used to track and analyse the behaviour of the mice. The arena was divided into three zones: outer (5 cm from the outer wall; 700 cm^2, 43.75% total area), middle (800 cm^2, 50 % total area), and inner (100 cm^2, 6.25 % total area; Fig. 18). Data were presented as time spent, entries and distance travelled in each zone. An entry to a zone was considered when the centre point of the animal crossed into that zone. Python Video Annotator (https://github.com/video-annotator/pythonvideoannotator) GUI was used to manually score the jumping and grooming behaviour of the mice (Al-Amri *et al.*, 2022).

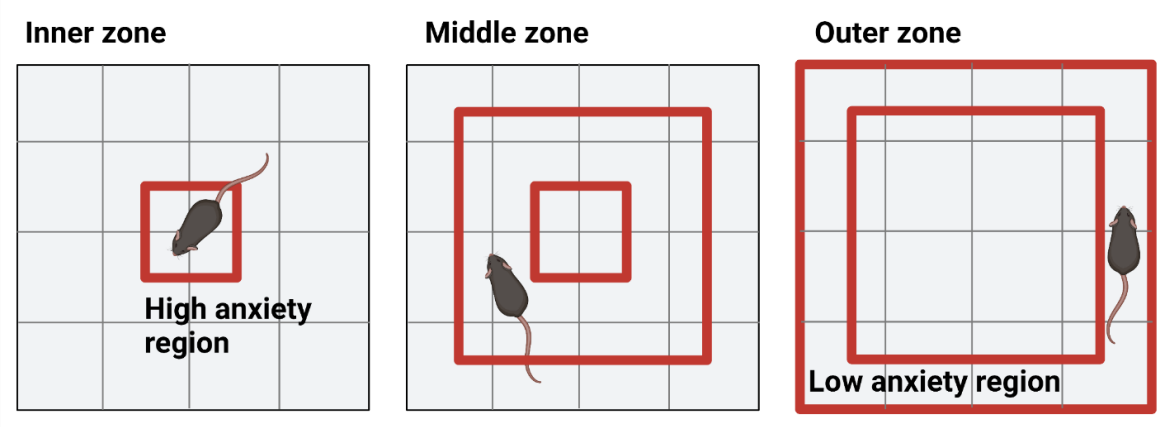

Figure 18. Open field test. Schematic representation of the open field test. An empty area is used to track the activity of the mouse. For analysis purposes the area is split into an inner zone, a middle zone, and an outer zone. Figure created with *BioRender.com.*

2.5.6 Barnes maze and reversal learning

Barnes maze is a laboratory tool used to measure learning and spatial memory (Fig. 19), which was developed by Carol Barnes to study spatial memory in rats (Barnes, 1979). *Pdzd8* mice (n=15) and WT controls (n=10) were individually placed in a Barnes maze (Al-Amri *et al.*, 2022). The maze comprised of a white circular region (122 cm diameter) with no walls, therefore, it was placed 40 cm above the ground. The arena contains 20 equidistant holes (5 cm diameter). An escape box (25 x 6 x 5 cm) was attached to the underside of one hole (the target hole) and its location remained the same for each mouse, however different locations, east or west, were used between mice. Mice were habituated for 2 minutes to the arena and the escape hole. During the learning phase (acquisition; Fig. 19) each mouse was individually positioned in the middle of the arena for 2 trials per day (each 120 seconds) over a 4 day period, with at least 2 hours between trials in the same day. If the mouse successfully identified the escaping box within the 120 seconds trial period, it could spend another 60 seconds in the escape box, and if the mouse did not manage to find the escape box within the first 120 seconds, it was gently guided towards the escape box using a 5 L beaker. Testing

day was 24 hours later, in which the escape box was removed, and mice were permitted to investigate the arena for 80 seconds (Fig. 19). All trials were video-recoded using ANY-maze software. For the acquisition period data were presented as the latency to enter the target hole, the primary path length and the number of errors performed prior to successfully locating the escape hole. The testing day data were presented as the time spend in the target quadrant (25 % of the arena with the target hole in the centre), the target sector (5 % slice area corresponding to the target hole), and the target hole (7 cm area around the target hole). The number of errors performed and the entry probability, which consisted of the percentage ratio between the number of entries to the target hole and the total number of hole entries, were also reported for the testing day (Al-Amri *et al.*, 2022). Navigation strategies for finding the target hole were classified and assessed using the Barnes maze unbiased strategy classification algorithm (Illouz *et al.*, 2016; Al-Amri *et al.*, 2022).

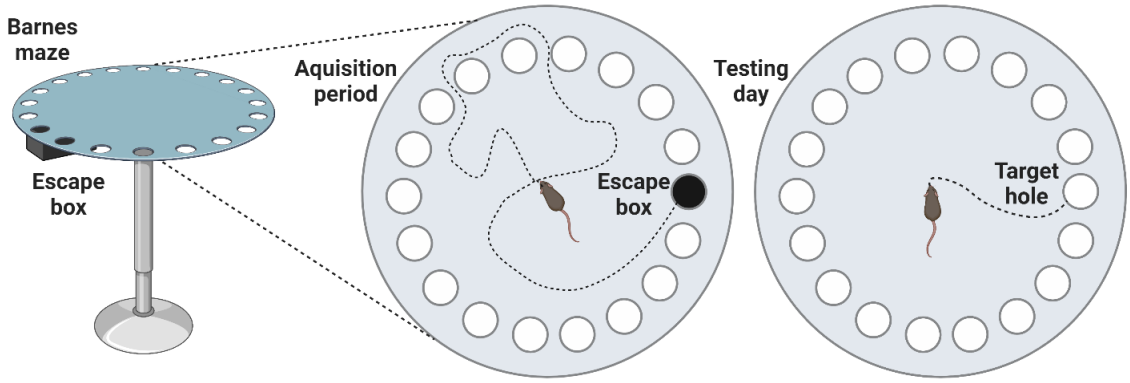

Figure 19. Barnes maze. Schematic representation of the Barnes maze raised off the ground and with an escape hole attached. Schematic representation of the surface area of the Barnes maze during acquisition (with escape hole attached) and during the testing day (without the escape hole attached). Figure created with *BioRender.com.*

2.5.7 Elevated plus maze

Anxiolytic behaviour was assessed by using an elevated plus maze (Fig. 20). *Pdzd8* homozygous (n=25; 8 males and 17 females) *Pdzd8* heterozygous (n=36; 16 males and 20 females) and WT controls (n=33; 13 males and 20 females) were individually placed in the centre of an elevated plus maze arena and allowed to explore for 5 minutes. Elevated plus maze contains 4 arms (30 cm long and 5 cm wide): 2 closed arms with opaque walls and 2 open arms (Fig. 20). ANY-maze software was used to video-record the 5 minute trials. Data were presented as the number of entries to the open and closed arms, the time spent in the open and closed arms, and distance travelled. Head dips were also counted by an experimenter blinded to the genotype and the sex of the mice (Al-Amri *et al.*, 2022).

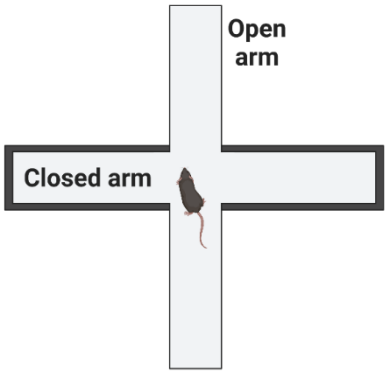

Figure 20. Elevated plus maze. Schematic representation of the elevated plus maze. The maze contains two closed arms and two open arms. Figure created with *BioRender.com.*

2.5.8 Y-maze spontaneous alternation

Y-maze spontaneous alternation behavioural experiment was employed to assess exploration and spatial memory in *Pdzd8* homozygous (n=30; 10 males and 20 females), *Pdzd8* heterozygous (n=22; 11 males and 11 females), and WT controls (n=32; 14 males and 18 females) (Al-Amri *et al.*, 2022). Mice were individually placed in a Y-maze arena (Fig. 21), which consists of 3 identical arms (35 x 5 x 15 cm, at a 120° from each other) and were allowed to explore for 5 minutes. ANY-maze software was used to video-record all trials.

Data were presented as number of arms entries and spontaneous alternations. Spontaneous alternations were scored by an experimenter blinded to the genotype and the sex of the animals. A successful alternation was considered when the animal entered three different arms consecutively (Fig. 21) (Al-Amri *et al.*, 2022).

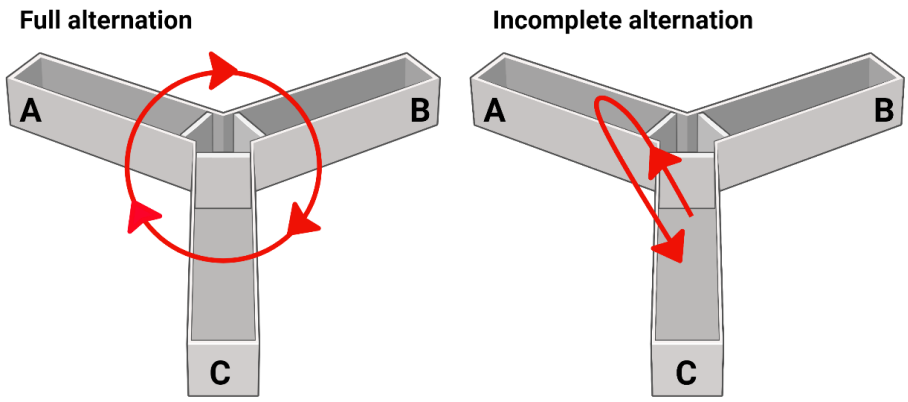

Figure 21. Y-maze spontaneous alternation. Schematic representation of the Y-maze, which contains three arms: A, B, C. A full alternation was considered when the mouse visited all the arms of the Y-maze one after another, such as ABC, CBA. An alternation was deemed incomplete when the mouse returned to the same arm, for example ACA, CBC. Figure created with *BioRender.com.*

2.5.9 Social interaction

Social interactions are a fundamental and adaptive component of mouse behaviour. Deficits in social interaction are commonly observed in mouse models of ID and ASD. Multiple behavioural assessments have been developed to evaluate various aspects of sociability, such as social dominance, novelty, recognition, memory and general social interest (Crawley, 2007). *Pdzd8* mice and WT controls underwent three social interaction paradigms: three-chamber social approach test, olfactory habituation and social discrimination test, and juvenile social interaction test.

Three-chamber social approach. General sociability and social novelty are assessed in the three-chamber social approach test (Fig. 22). Impairments in sociability and social novelty

can be detected using this paradigm, as mice typically spend more time with an unfamiliar mouse than a novel inanimate object (sociability) and will explore a novel mouse more than a familiar one (social novelty) (Wei, Talwar and Lin, 2021). The testing occurs in three periods, in a three-chamber arena that has openings between the chambers. The experimental mice were placed initially in the middle compartment and were left to habituate to the empty arena for 10 minutes. Following, in the left and right chambers of the arena an upturned cup was positioned and in one of these an unfamiliar mouse was placed (mouse 1). The other cup remained empty (novel object). The experimental mouse was placed back in the arena for another 10 minutes. Lastly, a novel mouse (mouse 2) was placed in the empty upturned cup, and the experimental mouse was allowed to explore the chambers for another 10 minutes. All sessions were video recorded and the interaction of the experimental mice with mouse 1, novel object and mouse 2 were tracked using ANY-maze software. Data were presented as percentage of time spent in the left and right chambers during the habituation, sociability, and social novelty stages. Additionally, discrimination indices were calculated for the sociability and social novelty stages by taking the ratio between the difference in the time spent in the left and right chambers and the total time spent in both chambers.

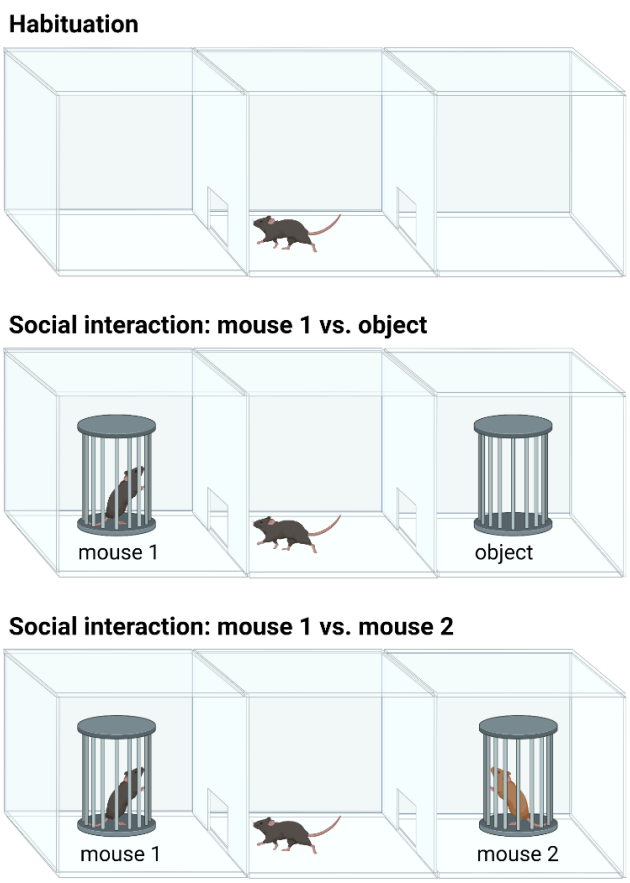

Figure 22. Three-chamber social approach. Schematic representation of the three-chamber experiment. Mice are habituated to an empty arena. In stage 1 (sociability), the interaction with an unfamiliar mouse (1) vs. an object is examined. In stage 2 (social novelty), the interaction between the initial mouse (1) and a novel mouse (2) is measured. Figure created with *BioRender.com.*

Juvenile social interaction. Mice are also more likely to interact with juvenile conspecific than with an adult conspecific (Jennings *et al.*, 2019). Therefore, reciprocal social interaction was assessed between adult *Pdzd8* or WT mice (n=8 / group) and juvenile conspecifics (21 days old; Fig. 23). Mice were individually tested in home cages without bedding. The experimental mice were habituated for 5 minutes to an empty cage. Following, a juvenile mouse was added, and the reciprocal social interaction was observed for 5 minutes. A different juvenile mouse was used for each experimental animal. The habituation period and

the juvenile interaction was recorded via ANY-maze. The reciprocal social interaction was manually tracked using Python Video Annotator (https://github.com/video-annotator/pythonvideoannotator). Social interaction was assessed in 3 different categories: approaches, anogenital sniffing and other interactions (sniffing the head, the body, climbing over / under each other, grooming each other).

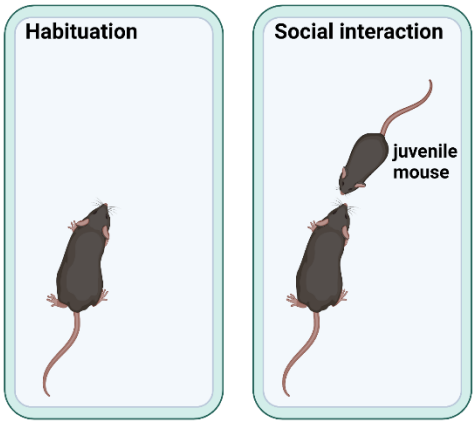

Figure 23. Juvenile social interaction. Schematic diagram of the social interaction with juvenile mice. Mice are habituated to an empty cage, following which a juvenile mouse is added in the cage. Figure created with *BioRender.com.*

Olfactory habituation and social discrimination. Mice rely heavily on olfactory cues during social interaction, which are important for choosing a mate, differentiating between individuals. Another way to test social interaction is by performing an olfactory habituation and discrimination paradigm (Qiu *et al.*, 2014). An olfactory habituation and social discrimination test measures two main factors. The habituation part tests memory, as mice become less interested in an odour that becomes familiar if they have intact memory and olfaction. The discrimination part measures the ability of a mouse to differentiate between socially relevant and non-socially relevant odours. An automated olfactory habituation and social discrimination behaviour test was conducted in a custom made 20 cm^2 arena (Fig. 24A). Socially relevant odours, such as female and male urine (1/3 dilution in mineral oil; BioIVT), and non-socially relevant odours, such as isoamyl acetate (isoA, banana; 0.001 % in mineral oil) were delivered with an olfactometer (Aurora Scientific). Odours were

presented as follows: 10 minutes habituation, 4 x 60 seconds of air (1000 SCCM), 4 x 60 seconds isoA, 4 x 60 seconds female urine, 4 x 60 seconds male urine, with an inter-trial interval of 60 seconds. An Arduino controlled sensor, based on PROBES (poking registered olfactory behaviour evaluation system) (Qiu *et al.*, 2014), was used to measure the investigation time following odour delivery (Fig. 24B).

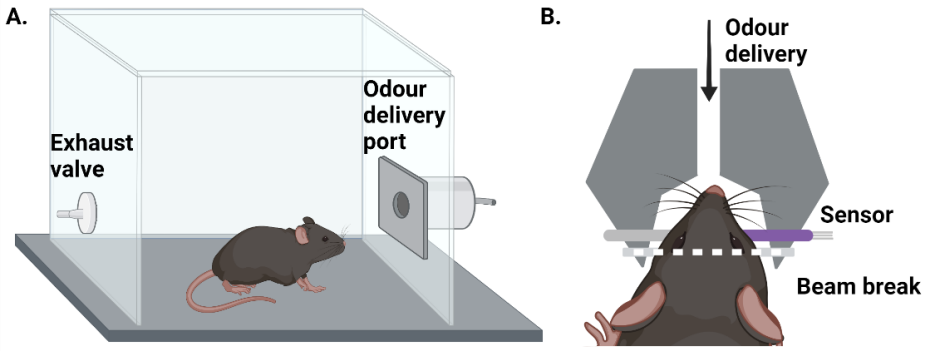

Figure 24. Olfactory habituation and social discrimination task. Schematic representation of the olfactory habituation and discrimination test. The testing box consists of a port connected to an olfactometer, through which odours are delivered (A). The delivery of an odour prompts the mouse to investigate the port, which contains a sensor. When the mouse places its head inside the port, the beam is broken, and the sensor is activated (B). Figure created with *BioRender.com.*

2.5.10 Comprehensive lab animal monitoring system (CLAMS)

An in-depth analysis of a rodents' behaviour and metabolism can be achieved using comprehensive lab animal monitoring system (CLAMS; Columbus Instruments). CLAMS is a set of live-in cage system which contains multiple sensors allowing for simultaneously monitoring of an animal's locomotor activity (XY and Z movement), wheel usage, feeding behaviour, O_2 consumption and CO_2 production (Fig. 25). *Pdzd8* male (n=9) and WT male controls (n=9) were singly housed in CLAMS cages for a period of 7 days. The CLAMS software automatically generates a report with the following parameters: VO_2 (volume of

oxygen consumed, mL / Kg / hr), VCO_2 (volume of carbon dioxide produced, mL / Kg / hr), respiratory exchange ratio, heat (Kcal / hr), accumulated food (grams), XY total activity (all horizontal beam breaks in counts), XY ambulatory activity (minimum 3 different, consecutive horizontal beam breaks in counts) and Z activity (all vertical beam breaks in counts), wheel running. The data were recorded at a 14 minute sampling rate. Mice were weighed before and after the experiment, as well as the water bottles, used to measure water consumption. The first 5 days were considered as habituation, and only the last 48 h were used for data analysis.

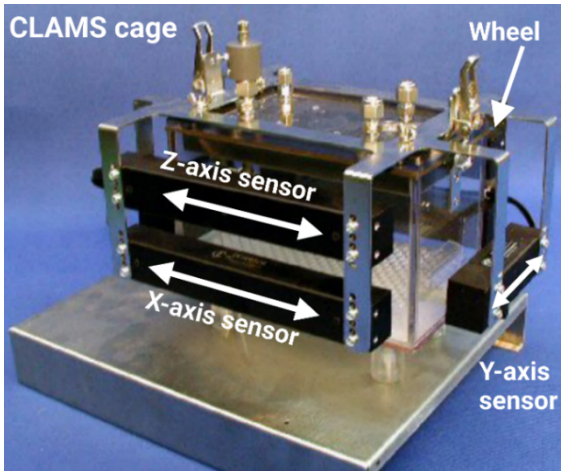

Figure 25. CLAMS system. An example of a CLAMS cage, with the sensors for detecting motion in X, Y, and Z directions. Wheels can be inserted in the front of the cage if desired. The picture was adapted from the CLAMS Brochure, Columbus Instruments.

2.5.11 Rodent activity detector (RAD)

Due to limited availability of CLAMS, larger scale monitoring of home-cage activity of singly house mice in real-time was performed using rodent activity detectors (RADs). Monitoring devices were built following the designs of Matikainen-Ankney and colleagues (Matikainen-Ankney *et al.*, 2019). In brief, RAD (Fig. 26A) uses a passive infrared (PIR) sensor (MSP430-PIR) to detect movement in home cages of animals while logging (M0 AdaLogger) the data onto a microSD card. Data can be directly visualized using the FeatherWing oLED display and it is logged as seconds of activity per minute. RAD is

powered by a 3.7 V rechargeable lithium ion battery, making it optimal for longer term usage (~ 10 days). The device is contained into a 3D-printed enclosure (modified with Sharper3D and printed with UltimakerCura 3D printer), which is placed in the mouse food holder in a cage and requires no maintenance once the experiment is started (Fig. 26B). *Pdzd8* homozygous (n=14), *Pdzd8* heterozygous (n=12) and WT controls (n=12) were singly housed in new cages, where a RAD device was placed. Data was recorded for 3 consecutive days to obtain information on 3 full light-dark cycles. First 3 hours of recording were considered habituation and these data were not included in the analysis. RAD cages were not disturbed once the experiment was started till the end of the experimental procedure.

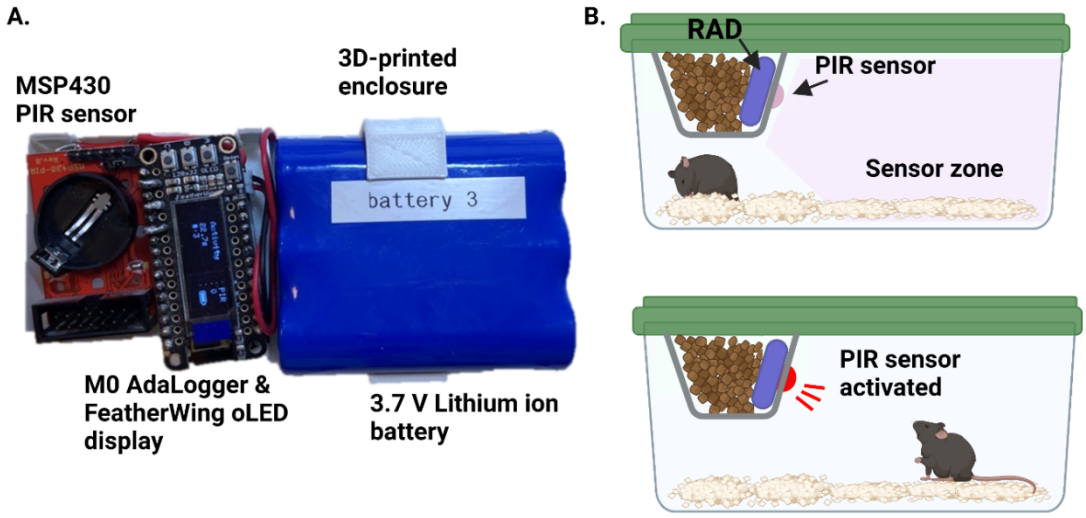

Figure 26. Rodent activity detector. Photo of the RAD device made to track mouse activity in home cages. A PIR sensor is connected to an M0 AdaLogger, where the data is saved onto a microSD card (not shown), and to an oLED display, where the activity can be seen live. The device is powered by a rechargeable lithium-ion battery, and it is enclosed in a 3D-printed support (A). The RAD is placed in the food hooper of a cage. The PIR sensor is activated and logs the activity when the mouse moves in the sensor zone (B). This figure was created with *BioRender.com*

2.6 Two-photon laser scanning microscopy – *in vivo* Ca^2 imaging

Changes in neuronal brain activity, such as spontaneous or evoked neuronal firing, are commonly observed in mouse models of ID and ASD in various settings, either *ex vivo* or *in vivo*. One approach to study brain activity *in vivo* is by performing two-photon Ca^{2+} imaging experiments, as Ca^{2+} is often used as a proxy for neuronal activity. Taking advantage of Thy1-GCaMP6s, *Pdzd8* mice and WT controls expressing this Ca^{2+} indicator underwent *in vivo* brain imaging experiments to assess spontaneous or evoked neuronal activity.

2.6.1. Acute and chronic cranial window surgeries

To allow *in vivo* Ca^2 imaging, a cranial window was implanted. Acute and chronic cranial window surgeries (craniotomies) (Holtmaat *et al.*, 2009) were performed on *Pdzd8* x Thy1-GCaMP6s and Thy1-GCaMP6s controls (2-4 months old).

Acute craniotomy. The acute surgical procedure was done as follows: the animal was anesthetised using intraperitoneal administration of Urethane (1.5 g / kg), which induced non-recovery anaesthesia. The mouse was moved to a surgical heating table, where temperature was monitored using an anal temperature probe (~37 °C). Prior to the start of the surgery, the mouse was also injected with a painkiller (Metacam, subcutaneous 5 mg / kg). Reflexes were checked to ensure the mouse was anaesthetised properly and the eyes were covered with a protective substance to prevent the corneas from drying. The skin on the head was removed, making sure all tissue (hair, skin, and periosteum) was properly cleared (Fig. 27A). The skull was scored with a blade to provide better adherence for the superglue and the dental cement. A stainless-steel head bar was fixed with dental cement, ventral to the area where the window was placed, so it could be later attached to a holder for acute Ca^{2+} imaging. A 3 mm-diameter craniotomy was performed over the left and right frontal association cortices (1.5 mm

longitudinal form bregma; Fig. 27B). Surgical sponges were used to stop any bleedings. The dura was kept intact and cortex buffer (7.4 pH, 135 mM NaCl, 5.4 mM KCl, 5 mM HEPES, 1.8 mM CaCl2 $2H_2O$) was added on top of it to prevent the surface of the brain from drying. A coverslip sealed with dental cement was fixed as a window (Fig. 27C, D). Mice which underwent acute cranial window surgeries were subsequently culled at the end of the *in vivo* Ca^{2+} imaging experiment.

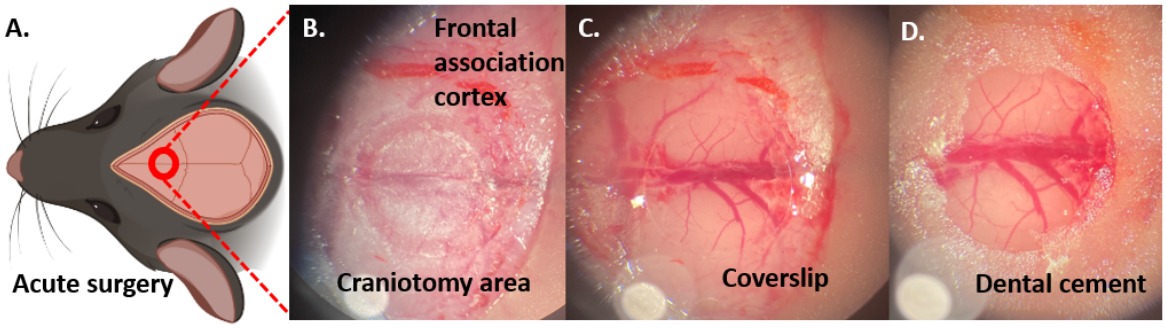

Figure 27. Acute cranial window implantation. Schematic diagrams of the surgical incision to reveal the frontal association cortex (A). Drilling the 3 mm diameter craniotomy over the frontal association cortex (B). Attachment of the coverslip over the exposed brain (C). Dental cement application around the craniotomy region to secure the coverslip (D). Figure created with *BioRender.com.*

Chronic craniotomy. In comparison to acute cranial window surgeries, chronic window implantation allows for multiple *in vivo* brain imaging sessions during an awake state. The chronic cranial window surgery followed a similar surgical procedure, with the following changes: to induce anaesthesia, the animal was placed in a restricted space where a mixture of 5% isoflurane and O_2 (1 l / min) was released, using Harvard Apparatus equipment. The mouse was moved to a surgical heating table and the isoflurane concentration was reduced to 1.5 - 2%. Prior to the surgery, the mouse was injected with multiple painkillers (Metacam, subcutaneous 5 mg / kg; Buprenorphine, intraperitoneal 0.1 mg / kg), an anti-inflammatory drug (Dexamethasone, intramuscular 2 mg / kg) and an antibiotic (Baytril, subcutaneous 2.5

mg / kg). For chronic surgeries, ear bars were appropriately fixed to keep the head of the animal stable (Fig. 28A), and the 3 mm-diameter craniotomy was performed before attaching a custom-made stainless-steel head bar (Fig. 28B, C, D, E, F). Importantly, chronic surgeries were performed using aseptic techniques, all instruments were properly sterilized with 70% ethanol, a UV sterilizer and a hot bead sterilizer before the surgery. Following this procedure, mice were given Bupernorphine (2 days post-surgery) and Baytril (10 days post-surgery), and closely monitored using the Mouse Grimace Scale (National Centre for the Replacement, Refinement and Reduction of Animal Research) to record if any prospective pain is detectable. Mice were handled 3 – 5 days pre-surgery and 5 days post-surgery they were ready to be used for awake imaging experiments.

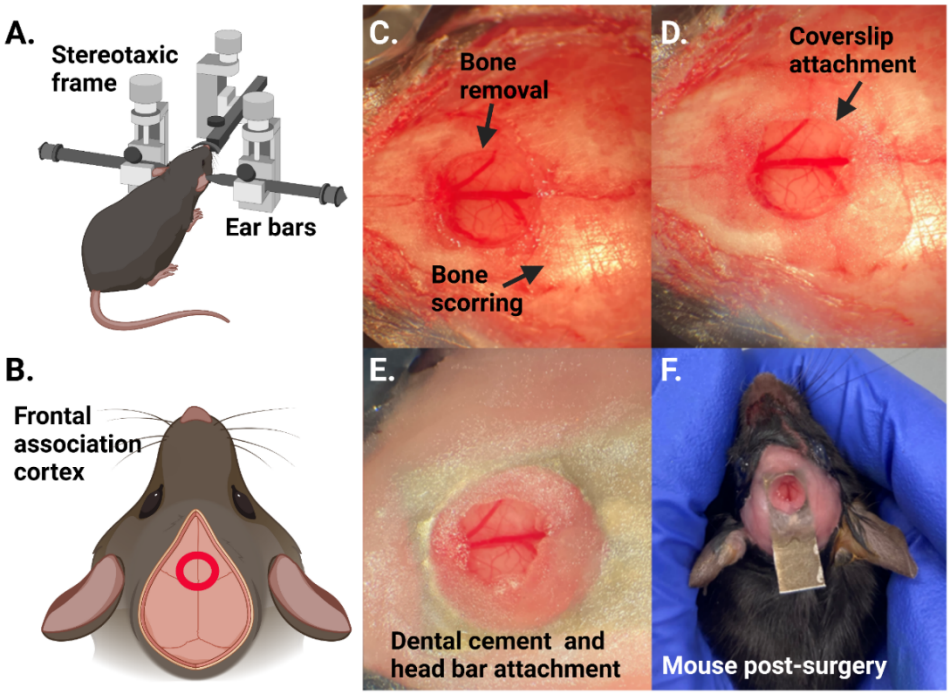

Figure 28. Chronic cranial window implantation. Schematic diagram of the surgery set-up: stereotaxic frame with ear bars in place (A). Schematic diagram of the surgical incision to reveal the frontal association cortex (B). Bone scoring and removal of the 3 mm diameter bone for the craniotomy (C). Attachment of the coverslip over the exposed frontal association cortex (D). attachment of the custom-made head bar and application of dental cement to secure the head bar (E). Image of a mouse following a chronic cranial window implantation surgery (F). Figure created with *BioRender.com.*

2.6.2. Two-photon laser scanning microscopy and Ca^{2+} imaging experiments

Technique. Both classical optical microscopy techniques, such as widefield and confocal fluorescence microscopy, as well as two-photon laser scanning microscopy (2P-LSM) are based on emitting light by exciting a fluorophore (Svoboda and Yasuda, 2006). In traditional fluorescence microscopy to bring a fluorophore to an excited state, only one single photons of a specific wavelength is absorbed. In contrast, with 2P-LSM, two photons arrive at the fluorophore simultaneously, within ~0.5 fs, causing both photons to be absorbed at the same time. As a result, the two photons combine their energy to promote the molecule, such as a GFP fluorophore, to an excited state. For example, GCaMP is excited by a wavelength of 460 nm in one photon microscopy, but a near-infrared wavelength of 920 nm in two photon microscopy. This is highly advantageous, as exciting a fluorophore with multiple photons lower energy is required and the low-energy infrared photons cause less scattering of the tissue (Svoboda and Yasuda, 2006). In traditional microscopy, high levels of light scattering allow only for small depth access, limiting the high resolution imaging abilities to about 100 μm from the surface of the tissue. The infrared light excitation happens only in the focal plane as this is constrained by the requirement of two photons to excite a molecule simultaneously. In the absence of multiphoton absorption, absorption occurs within the entire excitation light cone, resulting in out-of-focus light excitation. Therefore, the near-infrared excitation in 2P-LSM permit much better tissue penetration, ~ 1 mm. In addition, the lack of out-of-focus excitation in two photon microscopy also decreases phototoxicity and increases visibility (Svoboda and Yasuda, 2006). These advantage of two photon imaging over one photon is what makes it suitable for long term deep tissue imaging in an *in vivo* set-up.

2P-LSM imaging set-up. Two photon imaging requires a specialized optical set-up. Concentration of light in space and time is essential to create enough excitation light. An objective with a high numerical aperture can be used for so the laser beam to be concentrate in space. Concentration in time requires very expensive lasers, which emit ultrashort pulses. In this case a titanium-sapphire laser (MaiTai) was used. A Pockels cell is used to modulate and control the laser beam power. A telescope is used to expand the laser beam, which is scanned in X and Y-axis by scanning mirrors.

Fluorescent signals were imaged at 30 Hz using a custom-made two-photon laser scanning microscope (Fig. 29) equipped with a mode-locked Mai Tai DeepSee Ti-sapphire laser tuned to 920 nm (SpectraPhysics, Santa Clara, CA, USA) with a Nikon N16XLWD-PF 16x water-dipping objective (NA 0.8, Nikon, Tokyo, Japan).

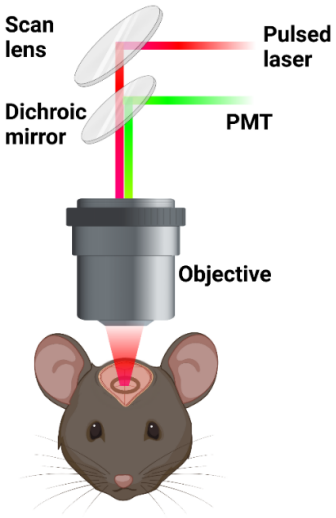

Figure 29. Two photon laser scanning microscope set-up. Schematic representation of the microscope used for *in vivo* Ca^{2+} imaging experiments. PMT – photo multiplier tube. Figure created with *BioRender.com.*

Acute imaging experiments. Following acute cranial window implantation, *Pdzd8* x Thy1-GCaMP6s and Thy1-GCaMP6s controls were transferred to the 2P-LSM set-up. An imaging session lasted for a maximum of 3 hour, and mice were continuously monitored to ensure there are no breathing issues. In acute experiments, spontaneous Ca^{2+} activity was recorded. The surface of the brain (pia) was detected and used to keep note of the depth of imaging.

Fluorescence Ca^{2+} activity was recorded at depths between 100 – 400 µm distance from the pia. Spontaneous Ca^{2+} activity was recorded from multiple regions of the brain (3 – 6 areas / mouse), with each recording lasting between 2 to 10 minutes. Scanning and image acquisition were controlled under ScanImage v.5 software (Pologruto et al., 2003). Mice were culled at the end of the experiment.

Chronic imaging experiments. Following chronic cranial window implantation (Day 0), mice had to be trained on the imaging set-up to get them accustomed to being head fixed, prior to the imaging sessions (Day 1 – 7; Fig. 30). The imaging se-up for awake imaging consisted of a Styrofoam ball contained in an enclosure, suspended by pressurized air delivered from underneath (Fig. 30). The head bar of the mouse was fixed in place under between 2 plaques. This allowed the mouse to 'freely' move on the ball in x- and y- direction while being head fixed. Mice were trained 10 – 20 minutes for at least 3 times before a brain imaging experiment (Fig. 30). Ca^{2+} imaging experiments (Day 7 – 49; Fig. 30) were performed following the training period and the approach was similar to acute surgeries. Each imaging sessions consisted of recording activity from multiple areas within the frontal association cortex, with mice imaged no longer than 2 hours per day. Mice were videoed throughout the imaging sessions to allow continuous monitoring of the animal (Fig. 31). Mice were allowed to be imaged multiple times for a maximum of 8 weeks from the day of the cranial window surgery.

Chronic imaging experiments were combined with olfactory stimulation which followed a similar protocol as described previously. An odour port as placed in front of the mouse's nose. Socially relevant odours, such as female and male urine (1/3 dilution in mineral oil), and non-socially relevant odours, such as isoamyl acetate (isoA, banana; 0.001 % in mineral

oil) were delivered with an olfactometer (Aurora Scientific). Odours were presented as follows: 5 seconds of IsoA, female urine, male urine, and air (1000 SCCM), with an inter-trial interval of 25 seconds. This sequence was repeated 10 times. Scanning and image acquisition were controlled under ScanImage v.5 software (Pologruto et al., 2003). The olfactometer protocol was controlled by a python script, and triggered the image acquisition. As the olfactometer signal was synchronously recorded using an I2C, this allowed for the data regarding odour delivery to be embedded in the ScanImage files generated. Mice were returned to their home cages following an imaging session.

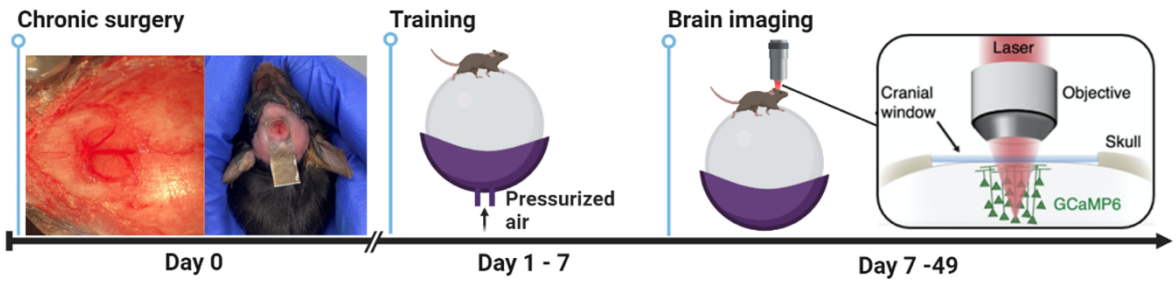

Figure 30. Chronic Ca^{2+} imaging experiments. Following the chronic cranial window surgery (Day 0), mice were trained head-fixed on the imaging set-up (Day 1 – 7). Ca^{2+} imaging experiment were commenced once the mice were accustomed and trained to the imaging set-up (Day 7 – 49). Figure created with *BioRender.com.*

2.6.3 Ca^{2+} imaging experiments: data processing and analysis

Suite2P: data processing. Ca^{2+} data generated were subsequently processed using Suite2P software (Pachitariu *et al.*, 2017). Briefly, Suite2P is a program specifically designed to investigate 2P-LSM recordings of Ca^{2+} activity and it follows multiple steps: image registration, ROI (region of interest) detection, quality control, and activity extraction. Raw data generated by ScanImage is in the form of tiff-file movies, which contain multiple frames. Raw data from an imaging area are concatenated and registration is applied. Registration computes a reference image and takes the frames in batches (200 frames) and aligns this to

the reference images, to correct for motion in x- and y-planes (Pachitariu *et al.*, 2017). Motion in z-plane is not easily corrected and it mostly occurred during the awake imaging experiments due to the increased movement of the mouse. Data was not used where a z-movement constituted an issue. ROI detection is based on principal component analysis, which results in sorting together pixels which are correlated in order to detect cells. Quality control was performed manually though the Suite2P graphical user interface (GUI), which allows to visualise the data and inspect each ROI detected (Pachitariu *et al.*, 2017). ROI that were visibly not cells or their traces were too noisy were discarded. Lastly, activity extraction involved removing the background signal (70 %) from each ROI detected to prevent background signal from contaminating the data. Parameters changed in Suite2P: tau – 1.25, anatomical – 1, spatial scale – 2/3. Suite2P generates multiple files containing all information on the ROI detected, such as the fluorescent traces, ROI maps. Subsequently, Anaconda (Python3) was used to analyse the Ca^{2+} activity.

Ca^{2+} imaging analysis. All Ca^{2+} data were presented as the change in the fluorescence intensity relative to the resting fluorescence intensity ($\Delta F/F$) is plotted for each cell (ROI) over time (seconds). A Savitzky-Golay filter was applied to all trances to smooth the data (parameters stated in figure legends).

For the acute imaging experiments, to detect action potentials, an algorithm which applied a median filter to the computed differential of a Ca^{2+} trace was used. The mean $\Delta F/F$ was calculated for each ROI detected to investigate the mean fluorescence intensity in *Pdzd8* mice and WT control. Then, the probability density was calculated by dividing mean $\Delta F/F$ by the number of ROI detected per genotype, to account for the difference in the number of cells detected. The percentage of active cells was also calculated from the total number of cells in

the field of view for the spontaneous Ca^{2+} data recorded. The total number of cells in the field of view was manually counted for each area imaged using Fiji, an image analysis software.

For awake imaging experiments, odour detection (sniffing) and locomotion were investigated from video data from awake imaging sessions (Fig. 31). Using Fiji, an ROI was manually drawn around the regions of interest: orofacial area to detect sniffing and forelimb paw to detect locomotion. Pixel values from these ROI were extracted in Fiji. Using python, Ca^{2+} traces, the olfactometer signal and the extracted ROIs from videos were aligned to be ablet to correlate these measurements. Lastly, neuronal responses were classified based on their Ca^{2+} transients during odour delivery. Neurons were grouped into 3 main classes, with neurons responsive to isoA, female urine and male urine. Cells were placed into a category if they displayed Ca^{2+} responses during 70% of the presentations of the same odour and a Venn diagram of this classification was plotted.

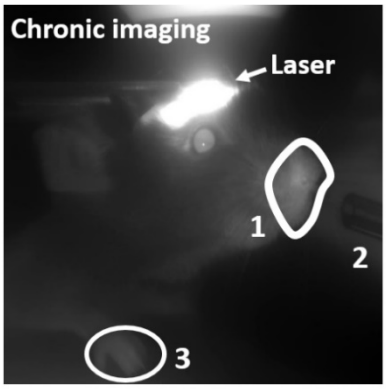

Figure 31. Mouse during awake imaging. Snapshot of a mouse during an awake imaging session and regions using for video analysis. Laser beam is visible. Example of region used to assess orofacial movement for odour detection (1). The odour delivery port is visible (2). Example of region used around the forepaw to detect locomotion (3).

2.7 Statistical analysis

Graphical representation of the data and statistical analysis were computed with GraphPad Prism 6.0 software (California, USA), unless stated otherwise. Data were tested for normality using Shapiro-Wilk test. The significance level was set to .05. The statistical was performed on biological replicates and test chosen for each data set were mentioned in the figure legends.

III. Results

3.1 *Pdzd8* basic characterization

3.1.1 *Pdzd8* mutation

We used a mutant mouse line, generated by the European Conditional Mouse Mutagenesis program, to investigate the role of Pdzd8 in intellectual disability. This mouse line has a mutation in *Pdzd8* gene (F333Fns1*; Fig. 9) that leads to premature stop codons, similar to the mutations found in family 1 and 2 (Fig. 7) (Al-Amri *et al.*, 2022). The *Pdzd8* mouse line harbours mutation which causes an 835 base pair deletion, including exon 3 (Fig. 32A). To confirm the presence of the *Pdzd8* mutation, brain mRNA was extracted from *Pdzd8* mice with either a heterozygous or a homozygous mutation (Fig. 32). Quantitative RT-PCR (Methods 2.3.1) confirmed the absence of *Pdzd8* exon 3 mRNA in *Pdzd8* homozygous mice compared to WT controls (Fig. 32B; $F(2, 12)=21.04$, $P=0.0001$, with post hoc comparisons $P=0.0005$). To double check that *Pdzd8* forward and reverse primes amplify the correct region (103 base pairs), the products of qRT-PCR were subsequently run on a gel. The gel revealed that the expected region is amplified and emphasized the absence of *Pdzd8* exon 3 mRNA in *Pdzd8* homozygous mice (Fig. 32C). Exon 3 mRNA from *Pdzd8* heterozygous mice showed a slight increase compared to WT controls, albeit not significant (Fig. 32B). The 835 base pair deletion is replaced by a *LacZ* cassette in *Pdzd8* mice, which can also be identified by qRT-PCR analysis and was used to verify the presence of *Pdzd8* mutation. As expected, *LacZ* relative expression was absent in WT mice. *Pdzd8* homozygous mice displayed increased *LacZ* presence ($F(2, 12)=104.1$, $P<0.0001$, with post hoc comparisons $P=0.0001$), while *Pdzd8* heterozygous mice showed more than 50% reduction in *LacZ* compared to homozygous mice ($F(2, 12)=104.1$, $P<0.0001$, with post hoc comparisons

P=0.0001; Fig. 32D) (Al-Amri *et al.*, 2022). This was anticipated as *Pdzd8* heterozygous mice contain *LacZ* only in one allele. *LacZ* gels showed the forward and reverse primers amplified the expected region (105 base pairs) and further supported the presence of *LacZ Pdzd8* mice and its absence from WT (Fig. 32E). Overall, these results demonstrate the existence of *Pdzd8* mutation in *Pdzd8* homozygous mice as shown by the lack of exon 3 mRNA and presence of *LacZ* in these mice (Al-Amri *et al.*, 2022).

The presence of premature stop codons, when not present in the last exon is generally associated with nonsense-mediated mRNA decay (Supek, Lehner and Lindeboom, 2021). The relative expression of *Pdzd8* exon 3 mRNA in *Pdzd8* heterozygous mice was expected to be reduced compared to WT as they contain a mutated allele, however a slight increase in this was detected (Fig. 32B). This suggest that mRNA decay might not occur as a consequence of this *Pdzd8* mutation. To further confirm this, primers were designed to amplify different regions along the *Pdzd8* gene and were examined by qRT-PCR analysis. Surprisingly, primers detecting a region between *Pdzd8* exon 1 and 2, which resides before the PDZD8 mutation, showed significantly increased mRNA relative expression in *Pdzd8* homozygous and heterozygous mice compared to WT ($F(2, 12)=19.12$, $P=0.0002$, with post hoc comparisons $P=0.0001$ and $P=0.004$, respectively; Fig. 32F). Primers amplifying a region between exon 4 and 5, which is located after the *Pdzd8* mutation, were also used. Relative mRNA expression of exon 4/5 in *Pdzd8* homozygous mice was comparable to WT (Fig. 32G). Conversely, an increase, albeit not significant, was observed in exon 4/5 mRNA in heterozygous mice compared to WT controls (Fig. 32G). These results suggest that mRNA-mediated decay does not appear to take place in *Pdzd8* mice despite the presence of a premature stop codon in exon 3 of the 5-exon gene.

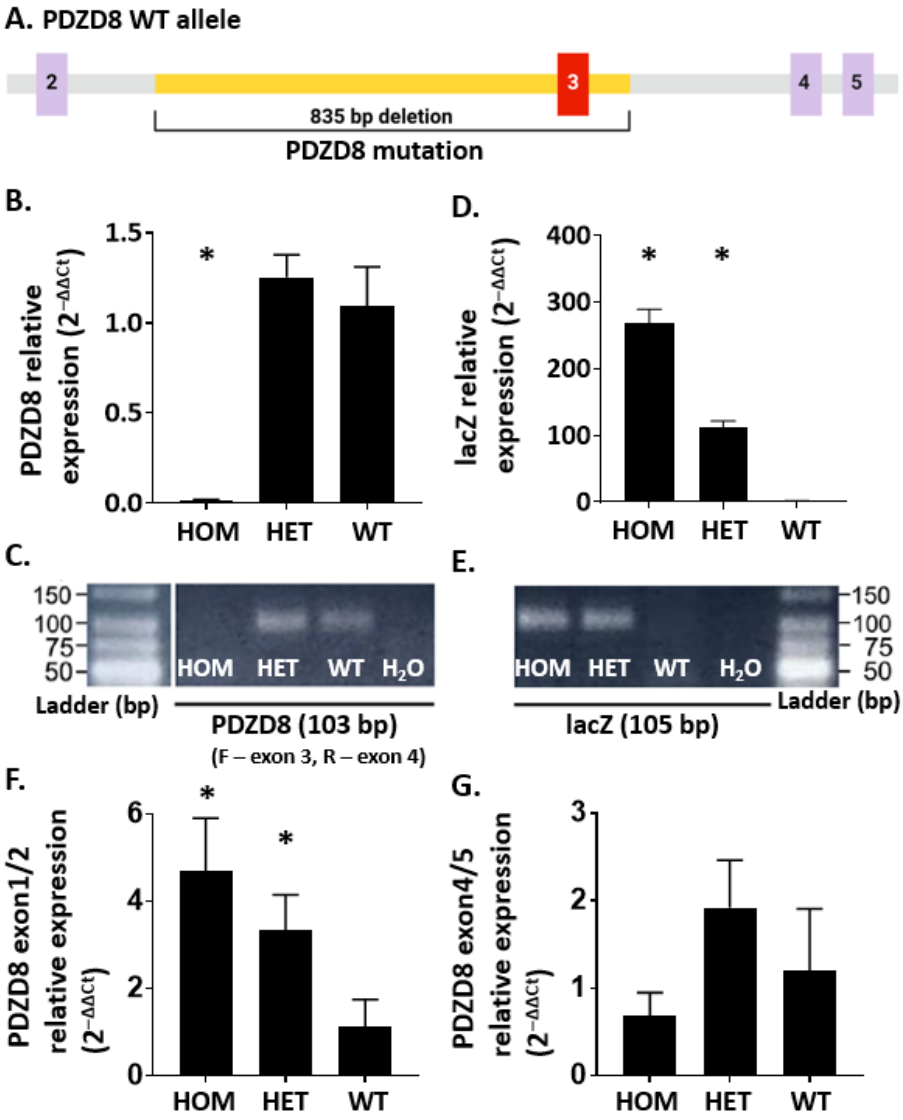

Figure 32. *Pdzd8* exon 3 mRNA expression is reduced in *Pdzd8* mice as shown by qRT-PCR analysis. Brain mRNA was extracted from 15 female mice (5 / genotype). PDZD8 WT allele with exons marked by purple boxes. *Pdzd8* mutation (yellow region) causes an 835 bp deletion including exon 3 (red box; A). *Pdzd8* exon 3/4 mRNA is absent in *Pdzd8* HOM mice compared to WT controls and HET animals (B). Gel electrophoresis of *Pdzd8* exon 3/4 primers (103-bp band) (C). LacZ mRNA expression is absent in WT mice compared to *Pdzd8* HET and HOM animals (D). Gel electrophoresis of LacZ primers (105-bp band) (E). *Pdzd8* exon 1/2 mRNA is increased both HET and HOM mice compared to WT (F). *Pdzd8* exon 4/5 mRNA is present in both HET and HOM mice (G). Relative mRNA expression was calculated by $2^{-\Delta\Delta Ct}$ method and data is presented as fold change relative to HPRT reference gene. Statistical analysis: one-way ANOVA with Dunnett's multiple comparison, significance level $p<0.05$ (indicated by *) compared to WT; data presented as mean ± standard error. WT – wild type, HET – heterozygous, HOM – homozygous, bp – base pairs, F – forward primer, R – reverse primer.

The presence of *Pdzd8* mutant mRNA suggested a possibility for this mRNA to be translated into protein in the *Pdzd8* homozygous mice. To confirm the lack of Pdzd8 in homozygous mice, an antibody against a 50-aa epitope (935-984 aa) at the C-terminus of Pdzd8 was used to detect Pdzd8 protein levels by western blotting (Methods 2.3.2, Fig. 9). Pdzd8 protein should be detected around 140 kDa and a band just above the 130 kDa mark was detected in WT samples using the Pdzd8 antibody (Fig. 33A). Pdzd8 protein was less abundant in heterozygous mice, with a reduction of ~ 60%, while it was completely absent in homozygous

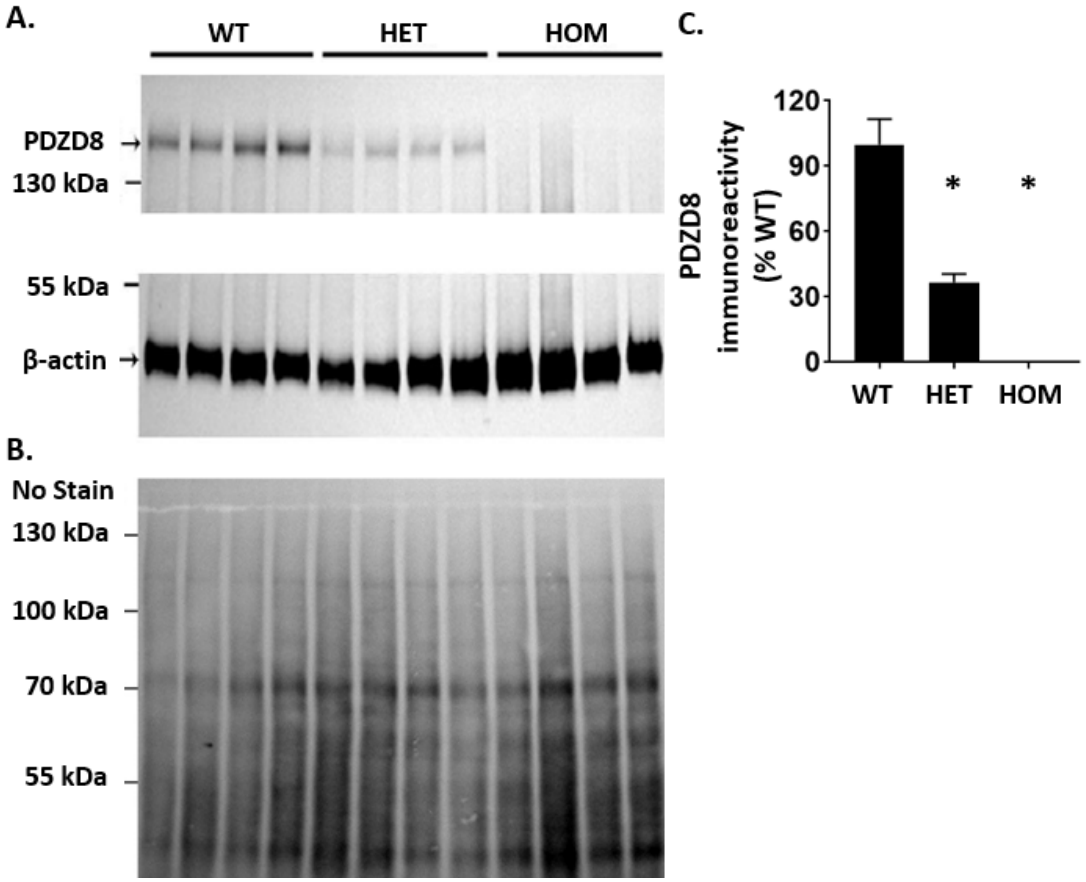

Figure 33. Pdzd8 protein is absent in *Pdzd8* HOM mice. Protein was extracted from 15 female mouse brains (4 / genotype) to perform western blot analysis. Pdzd8 protein levels are significantly reduced in both *Pdzd8* HET and HOM mice compared to WT controls (A, C). No Stain labelling shows the protein transfer on the membrane (B). Pdzd8 protein levels were normalized to β-actin (A) and presented was as a percentage of WT immunoreactivity (C). Statistical analysis: one-way ANOVA with Dunnett's multiple comparison, significance level $p<0.05$ (indicated by *); data presented as mean ± standard error. WT – wild type, HET – heterozygous, HOM – homozygous, kDa – kiloDaltons.

mice ($F(2, 9)=50.98$, $P<0.0001$, with post hoc comparisons $P=0.0003$ and $P=0.0001$, respectively; Fig. 33C). Therefore, western blot analysis confirmed the lack of full-length Pdzd8 protein in *Pdzd8* homozygous samples (Al-Amri *et al.*, 2022). An antibody against the N-terminus of Pdzd8 could have detected a putative truncated Pdzd8 protein but was not commercially available.

Initially, an immunofluorescence approach to detect Pdzd8 brain expression (Methods 2.4.1), was employed. Unfortunately, no reliable antibodies against Pdzd8 that are effective for immunofluorescence have been developed yet. A Thermo-Fisher anti-Pdzd8 antibody (A-11132) was tested at various dilutions, ranging from 1:100 to 1:1000; however, the staining was not successful as there was no difference in labelling between brain tissue sections from WT and *Pdzd8* mice.

As *Pdzd8* mice contain *LacZ* in the *Pdzd8* locus, a β-galactosidase staining kit was used as an alternative approach to investigate the expression pattern of *Pdzd8* at a brain regional level (Methods 2.4.1). *LacZ* staining was enhanced in the cerebral cortex (Fig. 34A), the olfactory bulb (Fig. 34B), and the hippocampus (Fig. 34C), as indicated by the presence of strong blue puncta, suggesting high levels of *Pdzd8* expression in these regions (Fig. 34). Nonetheless, *LacZ* labelling was present throughout the whole brain (Fig. 34A). The apparent presence of *Pdzd8* expression across the whole brain, with low regional specificity, as indicated by the *LacZ* staining, is in agreement with *Pdzd8* mouse brain RNA sequencing data from the Protein Atlas (Table 4). *Pdzd8* RNA expression was identified across many brain regions, such as cerebral cortex, hippocampus, olfactory bulb, hypothalamus, thalamus, with the highest levels of expression detected in basal ganglia (Table 4).

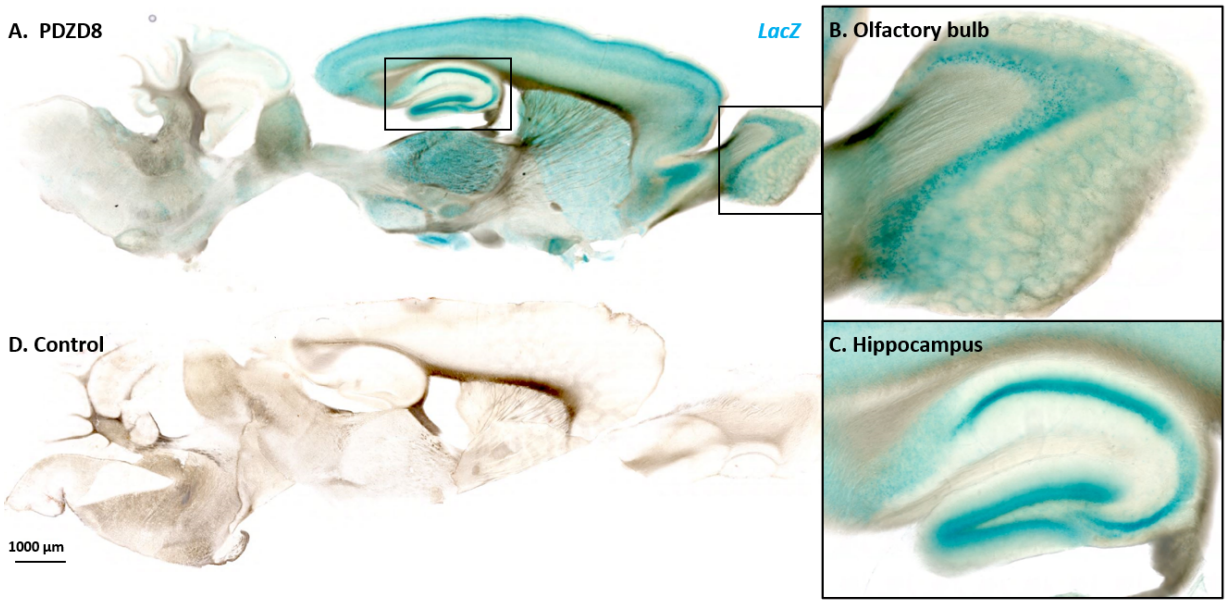

Figure 34. LacZ expression in the brain of *Pdzd8* mice. Sagittal sections from *Pdzd8* mouse brains and WT controls showing the expression of LacZ in the brains of *Pdzd8* mice and controls (A, C). Zoomed in regions of the olfactory bulb (B) and hippocampus (C) where there is enhanced LacZ labelling. Scale bar 1000 µm.

Brain region	Normalized Gene Expression Values (nTPM)
Frontal cortex	23.0
Occipital cortex	23.9
Retrosplenial and cingulate cortex	23.3
Somatosensory cortex	21.8
Olfactory bulb	23.8
Hippocampal formation	23.7
Amygdala	21.2
Basal ganglia	32.8
Thalamus	31.6
Hypothalamus	30.1
Midbrain	29.3
Pons and medulla	20.9
Cerebellum	13.3
White matter	21.5

Table 4. *Pdzd8* RNA expression in the mouse brain. Data obtained from the Human Protein Atlas. nTPM – normalized protein-coding transcripts per million.

3.1.2 *Pdzd8* mice – phenotype

A series of body measurements and behavioural tests were undertaken to start characterizing the *Pdzd8* mouse line. Age and sex-matched *Pdzd8* and WT mice were weighed prior to undergoing behavioural experiments (Results Chapter 2). Both *Pdzd8* males (n=27) and females (n=13) aged 2 – 3 months old weighed significantly less compared to WT males (n=34; $t(59)=12.10$, $P<0.0001$) and females (n=30; $t(39)=2.059$, $P=0.046$) (Fig. 35). Data obtained from the Sanger Institute from the same *Pdzd8* mutant mouse line supported these findings with respect to older mice. Body weight was tracked across age from 4 to 16 months old for both males and females. *Pdzd8* males (n=8) and females (n=8) had lower weights throughout all the measurements take from 4 to 16 months compared to WT males (n=33) and females (n=21) (Fig. 35) (Al-Amri *et al.*, 2022). Additionally, data obtained from Sanger Institute also displayed significantly reduced body length measurements in both *Pdzd8* male ($t(39)=5.852$, $P<0.0001$) and females ($t(26)=3.791$, $P=0.0008$) compared to WT controls (Fig. 35) (Al-Amri *et al.*, 2022). Overall, these results showed that *Pdzd8* mice are phenotypically different compared to age and sex-matched WT controls.

The smaller size of *Pdzd8* mice suggested that there might be a disparity in metabolism in this mouse line. To potentially understand the cause of this difference in size, age-matched *Pdzd8* males (n=9) and WT males (n=8, one animal was excluded due to welfare reasons) were individually placed in metabolic cages for a period of 7 days, with the first 5 days counting as a habituation period (Methods 2.5.10). These metabolic cages allowed for continuous monitoring of a wide variety of parameters, including movement, heat production, food intake, O_2 consumption and CO_2 production, with parameter readings taken on a 14-minute cycle.

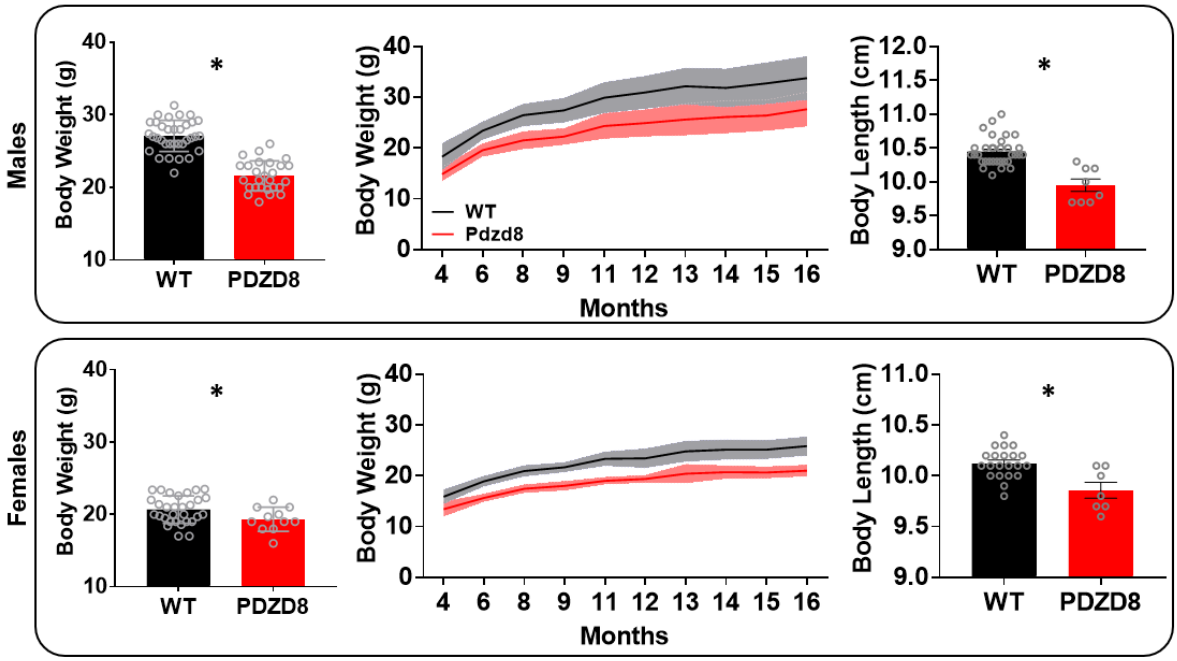

Figure 35. *Pdzd8* mice are smaller than WT controls. Mice used for behavioural experiments were weighed (2-3 months old). Both *Pdzd8* (red) male (n=27) and female (n=12) mice weighed less than age matched WT (black) males (n=34) and females (n=30). Differences in body weight measurements between *Pdzd8* (n=8 males, n=8 females) and WT (n=33 males, n=21 females) mice are sustained throughout the lifespan (4 – 16 months; data obtained from Sanger Institute). *Pdzd8* mice display reduced body length compared to age matched WT controls (data obtained from Sanger Institute). Statistical analysis: unpaired two-tailed independent t-test, significance level $p<0.05$ (indicated by *); data presented as mean ± standard error.

Motility data (Fig. 36) was collected separately as daily movement as detected by sensors on X, Y and Z-axes, and wheel usage, which was collected by a distinct sensor. *PDZD8* mice displayed heightened daily movement over a 2-day analysis period compared to WT controls, with increased activity becoming apparent over the night cycle, between 6 pm and 6 am (Fig. 36A). The total movement over the 2-day period was significantly increased in *Pdzd8* mice as opposed to WT controls ($t(15)=2.141$, $P=0.049$; Fig. 36B). The most striking difference in *Pdzd8* mice detected by the metabolic cages was the number of wheel turns accumulated. *Pdzd8* mice were using the wheel at a much higher rate compared to WT over a 2-day period (Fig. 36C), with the number of total wheel turns being significantly increased in *Pdzd8* mice

(U=5, P=0.001; Fig. 36D). This increase in activity in *Pdzd8* mice could be correlated with the leaner form (reduced soft tissue mass) observed in this mouse line compared to WT (Al-Amri *et al.*, 2022). Interestingly, wheel running is not only used as a measure of locomotor activity but also as a way of assessing stereotypical, repetitive behaviour in mouse models of autism (Karvat and Kimchi, 2012). Therefore, the significantly higher wheel usage recorded in *Pdzd8* mice could potentially be indicative of a stereotypical behaviour, common among autism and ID mouse models, rather than just an increase in overall motility. Additionally, this would support the findings collected from human subjects with a *Pdzd8* mutation, where repetitive behaviours were observed (Al-Amri *et al.*, 2022).

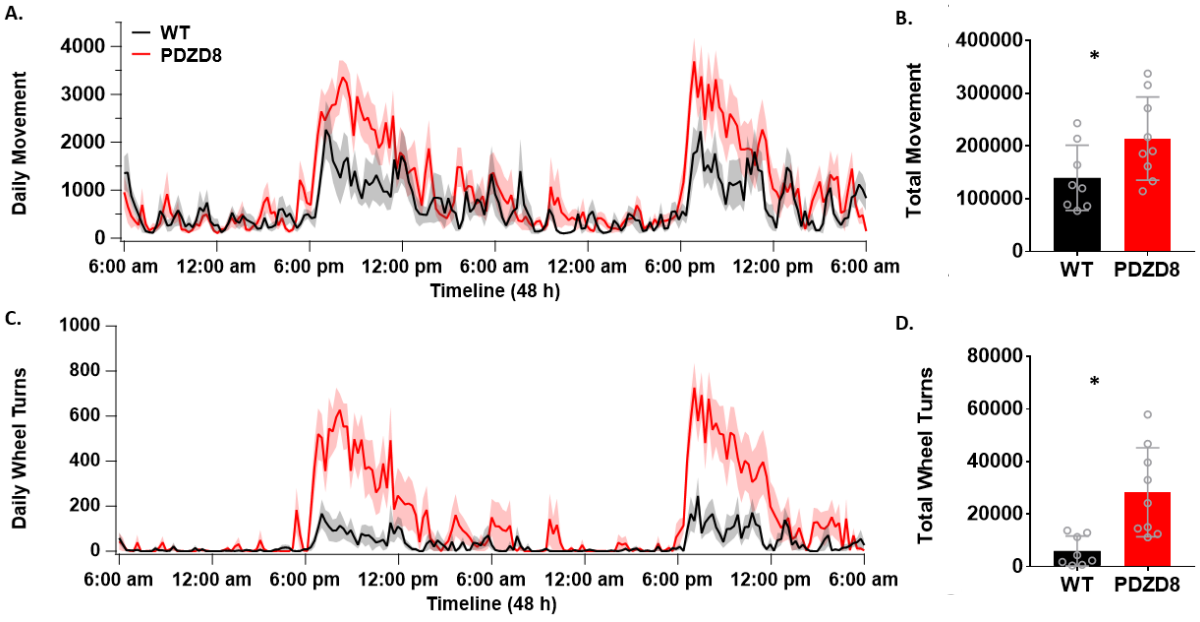

Figure 36. *Pdzd8* mice are hyperactive. *Pdzd8* mice (red) and age and sex-matched WT controls (black) (n=9 / genotype) were placed in metabolic cages, data is shown for a 2-day period. *Pdzd8* mice exhibit increased motility over a 2-day analysis period compared to WT controls (A, B). *Pdzd8* mice displayed increased wheel usage over a 2-day period in the metabolic cages compared to WT mice (C, D). Movement (sensors X, Y and Z-axis) and wheel turns were collected as the number of times the sensors were activated (beam breaks) in a 14-minute cycle; sum of total movement and wheel turns over the 2-day period were plotted. Statistical analysis: unpaired two-tailed independent t-test (B), nonparametric Mann-Whitney test (D), significance level $p<0.05$ (indicated by *); data presented as mean ± standard deviation.

The metabolic cages also detect heat production measured by assessing the caloric value of the food being metabolized. However, no difference in heat production between *Pdzd8* and WT mice was recorded over the 2-day period (Fig. 37A, B). The average heat production was also normalized to each individual mouse's body weight, as the *Pdzd8* mice are smaller; even with body weight normalisation no differences in calorimetric measurement were observed between the *Pdzd8* and WT mice (Fig. 37C).

Food consumption is also monitored by the metabolic cages. Daily recordings of food intake revealed no difference between *Pdzd8* mice and WT controls in the total amount of food consumed (Fig. 37D, E). Total food intake normalized by body weight also did not display any changes in *Pdzd8* mice (Fig. 37F). Additionally, water intake was manually measured before and after the metabolic cage experiments. No changes in the water consumption over a 7-day period were seen between the *Pdzd8* and WT mice (Fig. 37G). Surprisingly, even though *Pdzd8* mice displayed higher activity levels, there were no changes observed in the heat production, food intake and water intake in comparison to WT mice.

All mice placed in the metabolic cages were weighed before and after the 7-day experimental period to monitor health. In accordance with the previous results, *Pdzd8* mice weighed less compared to WT controls ($t(15)=4.962$, $P=0.0002$; Fig. 37H). Mice are usually expected to lose some weight following placement in the metabolic cages, due to them being singly housed in a novel environment. This was observed in WT animals ($t(7)=2.792$, $P=0.026$; Fig. 37I). Intriguingly, *Pdzd8* did not display any weight loss following the 7-day housing period in the metabolic cages (Fig. 37J).

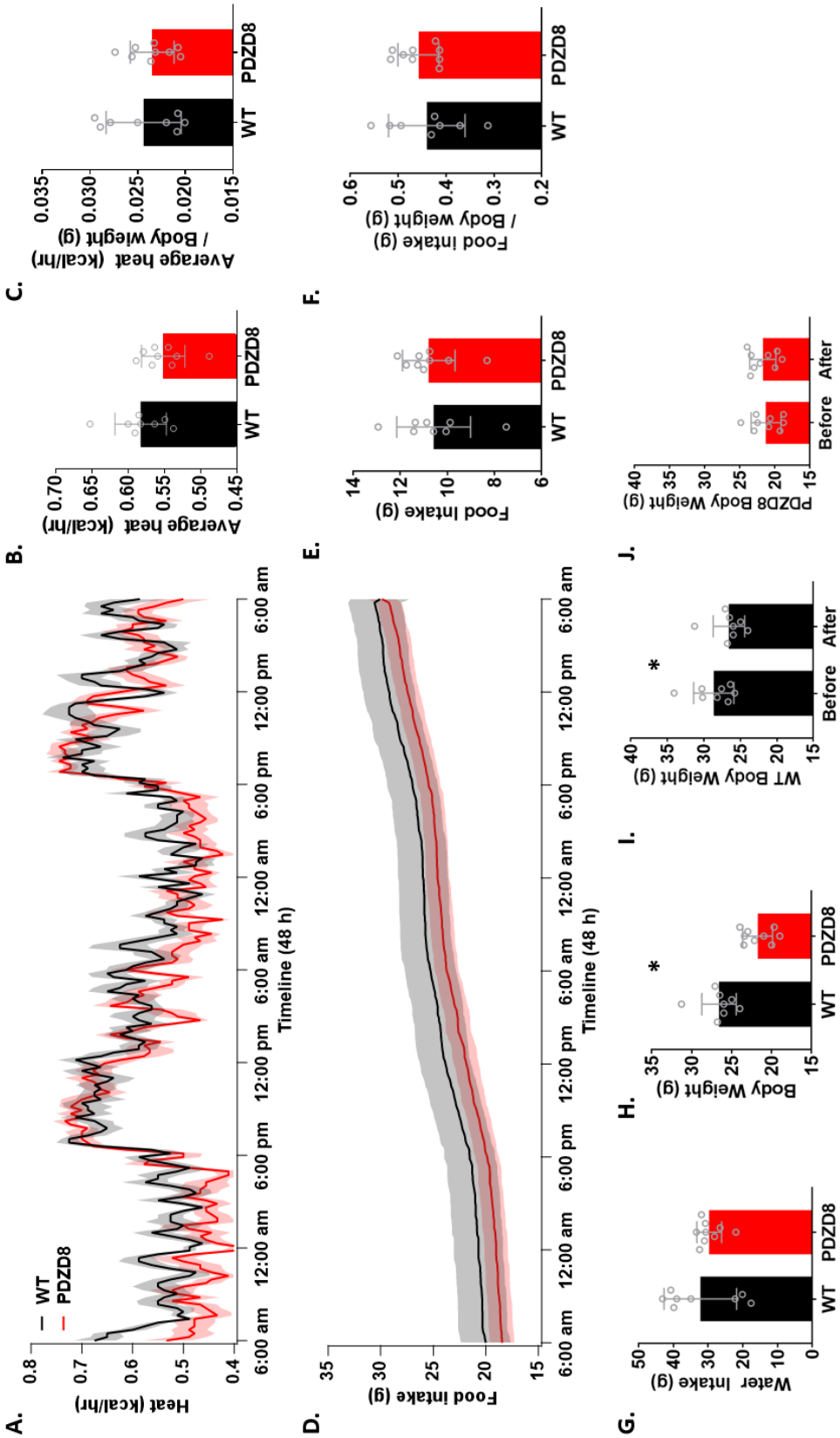
A.
B.
C.
D.
E.
F.
G.
H.
I.
J.
WT
PDZD8
Heat (kcal/hr)
Timeline (48 h)
6:00 am
12:00 am
6:00 pm
12:00 pm
Average heat (kcal/hr)
Body weight (g)
Food intake (g)
Water Intake (g)
WT Body Weight (g)
PDZD8 Body Weight (g)
Before
After
*

Figure 37. *Pdzd8* mice display no changes in heat production, food, and water intake. *Pdzd8* mice (red) and age and sex-matched WT controls (black) (n=9 / genotype) were placed in metabolic cages, data is shown for a 2-day period. *Pdzd8* mice show no difference in heat production compared to WT controls (A, B), even when normalized to body weight (C). Accumulative food intake over the two-day analysis period in the metabolic cages (D). No difference between *Pdzd8* mice and WT controls in the total food consumption (E) and total food intake normalized to body weight (F). No changes in water intake between *Pdzd8* and WT mice for the total time spent in the metabolic cages, seven days (G). *Pdzd8* mice weigh significantly less than WT controls (H); however, *Pdzd8* mice do not lose weight following a 7-day housing period in the metabolic cages (I), compared to WT controls, which lose weight (J). Statistical analysis: unpaired two-tailed independent t-test (B, C, E, F, G, H), paired two-tailed independent t-test (I, J), t-test significance level $p<0.05$ (indicated by *); data presented as mean ± standard deviation.

The increase in motility could be explained by changes in metabolic activity. To assess this, parameters such as O_2 consumption and CO_2 production are measured in the metabolic cages. Due to their increased activity, we expected higher CO_2 production in *Pdzd8* mice and this was observed with CO_2 being significantly higher in *Pdzd8* mice as opposed to WT ($t(15)=4.957$, $P=0.0002$; Fig. 38A, B). This significance was still present after normalizing the average CO_2 production to body weight ($t(15)=2.848$, $P=0.012$; Fig. 38C). Similarly, O_2 consumption was increased in the *Pdzd8* mice in contrast to WT mice ($t(15)=4.915$, $P=0.0002$; Fig. 38D, E). Average O_2 consumption normalized to body weight was also higher in *Pdzd8* mice ($t(15)=2.968$, $P=0.009$; Fig. 38F). Both O_2 consumption and CO_2 production levels were likely to be higher in *Pdzd8* mice due to increase in overall activity. Following, O_2 consumption and CO_2 production were used to determine the respiratory exchange ratio (Fig. 38G). The respiratory exchange ratio is a measure of the ratio between the volume of CO_2 produced by the body and the O_2 consumed, and it reveals the type of energy metabolized by the body. Generally, a value below 0.7 denotes fat metabolism. As respiratory exchange ratio values become closer 1, the body uses more carbohydrates as fuel. Respiratory

exchange ratio values above 1 signify ketosis, or protein breakdown. This occurs when there is no more fat or carbohydrates in the body to metabolize.

Surprisingly, there was no difference in the respiratory exchange ratio between *Pdzd8* mice and WT animals (Fig. 38G, H). Normalizing the average respiratory exchange ratio to body weight also showed no changes between the experimental groups (Fig. 38I). These results suggested that the hyperactivity observed in the *Pdzd8* mice does not seem to be caused by a change in metabolism, as both *Pdzd8* and WT mice were using a predominantly carbohydrate metabolic fuel source. Overall, the metabolic cage experiments revealed that a behavioural phenotype of *Pdzd8* mice was hyperactivity.

The metabolic cages yielded interesting results with regards to hyperactivity. However, using these cages was very costly and had limited availability for booking. Additionally, only 6 metabolic cages were available which severely restricted the number of animals that could be tested at once. Therefore, a cheap and high-throughput method of detecting movement was employed to be able to further investigate hyperactivity in *Pdzd8* mice. A series of rodent activity detectors were fabricated (Methods 2.5.11) based on previously published work (Matikainen-Ankney *et al.*, 2019). Each mouse was singly housed with an activity monitor, which enabled a higher number of mice to be tested as no other equipment was required. Therefore, both *Pdzd8* homozygous (n=14) and heterozygous (n=12) mice were assessed along with WT controls (n=12) (Fig. 39). Surprisingly, no significant difference in activity was detected between any of the genotypes (Fig. 39A). A slight increase in the night cycle activity could be observed in *Pdzd8* homozygous mice in the activity timeline (Fig. 39A). However, when the average activity during the night was calculated for each night cycle for individual mice, no significant changes were found between *Pdzd8* homozygous

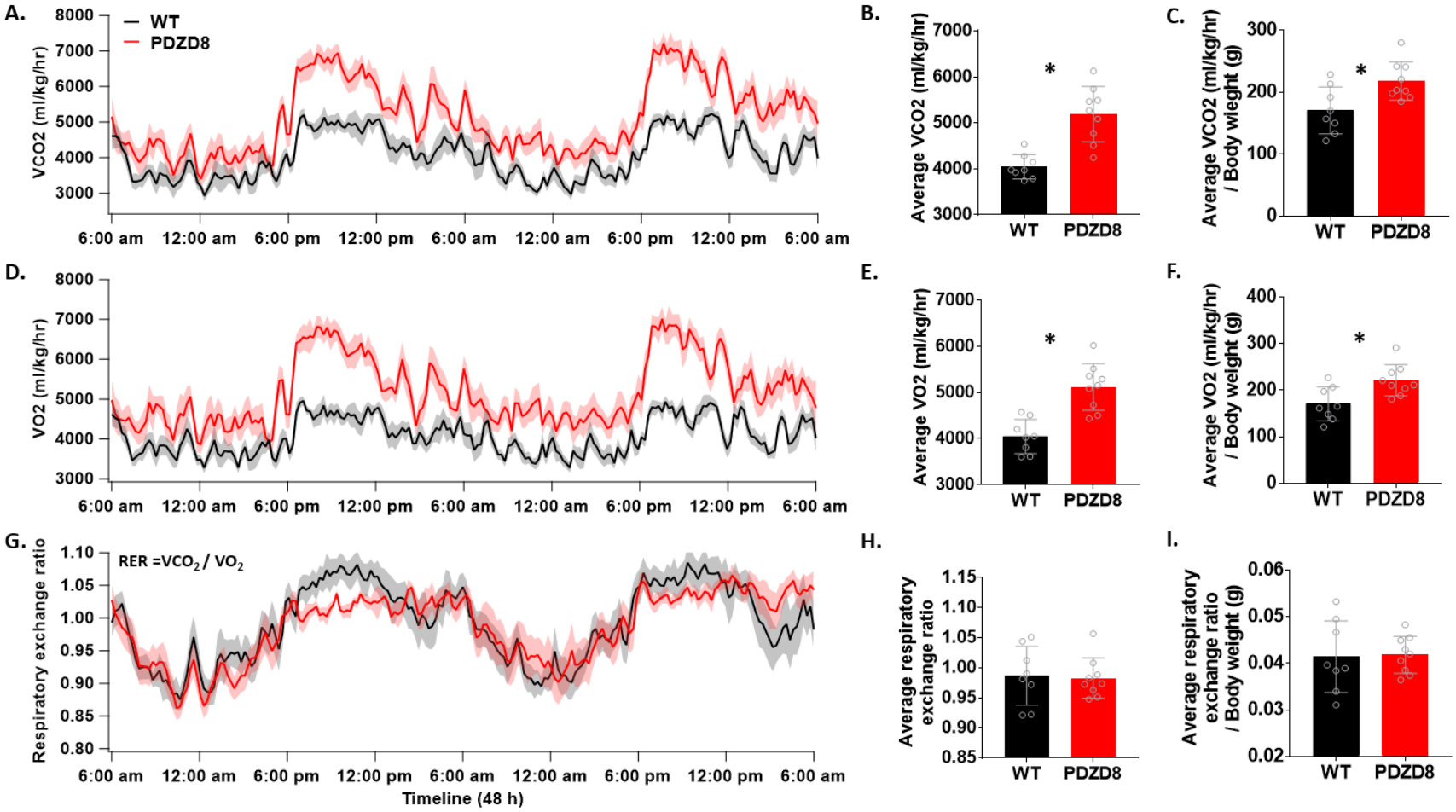
A.
WT
PDZD8
VCO2 (ml/kg/hr)
8000
7000
6000
5000
4000
3000
6:00 am
12:00 am
6:00 pm
12:00 pm
6:00 am
12:00 am
6:00 pm
12:00 pm
6:00 am
B.
Average VCO2 (ml/kg/hr)
WT
PDZD8
C.
Average VCO2 (ml/kg/hr) / Body weight (g)
D.
VO2 (ml/kg/hr)
E.
Average VO2 (ml/kg/hr)
F.
Average VO2 (ml/kg/hr) / Body weight (g)
G.
Respiratory exchange ratio
RER =VCO2 / VO2
1.10
1.05
1.00
0.95
0.90
0.85
0.80
Timeline (48 h)
H.
Average respiratory exchange ratio
I.
Average respiratory exchange ratio / Body weight (g)

Figure 38. *Pdzd8* mice exhibit no changes in the respiratory exchange ratio. *Pdzd8* mice (red) and age and sex-matched WT controls (black) (n=9 / genotype) were placed in metabolic cages. *Pdzd8* mice have increased production of CO_2 compared to WT over a two-day period (A, B). CO_2 production normalized to body weight (C). *Pdzd8* mice have increased O_2 consumption compared to WT mice (D, E). O_2 consumption normalized to body weight (F). Respiratory exchange ratio is similar between *Pdzd8* mice and WT controls (G, H), even when normalized to body weight (I). Statistical analysis: unpaired two-tailed independent t-test, significance level $p<0.05$ (indicated by *); data presented as mean ± standard deviation. VCO_2 – carbon dioxide output, VO_2 – oxygen consumption, RER – respiratory exchange ratio.

or heterozygous mice and WT controls (Fig. 39B). The results from the rodent activity detectors contradicted the data obtained from the metabolic cages. However, these manually built activity sensors are not as sensitive as the sensors used by the metabolic cages (Qiu *et al.*, 2014), which could explain the contrasting results. The daily movement detected by the metabolic cages (Fig. 36A, B), even though it was higher in *Pdzd8* mice than WT mice, was not as striking as the difference detected in the wheel usage. Given the lack of a wheel in the mouse home cages, it could be that other stereotypical behaviours potentially present, such as grooming, might not be as easily detected by the motion sensors in the rodent activity detectors.

The hyperactivity detected in *Pdzd8* mice in the metabolic cages was investigated further, by assessing the soft tissue mass and the brown adipose tissue in *Pdzd8* homozygous mice (Fig. 40). Data obtained from Sanger Institute showed that both *Pdzd8* male (n=8) and females (n=8) displayed deceased soft tissue mass, which included skin, muscle, and fat, in contrast to WT males (n=33; $t(39)=4.204$, $P=0.0001$) and females (n=21; $t(26)=5.363$, $P<0.0001$) (Fig. 40). This aligns with the fact that *Pdzd8* mice weigh less and are significantly more active than WT mice. Additionally, increased body fitness is associated with larger amounts of brown fat. Brown fat, also known as brown adipose tissue, is thought to be a “healthy fat”

due to its role in metabolizing calories to generate heat, rather than storing energy and calories as white fat. Thus, brown adipose tissue was measured in *Pdzd8* males (n=5) and females (n=5) and WT control males (n=5; t(8)=2.696, P=0.027) and females (n=5; U=4, P<0.0001) (Fig. 40). As anticipated, *Pdzd8* mice exhibited significantly higher levels of brown fat when normalized to their body weight compared to age and sex-matched WT controls (Fig. 40). Overall, these results suggest that *Pdzd8* mice are leaner than WT controls and corroborate the metabolic cage data in regards to hyperactivity.

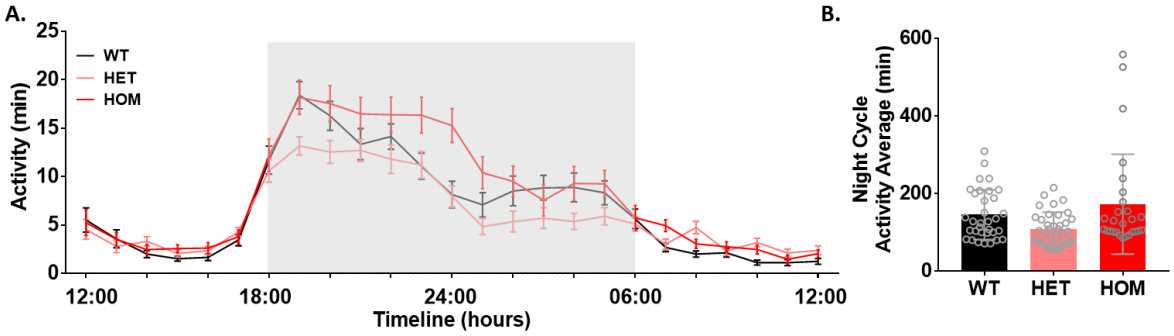

Figure 39. Rodent activity detector does not identify hyperactivity in *Pdzd8* mice. *Pdzd8* HOM (n=14; red), HET (n=12; pink) and age-matched WT (n=12; black) controls were individually housed with a rodent activity sensor. Timeline of daily average activity (night cycle – grey box) in *Pdzd8* HOM, HET, and WT mice; data is shown as minutes of activity within an hour, detected within a day, over a 3-day period (A). *Pdzd8* HOM and HET mice show no difference from WT mice in the night cycle average activity (B). Statistical analysis: Kruskal-Wallis non-parametric test with Dunn's multiple comparison, significance level p<0.05; data presented as mean ± standard error (A) or standard deviation (B). HET – heterozygous, HOM – homozygous.

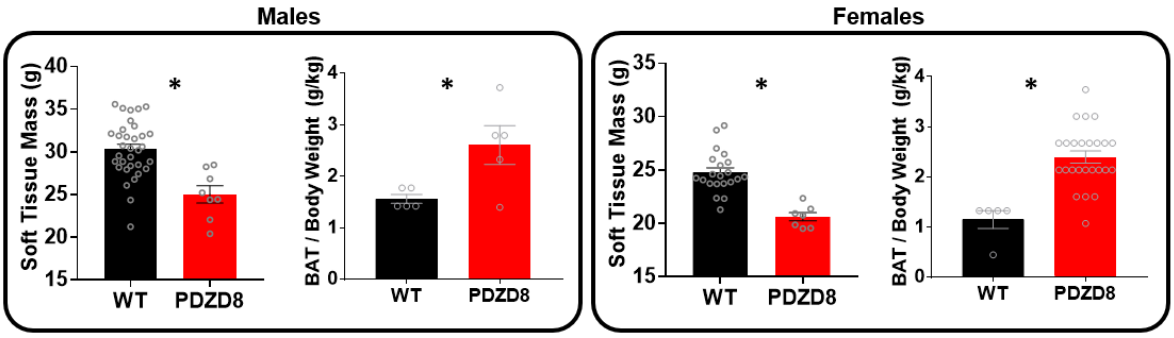

Figure 40. *Pdzd8* mice have decreased soft tissue and increased brown adipose tissue. *Pdzd8* males (n=8) and females (n=8) have decreased soft tissue mass (skin, muscle, fat) compared to WT males (n=33) and females (n=21; data obtained from the Sanger Institute). Both *Pdzd8* males (n=5) and females (n=25) have increased brown adipose tissue compared to WT males (n=5) and females (n=5). Statistical analysis: unpaired two-tailed independent t-test and nonparametric Mann-Whitney test, significance level $p<0.05$ (indicated by *); data presented as mean ± standard error. BAT – brown adipose tissue.

3.1.3 *Pdzd8* brain structural abnormalities

Thus far the data showed that not only *Pdzd8* mice are smaller compared to WT controls, but also potentially displayed stereotypical behaviour as recorded by the increased wheel running. This prompted further investigation into whether there were any overt brain alterations in *Pdzd8* mice compared to WT animals. Structural magnetic resonance imaging (Methods 2.4.4) was used to identify brain morphology variations in *Pdzd8* males (n=10) and females (n=22) versus WT males (n=17) and females (n=10) (Fig. 41A) (Al-Amri *et al.*, 2022). Volumetric analysis of brain morphology revealed a significant decrease in the overall brain volume in *Pdzd8* mice compared to WT controls ($t(47)=6.519$, $P<0.0001$; Fig. 41B). This was in agreement with the smaller body size detected in the *Pdzd8* mice. Additionally, this was also supported by the fact *Pdzd8* mouse brain weights were significantly smaller than the age and sex-matched WT controls ($t(8)=3.449$, $P=0.0008$; Fig. 41C, measured for the mice used in the qRT-PCR experiment). However, as *Pdzd8* mice are smaller, to accurately perform volumetric analysis of the brain, the brain volumes needed to be

normalized to body weight. Interestingly, when the brain volume was normalized to the average body weight, *Pdzd8* mice displayed significantly bigger brain volumes compared to WT mice ($t(47)=5.647$, $P<0.0001$; Fig. 41D). Further, to understand where this increase in brain volume resides, brain regional morphology was investigated and presented as a percentage of the absolute brain volume. This gives a measure of the relative size of brain regions that can be compare across mice with different overall brain sizes. Multiple brain regions had higher relative brain volumes in *Pdzd8* mice including: the cerebellum ($t(47)=5.382$, $P<0.0001$; Fig. 41E, J), olfactory bulb ($t(47)=9.479$, $P<0.0001$; Fig. 41F, I), hippocampus ($t(47)=4.968$, $P<0.0001$; Fig. 41G, K) and retrosplenial cortex ($t(47)=6.571$, $P<0.0001$; Fig. 41H, K) (Al-Amri *et al.*, 2022). An increase in the cerebellum relative size in the *Pdzd8* mice could be linked to the hyperactivity detected in this mouse line, due to its role in coordination of voluntary body movements (Stoodley, 2016). Several brain regions had relatively smaller sizes in *Pdzd8* mice such as the: thalamus ($t(47)=7.418$, $P<0.0001$; Fig. 41L, P), pallidum ($t(47)=6.249$, $P<0.0001$; Fig. 41M, P), corpus callosum ($U=13$, $P<0.0001$; Fig. 41N, K) and superior colliculus ($t(47)=8.684$, $P<0.0001$; Fig. 41O, Q) (Al-Amri *et al.*, 2022). Overall, the brain imaging data exposed structural brain abnormalities in the brains of *Pdzd8* mice in comparison to WT animals.

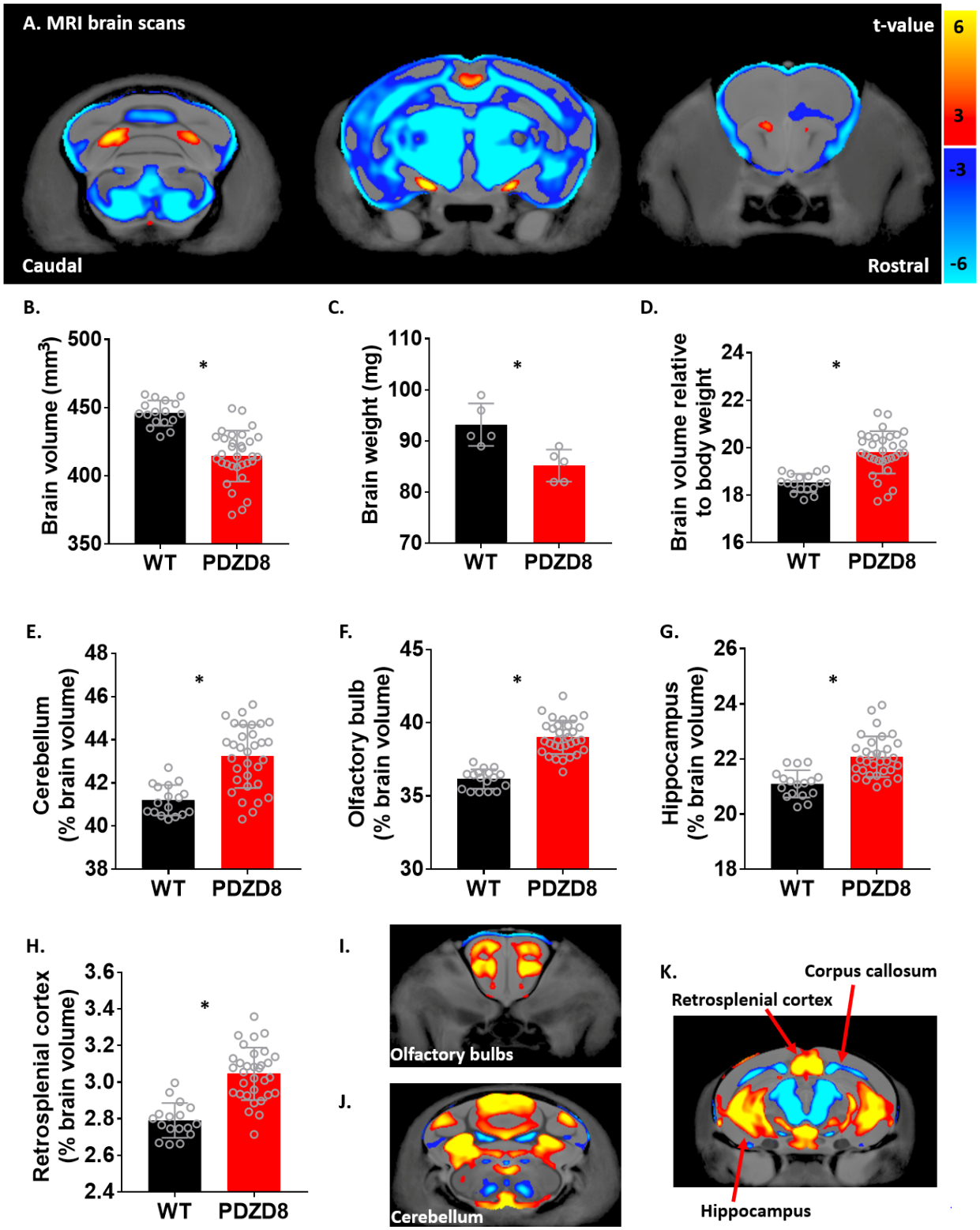
A. MRI brain scans
t-value
6
3
-3
-6
Caudal
Rostral
B.
Brain volume (mm3)
500
450
400
350
WT
PDZD8
C.
Brain weight (mg)
110
100
90
80
70
WT
PDZD8
D.
Brain volume relative to body weight
24
22
20
18
16
WT
PDZD8
E.
Cerebellum (% brain volume)
48
46
44
42
40
38
WT
PDZD8
F.
Olfactory bulb (% brain volume)
45
40
35
30
WT
PDZD8
G.
Hippocampus (% brain volume)
26
24
22
20
18
WT
PDZD8
H.
Retrosplenial cortex (% brain volume)
3.6
3.4
3.2
3.0
2.8
2.6
2.4
WT
PDZD8
I.
Olfactory bulbs
J.
Cerebellum
K.
Corpus callosum
Retrosplenial cortex
Hippocampus

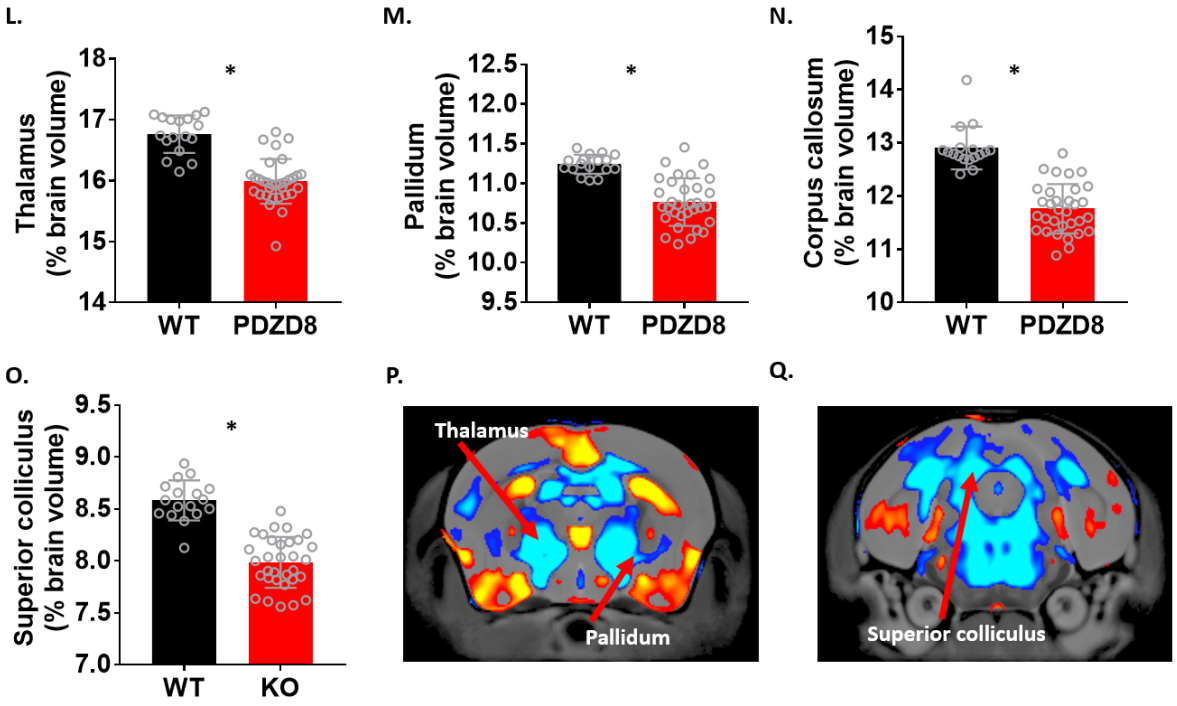

Figure 41. High-resolution structural magnetic resonance imaging reveals structural brain differences in *Pdzd8* mice. Structural magnetic resonance brain imaging was performed in *Pdzd8* mice (n=32; 10 males, 22 females) and WT controls (n=17; 7 males, 10 females). Voxel-wise volumetric analysis of two-dimensional coronal brain images of the whole brain and regional differences are indicated by red (increase) or blue (decrease) contour shading (A). *Pdzd8* mice have decreased absolute brain volume (mm^3) compared to WT (B). *Pdzd8* mice have decreased brain weight compared to WT mice; these data were taken from the mice used in the qRT-PCR experiment (C). However, *Pdzd8* mice have increased brain volume compared to WT when normalized to body weight (D). *Pdzd8* mice display increased relative volume (% of brain volume) of the cerebellum (E, J), olfactory bulb (F, I), hippocampus (G, K) and retrosplenial cortex (H, K) compared to WT mice. *Pdzd8* mice display decreased relative volume (% of brain volume) of the thalamus (L, P), pallidum (M, P), corpus callosum (N, K), and superior colliculus (O, Q) compared to WT mice. Statistical analysis: unpaired two-tailed independent t-test, nonparametric Mann-Whitney test (N), significance level $p<0.05$ (indicated by *); data presented as mean ± standard deviation.

No sex differences were detected. The global increase in the brain size relative to the body weight in *Pdzd8* mice implied that an increase in the number of neurons might be responsible for this. To further support this notion, both areas in the brain where adult neurogenesis happens, the hippocampus and olfactory bulbs, showed a significant increase in relative volume in the *Pdzd8* mice compared to WT controls.

I next sought to test whether changes in neurogenesis were observed in the brain regions showing increased relative sizes. To do this I took advantage of EdU labelling (Methods 2.4.3). A single dose of EdU was injected in *Pdzd8* (n=5) and WT (n=5) mice, which will get incorporated into newly dividing cells. Mice were kept for 7 days following which the olfactory bulb (Fig. 42) and the hippocampus (Fig. 43) were examined for EdU positive cells. An abundance of EdU positive cells were found in the olfactory bulbs of *Pdzd8* (Fig. 42A, B, C) and WT mice (Fig. 42D, E, F). In the olfactory bulb, newly formed neurons arrive in the granule cell layer from the lateral ventricle, and then spread to the rest of the olfactory bulb (Gage, 2000). Thus, the olfactory bulb area was divided into 2 regions, the granule cell layer, where most EdU positive cells should be found and the extra granule cell layer, which represented the rest of the olfactory bulb including the glomerular layer (Fig. 42G).

Surprisingly, the EdU positive cell density was lower in the granule cell layer area of *Pdzd8* brain sections compared to WT samples ($U=1307$, $P=0.001$; Fig. 42H). Similarly, assessment of the extra granule layer region revealed a decreased number in the EdU positive cell density relative to the area in the *Pdzd8* compared to WT mice ($U=897$, $P<0.0001$; Fig. 42I). In comparison to the olfactory bulb, the number of EdU positive cells detected in the hippocampus was much lower in both WT (Fig. 43B, C, D) and *Pdzd8* (Fig. 43E, F, G) mice. In the hippocampus, the dentate gyrus is the main region where neurogenesis takes place (Alvarez-Buylla and Garcıa-Verdugo, 2002), and where most of the EdU puncta was seen, only a few positive cells were detected outside this area. As a result, EdU positive cells in the hippocampus were displayed for the whole hippocampal region (Fig. 43A). Hippocampal EdU positive cell density was significantly lower in the *Pdzd8* mice compared

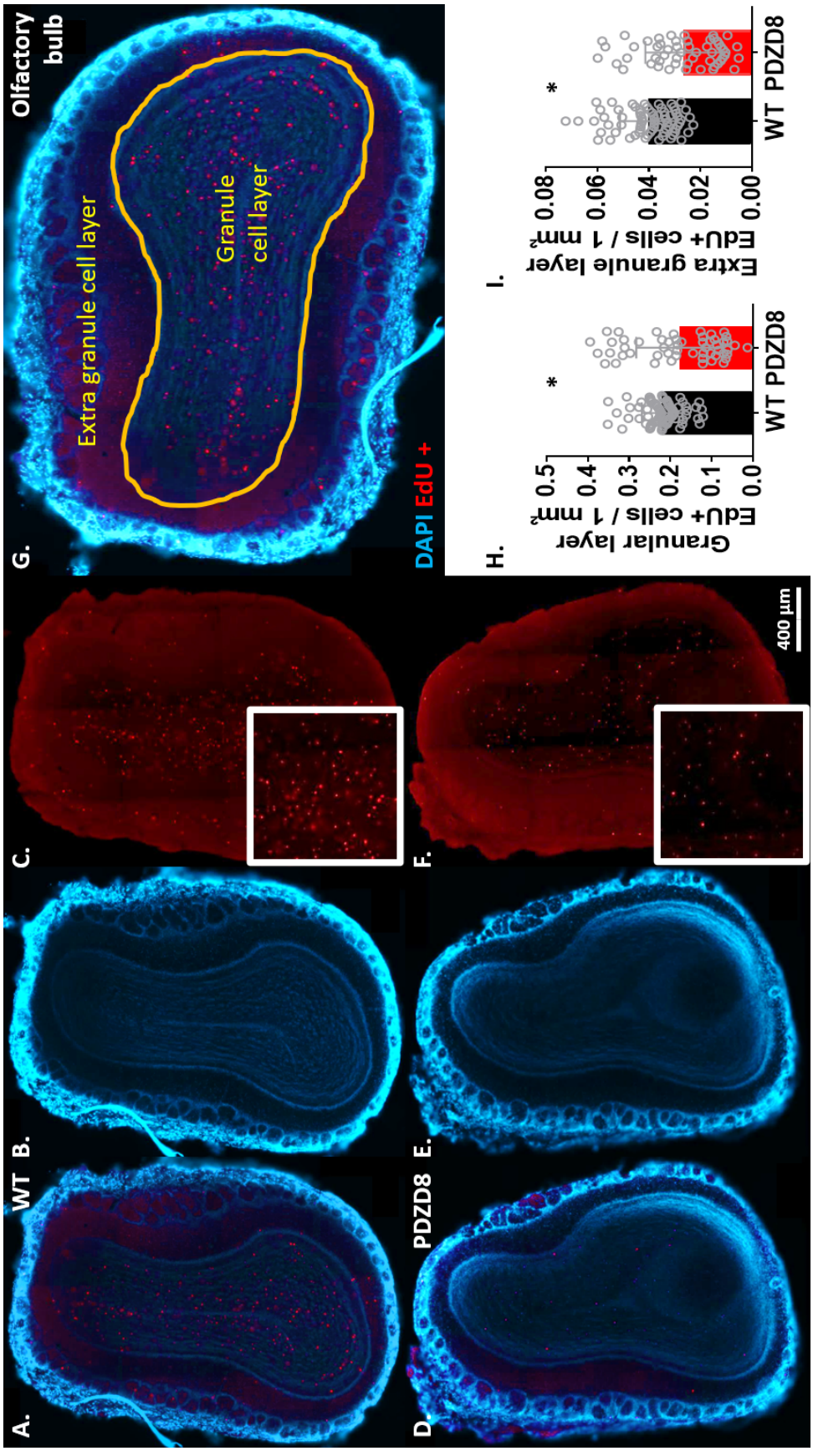
A.
WT
B.
C.
D.
PDZD8
E.
F.
400 µm
G.
Olfactory bulb
Extra granule cell layer
Granule cell layer
DAPI EdU +
H.
Granular layer
EdU+ cells / 1 mm²
0.0
0.1
0.2
0.3
0.4
0.5
*
WT
PDZD8
I.
Extra granule layer
EdU+ cells / 1 mm²
0.00
0.02
0.04
0.06
0.08
*
WT
PDZD8

Figure 42. Decreased neurogenesis in the olfactory bulbs of *Pdzd8* mice. Sequential coronal brain sections of the right hemisphere were taken from *Pdzd8* and WT controls (n=5 / genotype) for assessment of neurogenesis (EdU staining – red, DAPI staining – blue; A – G). Representative images EdU staining in the olfactory bulb of WT mice (A – C); zoomed in region with EdU cells (white box; C). Representative images of EdU staining in the olfactory bulb of *Pdzd8* (D – F); zoomed in region with EdU cells (white box; F). Representative image of the olfactory bulb areas analysed: granule cell layer (yellow-marked area) and extra granule cell layer (area outside the yellow marking; G). *Pdzd8* mice (n=54 sections) display a reduction in the granule cell layer EdU positive cells normalized by surface area compared to WT mice (n=73 sections; H). *Pdzd8* mice (n=54 sections) display a reduction in the extra granule cell layer EdU positive cells normalized to surface area compared to WT mice (n=73 sections; I). Brain sections were imaged with Zeiss Axioscan slide scanner at a x20 magnification. Cellpose algorithm was used to segment the EdU positive cells and measure the granule cell layer and extra granule cell layer surface areas. Data is presented as the number of EdU positive cells in a section normalized to the surface area. Statistical analysis: nonparametric Mann-Whitney test, significance level $p<0.05$ (indicated by *); data presented as mean ± standard deviation.

to WT (U=1286, P=0.001; Fig. 43I), similar to the EdU findings observed in the olfactory bulbs of *Pdzd8* mice.

Overall, these data suggest that there is a reduction in newly formed neurons in both neurogenic regions in adult brains of *Pdzd8* mice. Intriguingly, these results are in alignment with the reduction in the absolute volume of the brain in *Pdzd8* mice (Fig. 41B), but not when normalized to body weight (Fig. 41D). With the increase in the relative volume of the hippocampus and the olfactory bulbs in *Pdzd8* mice, an increase in neurogenesis in these brain regions was expected. However, it is also essential to note that if *Pdzd8* mutation might cause neurodevelopmental changes in mice, there is the possibility of these alterations in neurogenesis might have occurred during development and not in the adult brain. It would be interesting to investigate neurogenesis throughout development in *Pdzd8* mice to elucidate when this reduction in neurogenesis arises.

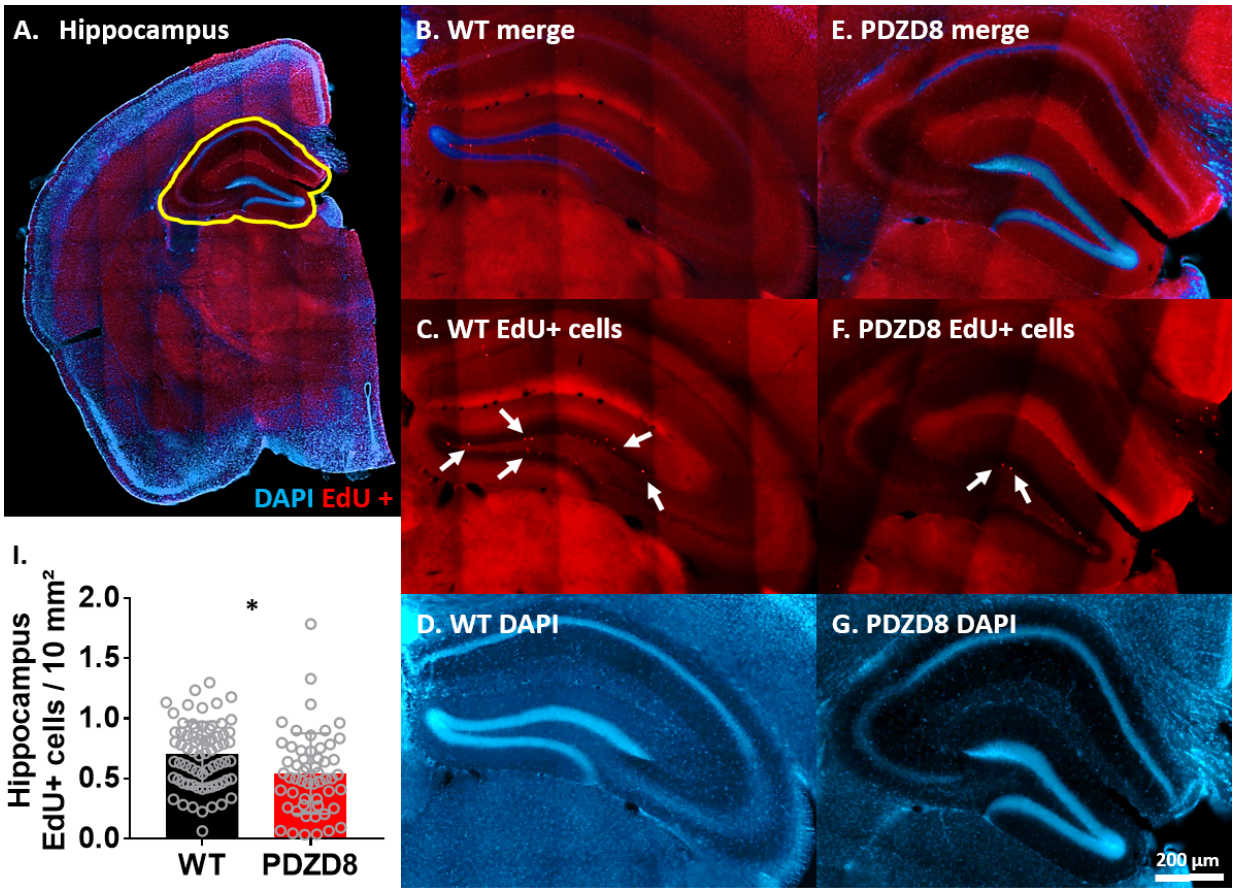

Figure 43. Decreased neurogenesis in the hippocampus of *Pdzd8* mice. Sequential coronal brain sections of the right hemisphere were taken from *Pdzd8* and WT controls (n=5 / genotype) for assessment of neurogenesis (EdU – red, DAPI – blue; A – G). Representative image of a section containing the hippocampus (yellow area; A). Representative images of EdU staining in the hippocampus of WT mice (B – D); example of EdU positive cells (indicated by white arrows; C). Representative images of EdU staining in the hippocampus of *Pdzd8* (E – G); example of EdU positive cells (indicated by white arrows; F). *Pdzd8* mice (n=55 sections) display a reduction in the hippocampal EdU positive cells normalized to surface area compared to WT mice (n=70 sections; I). Brain sections were imaged with a Zeiss Axioscan slide scanner at a x20 magnification. Cellpose algorithm was used to segment the EdU positive cells and measure the hippocampus surface area. Data is presented as the number of EdU positive cells in a section normalized to the surface area. Statistical analysis: unpaired two-tailed independent t-test, significance level $p<0.05$ (indicated by *); data presented as mean ± standard deviation.

Nevertheless, an increase in the number of neurons is not the only factor which could lead to an increase in the relative brain volume. An expansion in the dendritic arbour of individual neurons could also lead to a larger brain area. One way to assess this is by investigating dendritic spine density. Therefore, dendritic spines were investigated in *Pdzd8* mice (n=4) and WT controls (n=4) by performing Golgi-Cox staining (Methods 2.4.2). Dendritic spines were counted over a 10 µm section of a dendrite in multiple brain regions: the olfactory bulbs (Fig. 44), the hippocampus (Fig. 45), the frontal association cortex (Fig. 46) and the subthalamic nucleus (Fig. 47).

Dendritic spine counts were performed in the olfactory bulbs, as this region was previously found to be relatively enlarged in *Pdzd8* mice in the magnetic resonance imaging data (Fig. 44). In the olfactory bulb, granule cells are the only neurons which have dendritic spines. The number of spines over a 10 µm distance was counted in the granule cell layer of *Pdzd8* (n=27) and WT (n=57) mice (Fig. 44A, B, C, D). *Pdzd8* mice displayed an increased number of dendritic spines in the granule layer of the olfactory bulb compared to WT controls ($t(82)=3.443$, $P=0.0008$; Fig. 44E, F).

Dendritic spine numbers were also examined in the hippocampus, due to its relative expansion in *Pdzd8* mice (Fig. 45A). The hippocampal area was split into 3 subregions for investigating the spine densities: CA1 (Fig. 45B, C, D, E, F), the suprapyramidal blade of the dentate gyrus (Fig. 35G, I) and the infrapyramidal blade of the dentate gyrus (Fig. 45H, J). *Pdzd8* mice (n=69 dendrites) displayed a significantly increased number of dendritic spines over a 10 µm distance in comparison to WT mice (n=87 dendrites) in CA1 region ($t(154)=3.221$, $P=0.001$; Fig. 45E, F). However, the dendritic spine counts in the suprapyramidal blade (n=68) and infrapyramidal blade (n=57) of PDZD8 mice were not

altered compared to spine numbers in the suprapyramidal blade (n=75) or infrapyramidal blade (n=69) of WT mice (Fig. 45G, H, I, J).

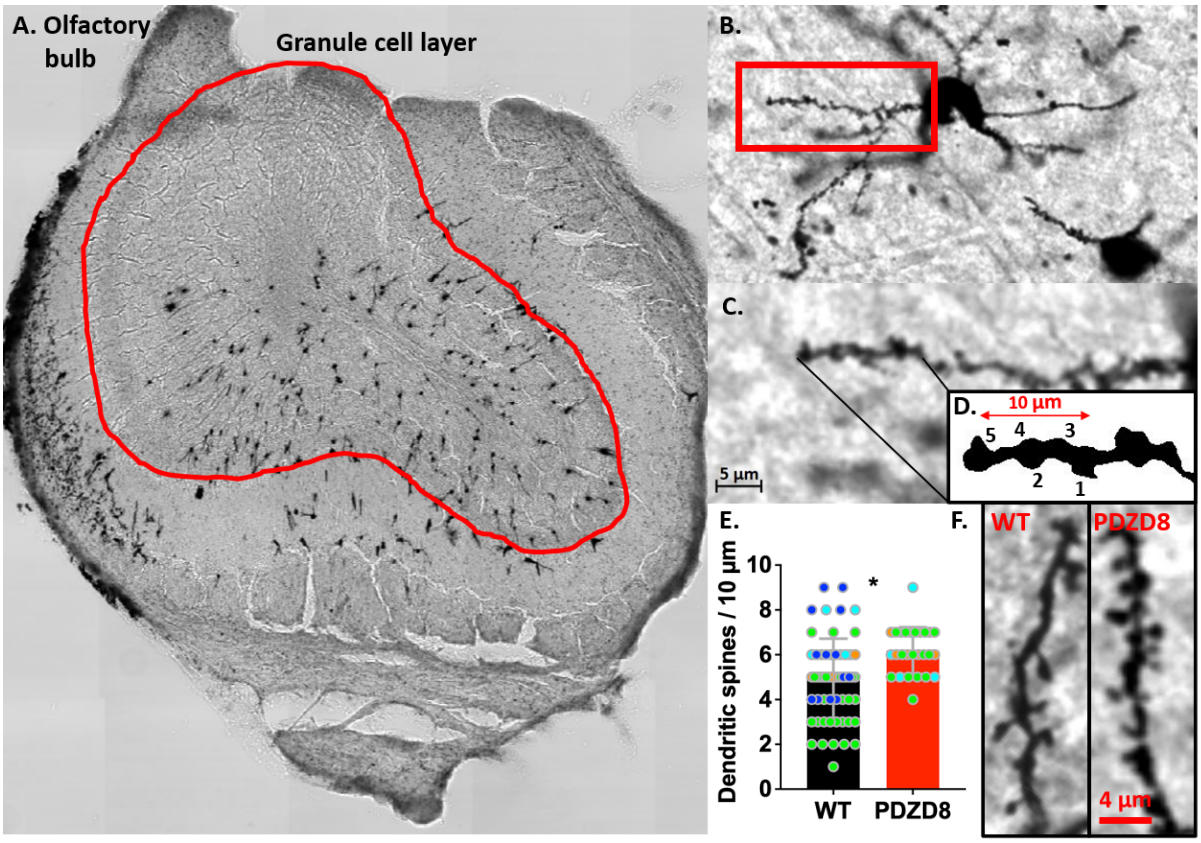

Figure 44. *Pdzd8* mice display increased density of dendritic spines in the olfactory bulb. Sequential coronal brain sections of the right hemisphere were taken from *Pdzd8* and WT controls (n=4 / genotype) for Golgi analysis of dendritic spines. Example of an olfactory bulb section, with the granule cell layer highlighted (red area; A). Zoomed in image of a granule cell layer neuron and a secondary dendrite (red rectangle) use for spine counting (B). Zoomed in image of the secondary dendrite with visible spines (C). Example of spine counting performed over a 10 µm distance across a dendrite, where 5 dendritic spines were identified (D). *Pdzd8* dendritic spine density (n=27 dendrites) were increased compared to WT (n=57 dendrites) counts in the granule cell layer of the olfactory bulb; spine counts are colour coded for each mouse (E). Representative images of dendritic spines from WT and *Pdzd8* olfactory bulb sections (F). Brain sections were imaged with Zeiss Axioscan slide scanner at a x20 magnification. Statistical analysis: unpaired two-tailed independent t-test, significance level $p<0.05$ (indicated by *); data presented as mean ± standard deviation.

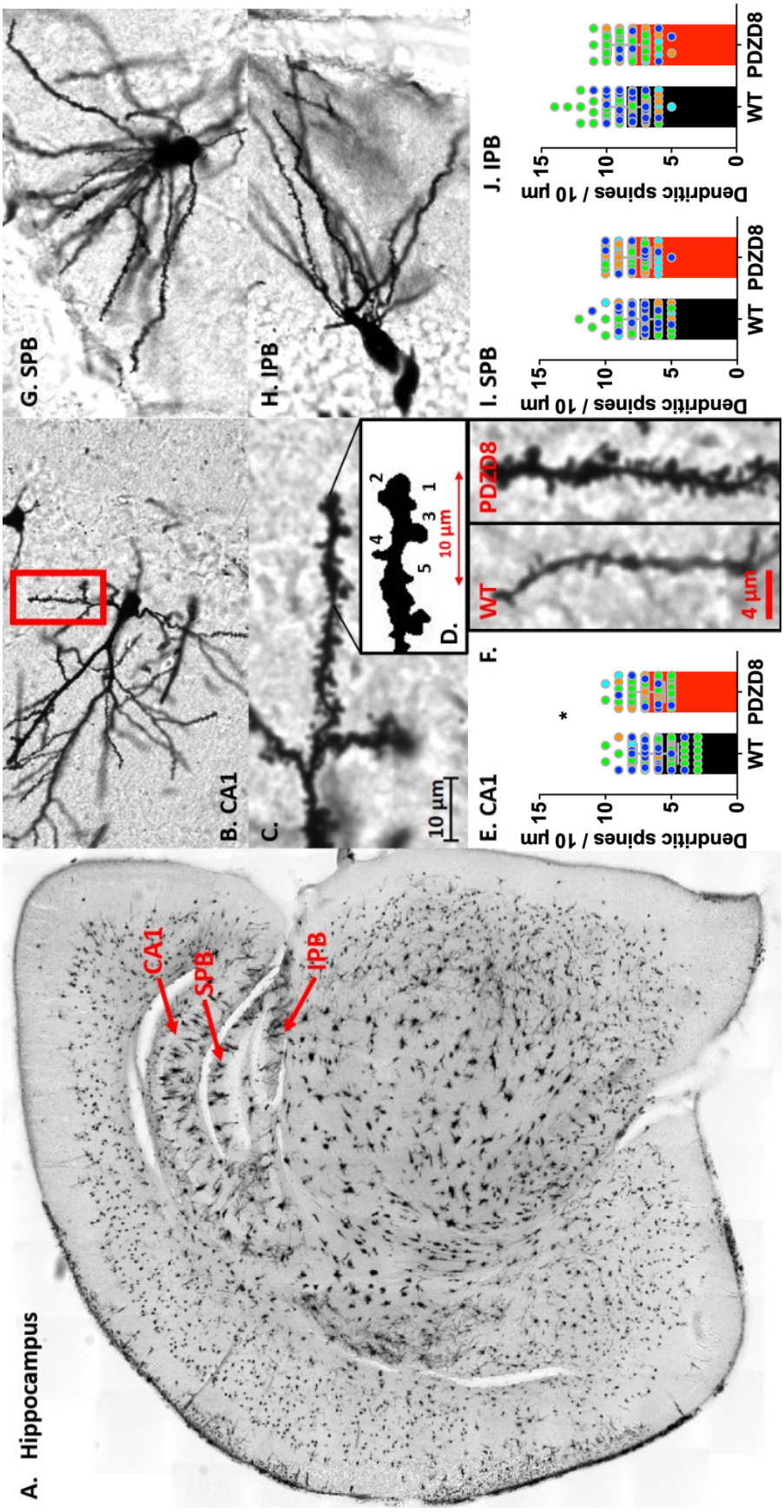
A. Hippocampus
CA1
SPB
IPB
B. CA1
C.
D.
10 µm
10 µm
1
2
3
4
5
E. CA1
Dendritic spines / 10 µm
WT PDZD8
*
F.
WT
PDZD8
4 µm
G. SPB
H. IPB
I. SPB
J. IPB

Figure 45. *Pdzd8* mice display increased density of dendritic spines in the CA1 region of the hippocampus. Sequential coronal brain sections of the right hemisphere were taken from *Pdzd8* and WT controls (n=4 / genotype) for Golgi analysis of dendritic spines. Example of a brain section containing the hippocampus, with the three regions investigated CA1, SPB and IPB (red arrows; A). Zoomed in image of a CA1 neuron and a tertiary dendrite (red rectangle) use for spine counting (B). Zoomed in image of the tertiary dendrite with visible spines (C). Example of spine counting performed over a 10 µm distance across a dendrite in CA1 region, where 5 dendritic spines were identified (D). *Pdzd8* dendritic spine numbers (n=69 dendrites) were increased compared to WT (n=87 dendrites) counts in the CA1 region of the hippocampus (E). Representative images of dendritic spines from WT and *Pdzd8* hippocampus CA1 region (F). Zoomed in image of a SPB neuron use for spine counting (G). Zoomed in image of a IPB neuron use for spine counting (H). *Pdzd8* dendritic spines counts (n=68 dendrites) were not significantly different compared to WT counts (n=75 dendrites) in the SPB of the dentate gyrus (I). *Pdzd8* dendritic spines counts (n=57 dendrites) were not significantly different compared to WT counts (n=69 dendrites) in the IPB of the dentate gyrus (J). Brain sections were imaged with a Zeiss Axioscan slide scanner at a x20 magnification. Statistical analysis: unpaired two-tailed independent t-test (E, I), nonparametric Mann-Whitney test (J), significance level $p<0.05$ (indicated by *); data presented as mean ± standard deviation. CA1 – hippocampal cornu ammonis 1, SPB – suprapyramidal blade of the dentate gyrus, IPB – infrapyramidal blade of the dentate gyrus.

The frontal association cortex is a region highly involved in integrating sensory inputs, which are often affected in individuals with ID and autism, as well as mouse models of these disorder (Barthas and Kwan, 2017). Due to its connections to ID, dendritic spine analysis was performed in the frontal association cortex in *Pdzd8* mice (n=70 dendrites) and WT controls (n=80 dendrites) (Fig. 46). However, no significant difference in the number of spines found over a length of 10 µm was detected between *Pdzd8* and WT mice (Fig. 46E).

Lastly, spine density was analysed in the subthalamic nucleus (Fig. 47A, B, C, D). Subthalamic nucleus is a part of the basal ganglia, which has been implicated in stereotypical and repetitive behaviours (Kim, Lim and Kaang, 2016). Subthalamic nucleus spine counts were assessed because *Pdzd8* mice used the running wheel significantly more than WT, which could be considered a repetitive behaviour. Dendritic spine counted over a 10 µm distance did not differ in *Pdzd8* mice (n=7 dendrites) in comparison to WT mice (n=11

dendrites) (Fig. 47E). However, the subthalamic nucleus is a very small region and spines only from a few dendrites could be counted, which could be a reason why no difference was detected.

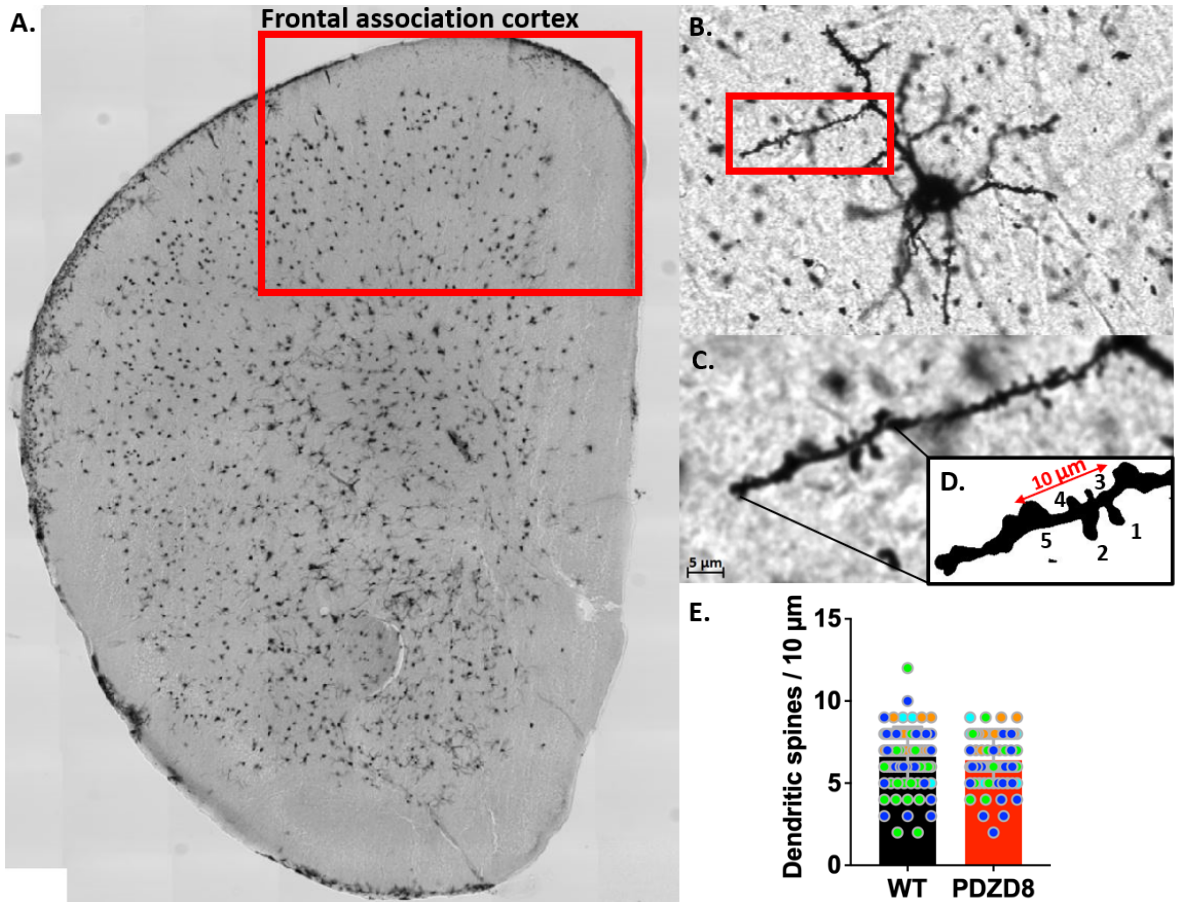

Figure 46. No changes in dendritic spine counts in the frontal association cortex of *Pdzd8* mice. Sequential coronal brain sections of the right hemisphere were taken from *Pdzd8* and WT controls (n=4 / genotype) for Golgi analysis of dendritic spines. Example of a frontal association cortex section (red rectangle) (A). Zoomed in image of a frontal association cortex neuron and a tertiary dendrite (red rectangle) use for spine counting (B). Zoomed in image of the tertiary dendrite with visible spines (C). Example of spine counting performed over a 10 µm distance across a dendrite, where 5 dendritic spines were identified (D). *Pdzd8* dendritic spine counts (n=70 dendrites) were similar to WT (n=80 dendrites) counts in the frontal association cortex; spine counts are colour coded for each mouse (E). Brain sections were imaged with Zeiss Axioscan slide scanner at a x20 magnification. Statistical analysis: unpaired two-tailed independent t-test, significance level $p<0.05$; data presented as mean ± standard deviation.

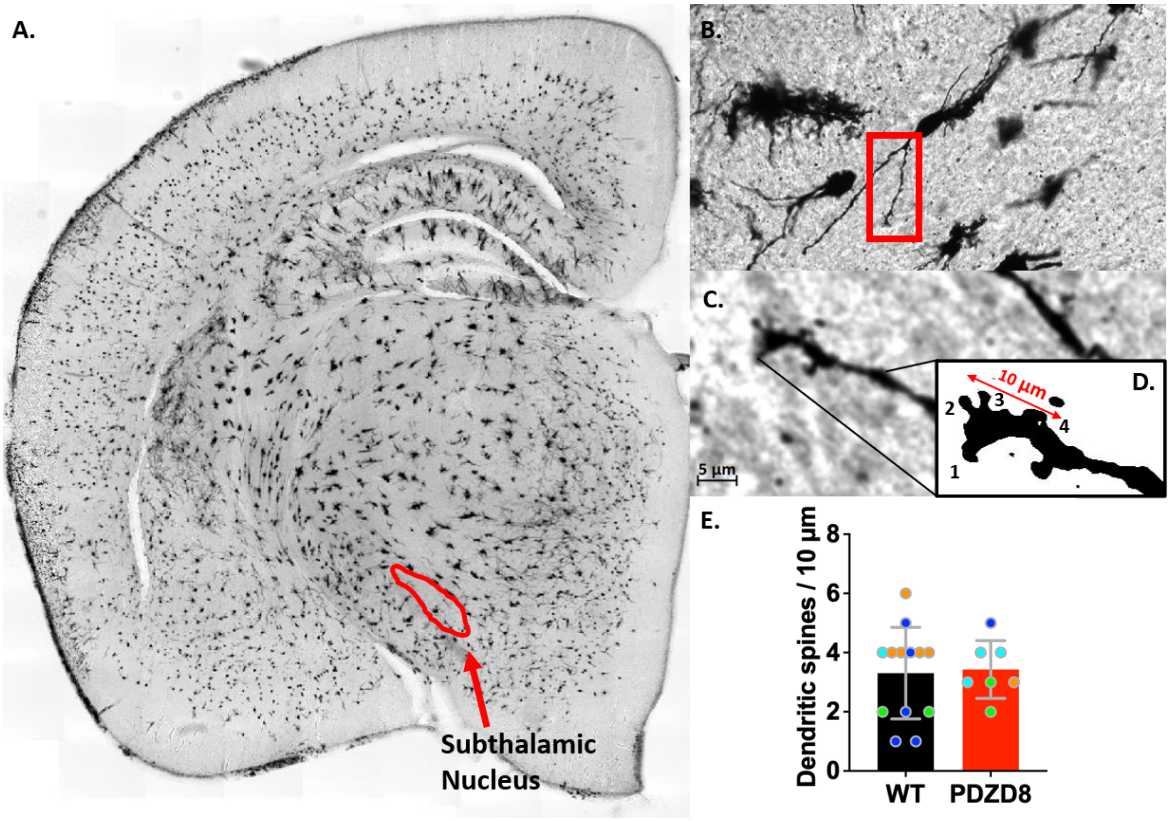

Figure 47. No changes in dendritic spine counts in the subthalamic nucleus of *Pdzd8* mice. Sequential coronal brain sections of the right hemisphere were taken from *Pdzd8* and WT controls (n=4 / genotype) for Golgi analysis of dendritic spines. Example of a brain section containing the subthalamic nucleus (red area; A). Zoomed in image of a subthalamic nucleus neuron and a secondary dendrite (red rectangle) use for spine counting (B). Zoomed in image of the secondary dendrite with visible spines (C). Example of spine counting performed over a 10 µm distance across a dendrite, where 4 dendritic spines were identified (D). *Pdzd8* dendritic spines counts (n=7 dendrites) were not significantly different compared to WT counts (n=11 dendrites) in the subthalamic nucleus; spine counts are colour coded for each mouse (E). Brain sections were imaged with a Zeiss Axioscan slide scanner at a x20 magnification. Statistical analysis: unpaired two-tailed independent t-test, significance level $p<0.05$; data presented as mean ± standard deviation.

Overall, the increase in dendritic spine numbers in the olfactory bulb and hippocampus of *Pdzd8* mice supports the morphological measurements observed in the magnetic resonance imaging experiment. These results indicated that one possible explanation for the relative volume of these brain regions in *Pdzd8* mice could be due an increase in the dendritic arbour via more spines present, rather than an increase in the number of neurons.

3.1.4 Altered mRNA expression of multiple genes in *Pdzd8* mice

Thus far, *Pdzd8* mice were found to exhibit alterations in brain growth, neurogenesis, and spine densities. Considering these changes, an array of qRT-PCR tests (Methods 2.3.1) was run to examine brain mRNA expression of genes linked to cerebral development and neurogenesis in *Pdzd8* homozygous (n=5) and heterozygous (n=5) mice and WT controls (n=5) (Fig. 48). Multiple genes linked to brain growth were assessed, such as AKT serine/threonine kinase 3 (*AKT3*), cyclin D2 and mammalian target of rapamycin (*MTOR*) (Dobyns and Mirzaa, 2019). AKT serine/threonine kinase 3 mRNA was significantly upregulated in *Pdzd8* homozygous mice compared to WT controls ($F(2, 12)=6.298$, $P=0.013$, with post hoc comparisons $P=0.009$), as well as in *Pdzd8* heterozygous animals ($F(2, 12)=6.298$, $P=0.013$, with post hoc comparisons $P=0.047$; Fig. 48). Cyclin D2 (*CCND2*) mRNA expression was enhanced in both *Pdzd8* homozygous and heterozygous animals ($F(2, 12)=12.44$, $P=0.001$, with post hoc comparisons $P=0.005$ and $P=0.0009$, respectively; Fig. 48). Additionally, mammalian target of rapamycin mRNA was also significantly increased in both homozygous and heterozygous mice compared to WT controls ($F(2, 12)=10.22$, $P=0.002$, with post hoc comparisons $P=0.004$ and $P=0.003$, respectively; Fig. 48). These results are in accordance with the increased relative brain volume observed of *Pdzd8* mice as AKT serine/threonine kinase 3, cyclin D2 and mammalian target of rapamycin are all involved in megalencephaly, a developmental abnormality characterized by brain overgrowth (Dobyns and Mirzaa, 2019).

Doublecortin (*DCX*) and neuronal nuclei (*NEUN*) mRNA expression was also probed as they are considered markers for neurogenesis and mature neurons, respectively (Rao and Shetty, 2004). Interestingly, doublecortin was significantly upregulated in *Pdzd8* homozygous and

heterozygous samples compared to WT ($F(2, 12)=5.461$, $P=0.02$, with post hoc comparisons $P=0.019$ and $P=0.037$, respectively; Fig. 48). Neuronal nuclei mRNA was also significantly upregulated in *Pdzd8* homozygous and heterozygous samples compared to WT controls ($F(2, 12)=9.643$, $P=0.003$, with post hoc comparisons $P=0.002$ and $P=0.014$, respectively; Fig. 48). This contradicts the EdU experimental findings where neurogenesis was decreased in *Pdzd8* animals. However, only mRNA expression was investigated for both doublecortin and neuronal nuclei, which could account for the difference in results, as protein levels were not checked. Additionally, EdU staining was assessed only in the hippocampus and the olfactory bulb, while the qRT-PCR data was obtained from whole brain homogenates. The subventricular zone is an area along the lateral ventricle where neurogenesis persists in the postnatal brain and where doublecortin is highly expressed (Yang *et al.*, 2004). As EdU staining was not assessed in this region, the qRT-PCR data from whole brain homogenates including the subventricular zone could potentially explain the increase in mRNA expression of doublecortin.

Cerebellum was among the brain regions relatively enlarged in the *Pdzd8* mice. As this region might be involved in the hyperactive phenotype of *Pdzd8* animals, a couple of cerebellar markers were investigated by qRT-PCR analysis, calbindin 1 (*CALB1*) and Purkinje cell protein 2 (*PCP2*). Expression of calbindin 1 mRNA was significantly enhanced in *Pdzd8* homozygous and heterozygous brain samples in comparison to WT samples ($F(2, 12)=9.744$, $P=0.003$, with post hoc comparisons $P=0.004$ and $P=0.005$, respectively; Fig. 48). Purkinje cell protein 2 mRNA expression was only significantly enhanced in *Pdzd8* heterozygous brain samples in comparison to WT samples ($H=8.34$, $P=0.007$, with post hoc comparisons $P=0.011$; Fig. 48). Both Purkinje cell protein 2 and calbindin 1 are markers for cerebellar

cells, which have been previously associated with the autistic behaviour, such a repetitive jumping (Lotta *et al.*, 2014). Therefore, the changes observed in the cerebellum of *Pdzd8* mice, such as the increase in relative volume and the increase in the mRNA expression cerebellar markers, could potentially be linked to the locomotor hyperactivity detected in these mice.

Additionally, alongside genes linked cerebral development and neurogenesis, qRT-PCR was used to run an array of markers related *Pdzd8* to better understand the consequences of *Pdzd8* protein loss. Markers involved in ER stress-related genes, mitochondria fusion and fission, and *Pdzd8* interactors were examined (Fig. 48). As *Pdzd8* interacts with the ER, multiple genes linked to ER stress were assessed, such as DNA damage inducible transcript 3 (*DDIT3*), activating transcription factor 4 (*ATF4*), and heat shock protein family A member 5 (*HSPA5*). DNA damage inducible transcript 3 mRNA had similar expression levels in *Pdzd8* homozygous and heterozygous mice as in WT controls (Fig. 48). In contrast, activating transcription factor 4 mRNA was upregulated in *Pdzd8* homozygous and heterozygous mice ($F(2, 12)=10.73$, $P=0.002$, with post hoc comparisons $P=0.015$ and $P=0.001$, respectively; Fig. 48). Heat shock protein family A member 5 was also upregulated in *Pdzd8* homozygous and heterozygous mice ($F(2, 12)=11.3$, $P=0.001$, with post hoc comparisons $P=0.004$ and $P=0.001$, respectively; Fig. 48). ER stress has been previously linked to ID (Caglayan *et al.*, 2015; Skopkova *et al.*, 2017). Heightened mRNA expression levels of ER stress markers, such as DNA damage inducible transcript 3 and activating transcription factory 4, have been found in children with various forms of ID (Skopkova *et al.*, 2017). Thus, Pdzd8 protein loss could potentially have the same effect, and lead to an enhanced cellular stress response which is seen in ID cases.

Pdzd8 protein also interacts with mitochondria. Therefore, markers for both mitochondria fusion and fission were assessed (Fig. 48). Mitofusin 1 (*MFN1*), mitofusin 2 (*MFN2*) and optic atrophy 1 (*OPA1*) are genes related to mitochondria fusion which were investigated in *Pdzd8* mutant mice. Mitofusin 1 mRNA levels were increased in both *Pdzd8* homozygous and heterozygous mice compared to WT controls ($F(2, 12)=10.41$, $P=0.002$, with post hoc comparisons $P=0.003$; Fig. 48). Optic atrophy 1 mRNA expression level was also upregulated in both *Pdzd8* homozygous and heterozygous mice compared to WT controls ($F(2, 12)=8.39$, $P=0.005$, with post hoc comparisons $P=0.006$ and $P=0.009$, respectively; Fig. 48). However, mitofusin 2 mRNA expression was only enhanced in *Pdzd8* homozygous mice ($F(2, 12)=3.548$, $P=0.061$, with post hoc comparisons $P=0.041$; Fig. 48). Mitochondrial fission was examined by analysing the fission 1 (*FIS1*) and dynamin 1 like gene (*DNM1L*) mRNA expression. No changes in mRNA expression levels in either fission 1 and dynamin 1 like gene were observed in *Pdzd8* homozygous and heterozygous samples compared to WT samples (Fig. 48). Both fusion and fission are key mitochondrial processes, which regulate mitochondrial morphology, function, and prevention of damage. Dysfunction in the proper functioning of mitochondria machinery has been previously linked to ID and ASD (Valenti *et al.*, 2014). Mitochondrial fusion and fission were investigated in children with ASD. Gene expression analysis revealed an increase in mitochondrial fusion related genes, such as mitofusin 1, mitofusin 2 and optic atrophy 1 (Goldenthal *et al.*, 2015). Similarly, *Pdzd8* mutant mice displayed an increase in the mRNA expression levels of mitochondrial fusion markers. Therefore, mitochondrial dysfunction observed following *Pdzd8* mutation might contribute to the morphological and behavioural changes seen in these mice.

Additionally, Pdzd8 protein cooperates with 2 main proteins, RAS-related GTP- binding protein (*RAB7*) and zinc FYVE-type containing 27 protein (*ZFYVE27*), both of which enable the interaction between endoplasmic reticulum, mitochondria, and late endosomes. RAS-related GTP-binding protein mRNA levels were increased in *Pdzd8* homozygous and heterozygous brain samples compared to WT ($F(2, 12)=7.146$, $P=0.009$, with post hoc comparisons $P=0.009$ and $P=0.017$, respectively; Fig. 48). However, similar mRNA levels of zinc FYVE-type containing 27 protein between *Pdzd8* homozygous and heterozygous mice and WT controls were detected (Fig. 48). PDZD8, RAS-related GTP-binding protein, and zinc FYVE-type containing 27 protein are key regulators of endoplasmic reticulum and late endosomes interactions, which are essential for degradation of endocytosed material (Elbaz-Alon *et al.*, 2020; Shirane *et al.*, 2020; Gao *et al.*, 2022). Thus, *Pdzd8* protein loss could lead to harmful effects arising from alterations in its interactions with other molecules.

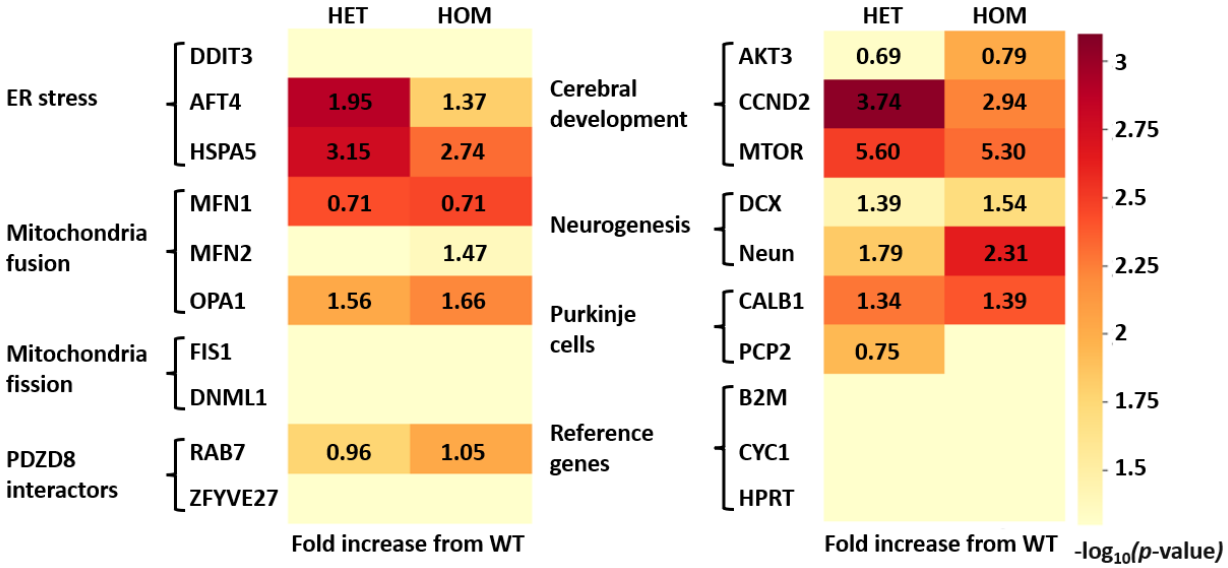

Figure 48. *Pdzd8* HOM and HET mice display increased mRNA expression of genes linked to endoplasmic reticulum stress, mitochondria, cerebral development, neurogenesis, and cerebellum. Brain mRNA was extracted from 15 female mice (5 / genotype). The following genes were upregulated in *Pdzd8* HET and HOM mice compared to WT controls: ER stress – AFTA, HSPA5; mitochondria fusion – MFN1, MFN2 (only in *Pdzd8* HOM), OPA1; Pdzd88 interactors – RAB7; cerebral development – AKT3 (only in *Pdzd8* HOM), CCND2, MTOR; neurogenesis – DCX, NEUN, cerebellum – CALB1, PCP2. Three reference genes were used – B2M, CYC1 and HPRT. Relative mRNA expression was calculated by $2^{-\Delta\Delta Ct}$ method. Statistical analysis: one-way ANOVA with Dunnett's multiple comparison, nonparametric Kruskal-Wallis with Dunn's multiple comparisons test (PCP2), significance level $p<0.05$. Data is presented as the negative logarithm in base 10 of the p-value of *Pdzd8* HET and HOM mice (a value >1.3 on the scale demotes a significant difference from WT mice). The numbers on the boxes corresponding to each gene represent the fold increase in the *Pdzd8* HET and HOM relative mRNA expression compared to WT for the mRNA significantly upregulated in *Pdzd8* mice, where 0.0 denotes no change and 1.0 indicates 100% increase. HET – heterozygous, HOM – homozygous, ER – endoplasmic reticulum, DDIT3 – DNA damage inducible transcript 3, ATF4 – activating transcription factor 4, HSPA5 – heat shock protein family A member 5, MFN1 – mitofusin 1, MFN2 – mitofusin 2, OPA1 – optic atrophy 1, FIS1 – fission 1, DNM1L – dynamin 1 like gene, RAB7 – RAS-related GTP-binding proteins, ZFYVE27 – zinc finger FYVE-type containing 27, AKT3 – AKT serine/threonine kinase 3, CCND2 – cyclin D2, MTOR – mammalian target of rapamycin, DCX – doublecortin, NEUN – neuronal nuclei, CALB1 – calbindin 1, PCP2 – Purkinje cell protein 2, B2M – β 2 macroglobulin, CYC1 – cytochrome C1, HPRT – hypoxanthine phosphoribosyl transferase.

3.1.5 Discussion

Thus far, I have identified numerous phenotypic differences in *Pdzd8* mice compared to WT controls. *Pdzd8* mice were found to be smaller, weigh less, show increased brown adipose tissue and heightened activity. These changes in body size and activity were also accompanied by alternations in brain structure. An increase in relative brain volume, in the size of the olfactory bulbs, hippocampus, cerebellum and retrosplenial cortex, and a decrease in thalamus, pallidum, corpus callosum and superior colliculus were observed in *Pdzd8* mice (Al-Amri *et al.*, 2022), together with reduced neurogenesis and enhanced spine density in the olfactory bulbs and hippocampus. Lastly, *Pdzd8* also displayed changes on a molecular level, with an increase in mRNA expression in multiple genes linked to cerebral development,

neurogenesis, mitochondria function, ER stress and Pdzd8 interactors. Such alterations are seen in ID mouse models (Golden, Buxbaum and De Rubeis, 2018; Verma *et al.*, 2019).

Abnormal brain growth, or macrocephaly is often observed in both humans and animal models with ID or ASD (Dobyns and Mirzaa, 2019; Yasin *et al.*, 2019). In accordance with these, *Pdzd8* mice displayed an overall increase in the brain volume relative to the body weight. Multiple genes linked to cerebral development, such as mammalian target of rapamycin, were found upregulated in *Pdzd8* mice. Dysregulation in mammalian target of rapamycin-related pathways have been previously implicated in ID and has been shown to cause macrocephaly in both humans and mouse models (Reijnders *et al.*, 2017; Zhang *et al.*, 2020; Yasin *et al.*, 2019), suggesting a possible cause for the increase in the brain volume and the upregulation of cerebral development-related mRNA expression identified in *Pdzd8* mice. Brain structural abnormalities were not yet determined in all children identified with a *PDZD8* mutation. However, one of the children from Family 1 exhibits an underdevelopment of the corpus callosum, known as hypoplasia of the splenium of corpus callosum (Al-Amri *et al.*, 2022). *Pdzd8* mice also showed an impairment in the corpus callosum. MRI scans revealed a decrease in the volume of the corpus callosum in *Pdzd8* mice compared to WT controls. Corpus callosum structural changes have been previously shown to be involved in ID. A mutation in the *ZDHHC9* gene, which has a role in post-translational trafficking and function of various proteins, has been shown to cause mild to moderate ID (Kouskou *et al.*, 2018). ZDHHC9 mice also displayed hypoplasia of the corpus callosum, with MRI scans revealing more than 30% reduction in the volume of the corpus callosum compared to WT mice (Kouskou *et al.*, 2018), similar to what was observed in *Pdzd8* mice. Therefore, *Pdzd8*

mice displayed similar brain volume abnormalities to what has been previously observed in the literature for other ID mutations.

Olfactory bulbs and the hippocampus were among the brain regions enlarged in the *Pdzd8* mice. Despite the abnormal brain growth, when neurogenesis was investigated in these two regions it was found to be decreased in *Pdzd8* mice. Various mouse models of ID report deficiencies in the neurogenic ability, such as reduced survival rate or a decrease in the number of newly formed neurons (Castillon *et al.*, 2018; Castillon *et al.*, 2020; Allegra *et al.*, 2017), which give support to our neurogenesis findings regarding *Pdzd8* mice. As neurogenesis was found decreased in *Pdzd8* mice, this suggested that a different mechanism could be linked to the macrocephaly observed in these mice. Hence, dendritic spine density was investigated. An increase in dendritic spines was detected in both the olfactory bulb and the hippocampus of *Pdzd8* mutants. Increased spine density leads to denser or bigger dendritic arbours, which could potentially explain the increase in brain volumes seen in *Pdzd8* mice. However, in regards to dendritic spine numbers, data from human studies points to a reduction in dendritic spines in ID (Kaufmann and Moser, 2000; Kasai *et al.*, 2021). An overall reduction in the spine density has been detected in various mouse models of ID, such *NLGN1-4* quadruple KO, double *SHANK1 – SHANK3* KO and *RAB39B* KO mice (Mignogna *et al.*, 2021; Mossa *et al.*, 2021; Wu *et al.*, 2019), which seems to contradict our Golgi results from *Pdzd8* mice. Nevertheless, these studies mainly report an overall reduction in mature dendritic spines found in mouse models of ID. An increase in immature spines, which are characterized by a thin and long appearance, is most commonly seen in both humans studies and preclinical models of ID (Kaufmann and Moser, 2000; Caldeira *et al.*, 2022; Mignogna *et al.*, 2021; Kasai *et al.*, 2021). The increase in spine density in *Pdzd8* mice could be due to

an abundance of immature spines. Unfortunately, due to the lower resolution of the images taken for this study (only x20 magnification), morphological dendritic spine classification was not possible. Another possible explanation for the increase in dendritic spines in *Pdzd8* mice could be linked to the cellular function of Pdzd8. Under normal conditions, Pdzd8 buffers Ca^{2+} from the ER into the mitochondria, however, when *Pdzd8* is KO, a reduction mitochondrial Ca^{2+} uptake is observed. As a consequence, dendritic Ca^{2+} transients are increased in amplitude (Hirabayashi *et al.*, 2017). Heightened Ca^{2+} activity in dendrites has been extensively linked to synaptic plasticity. LTP is known to cause structural plasticity, such as increase in the number of spines (Hruska *et al.*, 2018; Kasai *et al.*, 2021). Therefore, the *Pdzd8* mutation, due to higher Ca^{2+} activity it causes in dendrites, could directly impact the number of dendritic spines in *Pdzd8* mice. Overall, neurogenesis and spine density are often affected in ID and *Pdzd8* mice seem to display a similar phenotype.

The *Pdzd8* mutation directly impacts mitochondrial function, as it hinders Ca^{2+} uptake into these organelles (Hirabayashi *et al.*, 2017; Hewitt *et al.*, 2020). Fission and fusion are the two processes that occur in mitochondria (Giacomello *et al.*, 2020; Kleele *et al.*, 2021). When the mRNA expression of fission and fusion related genes was investigated, only fusion-related mRNA was upregulated in *Pdzd8* mice. Mitofusin 1, mitofusin 2 and optic atrophy 1 mRNA expression was increased in *Pdzd8* mice compared to WT control. Increase in mitochondrial fusion related genes expression was observed in children with ASD as well (Goldenthal *et al.*, 2015), similarly to what is was observed in *Pdzd8* mice. There is a general consensus of altered mitochondrial morphology and function in both human and preclinical studies of ID (Wilson *et al.*, 2020; Oláhová *et al.*, 2021; Valenti *et al.*, 2014). It would be interesting to further investigate mitochondrial morphology in *Pdzd8* mice, especially as

morphological changes in mitochondria have been associated with increased brown adipose tissue (Mattson, 2010). Higher levels of brown fat tissue is observed in leaner individuals and its increased capacity to metabolise energy substrates to generate heat has been attributed in part to increase in mitochondrial numbers and size (Mattson, 2010; Lu *et al.*, 2018). Elevated levels of mitofusins and optic atrophy 1 were also correlated with increased brown adipose tissue (Lu *et al.*, 2018). *Pdzd8* mice were more active and leaner than WT controls, with elevated levels of brown adipose tissue. Due to the functional role of Pdzd8 and its links to mitochondria, it would be interesting to investigate whether these changes in brown fat adipose tissue recorded in *Pdzd8* mice might be correlated with changes in mitochondrial morphology, such as increase in the number of mitochondria or the size of these organelles.

Pdzd8 has also been shown to have crucial functions in tethering the ER to other organelles such as late endosomes, via interaction with protrudin and Rab7 (Shirane *et al.*, 2020; Elbaz-Alon *et al.*, 2020; Gao *et al.*, 2022). When markers for ER stress and Pdzd8 interactors were assessed in *Pdzd8* mice via qRT-PCR, an increase in the mRNA expression of multiple ER stress markers and Pdzd8 interactors have been observed. Changes in ER stress and Pdzd8 interactors were expected, as *Pdzd8* mice harbour a mutation present after the SMP domain (Fig. 6), which would effectively impact the interaction between ER with Pdzd8 interactors, as their binding site on Pdzd8 was found to be after the SMP domain (Gao *et al.*, 2022; Elbaz-Alon *et al.*, 2020; Guillén-Samander, Bian and De Camilli, 2019). Interestingly, among Pdzd8 interactors, only Rab7 mRNA expression was enhanced in *Pdzd8* mice compared to WT controls. Rab7 binding site was located to the C1 and CC domains on Pdzd8 (Fig. 6), which would not be present even if a truncated version of Pdzd8 protein would be generated. However, protrudin mRNA expression was comparable between *Pdzd8* mice and WT

controls. Protrudin was also found to bind to the TM domain of the Pdzd8 to facilitate interactions between ER and late endosomes (Shirane *et al.*, 2020; Elbaz-Alon *et al.*, 2020). This could be explained potentially by the presence of a truncated Pdzd8 protein, which might enable interaction between these proteins, as in theory it would have an intact TM domain. However, the interaction between Pdzd8, protrudin, Rab7 with ER and late endosomes are still not fully understood. Nonetheless, ER stress caused by impairments to the ER machinery and related pathways have been associated with ID (Caglayan *et al.*, 2015; Skopkova *et al.*, 2017). Due to the essential role on Pdzd8 in ER and mitochondria interactions, it could be assumed that some of the phenotypes observed in *Pdzd8* mice might arise from dysfunction in these organelles. However, more research would be required to understand the mechanisms behind the changes observed in *Pdzd8* mice.

3.2 *Pdzd8* mice and intellectual disability

Pdzd8 mice displayed hyperactive behaviour compared to WT controls, as shown by enhanced ambulatory activity and increased wheel usage in the metabolic cage experiments. Additionally, brain structural abnormalities were detected across multiple key brain regions involved in learning, memory, cognition, and motor control. ID and ASD are often associated with deficits in learning and memory, changes in response to anxiogenic conditions, and alteration in social interactions. Therefore, a series of behavioural tests were employed to further investigate the phenotypic consequences of mutating *Pdzd8*.

3.2.1 Exploratory and anxiolytic behaviour in PDZD8 mice

An open field paradigm was used to assess exploratory behaviour (Walsh and Cummins, 1976) in *Pdzd8* mice (Methods 2.5.5; Fig. 1) (Al-Amri *et al.*, 2022). The distance travelled in the open field was not significantly different between *Pdzd8* mice (n=22; 10 males and 12 females) and WT controls (n=27; 13 males and 14 females) (Fig. 49A). However, *Pdzd8* mice showed reduced habituation to the open field as the exploratory activity declined at a slower rate compared to WT mice (Fig. 49A) (Al-Amri *et al.*, 2022). When the ambulatory activity over time was split by sex, it became apparent that the reduction in habituation could be attributed to *Pdzd8* female mice (Fig. 49C), as *Pdzd8* males habituated at the same pace as the WT mice (Fig. 49B).

The open field was also used to measure anxiety (Walsh and Cummins, 1976). The centre of the arena, referred to here as the inner zone (Fig. 49D), is thought to be an anxiogenic area for mice as it is an open space. Mice prefer to spend more time around the walls of the arena, referred to as the outer zone (Fig. 49F), as this is considered a safer environment. *Pdzd8* mice spent significantly more time in the inner zone of the open field ($H(3)=12.32$, $P=0.006$) and

similar to the habituation data post hoc comparisons showed that only the *Pdzd8* female mice displayed this behaviour (P=0.025, Fig. 49G). This is indicative of reduced anxiety in *Pdzd8* female mice but not in male *Pdzd8* mice. Diminished anxiety in *Pdzd8* females is further supported by the fact that *Pdzd8* female mice also spent significantly more time in the intermediate zone on the arena (F(3,45)=2.963, P=0.042, with post hoc comparisons p=0.017; Fig. 49H) and significantly less time in the outer zone compared to WT females (F(3, 45)=3.201, P=0.032, with post hoc comparisons P=0.013; Fig. 49I) (Al-Amri *et al.*, 2022). This reduced anxiety phenotype was not observed in *Pdzd8* male mice, which spent a comparable amount of time to WT male mice in all three different regions of the arena (Fig. 49G, H, I). The number of entries to a particular zone of the arena is also used as a measure of anxiety levels and this metric also showed the same effect; *Pdzd8* female mice had increased number of entries to the inner zone of the arena (F(3, 45)=4.686, P=0.006, with post hoc comparisons P=0.009; Fig. 49J), and reduced number of entries to the outer zone compared to WT female mice (F(3,45)=4.712, P=0.006, with post hoc comparisons P=0.012; Fig. 49L), while the number of entries to the intermediate zone were comparable between the two genotypes (Fig. 49K). However, no differences in the number of entries were detected in male mice between the two genotypes (Fig. 49J, K, L). Additionally, the overall distance travelled by *Pdzd8* female mice was significantly higher than that of WT females in the inner (H(3)=8.893, P=0.03, with post hoc comparisons P=0.026) and intermediate zone (F(3,45)=3.146, P=0.034, with post hoc comparisons P=0.007; Fig. 49M, N) (Al-Amri *et al.*, 2022). Still no changes were detected in the total distance travelled per zone in *Pdzd8* male mice (Fig. 49M, N, O). These findings further highlight a change in the behavioural response to an anxiogenic environment in *Pdzd8* mice which is sex dependent.

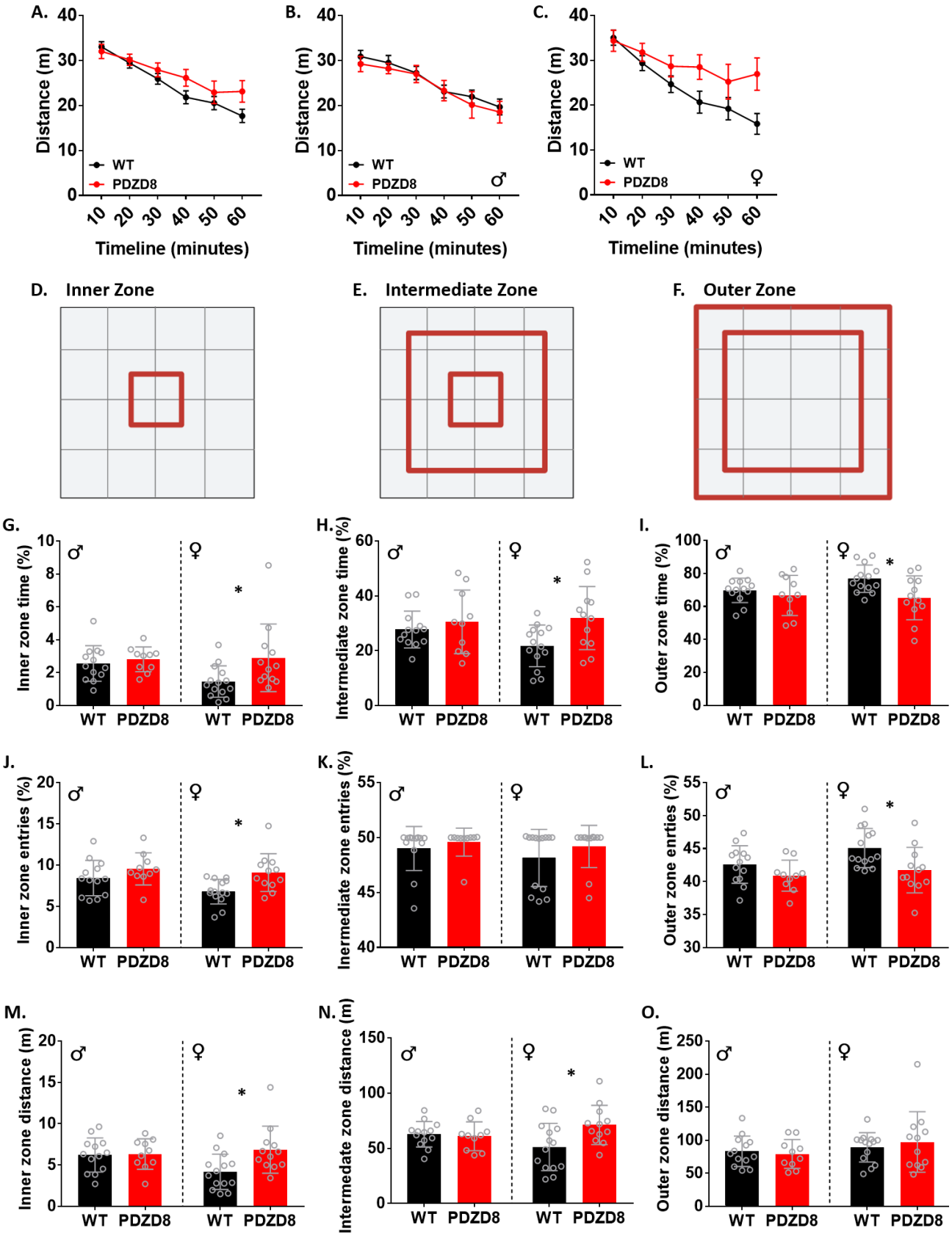
A.
B.
C.
Distance (m)
Timeline (minutes)
WT
PDZD8
♂
♀
D. Inner Zone
E. Intermediate Zone
F. Outer Zone
G.
H.
I.
Inner zone time (%)
Intermediate zone time (%)
Outer zone time (%)
J.
K.
L.
Inner zone entries (%)
Inermediate zone entries (%)
Outer zone enrties (%)
M.
N.
O.
Inner zone distance (m)
Intermedate zone distance (m)
Outer zone distance (m)

Figure 49. Increased exploratory behaviour and decreased anxiety in *Pdzd8* mice. Anxiolytic and exploratory behaviour were investigated in *Pdzd8* (n=22; 10 males and 12 females) and WT (n=27; 13 males and 14 females) by using an open field paradigm. Both *Pdzd8* and WT mice showed decrease in distance travelled over the 60 minute test (A). *Pdzd8* males did not differ from WT males in the distance travelled over time (B). *Pdzd8* females showed a slower reduction in ambulatory activity over time compared to WT females (C). Representative images of the open field arena with the areas analysed: the inner zone (D), the intermediate zone (E), and the outer zone (F). *Pdzd8* male mice did not differ in the amount of the spent in the inner zone (G), the intermediate zone (H), or the outer zone (I) compared to WT males. *Pdzd8* female mice displayed increased time spent in the inner zone (G) and the intermediate zone (H), but not the outer zone (I) compared to WT females. *Pdzd8* male mice did not show differences in the number of entries to the inner zone (J), the intermediate zone (K), or the outer zone (L) compared to WT males. *Pdzd8* female mice displayed a higher number of entries to the inner zone (J), no difference in the number of entries to the middle zone (K), and significantly lower entries to the outer zone (L) compared to WT females. *Pdzd8* male mice showed no difference in the ambulatory activity in the inner zone (G), the intermediate zone (H), or the outer zone (I) compared to WT males. *Pdzd8* female mice had higher levels of ambulatory activity in the inner zone (G) and the intermediate zone (H), but not the outer zone (I) compared to WT females. Data were recorded using ANY-maze software. Statistical analysis: Kruskal-Wallis nonparametric test with Dunn's multiple comparisons test (G, K, M, O), one-way ANOVA with Sidak's multiple comparisons test (H, I, J, L, N), significance level $p<0.05$ (indicated by *); data presented as mean ± standard deviation. Adapted from *Al-Amri et al., 2022.*

To further investigate anxiety in *Pdzd8* mice, two more behavioural tests which probe for anxiety were performed: the elevated plus maze and the light-dark box. The elevated plus maze is a behavioural test which contains two closed arms, deemed low anxiety inducing areas, and two open arms, which are thought to be highly anxiogenic (Methods 2.5.7) (Al-Amri *et al.*, 2022). The activity of *Pdzd8* homozygous (n=25; 8 males and 17 females) and heterozygous (n=36; 16 males and 20 females) on the elevated plus maze was compared to WT controls (n=33; 13 males and 20 females). Data from qRT-PCR experiments showed changes in the mRNA levels in both *Pdzd8* homozygous and heterozygous mice. Therefore, *Pdzd8* heterozygous mice also underwent testing on a subset of behavioural experiments, such as elevated plus maze, to check whether any behavioural phenotype was apparent when *Pdzd8* mutation is present only in one allele.

We found that female *Pdzd8* mice entered the open (anxiogenic) arms of the maze significantly more than their WT controls (H(2)=7.788, P=0.02, with post hoc comparisons P=0.043; Fig. 50C), but the time spent in the open arm was not different between genotypes (Fig. 50D) (Al-Amri *et al.*, 2022). Similar to open field data we found no significant difference in any metrics between male *Pdzd8* and WT mice (Fig. 50). Analysing the number of entries to the closed arms of the maze revealed no differences in the *Pdzd8* homozygous, heterozygous and WT controls within both male and female mice (Fig. 50A). *Pdzd8* homozygous, heterozygous male and females also spent comparable amounts of time on the closed arms of the elevated plus maze as the WT male and female mice (Fig. 50B). No changes were observed in *Pdzd8* homozygous males and *Pdzd8* heterozygous male and female mice regarding the number on entries or the amount of time spend on the open arms of the maze (Fig. 50C, D). These results suggest that only *Pdzd8* homozygous female displayed a reduced anxiety phenotype on the elevated plus maze. Another way to assess anxiety levels on the elevated plus maze is to measure the number of times mice perform head dips when present of the open arms of the maze. Only *Pdzd8* homozygous female mice performed differently from WT controls, exhibiting significantly more head dips (H(3)=11.6, P=0.003, with post hoc comparisons P=0.007; Fig. 50E). All three genotypes had similar ambulatory levels during the elevated plus maze, with no gender differences recorded (Fig. 50F). Overall, elevated plus maze results give support to the open field data. These data showed that only *Pdzd8* homozygous female mice were less anxious on both the open field and the elevated plus maze. Additionally, *Pdzd8* heterozygous males and females did not seem to show any alterations compared to WT mice, implying that a homozygous deletion of *Pdzd8* is necessary to cause behavioural changes. These data agree with the human data

obtained from the two middle eastern families, where only the children with a homozygous *PDZD8* mutation displayed ID and ASD symptoms (Al-Amri *et al.*, 2022).

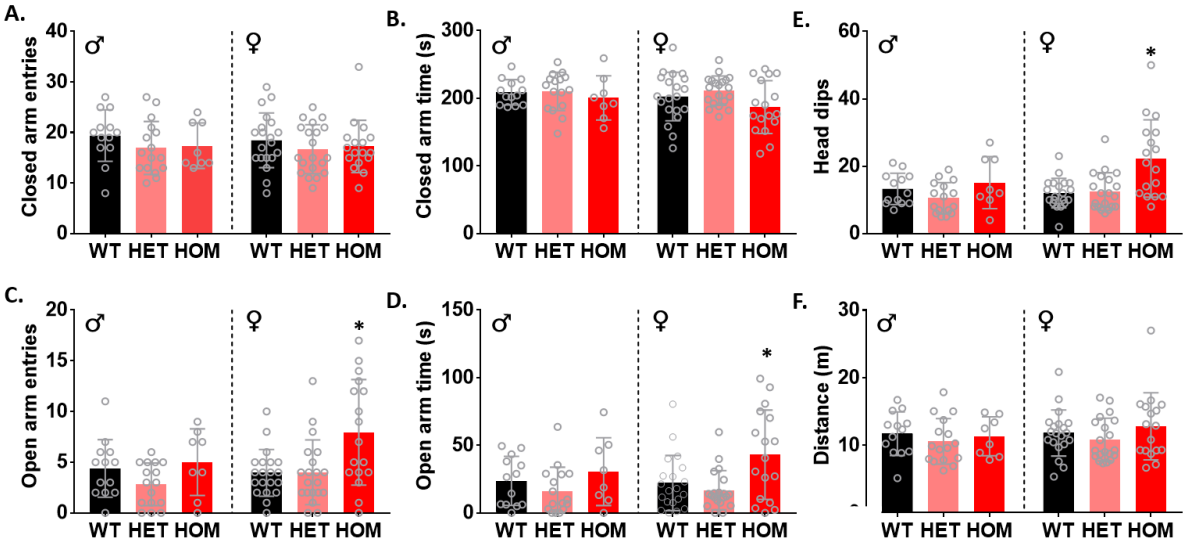

Figure 50. *Pdzd8* female mice were less anxious on the elevated plus maze. Anxiolytic behaviour was investigated in *Pdzd8* homozygous (n=25; 8 males and 17 females), *Pdzd8* heterozygous (n=36; 16 males and 20 females) and WT (n=33; 13 males and 20 females) using an elevated plus maze experiment. No gender differences were found between *Pdzd8* homozygous, heterozygous and WT mice in the number of entries to the closed arms of the maze (A). No gender difference was found between *Pdzd8* homozygous, heterozygous, and WT mice in time spend on the closed arms of the maze (B). *Pdzd8* homozygous female mice entered the open arms of the maze significantly more than the *Pdzd8* heterozygous and WT females; no differences between genotypes in the number of entries to the open arms were recorded in the male mice (C). *Pdzd8* homozygous female mice spent significantly more time in the open arms of the maze compared to *Pdzd8* heterozygous and WT females; no genotype differences in the amount of time spent on the open arms were recorded in the male mice (D). *Pdzd8* homozygous female mice performed significantly more head dips on the open arms of the maze in comparison to the *Pdzd8* heterozygous and WT females; no genotype differences in the number of head dips performed on the open arms of the maze were recorded in the male mice (E). No gender differences in distance travelled was detected between *Pdzd8* homozygous, heterozygous and WT mice (F). Data were recorded using ANY-maze software. Head dips were manually scored by an experimenter blinded to the genotypes of the mice. Statistical analysis: non-parametric Kruskal-Wallis test with Dunn's multiple comparisons test (males and females analysed separately), significance level $p<0.05$ (indicated by *); data presented as mean ± standard deviation. HET – heterozygous, HOM – homozygous. Adapted from *Al-Amri et al., 2022.*

The light-dark box (Methods 2.5.3, Fig. 51A) is another paradigm used to measure anxiolytic behaviour in mice. The amount of time mice spend in the light side of the box is correlated with decreased anxiety levels (Bourin and Hascoët, 2003). Surprisingly, *Pdzd8* female mice (n=8) did not display an increase in the number of entries to the light side compared to WT females (n=8; Fig. 51B). *Pdzd8* females showed no significant difference in the amount of time they spent in the light side of the box compared to WT controls (Fig. 51C). The latency to the first entry in the light side of the arena is also thought to be indicative of anxiety in mice. When the latency to the first entry was examined, *Pdzd8* mice also showed no changes in the time it took to enter the light side in comparison to WT controls (Fig. 51D). Nonetheless, the ambulatory activity in the light side of the box is significantly enhanced in the *Pdzd8* mice compared to controls ($t(14)=3.009$, $p=0.009$), as shown by the increased distance travelled (Fig. 51E). The number of light side entries and the time spent in the light side were plotted against timeline of the experiment, to understand whether the slight increase detected in the time spent in the light side might be influenced by habituation. However, no differences in the number of entries (Fig. 51F) or the time spent in the light side (Fig. 51G) across time were observed between *Pdzd8* mice and WT controls. Interestingly, *Pdzd8* female mice did not exhibit a low anxiety phenotype during the light-dark box experiment, as shown by previous behavioural tests, the open field and the elevated plus maze. One variable that could have impacted the results of the light-dark box was the number of animals used. Due to time and animal breeding constraints a smaller sample size was used in the light-dark box compared to the open field and elevated plus maze. An increase in the sample size might have rendered the slight changes seen in *Pdzd8* mice in the time spent in the light side (Fig. 51C) and the latency to the first entry (Fig. 51D) significantly different. To this effect,

power calculations were performed on the data from the time spent in the light side, which showed that an n of 19 / group (n=18.914, power=0.8, P=0.05) would be necessary to reveal a significant difference between genotypes, given the variance and means of the data shown in Figure 51C.

Thus far, the data obtained from the open field and the elevated plus maze point to reduction on anxiety in the *Pdzd8* homozygous female mice compared to WT controls.

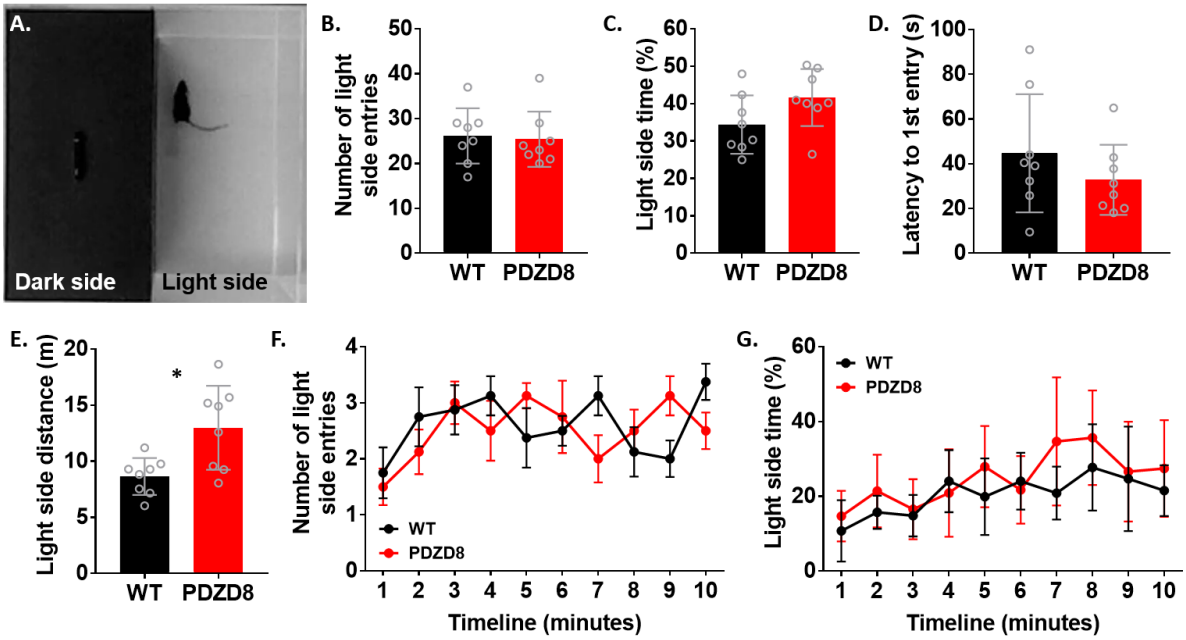

Figure 51. *Pdzd8* behaved normally in light-dark box paradigm. Anxiolytic and exploratory behaviour were investigated in *Pdzd8* (n=8) and WT (n=8) by using a light dark box behavioural test (A). *Pdzd8* mice displayed no difference in the number of light side entries in comparison to WT mice (B). *Pdzd8* mice spent similar amount of time in the light side compartment compared to WT mice (C). *Pdzd8* and WT mice had similar latencies to the first entry in the light side compartment (D). *Pdzd8* mice displayed more activity in the light side compartment compared to WT mice (E). Timeline of the number of light side entries (F) and time spent in the light side showed no differences between *Pdzd8* and WT mice. Data were recorded using ANY-maze software. Statistical analysis: nonparametric unpaired Mann-Whitney test (B), unpaired two-tailed independent t-test (C, D, E), significance level $p<0.05$ (indicated by *); data presented as mean ± standard deviation.

3.2.2 Repetitive behaviours in *Pdzd8* mice

In chapter 2 we showed that *Pdzd8* mice displayed significantly higher levels of wheel usage compared to WT mice. As mentioned previously, wheel running is also used as a measure of stereotypical, repetitive behaviour (Karvat and Kimchi, 2012). Therefore, repetitive behaviour was further analysed in *Pdzd8* mice. While performing various behavioural experiments, *Pdzd8* mice were frequently seen exhibiting spontaneous hindlimb repetitive jumps in their home cages, mainly against the walls of the cage, both when housed alone or in group (videos available) (Al-Amri *et al.*, 2022). Thus, data from the open field experiment (Methods 2.5.5) was used to assess repetitive behaviour, as it offered an hour long recording of the mice's activity (Fig. 52A). The number of jumps were manually counted in the *Pdzd8* mice (n=22; 10 males and 12 females) and WT controls (n=27; 13 males and 14 females). *Pdzd8* mice displayed a significantly greater number of jumps compared to WT controls during the open field, when data from both genders were pooled together (U=146; p=0.0219; Fig. 52B). However, when jumping data were separated by sex to understand whether there is a gender effect, no significant difference in jumping behaviour was observed between *Pdzd8* mice and WT controls (Fig. 52C) (Al-Amri *et al.*, 2022). Nevertheless, an increase in the number of jumps was seen in both *Pdzd8* male and female mice compared to WT males and females (Fig. 52C). This suggested that heightened jumping behaviour is not gender-specific, as was previously seen with anxiolytic behaviour.

Excessive self-grooming is also considered a stereotypical, repetitive behaviour, often seen in animal models of ID and ASD (Kim, Lim and Kaang, 2016). Data from the open field was used to manually score self-grooming. However, no differences in self-grooming were

detected between *Pdzd8* mice and WT controls, both when data were pooled together or when separated by gender (Fig. 52D, E).

Compulsive and stereotypical behaviours detected in mice are very variable; besides hyperactivity, jumping and self-grooming, behaviours such as circling, rearing and repetitive burying are also considered as lower order stereotypical behaviours (Kim, Lim and Kaang, 2016). Rearing, both supported (against the walls) and unsupported, as well as circling were

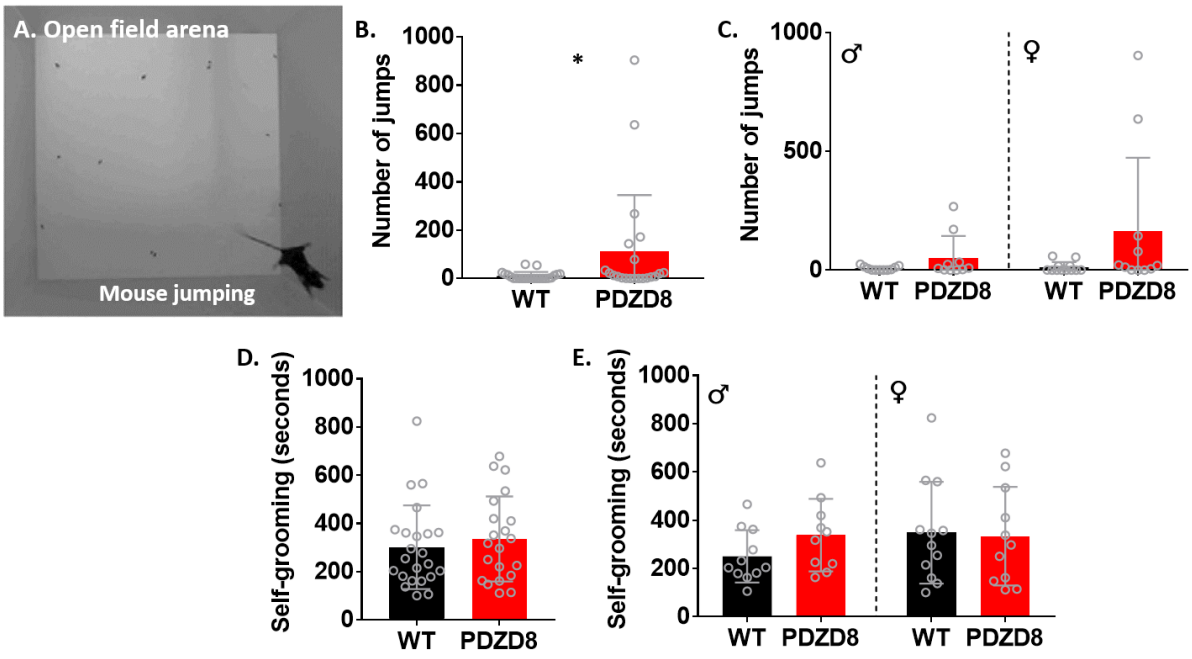

Figure 52. Increased hindlimb jumping in *Pdzd8* mice. Repetitive behaviour – jumping and grooming – were investigated in *Pdzd8* (n=22; 10 males and 12 females) and WT (n=27; 13 males and 14 females) by using an open field paradigm. Representative image of the open field arena with a mouse *Pdzd8* performing repetitive hindlimb jumps (A). *Pdzd8* mice performed significantly more hindlimb jumps compared to WT controls (B). No gender effect was observed in the jumping behaviour (C). *Pdzd8* mice spent similar amount of time self-grooming as the WT controls (D). No gender differences were observed in self-grooming between *Pdzd8* and WT mice (E). Data were recorded using ANY-maze software. Data were manually scored by experimenters blinded to the genotype of the animals. Statistical analysis: non-parametric Mann Whitney test (B, D) and Kruskal-Wallis nonparametric test with Dunn's multiple comparisons test (C), one-way ANOVA with Sidak's multiple comparisons test (E), significance level $p<0.05$ (indicated by *); data presented as mean ± standard deviation. Adapted from *Al-Amri et al., 2022.*

manually scored using the open field data. However, no difference in the either rearing or circling was observed between *Pdzd8* mice and WT controls (data not shown).

Lastly, repetitive burying was measured in *Pdzd8* female mice (n=8) and WT female controls (n=8) by performing a marble burying paradigm (Methods 2.5.4). The number of marbles buried were manually counted an hour after the animals were individually placed in the cage which contained the marbles (Fig. 53A). However, no significant difference in marble burying behaviour was noted between the *Pdzd8* and WT females, although, the number of marbles buried by *Pdzd8* mice was more variable compared to WT (Fig. 53B).

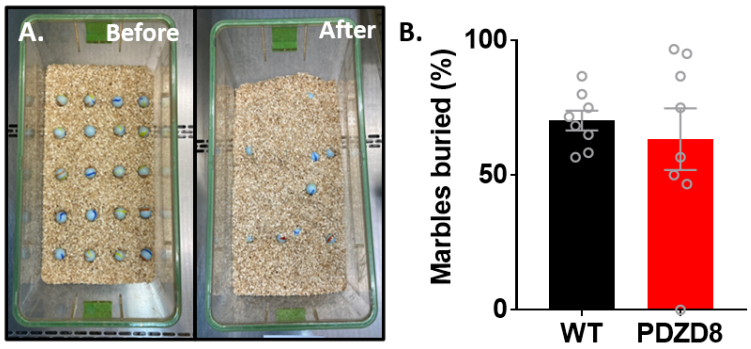

Figure 53. *Pdzd8* mice show no difference in the marble burying test. *Pdzd8* mice (n=8) and WT controls (n=8) were tested for compulsive behaviour using the marble burying paradigm; 20 marbles were set in the same position before a mouse was placed in the cage (A). *Pdzd8* mice displayed no difference in the number of marbles buried compared to WT mice (B). Data were measured by taking photographs after the mouse was removed from the cage containing the marbles. Data were manually scored by 3 different scientists, blinded to the experimental conditions. Statistical analysis: unpaired two-tailed independent t-test (B), significance level $p<0.05$; data presented as mean ± standard deviation.

Overall, these data suggested that *Pdzd8* mice exhibited excessive jumping behaviour compared to WT controls, which is indicative of repetitive behaviour. This is in accordance with the metabolic cage data, which showed that *Pdzd8* mice were hyperactive and had significantly increased wheel usage compared to WT mice. Other stereotypical behaviours, such as self-grooming, circling, rearing, and repetitive burying were not present in the *Pdzd8*

mice. However, it is not uncommon to see only one type of repetitive behaviour in mouse models of ID and ASD (Kim, Lim and Kaang, 2016). Additionally, the timelines from the metabolic cage data (Fig. 36A, C), clearly showed that hyperactivity and wheel usage were heightened in *Pdzd8* mice during the night cycle, as activity levels during the day were comparable between *Pdzd8* and WT mice. All other behavioural tests were conducted throughout the mice's light cycle, which could also explain the lack of differences in the other stereotypical behaviour assessed, as these differences might be apparent only during night cycle, when mice are generally more active.

3.2.2 Learning and memory in *Pdzd8* mice

Pdzd8 mice displayed structural abnormalities in brain regions related to learning and memory, such as the hippocampus. Additionally, EdU and Golgi staining in chapter 3.1 revealed further cellular alternations in this region. Therefore, multiple tests to probe for learning and memory were employed.

The Barnes maze paradigm (Methods 2.5.6) was used to assess learning and spatial memory (Barnes, 1979) in *Pdzd8* female mice (n=15) and WT female controls (n=10) (Al-Amri *et al.*, 2022). The ability to learn is tested in the Barnes maze during the acquisition period, where mice are tasked to learn the location of the escape hole on the Barnes maze (Fig. 54). *Pdzd8* mice did not display any significant learning impairment during the acquisition phase of the Barnes maze test. This was shown by the comparable decline in the time to reach the escape box across the four acquisition days, between the *Pdzd8* mice and WT controls (Fig. 54A). The distance travelled to the target hole, referred to as the primary path length, was also similar between the *Pdzd8* and WT mice throughout the acquisition period (Fig. 54B). Additionally, the number of times mice tried to enter a different hole prior to finding the

designated escape box, referred to as errors, was also similar between the *Pdzd8* mice and WT controls during the acquisition period (Fig. 54C) (Al-Amri *et al.*, 2022). Overall, *Pdzd8* mice did not exhibit learning difficulties in the Barnes maze.

Following the acquisition period, mice were assessed on the time they required to find the target hole, from which the escape box was removed, this was referred to as the testing day (Fig. 54). *Pdzd8* mice spent significantly less time in the target quadrant of the Barnes maze arena compared to WT controls ($U=37$, $P=0.003$; Fig. 54D, E). When the activity in a smaller area around the target hole was measured, *Pdzd8* mice also showed a reduction in the amount of time spent in the target sector ($t(23)=3.19$, $P=0.004$; Fig. 54F, G). Similarly, the time spent in the area adjacent to the target hole (7 cm diameter) was also significantly reduced in *Pdzd8* mice in comparison to WT controls ($U=36$, $P=0.03$; Fig. 54H, I). The number of errors made by *Pdzd8* mice were similar to the number of errors made by the WT mice (Fig 54J), but probability for the *Pdzd8* mice finding the target hole was significantly lower than for WT controls ($t(23)=3.696$, $P=0.001$; Fig. 54K, L) (Al-Amri *et al.*, 2022).

Overall, these results suggested that despite intact learning in *Pdzd8* mice, hippocampal dependent spatial memory seemed to be affected, as *Pdzd8* mice performed poorly in comparison to WT controls during the Barnes maze testing day. The hippocampus is involved in spatial memory. Therefore, the Barnes maze data supports previous findings, which showed structural abnormalities at the level of the hippocampus. Additionally, increased neurogenesis has been previously associated with spatial memory (Abrous and Wojtowicz, 2015). These data are in agreement with this statement, as both a reduction in hippocampal neurogenesis and an impairment in spatial memory were observed in *Pdzd8* homozygous mice.

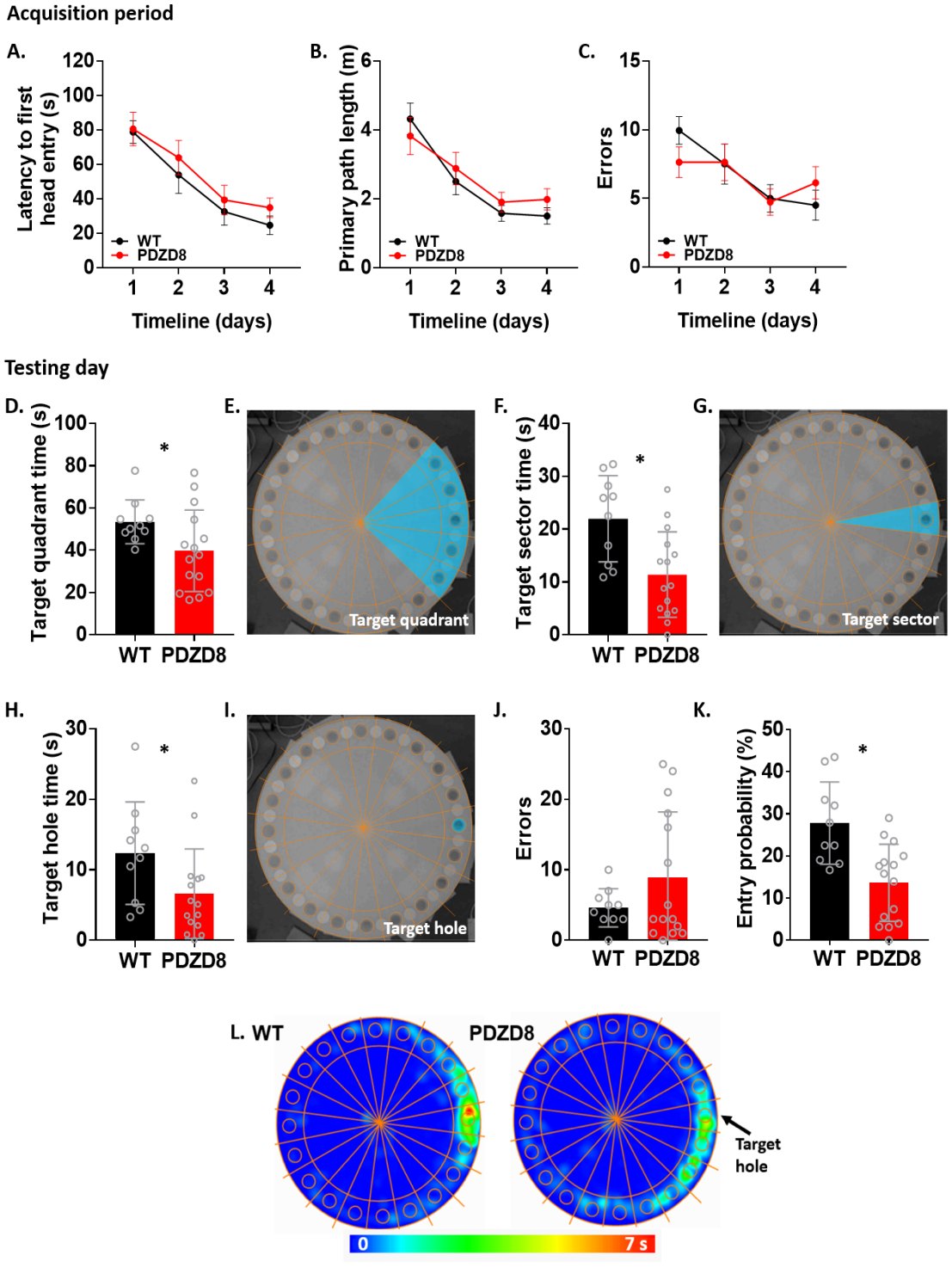
Acquisition period
A.
Latency to first head entry (s)
WT
PDZD8
Timeline (days)
B.
Primary path length (m)
WT
PDZD8
Timeline (days)
C.
Errors
WT
PDZD8
Timeline (days)
Testing day
D.
Target quadrant time (s)
WT PDZD8
E.
Target quadrant
F.
Target sector time (s)
WT PDZD8
G.
Target sector
H.
Target hole time (s)
WT PDZD8
I.
Target hole
J.
Errors
WT PDZD8
K.
Entry probability (%)
WT PDZD8
L. WT
PDZD8
Target hole
0
7 s

Figure 54. *Pdzd8* mice exhibited intact learning but impaired long term memory. Learning and long-term memory were investigated in *Pdzd8* (n=15) and WT (n=10) using a Barnes maze. During acquisition period, 4 days, mice learnt to identify the location of the target hole. *Pdzd8* mice had comparable latencies to WT mice to the first head entry in the target whole over the 4 training days (A). *Pdzd8* mice travelled a similar path length to the target hole during the 4 days of training as the WT mice (B). *Pdzd8* mice made a similar number of errors prior to locating the escape hole as the WT controls (C). *Pdzd8* mice spent less time in the target quadrant compared to WT mice (D). Representative image on the target quadrant highlighted in blue (E). *Pdzd8* mice spent less time in the target sector in comparison to WT mice (F). Representative image on the target sector highlighted in blue (G). *Pdzd8* mice spent less time in the target hole compared to WT mice (H). Representative image on the target hole highlighted in blue (I). *Pdzd8* mice performed more errors in identifying the target hole compared to WT controls on the testing day (J). *Pdzd8* mice showed decreased entry probability for the target hole; entry probability represents the percentage of the ratio of the number of entries to the target hole to the total number of entries (K). Representative activity heat maps of the *Pdzd8* and WT mice during the testing day (L). Data were recorded using ANY-maze software. Statistical analysis: non-parametric Mann Whitney test (D, H, J), unpaired two-tailed independent t-test (F, K), significance level $p<0.05$ (indicated by *); data presented as mean ± standard deviation. Adapted from *Al-Amri et al., 2022.*

As spatial memory was affected in *Pdzd8* mice, the Barnes maze unbiased strategy classification algorithm (Illouz *et al.*, 2016) was used to investigate whether navigational strategies differ between *Pdzd8* and WT mice (see Methods 2.5.6). Exploration strategies were classified into three categories: spatial, serial, and random (Fig. 55A). Both *Pdzd8* mice and WT controls exhibited similar navigation strategies during acquisition period (Fig. 55B, C). An initial increase in the random approach to exploration was seen as mice learned where the escape box was located, which then transitioned to a spatial navigation strategy towards the end of the acquisition period for both *Pdzd8* (P=0.004) and WT (P=0.006) mice (Fig. 55B, C). Throughout the testing day both *Pdzd8* and WT mice mainly used the spatial navigational strategy. Therefore, despite *Pdzd8* mice showing a deficit in spatial memory, no differences in the navigational strategies were recorded in *Pdzd8* mice (Al-Amri *et al.*, 2022).

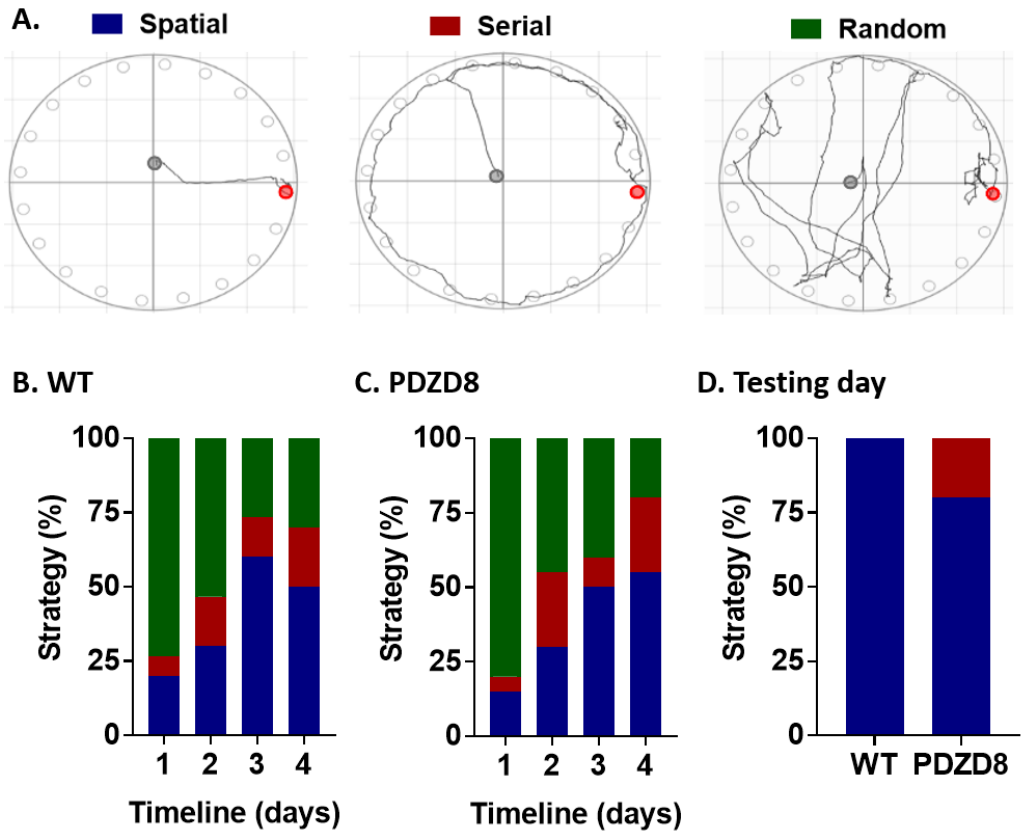

Figure 55. *Pdzd8* mice displayed normal navigation strategies in the Barnes maze. Exploration strategies – spatial, serial, and random – were investigated in *Pdzd8* (n=15) and WT (n=10) during the Barnes maze experiment (A). WT mice displayed an increase towards spatial navigation strategy over the 4 training days (B). *Pdzd8* mice displayed an increase towards spatial navigation strategy over the 4 training days (C). Both WT and *Pdzd8* mice navigated using a spatial strategy during the testing day (D). Data were recorded using ANY-maze software and analysed with the Barnes maze unbiased strategy classification algorithm (Illouz et al., 2016). Statistical analysis: Fisher's exact test, significance level $p<0.05$; data presented as mean ± standard error. Adapted from *Al-Amri et al., 2022.*

Pdzd8 mice (n=15) and WT controls (n=10) which underwent Barnes maze testing, also underwent reversal learning on the Barnes maze. Reversal learning assesses the cognitive ability to supress an already learned behaviour (Gandhi and Lee, 2021). Reversal learning has been previously linked to impulsivity and compulsivity, and it has been used as a measure of higher order repetitive behaviours because it is thought to measure cognitive rigidity and resistance to change (Gandhi and Lee, 2021; Kim, Lim and Kaang, 2016; Izquierdo and

Jentsch, 2012). The reversal learning paradigm on Barnes maze was similar to the initial protocol, except for the fact that the position of the escape hole was changed (Methods 2.5.6, Fig. 56). *Pdzd8* mice and WT controls performances were comparable on the reversal learning test during the acquisition period. No changes were detected in either the latency to first escape hole entry or the primary path length (Fig. 56A, B). Additionally, no changes were observed on testing day, as *Pdzd8* mice spent comparable amount of time in the target quadrant (Fig. 56C, E) and the target hole (Fig. 56D) as the WT controls. Overall, these results indicated that relearning the new location of the escape hole was not affected in *Pdzd8* mice, nor was their spatial memory, as *Pdzd8* mice were equally able to identify the target hole during the testing day. According to previous literature on the ability to perform a reversal learning task, *Pdzd8* mice did not exhibit cognitive rigidity indicative of higher order repetitive behaviours. These results implied that *Pdzd8* homozygous mice might only display lower order repetitive behaviours, characterized by more simple motor behaviours, rather than more complex repetitive behaviours, generally linked to defects in executive functions (Izquierdo and Jentsch, 2012; Gandhi and Lee, 2021).

As spatial learning was affected in *Pdzd8* mice on the Barnes maze, another behavioural paradigm which probes for spatial working learning was employed. Y-maze spontaneous alternation test measures exploratory behaviour and short-term spatial memory (Methods 2.5.8). *Pdzd8* homozygous (n=30; 10 males and 20 females) or heterozygous (n=22; 11 males and 11 females) mice's arm entries and percentage of complete alternations were compared to WT controls (n=32; 14 males and 18 females) on the Y-maze spontaneous alternation paradigm (Fig. 57) (Al-Amri *et al.*, 2022). *Pdzd8* homozygous and heterozygous mice had roughly equivalent number of arm entries on the Y-maze, with no differences recorded within

gender groups (Fig. 57B). Additionally, the percentage of full alternations performed by the *Pdzd8* homozygous or heterozygous were comparable with the WT controls, as no genotypes or sex differences were observed (Fig. 57A, C). Overall, these data indicated that *Pdzd8* mice did not display spatial working memory deficits on the Y-maze paradigm.

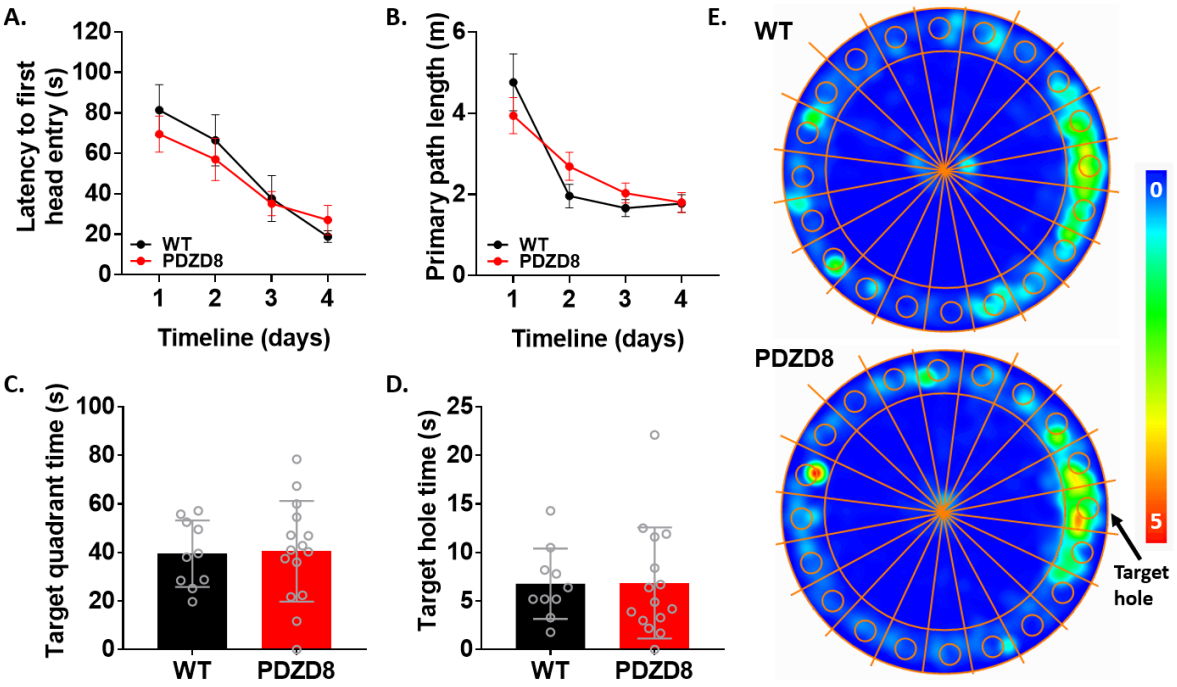

Figure 56. *Pdzd8* mice exhibited no changes in reversal learning. Resistance to change and learning was investigated in *Pdzd8* (n=15) and WT (n=10) using a reversal learning paradigm in Barnes maze. During acquisition period, 4 days, mice re-learnt to identify the location of the target hole, which was changed to the opposite side of the Barnes maze. *Pdzd8* mice had comparable latencies to the first head entry in the target whole over the 4 re-training days as the WT mice (A). *Pdzd8* mice travelled a similar path length to the target hole during the 4 days of re-training as the WT mice (B). No differences were detected in the amount of time spent in the target quadrant between *Pdzd8* and WT mice during the testing day of the reversal learning (C). No differences were detected in the amount of time spent in the target home between *PDzd8* and WT mice during the testing day (D). Representative heat maps of activity of the *Pdzd8* and WT mice during the testing day of reversal learning (E). Data were recorded using ANY-maze software. Statistical analysis: unpaired two-tailed independent t-test (C), non-parametric Mann Whitney test (D), significance level $p<0.05$; data presented as mean ± standard deviation.

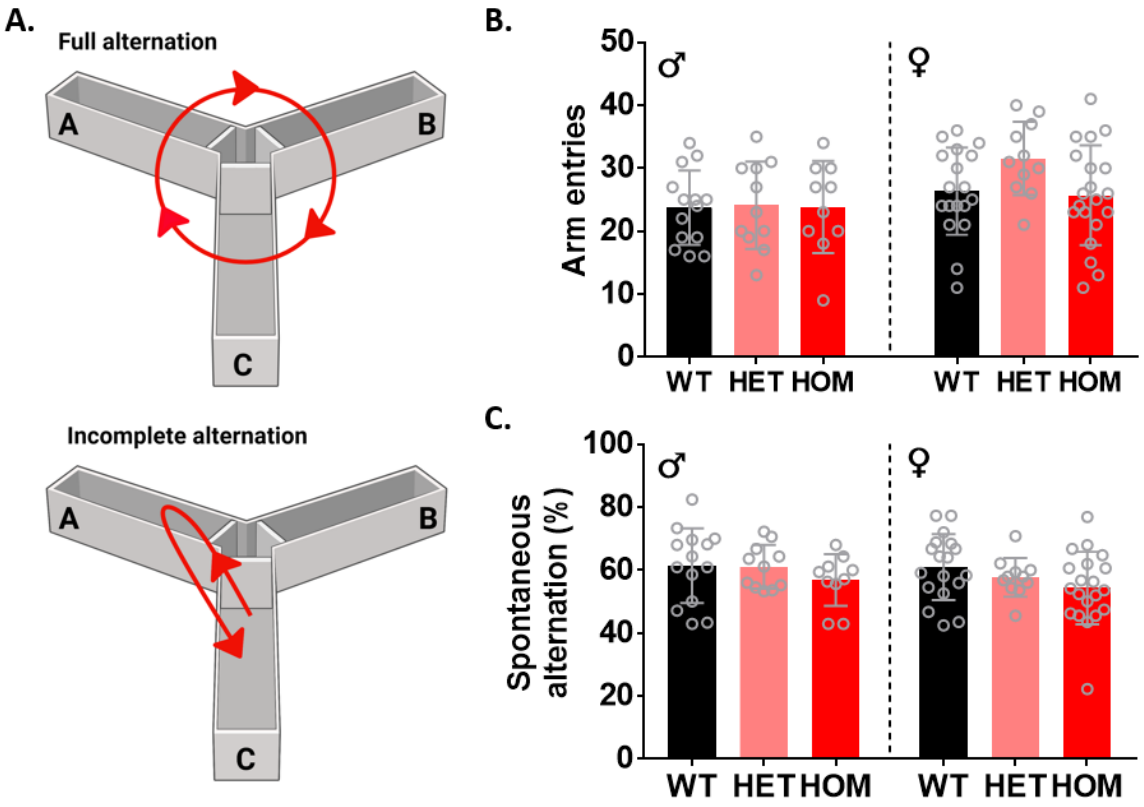

Figure 57. No changes in spatial memory in *Pdzd8* mice on a spontaneous alternation task. Short term spatial memory and exploratory behaviour were investigated in *Pdzd8* homozygous (n=30; 10 males and 20 females), *Pdzd8* heterozygous (n=22; 11 males and 11 females) and WT (n=32; 14 males and 18 females) using a spontaneous alternation Y-maze task. Schematic representation of the Y-maze, with an example of what was considered a complete alternation (top) and an incomplete alternation (bottom) (A). No gender differences were recorded in the number of arm entries on the Y-maze between *Pdzd8* homozygous or heterozygous mice and WT controls (B). No gender or genotype effects were seen in the number of correctly performed spontaneous alternations between *Pdzd8* homozygous or heterozygous and WT mice (C). Data were recorded using ANY-maze software. Spontaneous alternations were manually scored by an experimenter blinded to the genotype and the sex of the animals. Statistical analysis two-way ANOVA, significance level $p<0.05$; data presented as mean ± standard deviation. HET – heterozygous, HOM – homozygous. Adapted from *al-Amri et al., 2022.*

Thus far, *Pdzd8* homozygous mice showed a slight impairment in hippocampal spatial working memory on the Barnes maze, even though their learning ability seemed to be intact. As learning difficulties are often seen in children with ID and ASD, as well as in animal models of these disorders, learning was further examined in *Pdzd8* mice. Associative learning refers to the ability to form connections, or associations, between certain events or experiences, and it is often altered in ID and ASD. The most common way to assess associative learning in mice is by performing a classical conditioning paradigm, such as fear conditioning (Methods 2.5.1). Fear conditioning was examined over three days in *Pdzd8* mice (n=17; 8 males and 9 females) and WT controls (n=8; 4 males and 4 males); data was pooled together due to lower sample size in the WT control group (Fig. 58). On the first day of the experiment, *Pdzd8* and WT mice were individually placed in the fear conditioning chamber, where a loud noise, referred to as cue, was played followed by a foot shock. *Pdzd8* and WT mice displayed similar levels of freezing during the first 30 seconds after being placed in the chamber but the *Pdzd8* showed higher levels of freezing behaviour during the rest of the 2 minute habituation period (Fig. 58A). Overall, *Pdzd8* mice displayed significantly higher levels of freezing in the habituation period ($t(23)=2.411$, $P=0.024$; Fig. 58B) but with the foot shock both genotypes increased their freezing behaviour to similar levels (Fig. 58C).

The following day mice underwent context testing, in which they were place in the same environment where the fear conditioning took place. *Pdzd8* mice generally exhibited more freezing behaviour compared to WT controls throughout the 3 minutes of the context test (Fig. 58D) and this was significantly different from WT controls ($U=20$, $P=0.003$; Fig. 58E). As *Pdzd8* mice displayed higher freezing levels during the 2 minute habituation period on

the first day, which could be indicative of a generalized freezing behaviour and could be interpreted as a confounding variable, the freezing levels during the context testing were normalized to the freezing levels during the 2 minute habituation period from the previous day. However, the normalized freezing behaviour was still significantly higher in *Pdzd8* mice in comparison to WT mice ($U=32$, $P=0.036$; Fig. 58F). These results pointed towards an altered contextual fear conditioning phenotype in *Pdzd8* mice. On the final day, cue-dependent fear conditioning was assessed. *Pdzd8* and WT mice were placed in a new environment, in which the cue used during fear conditioning was presented. As expected, *Pdzd8* mice displayed higher levels of freezing compared to WT mice during the 3 minute habituation to the new environment, as well as throughout the 3 minute presentation of the cue (Fig. 58G). The total amount of freezing during both the habituation period and the cue presentation on the third testing day was significantly higher in *Pdzd8* mice compared to WT controls ($H(3)=30.47$, $P<0.0001$, with post hoc comparisons $P=0.039$ and $P=0.026$, respectively; Fig. 58H). Freezing levels during the cue presentation were also normalized to the freezing levels during the habituation period in the cue-dependent testing experiment, to account for the increased baseline freezing activity seen in the *Pdzd8* mice. Even with this correction *Pdzd8* mice still exhibited heightened freezing behaviour compared to WT mice in response to the cue presentation ($t(23)=2.088$, $P=0.048$; Fig. 58I).

Despite showing increased baseline freezing throughout the fear conditioning paradigm, *Pdzd8* mice exhibited altered contextual and cue-dependent fear conditioning, even when freezing levels were normalized to baseline conditions. Context-dependent fear conditioning is thought to be hippocampal dependent, while cue-dependent conditioning is thought to engage other brain regions as well, such as the amygdala. The previous structural and cellular

abnormalities observed at the level of the hippocampus could explain the differences observed between *Pdzd8* mice and WT controls during fear conditioning and Barnes maze, as both behavioural tests are replying on the proper functioning of the hippocampus.

Mice which underwent fear conditioning were also used in a forced swim experiment, where animals are placed in a container with water and their mobility and freezing behaviours are measured (Methods 2.5.2). The forced swim test is thought to measure depressive-like activity. However, the interpretation of the test is controversial (Can *et al.*, 2012; Armario, 2021). When mice are placed in the water, they generally struggle and displayed increased movement. However, after a period mice stop struggling. This change in behaviour is thought

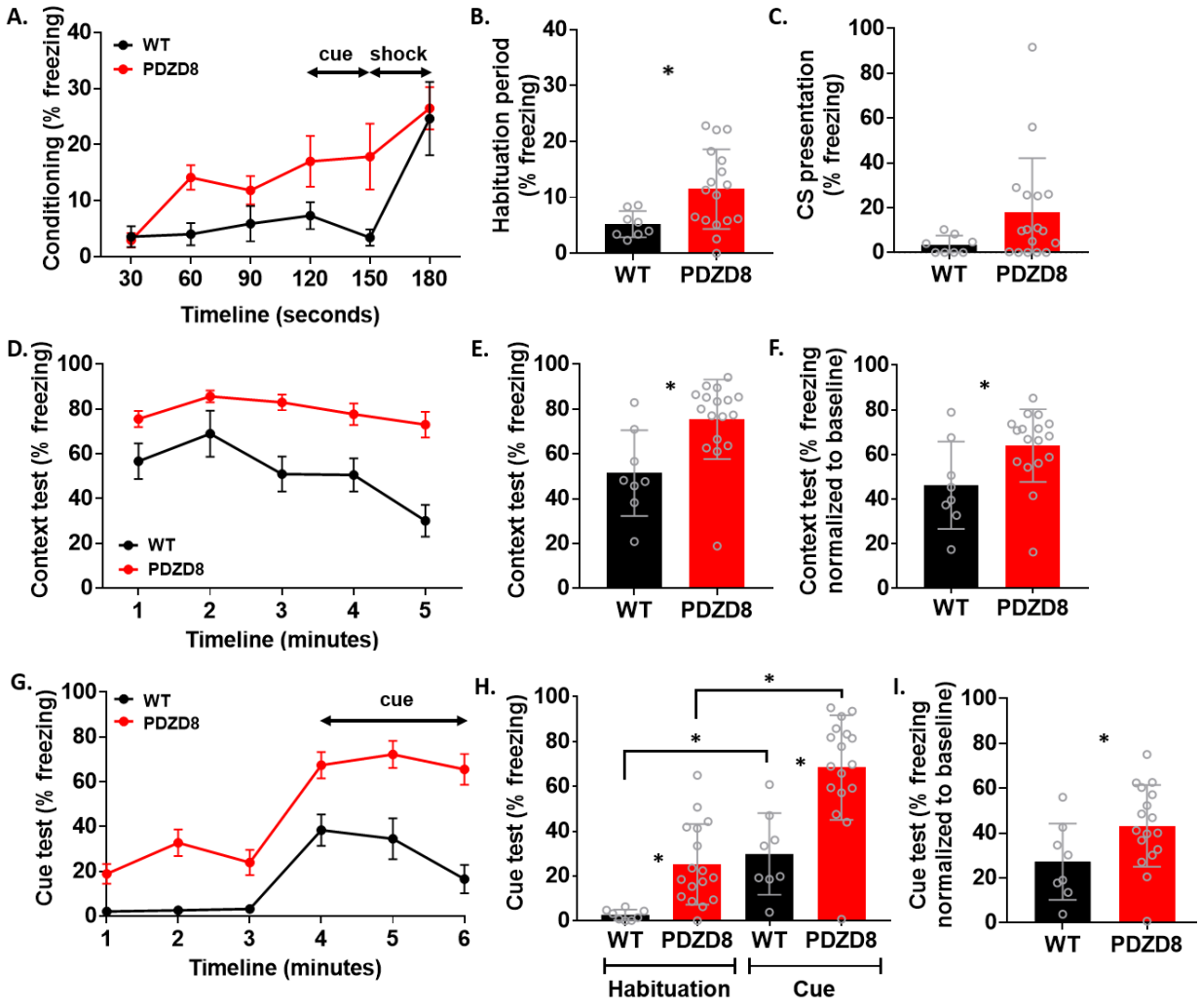

Figure 58. Fear conditioning was altered in *Pdzd8* mice. Context and cue dependent fear conditioning were tested in *Pdzd8* (n=17; 8 males and 9 females) and WT (n=8; 4 males and 4 females) to investigate associative learning. Higher levels of freezing behaviour were observed in *Pdzd8* mice compared to WT mice during fear conditioning paradigm: 3 minute protocol, with 2 minutes habituation to the fear conditioning cage, and 30 seconds conditioned stimulus presentation (36000 Hz, 80 dB) followed by 2 seconds of 1 mA shock stimulus (A). *Pdzd8* mice displayed an increase in freezing during habituation period (B), and significantly more freezing during the presentations of the conditioned stimulus (C). Timeline of freezing in *Pdzd8* and WT mice during context-dependent fear conditioning testing (D). *Pdzd8* mice displayed higher freezing levels during context testing compared to WT mice (D, E). *Pdzd8* and WT mice normalized freezing levels to the 2 minutes habituation period form the fear conditioning paradigm (F). Timeline of cue-dependent fear conditioning testing (G). *Pdzd8* mice showed higher levels of freezing during both habituation and cue presentation in the cue-dependent test (H). Normalization of freezing levels to the habituation period in *Pdzd8* and WT mice during cue-dependent testing. Data were recorded using ANY-maze software. Statistical analysis: unpaired two-tailed independent t-test (B, F, I), non-parametric Mann Whitney test (C, E, F), and non-parametric Kruskal-Wallis test with Dunn's multiple comparisons test (H), significance level $p<0.05$ (indicated by *); data presented as mean ± standard error (A, D, G) and standard deviation. CS – conditioned stimulus.

to be associated with despair and a decreased desire to continue. Therefore, this test is often used to measure depression. However, the stop in struggling could equally be interpreted as the mice learning they can float. These mice have never been exposed to water and their ability to swim is not known to them. Regardless of the interpretations of the results, *Pdzd8* mice did not display any difference compared to WT mice when subjected to the forced swim test (Fig. 59). The time spent freezing (Fig. 59A), the number of freezing episodes (Fig. 59B), the time spent immobile (Fig. 59C), as well as the distance travelled (Fig. 59D) were all comparable between *Pdzd8* mice and WT controls.

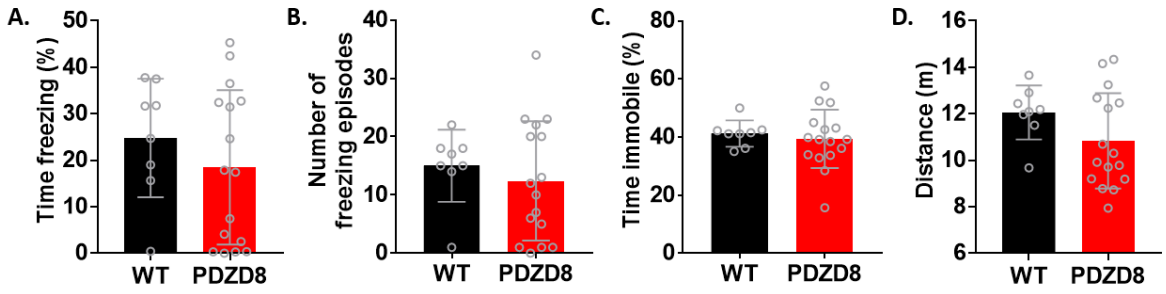

Figure 59. No changes detected in forced swim test in *Pdzd8* mice. Forced swim test was employed in *Pdzd8* (n=17; 8 males and 9 females) and WT (n=8; 4 males and 4 females) to assess depressive-like behaviour. *Pdzd8* and WT mice displayed similar levels of freezing behaviour (A). No changes in the number of freezing episodes detected between *Pdzd8* mice and WT (B). No difference in time spend immobile was detected in *Pdzd8* mice (C). Distance measurements were similar between *Pdzd8* mice and WT controls (D). Data displayed corresponds to the last 4 minutes of the forced swim test, with the first 2 minutes considered as habituation. Data were recorded using ANY-maze software. Statistical analysis: non-parametric Mann Whitney test (B), unpaired two-tailed independent t-test (A, C, D), significance level $p<0.05$; data presented as mean ± standard deviation.

3.2.3 Social interaction on *Pdzd8* mice

One of the major contributing symptoms observed in children with ID and ASD stems from difficulties in social interaction (Chen and Hong, 2018; Fernández, Mollinedo-Gajate and Peñagarikano, 2018). Therefore, social interaction was investigated *Pdzd8* mice.

There are multiple paradigms which are commonly used to measure social interaction. However, recently it was published that the biggest difference in social interaction is observed when the experimental animals are interacting with juvenile mice (Jennings *et al.*, 2019). Surprisingly, it was shown that mice were equally likely to interact with an adult mouse and a 3D-printed model of a mouse; however, mice spend significantly more time with a juvenile mouse (Jennings *et al.*, 2019). Based on these results, social interaction with a juvenile (Methods 2.5.9) was first assessed in *Pdzd8* female mice (n=8) and WT female controls (n=8) (Fig. 60A). Mice were initially habituated to an empty cage. No differences in the total amount of distance travelled during the 5 minute habituation period was observed between *Pdzd8* and WT mice (Fig. 60B). When distance travelled was investigated as a function of time, still no changes between the two genotypes were recorded (Fig. 60C). Social interaction was assessed during a 5 minute exposure to a juvenile mouse. The overall

interaction between *Pdzd8* or WT mice with a same-sex juvenile was comparable between genotypes (Fig. 60D). To understand whether a subtler social interaction deficit might be present, the social interaction episodes were further categorized into anogenital sniffing interaction and other interactions, which included sniffing the head, the body, climbing over / under each other and grooming each other. The amount of time spent performing anogenital sniffing was roughly equivalent between *Pdzd8* and WT mice (Fig. 60E). Similarly, the rest of the social interactions towards the juvenile mouse did not differ between the two genotypes (Fig. 60F). Additionally, the number of juvenile mouse approaches were quantified. However, no changes in this parameter were observed between *Pdzd8* and WT mice (Fig. 60G). Lastly, the anogenital sniffing and the overall interactions were plotted over time. It was previously shown that the first 2 minutes of the social interaction are most important and subtler changes could be observed during the initial approaches (Jennings *et al.*, 2019). However, *Pdzd8* mice interact similarly to WT mice with a juvenile when either anogenital sniffing (Fig. 60H) or the overall interaction (Fig. 60I) are plotted across time.

Overall, these data suggested that *Pdzd8* mice do not show a social interaction deficit. However, this paradigm only assesses the interaction between 2 mice. A three-chamber social approach was next employed (Methods 2.5.9) to investigate social interaction in *Pdzd8* (n=13) and WT (n=10) female mice (Fig. 61). This behavioural paradigm not only measures the interaction between a mouse with a conspecific versus an object, but also the interaction between a mouse with a familiar versus a novel mouse. *Pdzd8* mice and WT control displayed similar habituation, as shown by comparable amounts of time spent in both the empty the left and right chamber of the apparatus (Fig. 61A). Both *Pdzd8* mice and WT controls were interacting more with the novel mouse (mouse 1) versus the object ($F(1, 40)=19.16$,

P=0.0001; Fig. 61B). This suggested that *Pdzd8* mice exhibited normal social interaction, which supported the findings from the juvenile social interaction experiment. However, when the interaction with a familiar mouse (mouse 1) versus a novel mouse (mouse 2) was assessed, only WT mice showed a preference for interacting with the novel mouse (F(1, 40)=8.501, P=0.005, with post hoc comparisons P=0.007; Fig. 61C). *Pdzd8* mice did not seem to distinguish between the familiar mouse and the novel mouse (Fig. 61C). Discrimination indices were calculated to further highlight the inability of *Pdzd8* mice to differentiate between the familiar mouse and the novel mouse (Fig. 61D, E). Interestingly, these results suggested a social discrimination impairment in the *Pdzd8* mice.

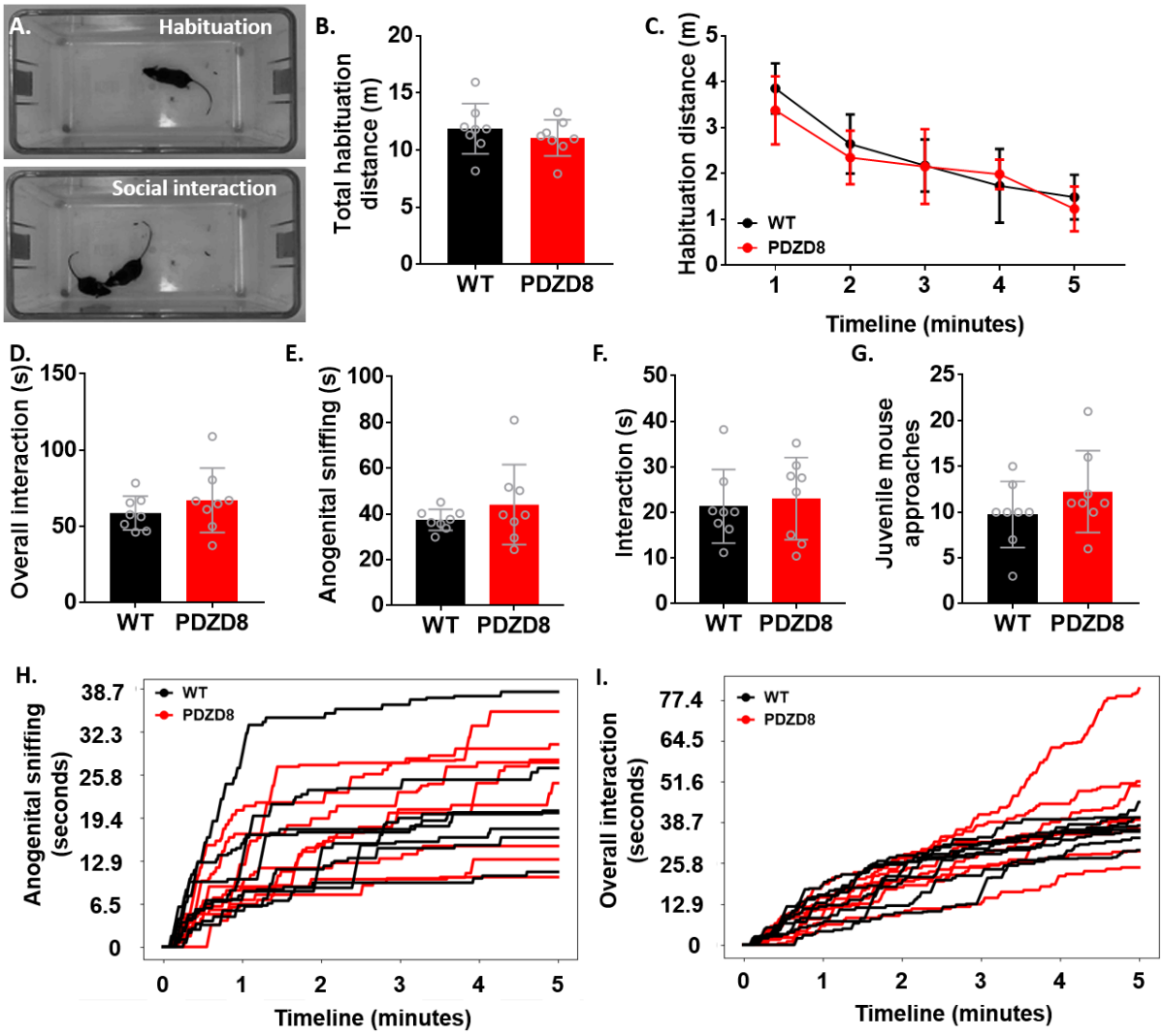

Figure 60. *Pdzd8* mice showed no changes in social interaction with a juvenile mouse. *Pdzd8* (n=8) and WT (n=8) mice were individually placed in home cages with a different juvenile mouse (21 days old, sex-matched) each to investigate social interaction (A). *Pdzd8* mice showed no difference in the movement during the 5 minute habituation period compared to WT mice; data were tracked using ANY-maze software (B, C). *Pdzd8* mice showed no difference in the overall interaction with the juvenile mouse during a 5 minute period compared to WT (D). *Pdzd8* mice displayed no difference in anogenital sniffing compared to WT mice (E). *Pdzd8* mice showed no changes in other forms of interaction (sniffing the head, the body, climbing over / under each other, grooming each other) with the juvenile animal compared to WT controls (F). *Pdzd8* mice displayed similar number of juvenile approaches as the WT mice (G). Cumulative plots of the anogenital sniffing (H) and the overall interaction (I) showed comparable levels of social interaction with a juvenile mouse over time between *Pdzd8* and WT animals. Data were recorded using ANY-maze software, and the reciprocal social interaction as manually tracked using Python Video Annotator. Statistical analysis: unpaired two-tailed independent t-test (B, D, E, F, G), significance level $p<0.05$; data presented as mean ± standard deviation.

The social interaction analysis revealed that an overall deficit in the social interaction is absent in *Pdzd8* mice. However, social recognition and discrimination seem to be affected.

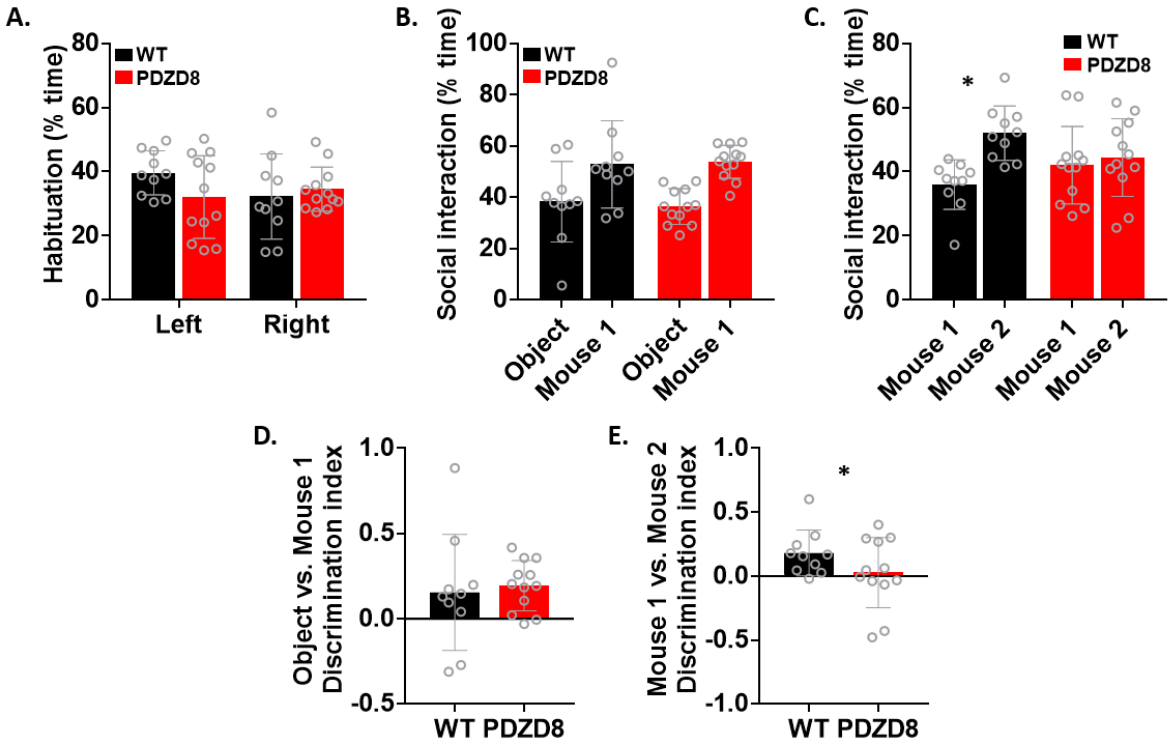

Figure 61. Social discrimination altered in *Pdzd8* mice. Sociability and social novelty were tested in *Pdzd8* (n=12) and WT (n=10) female mice by using the three chamber social interaction paradigm. *Pdzd8* mice and WT controls spent similar times in the left and right compartment of the behavioural test (A). Both *Pdzd8* and WT mice favoured interacting with a novel mouse (Mouse 1) compared to an object (B, D). *Pdzd8* mice did not prefer to interact with a novel mouse (Mouse 2) compared to a familiar mouse (Mouse 1) as WT did (C, E). Discrimination indices were calculated by taking the ratio between the difference in the time spent in the 2 compartments and the sum of the time spent in both compartments (D, E). Data were recorded using ANY-maze software. Statistical analysis: two-way ANOVA test (A, B) with Tukey's multiple comparisons test (C), one sample t-test (D, E), significance level $p<0.05$ (indicated by *); data presented as mean ± standard deviation.

3.2.4 Discussion

This chapter highlighted numerous behavioural deficits observed in *Pdzd8* mice. The *Pdzd8* mutation revealed an anxiolytic phenotype in the open field and the elevated plus maze paradigms. Open field data also exposed a repetitive behaviour caused by *Pdzd8* mutation; *Pdzd8* mice displayed excessive jumping activity compared to WT controls. Additionally, hippocampal dependent long-term memory was impaired in *Pdzd8* mice when tested on the Barnes maze (Al-Amri *et al.*, 2022). Despite learning ability being intact in the Barnes maze, *Pdzd8* mice showed abnormal associative learning during both cue- and context-dependent fear conditioning. Lastly, social interaction was examined by performing multiple behavioural tests, juvenile social interaction, and three-chamber social approach test, which revealed a social recognition or discrimination deficit in *Pdzd8* mice, rather than an overall social interaction impairment. The array of deficits recorded in *Pdzd8* mice in different aspects of behaviour, from learning, memory, to anxiety and social interaction, are often found in human studies and preclinical models of ID and ASD (Golden, Buxbaum and De Rubeis, 2018; Verma *et al.*, 2019).

Anxiogenic behaviour often occurs in individual with ID and ASD and it has been associated with other phenotypes such as obsessive compulsive disorder or phobias (Helverschou and Martinsen, 2011; Wilkes and Lewis, 2018). However, *Pdzd8* mice displayed reduced anxiety in both the open filed and elevated plus maze (Al-Amri *et al.*, 2022). Data from various mouse models of ID suggests that impairments in anxiety are generally present, however, the direction of the impairment is varied depending on the mouse model used (Verma *et al.*, 2019). A mouse model of *NLGN2* KO displayed a reduction in anxiety on elevated plus maze (Liang *et al.*, 2015). Similarly, a mouse model containing a *SYNGAP1* mutation exhibited decreased anxiety on the elevated plus maze and the open field paradigms (Guo *et al.*, 2009). However, *SHANK2* mutation led to increased anxiety in mice containing this mutation (Won *et al.*, 2012). Overall, these data imply that despite the discrepancies in anxiety in mouse models of ID, an overall impairment in anxiety is observed in ID models.

Alongside the anxiety phenotype, the open field data also revealed the occurrence of a repetitive behaviour in *Pdzd8* mice. Repetitive behaviours, such as circling, excessive grooming, rearing, jumping can be observed across mouse models of ID (Kim, Lim and Kaang, 2016). *Pdzd8* mice showed increased repetitive hindlimb jumping, which has been found in other ID mouse models, such as *SHANK2* KO (Won *et al.*, 2012). In addition to repetitive jumping, *Pdzd8* mice were hyperactive and displayed high levels of wheel usage when put in metabolic cages. Wheel running has also been used as an indicator for repetitive behaviour (Karvat and Kimchi, 2012). Moreover, one of the children with the *PDZD8* mutation exhibits obsessive compulsive behaviour in the form of repetitive hand clapping (Al-Amri *et al.*, 2022). It is worth noting that even though only a few of the *Pdzd8* mice displayed increased jumping activity, compared to such drastic increase in the wheel running,

repetitive jumping was measured from a one hour long open field recording, while wheel usage was taken from a two day long recording. The length of the recording, and the fact that the repetitive jumping was counted through the light cycle, might have impacted these results. Taken together, these data support the presence of a stereotypical behaviour caused by a mutation in *Pdzd8*, which is in agreement with other literature reporting repetitive behaviours in ID. Previous studies also report a high variability in the type of repetitive behaviour seen in models of ID, and often only one or two stereotypical behaviours are detected in a mouse model (Kim, Lim and Kaang, 2016). For example, a *FMR1* KO model displayed increased marble burying, while a mutation in *SHANK3* led to excessive self-grooming (Dölen *et al.*, 2007; Wang *et al.*, 2016). This is similar to what was found in PDZD8 mice, as only increased jumping and wheel running were identified as repetitive behaviours.

Lastly, repetitive behaviours have been linked to an excitation – inhibition imbalance at the level of various brain regions, such as basal ganglia, thalamus and cerebellum, especially due to their involvement in coordinating movement (Nelson and Valakh, 2015; Gandhi and Lee, 2021). *Pdzd8* mice had relative smaller volumes of the thalamus and the pallium, a part of the basal ganglia (Al-Amri *et al.*, 2022). The decrease in the volume of these brain regions suggest they might be involved in generating the repetitive behaviours seen in *Pdzd8* mice Additionally, the highest expression of *Pdzd8* in the brain was found in the basal ganglia, while the second highest expression was in the thalamus (Human Protein Atlas, Table 4). Therefore, repetitive behaviours observed in *Pdzd8* mice might also be linked to the high expression of *Pdzd8* in the basal ganglia and the thalamus.

Learning and memory have also been assessed in *Pdzd8* mice as cognitive deficits contribute significantly to ID symptomatology in both humans and animal models (Li, Long and Yang,

2015; Golden, Buxbaum and De Rubeis, 2018). *Pdzd8* mice displayed impaired long-term memory on the Barnes maze test. In agreement, data from our collaborators on fruit flies containing a knockdown mutation of the *Pdzd8* ortholog also showed deficits in long-term memory on a courtship conditioning assay (Al-Amri *et al.*, 2022). Short-term memory was intact in both *Pdzd8* mutant mice and fruit flies (Al-Amri *et al.*, 2022). The disruptions in long-term memory in both mice and fruit flies, supports the cognitive impairment found in the children with a *Pdzd8* mutation (Al-Amri *et al.*, 2022), and provides a link between *Pdzd8* disturbance and cognitive disability across multiple species.

Despite an impairment in long-term memory, spatial learning was intact in *Pdzd8* mice when tested on the Barnez maze (Al-Amri *et al.*, 2022). However, *Pdzd8* mice revealed altered associate learning during both contextual- and cue- dependent fear conditioning. *Pdzd8* mice displayed increased freezing behaviour indicative of heightened fear. Increased freezing during fear conditioning was also found in a mouse model of ASD with a mutation in the mitochondrial DNA (Yardeni *et al.*, 2021). However, mouse models of ID are often associated with impaired associative learning, therefore a reduction in freezing behaviour (Zhang *et al.*, 2015; Ali *et al.*, 2021; Golden, Buxbaum and De Rubeis, 2018). These results were surprising as increased freezing is not only associated with fear but also with anxiety, which contradicted the reduced anxiolytic phenotype observed in *Pdzd8* mice. The brain circuitry underlying learning, memory and anxiety is highly complex (Li, Long and Yang, 2015; Adhikari, 2014). Intact spatial long-term memory and both context- and cue-dependent fear conditioning are highly dependent on the normal function of the hippocampus (Li, Long and Yang, 2015). *Pdzd8* mice displayed abnormally enlarged hippocampal volume, decreased hippocampal neurogenesis and increased spine density in the CA1 region of the

hippocampus, which could all potentially contribute to the deficits seen in long-term memory and the altered associative learning. Emotional control, such as fear encoding and anxiety, are also dependent on other brain regions, such as the amygdala (Duvarci and Pare, 2014), which did not differ in size between *Pdzd8* mice and WT controls. The discrepancy in anxiety phenotype observed between tests in *Pdzd8* mice, could stem from the fact that associative learning involves the coordination of different brain regions. Nonetheless, more research would be required to better understand these behavioural phenotypes in *Pdzd8* mice.

To further support the learning and memory impairments detected in *Pdzd8* mice, our collaborators identified altered LTP in *Pdzd8* mice hippocampal slices. A protocol of three trains of theta-burst stimulation induced a lower LTP in *Pdzd8* mice hippocampal slices (Al-Amri *et al.*, 2022). Given the vital role of Ca^{2+} in synaptic plasticity and the fact that *Pdzd8* mutation affects dendritic Ca^{2+} transients (Ho, Lee and Martin, 2011; Hirabayashi *et al.*, 2017), it is possible that the deficits seen in LTP in the hippocampus might contribute to the hippocampal-dependent learning and memory impairments in *Pdzd8* mice. Additionally, LTP was intact in *Pdzd8* when induced by less intense protocols, such as one theta-burst stimulation (Al-Amri *et al.*, 2022). This could account for the intact learning and short-term memory observed, as only a maximal stimulation protocol revealed a slight impairment in LTP, and similarly the increase in cognitive demand of the Bernes maze revealed a long-term memory deficit.

Social interaction was also investigated in *Pdzd8* mice. An initial assessment revealed no deficits in social interaction with a juvenile mouse or during interaction with a novel adult mouse. However, a social discrimination or recognition impairment was observed during interaction between *Pdzd8* mice and a novel versus familiar mouse. Deficits in social

interaction are common among individuals with ID and mouse models of this disorder (Chen and Hong, 2018). Multiple mouse models of ID, such as *PTEN* KO (Southwell *et al.*, 2020), *SHANK3* KO (Yang *et al.*, 2012), or *SHANK1* and *SHANK3* double KO (Mossa *et al.*, 2021) exhibit altered social interaction. Social recognition deficits have also been linked to ID (Fernández, Mollinedo-Gajate and Peñagarikano, 2018). An *FMR1* mutant mouse displayed reduced social interaction with a novel mouse versus the familiar mouse in the three-chamber social interaction paradigm (Tian *et al.*, 2017), similar to our findings from *Pdzd8* mice. As social interaction in mice primarily relies on olfaction, these changes seen in social discrimination might be related to the olfactory bulb abnormalities observed *Pdzd8* mice. Not only is *Pdzd8* highly expressed in the olfactory bulbs, but *Pdzd8* mutant mice had reduced neurogenesis, increased dendritic spine density, and increased relative volume of the olfactory bulb. In support of this, increase in spine density and aberrant morphology on olfactory bulb spines were also detected in an *FMR1* KO mouse model (Bodaleo *et al.*, 2019). Therefore, these structural abnormalities in the olfactory bulbs of *Pdzd8* mice are present in other mouse models of ID and might contribute to the social recognition deficits recorded.

Pdzd8 mice also displayed sex differences. Both male and female *Pdzd8* mice presented similar reductions in body weight, length and relative brain volumes. However, increased exploratory behaviour and reduced anxiety was only present in females. Surprisingly, ASD and ID are more common in male individuals (Ferri, Abel and Brodkin, 2018). This tendency is also present in the children identified with a *PDZD8* mutation, where three out of four are males (Al-Amri *et al.*, 2022). One of the strongest phenotypes observed in *Pdzd8* mice was the increase in wheel running. Unfortunately, due to the limited availability and capacity of metabolic cages, this was only investigated in males. However, both males and females

displayed repetitive hindlimb jumping activity. Therefore, it would be interesting to investigate if sex differences would be present in the repetitive wheel usage in *Pdzd8* mice.

Overall, the behavioural changes observed in *Pdzd8* mice complement the structural abnormalities presented in the previous chapter. Taken together these findings shed some more light into the role of *Pdzd8* and how mutations in this gene might lead to ID.

3.3 PDZD8 mice and neural activity

I have shown that *Pdzd8* mice displayed differences from WT mice on a number of measurements, from brain structural and cellular abnormalities to behavioural alternations in memory, learning and social recognition. Previously, it was shown that lack of *Pdzd8* was able to affect neuronal Ca^{2+} dynamics in cultured neurons, by increasing Ca^{2+} activity in dendrites (Hirabayashi *et al.*, 2017). This subcellular role of Pdzd8 combined with the numerous structural and behavioural changes observed in *Pdzd8* mice, suggested that neuronal activity might also be affected in *Pdzd8* mice. To this effect, I aimed to investigate *in vivo* neuronal activity in *Pdzd8* mice and WT controls in combination with an olfactory-based social discrimination paradigm.

3.3.1. Impaired olfactory-based social discrimination in *Pdzd8* mice

Impairments in social interaction have been extensively linked to ID and ASD (Chen and Hong, 2018; Fernández, Mollinedo-Gajate and Peñagarikano, 2018). The three chamber social interaction paradigm revealed an impairment in social discrimination in *Pdzd8*, as mutant mice were unable to distinguish between a familiar mouse and a novel one (Fig. 61). Mice rely heavily on an intact olfactory system for social interaction. Therefore, an olfactory habituation and social discrimination paradigm was employed to further assess the social recognition impairment (Methods 2.5.9, Fig. 62) (Qiu *et al.*, 2014). An olfactometer was used to deliver socially relevant odours, such as female or male urine, and non-socially relevant odours, isoamyl acetate (isoA), through a port, where a beam brake sensor was used to measure odour investigation time recorded via an Arduino microcontroller controlled (Fig. 62A, B). WT mice (n=21; 13 males and 8 females) displayed habituation and discrimination abilities to both the non-socially relevant odour, as well as the socially relevant odours,

female, and male urine (Fig. 62C). WT mice were able to differentiate between odours when the odour delivery changed from air to isoA (W=91, P=0.03; with Holm-Sidak method corrections p=0.03), isoA to female urine (W=169, P<0.0001; with Holm-Sidak method corrections P=0.0003) and female urine to male urine (W=153, P<0.0001; with Holm-Sidak method corrections P=0.0003), as shown by the significant increase in the investigation time when the odour was changed. As the key measurement of this paradigm is the ability to discriminate between different odours I used a non-parametric Wilcoxon matched-pairs signed rank tests to compare the last presentation of one odour with the first presentation of the new odour. WT mice were not only able to discriminate between the air and the non-social odour, but were also able to discriminate between female and male urine (Fig. 62C). WT mice displayed intact short-term memory as they habituated to an odour, as shown by the decrease in the investigation time following the four presentations of the same odour. Habituation was observed in WT mice across the socially relevant and non-relevant odours presented (Fig. 62C). In stark contrast, *Pdzd8* mice (n=16; 8 males and 8 females) were only able to differentiate between odours when the change from isoA to female urine took place (W=39, P=0.019, with Holm-Sidak method corrections P=0.05), suggesting that *Pdzd8* mice could detect female urine odour (Fig. 62D). *Pdzd8* mice also habituated to female urine as shown by the decrease in the amount of investigation time following the four presentation of female urine (Fig. 62D). However, *Pdzd8* mice displayed a reduction in the investigation time with isoA and male urine across all four odour presentations compared to WT mice, which is indicative of an impairment in odour discrimination. Additionally, the inability to discriminate between female and male urine (Fig. 62D) further supports the impairment in social discrimination observed in *Pdzd8* mice in the three chamber social interaction

paradigm. Overall, *Pdzd8* mice spent less time interacting with all odours presented (Fig. 62E), and displayed significantly lower interaction time with the socially relevant odours (U=66, P=0.001; Fig. 62F), which is often seen in models of ID and ASD (Silverman *et al.*, 2010).

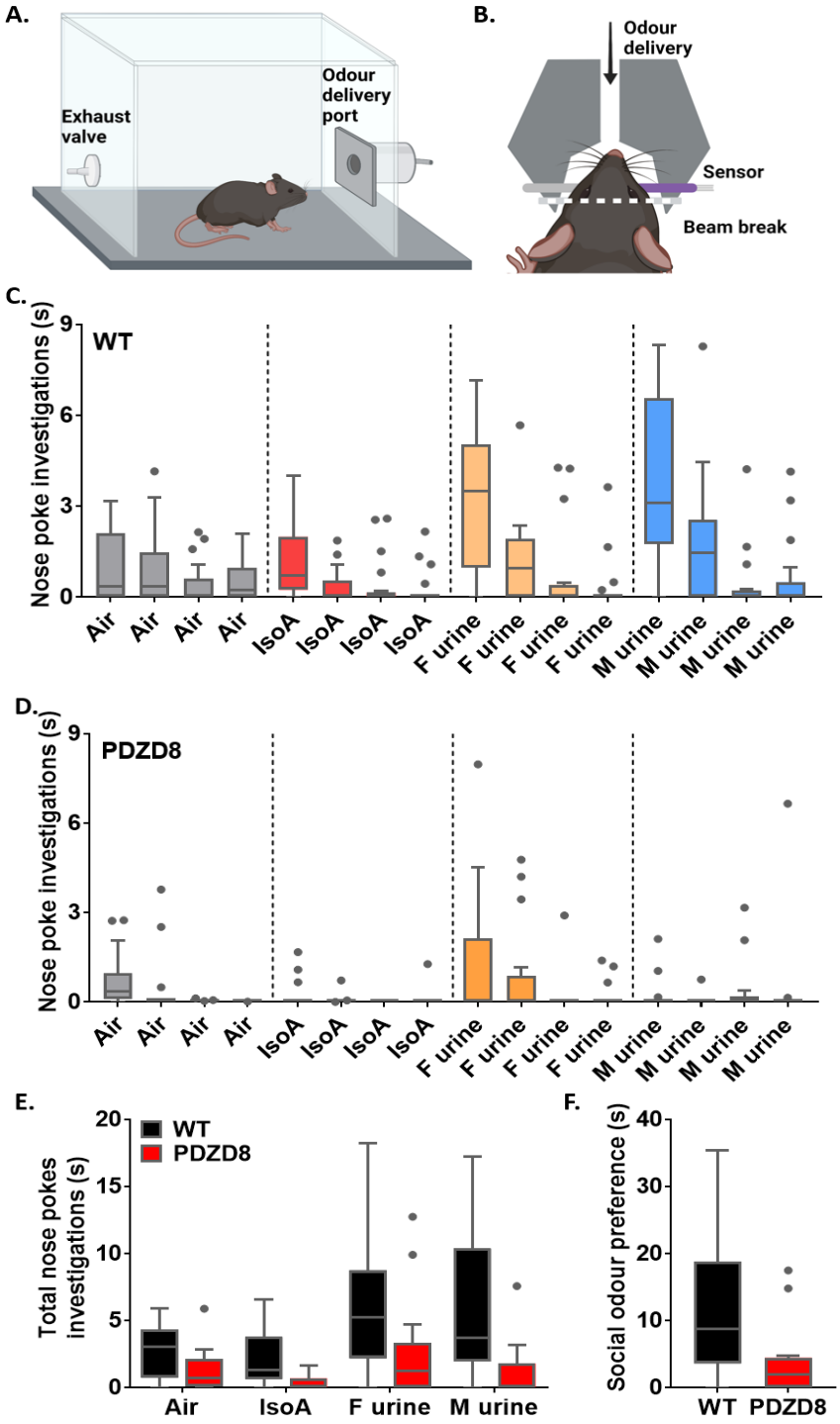

Figure 62. *Pdzd8* mice showed impairments in social odour discrimination. Social odour discrimination was assessed in *Pdzd8* mice (n=16; 8 males and 8 females) and WT controls (n=21; 13 males and 8 females) using an olfactory habituation and social odour discrimination paradigm. Representative diagram of the custom made chamber for olfactory stimulation (A). Representative diagram of the odour detection system: the odour is delivered through a port where a sensor beam is activated when the mouse investigates the port, referred to as nose poke investigations (B). Odour investigation time (seconds) of WT mice following four odour presentations: air (20 psi), isoA (0.001%), female urine (1:3), male urine (1:3) (C). Odour investigation time (seconds) of *Pdzd8* mice following four odour presentations: air (20 psi), isoA (0.001%), female urine (1:3), males urine (1:3) (D). Total investigation time (seconds) for each odour delivered for *Pdzd8* and WT mice (E). Total investigation time (seconds) for the social odours, female and male urine, for *Pdzd8* and WT mice (F). Data were recorded using a custom made Python script. Statistical analysis: non-parametric Wilcoxon matched-pairs signed rank test, with Holm-Sidak correction method (C, D), non-parametric Mann Whitney test (F), significance level $p<0.05$; data presented as box plots using Tukey's method from GraphPad Prism, where outliers denote values greater than the sum of 75th percentile plus 1.5 times the interquartile range. F urine – female urine, M urine – male urine, isoA – isoamyl acetate (banana). Figure created with BioRender.com.

Pdzd8 mice exhibited sex differences on a number of behavioural paradigm, with *Pdzd8* female mice displaying significant behavioural alterations compared to WT controls. To check whether the social odour discrimination impairment observed in *Pdzd8* mice could be driven by sex, data was split by gender (Fig. 63). Both WT males and females showed similar investigation time throughout the habituation and odour discrimination paradigm, with no apparent sex difference (Fig. 63A, B). WT male mice displayed significantly increased investigation time when odour delivery changed from control air to isoA (W=52, P=0.042; with Holm-Sidak method corrections p=0.042), from isoA to female urine (W=64, P=0.002; with Holm-Sidak method corrections p=0.0306), and from female urine to male urine (W=55, P=0.002; with Holm-Sidak method corrections p=0.006; Fig. 63A). Similarly, WT female mice showed significantly enhanced investigation time when odour delivery changed from isoA to female urine (W=28, P=0.015; with Holm-Sidak method corrections p=0.046) and from female urine to male urine (W=28, P=0.015; with Holm-Sidak method corrections

p=0.046; Fig. 63B). However, no significant discrimination was observed in WT females between air delivery and isoA (Fig. 63B). No sex differences were detected in *Pdzd8* mice either (Fig. 63C, D). Both *Pdzd8* male and female mice exhibited comparable odour interaction profiles, with males and females mainly investigating the female urine odour. However, *Pdzd8* sex-split data did not show a significant discrimination when the odour delivery changed from isoA to female urine. Overall, these data imply that a social odour discrimination impairment is present in *Pdzd8* mice, however, this is not sex-specific.

Pdzd8 mice investigated female urine less than WT controls, and displayed almost no interest in male urine or isoA. This implied that an impairment in odour detection could be present, rather than a social odour discrimination problem. Sniffing is thought to be a good measurement of odour detection (Wesson *et al.*, 2008). Therefore, some *Pdzd8* mice which underwent chronic Ca^{2+} imaging experiments (next section) had their ability to detected odours tested (Fig. 64). Videography was used to measure changes in orofacial movement in head-fixed mice following female and male urine odour presentations (Fig. 64A, B). Head-fixed mice were used as this eliminated the ability of mice to evade investigating the odours. Both female and male urine odour stimulations elicited oro-facial movements likely corresponding to sniffing in *Pdzd8* mice (n=3), detected as an increase in the orofacial movement (Fig. 64C). This implied that *Pdzd8* mice were able to detect the odours delivered.

Taken together with the previous finding from the cross-habituation assay, these data suggest that *Pdzd8* mice were able to detect odours but were not interested enough to investigate them.

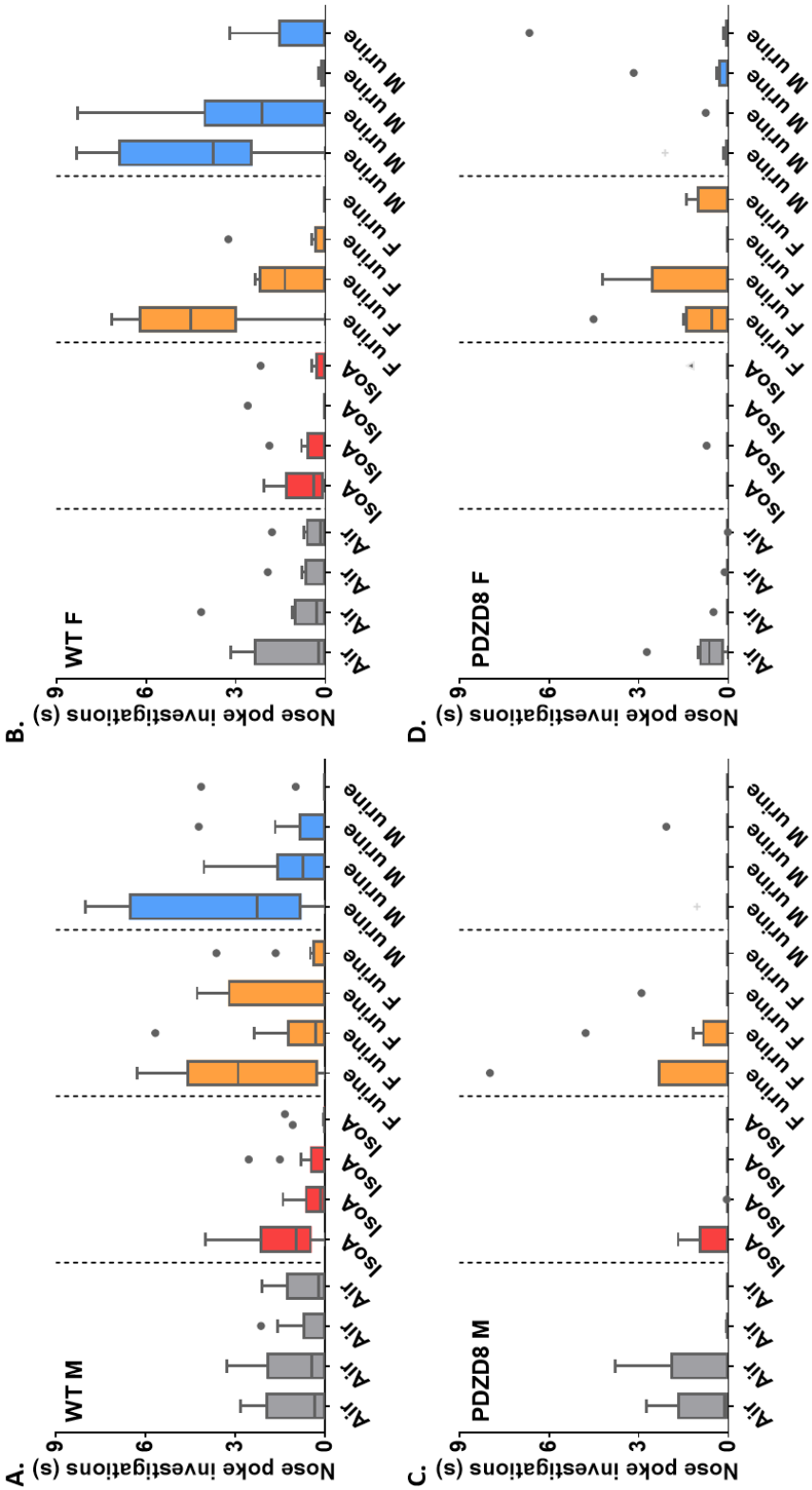
A.
WT M
Nose poke investigations (s)
0
3
6
9
Air
Air
Air
Air
Air
IsoA
IsoA
IsoA
IsoA
IsoA
F urine
F urine
F urine
F urine
F urine
M urine
M urine
M urine
M urine
M urine
B.
WT F
C.
PDZD8 M
D.
PDZD8 F

Figure 64. **No sex differences observed in social odour discrimination in *Pdzd8* mice.** Social odour discrimination was assessed in *PDzd8* mice (n=16; 8 males and 8 females) and WT controls (n=21; 13 males and 8 females) using an olfactory habituation and social odour discrimination paradigm. Odour investigation time (seconds) of WT male (A) and female (B) mice following four odour presentations: air (20 psi), isoA (0.001%), female urine (1:3), male urine (1:3). Odour investigation time (seconds) of *Pdzd8* male (C) and female (D) mice following four odour presentations: air (20 psi), isoA (0.001%), female urine (1:3), male urine (1:3). Data were recorded using a custom made Python script. Statistical analysis: non-parametric Wilcoxon matched-pairs signed rank test, with Holm-Sidak correction method (C, D), significance level $p<0.05$ (indicated by *); data presented as box plots using Tukey's method from GraphPad Prism, where outliers denote values greater than the sum of 75th percentile plus 1.5 times the interquartile range. F urine – female urine, M urine – male urine, isoA – isoamyl acetate (banana), M – male, F – female.

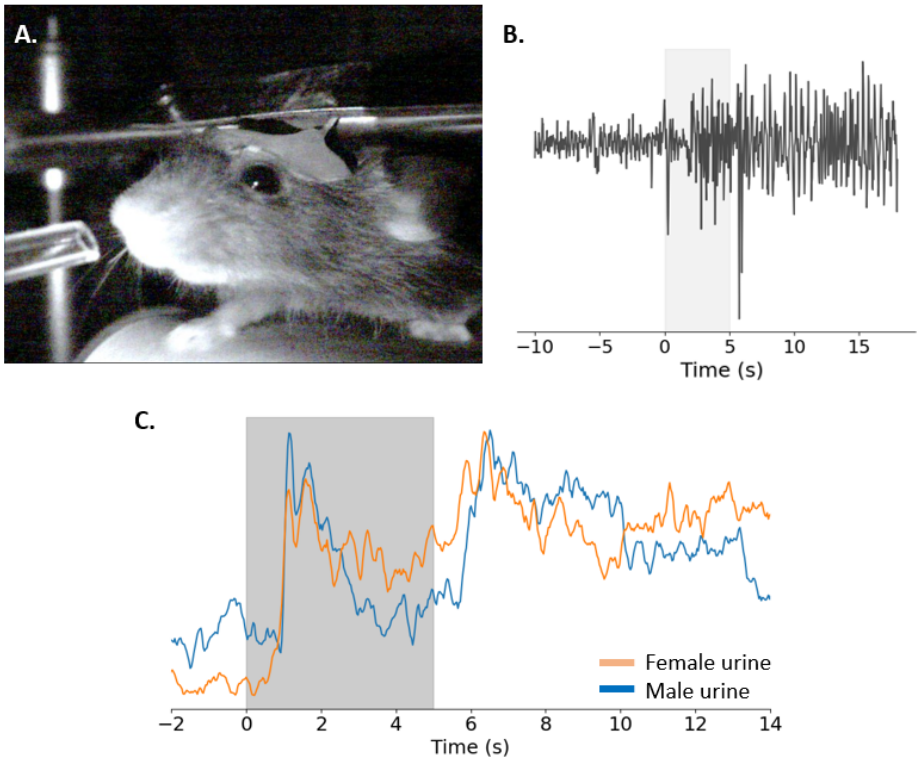

Figure 63. *Pdzd8* displayed social odour detection ability. Odour detection was assessed in head-fixed *Pdzd8* mice (n=3) by videoing and measuring the orofacial movements following three presentations (5 second stimulation) of social odours, male and female urine. Example of a head-fixed *Pdzd8* mouse on a treadmill, with the odour port visible (A). Example trace of orofacial movement detected following an odour stimulation (grey box, B). Mean orofacial responses to male (blue) and female (orange) urine of *Pdzd8* mice (C). A rectangular region of interest around the nose of the mouse was manually drawn to extract orofacial movement, data was presented as mean traces from all *Pdzd8* mice

3.3.2. Altered *in vivo* spontaneous neuronal activity in *Pdzd8* mice

Pdzd8 mice were found to exhibit impairments in social odour discrimination, despite being able to detect social odours, suggesting that changes in neural dynamics linked to odour processing at the level of olfactory bulb or higher order cortices might occur in these mice as well. As *Pdzd8* mutation affects neuronal Ca^{2+} activity levels (Hirabayashi *et al.*, 2017), spontaneous neuronal activity was subsequently investigated using Ca^{2+} activity as a proxy for detecting neuronal changes. Neuronal Ca^{2+} activity was measured in *Pdzd8* and WT mice which expressed a genetically encoded Ca^{2+} indicator in excitatory neurons (Thy1-GCAMP6; Methods 2.2).

Pdzd8 mice displayed structural changes of the olfactory bulb, increased relative size, enhanced number of dendritic spines and reduced neurogenesis, suggesting that functional changes might be present as well. Therefore, the aim was to initially investigate neural activity in the olfactory bulb, by performing a craniotomy (Methods 2.6.1) over the olfactory bulbs (data not shown). However, due to sparse labelling of excitatory cells in the olfactory bulbs of the Thy1-GCaMP6s line used, neural activity in *Pdzd8* and WT controls could not be properly assessed. Additionally, responses to socially relevant odours are encoded in a subset of glomeruli present in the ventral olfactory bulb (Bear *et al.*, 2016; Cockerham, Margolis and Munger, 2009). Unfortunately, the craniotomy exposes the dorsal side of the olfactory bulbs, making it impossible to access the glomeruli which respond to mouse urinary pheromones, without using different techniques for deep tissue imaging. Due to reduced labelling and the inability to assess odour-evoked neural responses, Ca^{2+} activity could not be properly investigated in the olfactory bulbs.

However, it was recently shown that persistent odour representations are found at the level of mPFC (Wang *et al.*, 2020), an area highly involved in ID and autism (Southwell *et al.*, 2020; Wang *et al.*, 2018), especially the frontal association cortex, which is a hub for integrating sensory input (Barthas and Kwan, 2017). Therefore, fluorescence Ca^{2+} activity was investigated in the frontal association cortex in *Pdzd8* (n=5) and WT controls (n=6), by performing a craniotomy over both frontal association cortices (Fig. 65A, B, C, D).

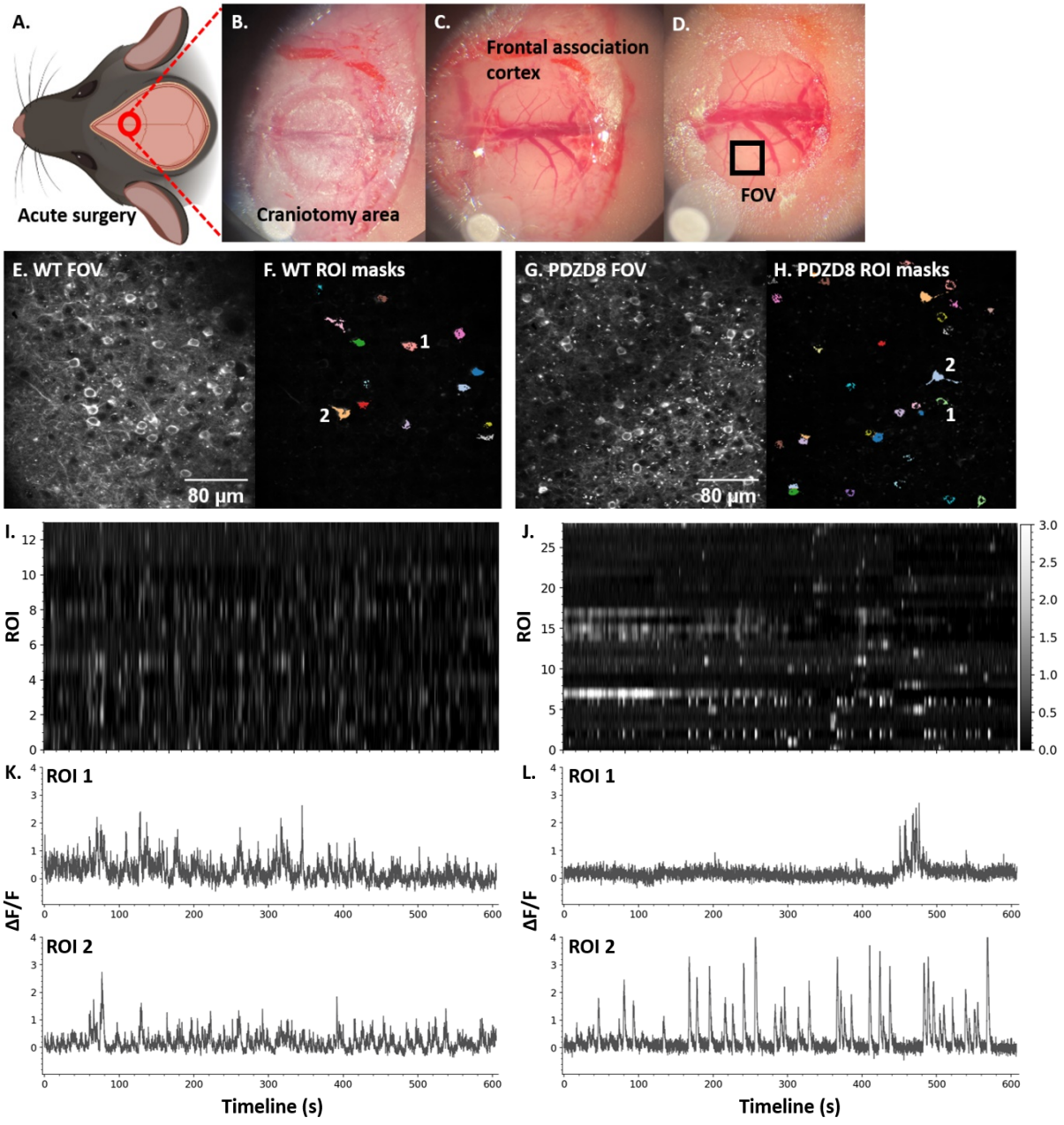

Figure 65. *In vivo* spontaneous cortical Ca^{2+} activity in anesthetized mice. Spontaneous neuronal activity was assessed *in vivo* in anesthetized *Pdzd8* mice (n=5) and WT controls (n=6), by using a genetically encoded calcium indicator, GCAMP6s, expressed under the Thy1 promoter for excitatory cells. Diagram of an acute surgery, where a craniotomy was performed of the frontal association cortex (A). Representative image of a 3 mm craniotomy drilling (B). Representative image of an exposed frontal association cortex with a coverslip attached to enable brain imaging (C). Representative image of a finished craniotomy sealed with dental cement and an example of a field of view used during imaging experiments (black rectangle; D). Example of an imaging plane (E) and the cells detected by Suite2P software (numbers 1 and 2 denote ROI in panel K; F) in a WT mouse. Example of an imaging plane (G) and the cells detected by Suite2P software (numbers 1 and 2 denote ROI in panel L; H) in a *Pdzd8* mouse. Raster plots of Ca^{2+} activity in a WT mouse from all cells detected in panel F (I) and in a *Pdzd8* mouse from all cells detected in panel H (J), where the change in the fluorescence intensity relative to the resting fluorescence intensity (ΔF/F) is plotted for each cell (ROI) over time (seconds). A higher value on the ΔF/F colormap legend denotes increased in fluorescence activity, while a value of 0 denotes no fluorescence activity. Examples of individual spontaneous Ca^{2+} traces filtered with the Savitzky-Golay filter from WT (K) and *Pdzd8* (L) mice, plotted as ΔF/F over time (seconds). Data was processed with Suite2P software, analysed and plotted in python. FOV – field of view, ROI – regions of interest.

Initially, Ca^{2+} imaging was performed in anesthetized mice to assess spontaneous neuronal responses (Methods 2.6.2). *In vivo* Ca^{2+} imaging displayed spontaneously active neurons in the frontal association cortex of WT controls (Fig. 65E, F, I, K), as well as *Pdzd8* mice (Fig. 65G, H, J, L). Taking a closer look at individual Ca^{2+} responses in WT controls (Fig. 66A) and PDZD8 mutants (Fig. 66B) revealed a high degree of variability in both genotypes, which is commonly observed when recording spontaneous Ca^{2+} activity. This heterogeneity in spontaneous Ca^{2+} activity was observed within the same mouse (Fig. 65K, L) and across all the mice investigated in both genotypes (Fig. 66A, B), with no obvious changes observed in *Pdzd8* mutants.

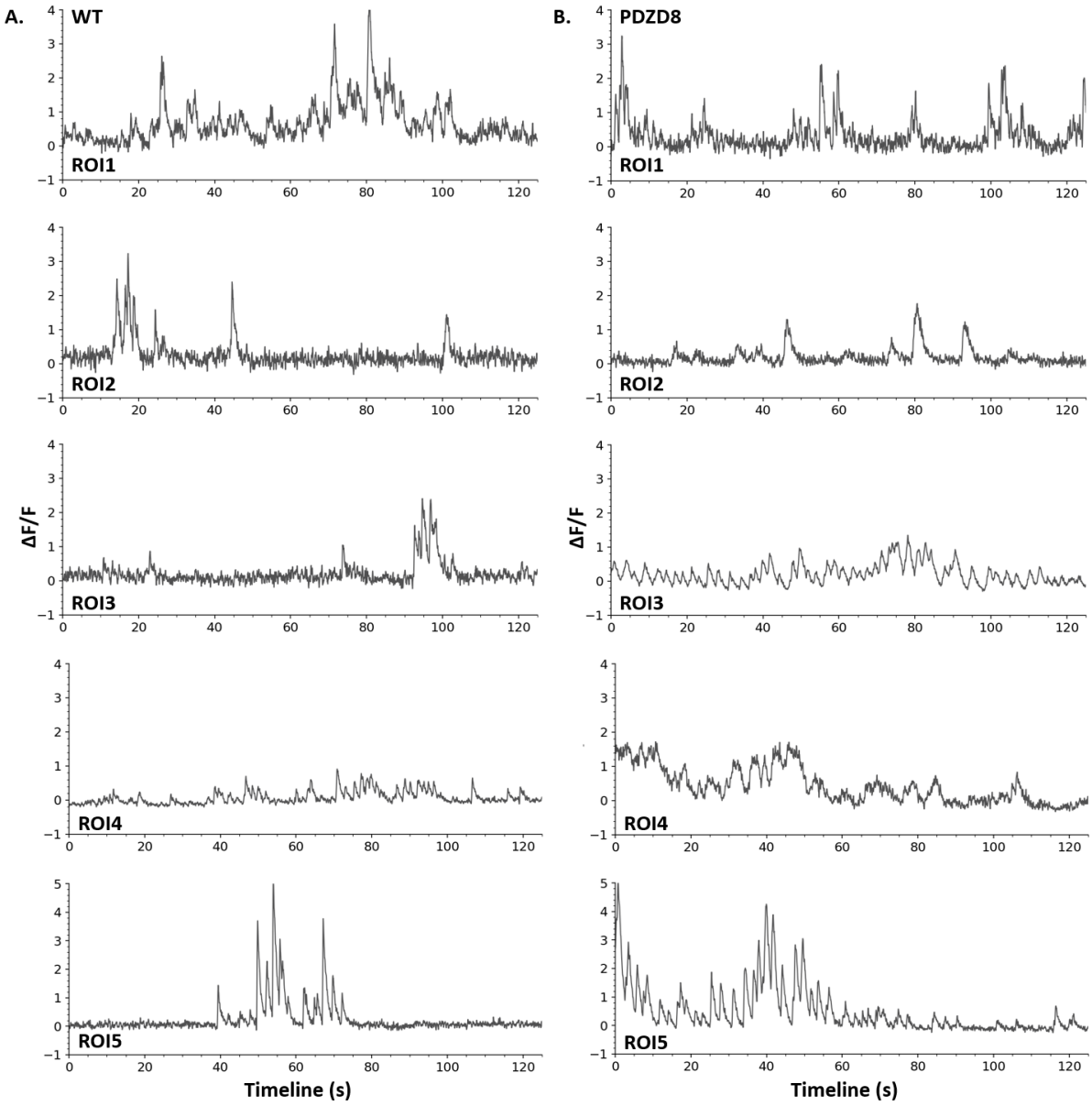

Figure 66. Heterogeneity of spontaneous neuronal activity detected *in* vivo in both *Pdzd8* and WT mice. *In vivo* spontaneous Ca^{2+} traces recorded from *Pdzd8* mice (n=5) and WT controls (n=6) revealed highly heterogenous neuronal activity. Examples of five fluorescence Ca^{2+} activity traces across WT mice highlighting the variability of neuronal traces recorded (A). Examples of five fluorescence Ca^{2+} activity traces across *Pdzd8* mice highlighting the variability of neuronal traces recorded (B). Data is plotted as the change in the fluorescence intensity relative to the resting fluorescence intensity (ΔF/F) over time (seconds), and Ca^{2+} traces were filtered with the Savitzky-Golay filter. Data was processed with Suite2P software, analysed and plotted in python. ROI - region of interest.

To further investigate if there are any changes in the spontaneous fluorescence Ca^{2+} activity, Ca^{2+} spikes were subsequently assessed. An algorithm was used to detect the number of Ca^{2+} spikes for each cell (region of interest) identified in WT and *Pdzd8* mice (Fig. 67A). This algorithm worked well on detecting spikes in neurons which had sparse activity (Fig. 67A, example 1). However, in cells which displayed high levels of spontaneous activity, the accuracy of detecting fluorescent Ca^{2+} events was decreased (Fig. 67A, example 2). Suite2P (Methods 2.6.2) detected 307 spontaneously active cells across WT mice and 207 cells across *Pdzd8* mice (Fig. 67). Due to the high number of cells detected and their increased heterogeneity, it was not possible to tune the algorithm to accurately detect Ca^{2+} events across such variability in responses. Therefore, the mean fluorescence activity was compared between WT controls and *Pdzd8* mice. This approach was chosen as it is less biased, as an increase in fluorescence activity would be depicted by a higher mean $\Delta F/F$ value. *Pdzd8* mice displayed increased mean fluorescence activity in the frontal association cortex compared to WT controls (two-sample Kolmogorov-Smirnov test, $P<0.0001$), as shown by the probability density histogram, which was plotted to account for the difference in the number of cells detected per genotype (Fig. 67B).

Additionally, the percentage of spontaneously active cells was calculated in both *Pdzd8* mice and WT controls. *Pdzd8* mice had significantly higher number of cells being spontaneously active from the total number of cells detected in the field of view compared to WT controls (Fisher's exact test, $P=0.04$; Fig. 67C). Overall, these results highlighted that *Pdzd8* mice also showed alternations in the neuronal activity, as they exhibited increased spontaneous Ca^{2+} responses in comparison to WT mice. These data from *in* vivo Ca^{2+} imaging experiments of neuronal activity in the frontal association cortex of *Pdzd8* mutant mice are

in agreement with the role Pdzd8 is thought to have on Ca^{2+} activity in dendrites, whereby it leads to increased dendritic Ca^{2+} following *Pdzd8* KO mutation (Hirabayashi *et al.*, 2017). Moreover, these results support previous literature which reports aberrant neuronal dynamics in numerous models of ID and ASD (Golden, Buxbaum and De Rubeis, 2018).

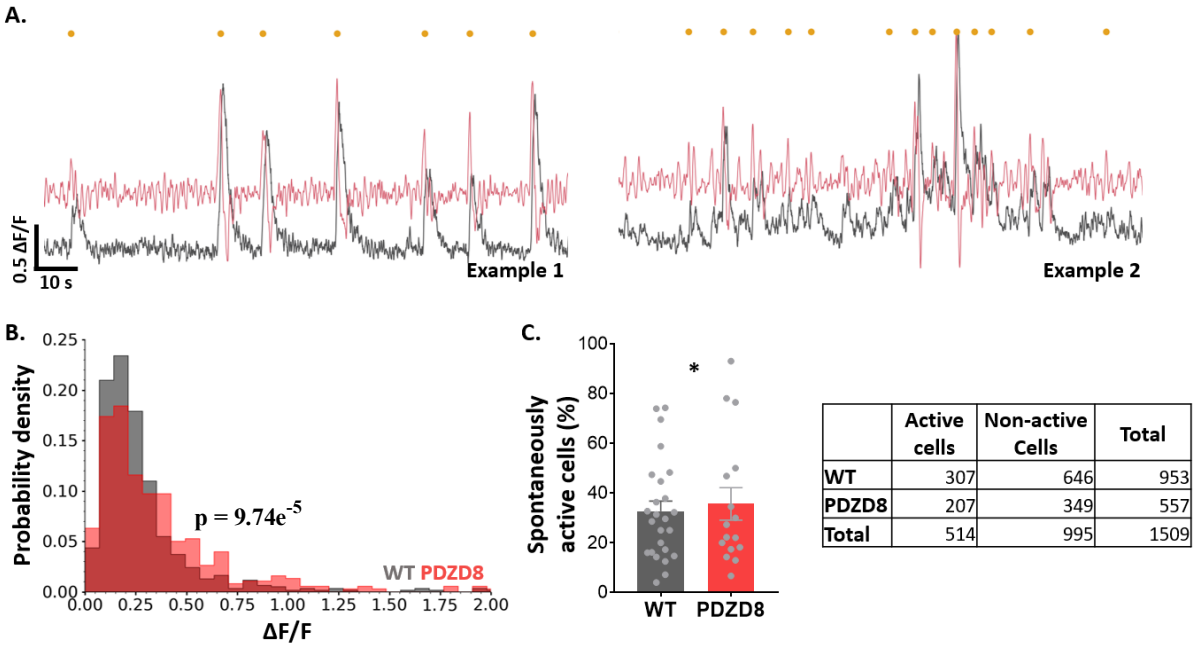

	Active cells	Non-active Cells	Total
WT	307	646	953
PDZD8	207	349	557
Total	514	995	1509

Figure 67. *Pdzd8* mice displayed increased neuronal activity *in vivo*. *In vivo* spontaneous Ca^{2+} activity was recorded from the frontal association cortex in anesthetized *Pdzd8* mice (n=5) and WT controls (n=6). An algorithm, which computes the differential (red trace) of the fluorescent Ca^{2+} traces (black trace), was used to identify Ca^{2+} events (yellow dots) in all spontaneously active cells. Example 1 denotes a successful attempt to accurately identify Ca^{2+} events and Example 2 denotes an unsuccessful attempt to accurately identify Ca^{2+} events; Ca^{2+} traces were filtered with a Savitzky-Golay filter (A). *Pdzd8* neurons (207) displayed significantly increased mean fluorescence intensity compared to WT neurons (307); the mean of ΔF/F (the change in the fluorescence intensity relative to the resting fluorescence intensity) was computed for each cell detected, then divided by the number of cells found per genotype to generate a probability density histogram (B). *Pdzd8* mice displayed significantly increased percentage of spontaneously active cells from the total number of cells in the field of view compared to WT controls; the table reports the number of active and non-active cells identified (C). Statistical analysis: two-sample Kolmogorov-Smirnov test (B), two-tailed Fisher's exact test (2x2 contingency table displayed; C), significance level $p<0.05$ (indicated by *); data was processed with Suite2P software, analysed and plotted in python.

3.3.3. Chronic *in vivo* awake imaging: establishment and proof of concept

Thus far, *Pdzd8* mice exhibited behavioural deficits, such as impaired social odour-based discrimination, as well as heightened spontaneous neuronal activity compared to WT controls. Therefore, I next sought to investigate whether there is a direct connection between changes observed in the social odour discrimination paradigm and the aberrant neuronal activity recorded.

Anaesthesia has been previously shown to significantly dampen cortical Ca^{2+} transients *in vivo* (Greenberg, Houweling and Kerr, 2008). Additionally, assessing the impact of odour stimulation on cortical activity under anaesthetic conditions would be very difficult as it was recently shown that cortical odour representations are attenuated under anaesthesia or completely absent (Pashkovski *et al.*, 2020). Hence, I have established chronic *in vivo* Ca^{2+} imaging experiments in awake mice (Methods 2.6.1) in order to investigate odour-evoked neuronal activity in the frontal association cortex in *Pdzd8* mice and WT controls (Fig. 68).

Chronic surgery differs from acute surgery as it allows the animal to recover following the window implantation. The advantages of chronic surgery over the acute method are the ability to perform brain imaging during an awake state and the possibility to perform multiple brain imaging experiments using the same mouse, which enable tracking of neuronal activity over time. As mice are awake and moving during brain imaging experiments, proper head bar fixation is crucial to enable successful imaging experiments. Multiple head bars were designed and tested (not shown) to find a model suitable for the imaging set-up, with a final head bar design made from stainless steel that contains a 5 mm diameter hole, which allows the head bar to be securely attached all around the craniotomy area (Fig. 68A chronic surgery). Following recovery form surgery, mice were head fixed for at least 3 times before

an experiment to get them accustomed to the imaging set-up, which consisted of a Styrofoam ball that allowed movement across x- and y-axis (Fig. 68A training). Subsequently, chronic imaging experiments were performed to assess fluorescence Ca^{2+} activity *in vivo* in an awake state (Fig. 68A brain imaging). Animals were continuously monitored during Ca^{2+} imaging experiments to ensure no issues occurred during imaging and subsequently, videos could be used as a potential measure for pupil dilation, locomotion or sniffing activity (Fig. 68B). Therefore, neural activity (Fig. 68C) could be correlated with multiple parameters.

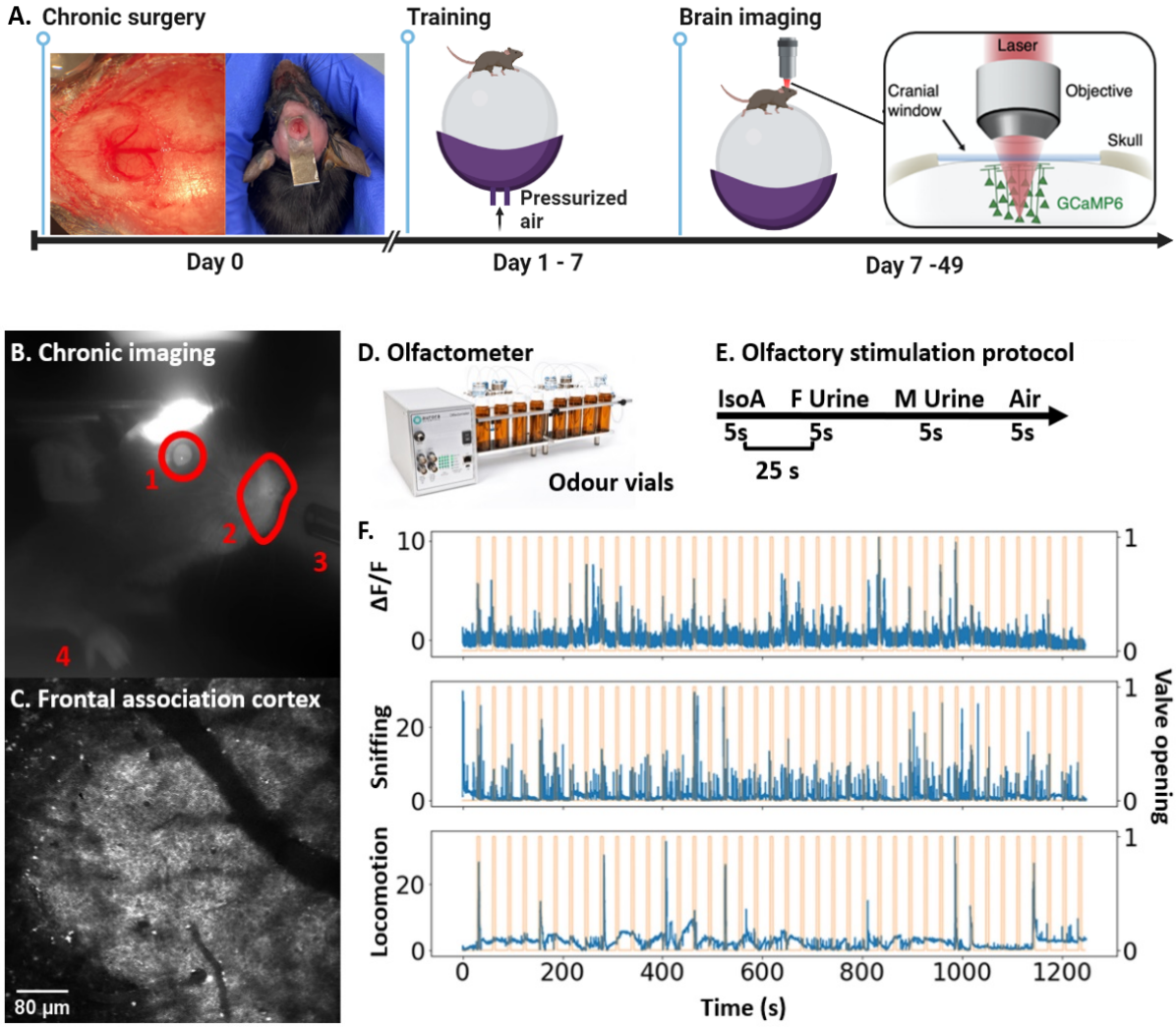

Figure 68. Chronic window surgery and awake imaging set-up. Chronic surgery (day 0): example of a craniotomy performed over the frontal association cortex for a chronic imaging experiment and the mouse awake following the surgery; training (day 1 - 7): schematic representation of the training period where the mouse is head-fixed on a ball on which can move in x- and y-direction in order to get accustomed to the imaging set-up; brain imaging (day 7 - 49): schematic representation of the imaging experiments (A). A snapshot from a video depicting a mouse during an awake imaging session (the bright spot is the laser beam); in red are highlighted potential regions of interested: the pupil (1), the nose (for sniffing; 2), odour port (3), forelimb paw (for locomotion; 4) (B). The imaging plane (C). Representative image of the olfactometer device used for delivering odours (D). Olfactory stimulation protocol consisting of 5 seconds odour stimulation in the following order: banana, female urine, male urine, and air, with an inter-trial interval of 25 seconds, and this sequence repeated 10 times (E). Example of fluorescence Ca^{2+} trace displayed as the $\Delta F/F$ (the change in the fluorescence intensity relative to the resting fluorescence intensity) over time (top panel); example of a sniffing trace displayed as orofacial movement over time (middle panel); and an example trace of locomotion displayed as forelimb movement over time (bottom panel). Orange lines demote the valve opening times, when the odours were delivered (F). Data was processed with Suite2P software, analysed and plotted in python. F urine – female urine, M urine – male urine, isoA – isoamyl acetate (banana).

For example, an olfactometer was used to deliver socially relevant odours, female and male urine, and non-socially relevant odours, such as isoA during an awake imaging experiment (Fig. 68D, E). Odour-evoked cortical fluorescent Ca^{2+} transients could be then correlated with sniffing activity and locomotion (Fig. 68F).

Cortical neurons from the mPFC have been shown to elicit responses following olfactory stimulation and ensembles of neurons in the this region were shown to persistently represent different odour objects following an olfactory learning paradigm (Wang *et al.*, 2020). Based on this idea, the olfactory stimulation protocol mentioned previously was used to measure odour-evoked Ca^{2+} transients in the frontal association cortex in naïve WT mice during an awake state. Here is an example from one WT mouse (Fig. 69A). All neurons displaying Ca^{2+} activity were segmented using Suite2P software (Fig. 69B). Subsequently, neurons which exhibited responses to odorant simulations were classified based on their responsiveness to the odours delivered (Fig. 69C). Three main populations of neurons were identified, which

increased their activity following stimulation with isoA, female urine or male urine (Fig. 69D, E). For example, some neurons elicited responses following female urine and not isoA, while some other neurons were not displaying any changes in activity during presentations of socially relevant odours (Fig. 69E).

Even though there is a slight overlap between these neuronal ensembles, odour-evoked responses to the non-social odour are largely separated from the odour-evoked responses to the socially relevant odours. The same degree of separation was observed in WT between the two socially relevant odours, female urine and male urine (Fig. 69D). Based on these results, the hypothesis was that in *Pdzd8* mice these two ensembles of neurons which encode for distinct socially relevant odours might display a higher level of overlap. The social discrimination impairment observed in *Pdzd8* mice, in which these mice displayed an inability to distinguish between female and male urine, could be the result of aberrant encoding of odours at the level of the cortex. Unfortunately, the establishment of the chronic window implantation and awake imaging was a lengthy process and due to time constraints imposed by the covid pandemic it was not possible to test this hypothesis.

Overall, the myriad of changes observed in *Pdzd8* mice, from molecular and structural abnormalities to neuronal and behavioural impairments, strongly characterize deficits observed in ID and ASD models (Golden, Buxbaum and De Rubeis, 2018). *In vivo* Ca^{2+} imaging in awake mice could constitute an effective platform for directly linking some of the deficits observed in PDZD8 mice.

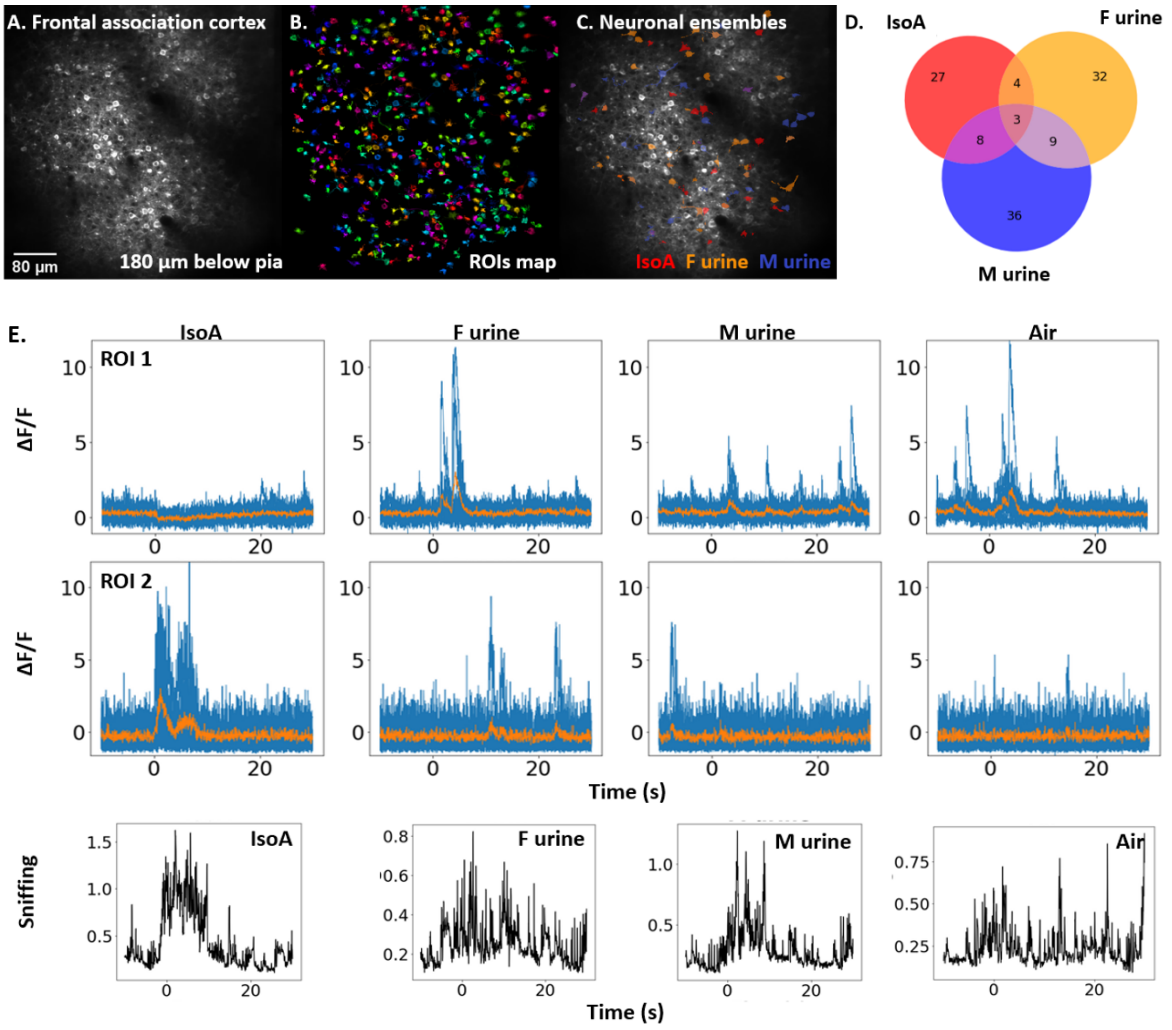

Figure 69. Odour-evoked ensembles of neurons in WT mice. Olfactory stimulation in a WT mouse revealed separate ensembles of neurons tuned different odour objects (isoA, female urine and male urine) during *in vivo* awake imaging. Representative image of the field of view (A). Representative image of the cells identified (B). Colour coded map of neuronal ensembles responding to isoA (red), female urine (orange), and male urine (blue; C). Venn diagram of the neuronal populations identified: isoA 27 cells, female urine 32 cells, and male urine 36 cells (D). Two example of neurons (ROI1, ROI2) and their Ca^{2+} activity during multiple odour stimulation (isoA, female urine, male urine, and air) superimposed (5 seconds starting at 0); the mean activity displayed by the orange trace. Data is plotted as the ΔF/F (the change in the fluorescence intensity relative to the resting fluorescence intensity) over time (seconds). Sniffing traces during to the presentation of the odours delivered (E). Data was processed with Suite2P software, analysed and plotted in python. ROI – region of interest, F urine – female urine, M urine – male urine, isoA – isoamyl acetate (banana).

3.3.4 Discussion

This chapter aimed to further understand the social discrimination deficits previously observed in *Pdzd8* mice and assess whether there is a link between these deficits and neural activity. *Pdzd8* mice displayed significantly impaired social discrimination on the olfactory habituation and social discrimination paradigm. *Pdzd8* mutants displayed both a reduced interaction with the social odours, as well as an inability to differentiate between female and male urine. *In vivo* neuronal Ca^{2+} activity assessment in anesthetized mice revealed an increase in the neuronal spontaneous activity and the number of spontaneously active cells in *Pdzd8* mice. Lastly, establishment of *in vivo* Ca^{2+} imaging in awake mice aimed to ascertain a connection between altered neuronal activity and impaired social discrimination. However, due to the impact of covid it was impossible to reach this goal. Nonetheless, the social recognition and discrimination deficits, and the aberrant neuronal dynamics are changes often detected in both humans and mouse models of ID and ASD (Fernández, Mollinedo-Gajate and Peñagarikano, 2018; Golden, Buxbaum and De Rubeis, 2018; Verma *et al.*, 2019).

Social discrimination is crucial for survival, and an inability or lack of interest in investigating social stimuli is common amongst mouse models of ID and autism (Fernández, Mollinedo-Gajate and Peñagarikano, 2018). A decrease in the interaction and an inability to discriminate social odours characterized *Pdzd8* mice. Olfactory based impairments are seen across various mouse models of ID. In a double KO of *SHANK2/3*, presentations of both male and female urine resulted in reduced ultrasonic vocalizations and investigation time in the mutant mice compared to WT controls (Garrido *et al.*, 2022). A mouse model containing a mutation in *KIRREL3* gene, which has been previously linked to ID and autism, displayed

abnormal social discrimination as well. *KIRREL3* KO mice showed normal interaction during an initial presentation of a social odour. However, a subsequent presentation of a different social odour revealed an inability of these mice to distinguish between the social odours delivered (Hisaoka *et al.*, 2018), similarly to what was observed in *Pdzd8* mice. This indicates an inability to discriminate between social odours and / or an impairment in social memory. Piriform cortex, which is an important structure in the olfactory pathway (Wei, Talwar and Lin, 2021; Chen and Hong, 2018), is thought to be critical in the generation of olfaction-related memories and olfactory discrimination (Bekkers and Suzuki, 2013). Altered discrimination or olfactory performance is also present in *FMR1* KO mouse models (Bodaleo *et al.*, 2019). An *FMR1* KO displayed reduced LTP in the piriform cortex (Bodaleo *et al.*, 2019), which could potentially expose an abnormality in the plasticity or circuitry behind olfactory-related memories as a cause for this inability to discriminate between social odours in ID models. *Pdzd8* mice exhibited a reduction in hippocampal LTP (Al-Amri *et al.*, 2022). It would be interesting to see if any synaptic plasticity changes occur in the piriform cortex of *Pdzd8* mice. Nonetheless, in a recent study, another brain region, the retrosplenial cortex, has been identified an important in social memory (Garrido *et al.*, 2022). Specific deletion of *SHANK2/3* in the retrosplenial area was correlated to the social memory impairment. In a social interaction paradigm, *SHANK2/3* KO mice investigated the novel mouse compared to a familiar one significantly less than WT controls. However, specific chemogenetic activation of the retrosplenial area rescued this social recognition deficit (Garrido *et al.*, 2022). Interestingly, *Pdzd8* displayed an increase in the relative volume of the retrosplenial cortex compared to WT mice, which could potentially contribute to the social recognition deficits observed in this mouse line.

A neuronal excitation – inhibition imbalance is the most prevalent neurobiological theory behind neurodevelopmental disorders, such as ID and autism, with studies reporting either an increase or a decrease in the excitation – inhibition ratio (Port, Oberman and Roberts, 2019; Canitano and Palumbi, 2021). As such, *Pdzd8* mice displayed increased spontaneous Ca^{2+} activity in excitatory neuron in the frontal association cortex compared to WT controls. Optogenetically increasing the excitation at the level of the mPFC on its own is able to cause social interaction impairments in free moving mice in a juvenile social interaction test, similar to what is observed in models of autism, while increases in the inhibitory activity partially rescued these deficits (Yizhar *et al.*, 2011). Multiple mouse models of ID and ASD exhibit cortical hyperexcitability (Golden, Buxbaum and De Rubeis, 2018; Verma *et al.*, 2019), which is in line to what it was seen in *Pdzd8* mice.

In a recent study, four mouse models of ASD, *FMR1*, *CNTNAP2,* 16p11.2 deletion, and *TSC2*, which were previously shown to exhibit an elevation in the excitatory activity, were shown to display this hyperexcitability in the somatosensory cortex due to a reduction in the feedforward inhibition in the cortical layer 2 and 3 (Antoine *et al.*, 2019). Neuronal activity was investigated only in the excitatory neurons in *Pdzd8* mice. However, RNA sequencing data from Allen Cell database on *Pdzd8* revealed expression of *Pdzd8* in both glutamatergic and GABAergic neurons in the human primary motor cortex (Al-Amri *et al.*, 2022; Bakken *et al.*, 2021). In mice we intended to understand the expression profile of *Pdzd8* in the brain via immunofluorescence staining, but due to a lack of a good Pdzd8 antibody this could not be done. Nonetheless, as *Pdzd8* seems to be expressed in inhibitory neurons, it would be interesting to consider whether and how *Pdzd8* mutation affects inhibitory neuronal activity

In *Pdzd8* mice, the increase in excitatory activity *in vivo* could potentially be caused by larger Ca^{2+} transients in dendrites, as this was previously shown to be the results of *Pdzd8* mutation *in vitro* (Hirabayashi *et al.*, 2017). This increase in spontaneous activity in *Pdzd8* mice most likely leads to synaptic strengthening happening at lower thresholds, which potentially steers neurons towards inappropriate wiring. Neurons are only able to operate over set ranges of their properties, for example they have a certain membrane potential, spike rate, even a certain number of spines under normal conditions, and homeostatic mechanisms are responsible for keeping these in check (Ho, Lee and Martin, 2011). However, in our case, the *Pdzd8* mutation might push the system to its limits causing homeostatic mechanisms to fail and subsequently leading to aberrant neuronal activity, which might be responsible for the behavioural impairments observed in *Pdzd8* mice. It has already been shown that heightened excitatory activity in the cortex, on its own, generates behavioural deficits in mice (Yizhar *et al.*, 2011). Additionally, what could potentially support this theory is the spine density data obtained from *Pdzd8* mice, which not only displayed increased spine density, but a reduced variance in spine counts compared in the olfactory bulb and the hippocampus. This reduction in variance can be observed even in the spine density data from the frontal association cortex, despite the spine counts not being significantly different from WT controls. However, further research needs to be done to understand what the mechanism behind these neuronal changes is *in vivo* and how this ultimately leads to behavioural impairments.

One way to directly link neuronal activity to behavioural output is by simultaneously recording brain activity during a behavioural paradigm. As such, *in vivo* Ca^{2+} imaging in awake mice was performed coupled simultaneous odour stimulation to assess neuronal Ca^{2+} responses during presentations of socially relevant odours. Due to time constraints imposed

by the covid pandemic it was not possible to test whether socially relevant odours elicit different neuronal responses in *Pdzd8* mice compared to WT controls. As presented above, we have seen separate neuronal ensembles responding to distinct odour objects in the frontal association cortex in a WT mouse. These odour-induced neuronal engrams in the mPFC have been previously shown to strengthen with learning (Wang *et al.*, 2020). It would be interesting to see not only if *Pdzd8* mice display changes in these odour-related neuronal ensembles but also if these engrams might alter through learning. *Pdzd8* mice were shown to have altered learning during an associative learning task. Also, the PFC has been extensively involved in learning, in both early phases of learning as well as recall (Dixsaut and Gräff, 2021; Kitamura *et al.*, 2017). Therefore, neuronal activity in the frontal association cortex of *Pdzd8* mice might also be different during associative learning tasks. To test this out in *Pdzd8* mice an associate learning paradigm could be employed, coupled with simultaneous Ca^{2+} imaging of brain activity. For example, odour stimulation could be paired with a water reward, or an innate fear-inducing odour, such as fox urine, could be paired with a sound, to mimic a classical fear conditioning paradigm.

The advantages of chronic Ca^{2+} imaging would allow for neuronal activity to be tracked throughout the whole behavioural paradigm. Thus, odour-evoked Ca^{2+} transients can be monitored prior to the learning test, during the learning phase, and after the learning period. Additionally, recall can be assessed weeks following the initial learning to investigate long term memory as well. As *Pdzd8* mice displayed alterations in both learning and memory during various behavioural paradigms, these changes at the level of behaviour could potentially be mirrored in the neuronal brain activity in *Pdzd8* mutants.

Overall, *in vivo* Ca^{2+} imaging in awake mice would constitute a powerful tool which might allow for a more in depth understanding of how neuronal changes in *Pdzd8* mice are responsible for the behavioural deficits observed.

IV. Conclusions

4.1 Summary: *Pdzd8* mutant mice as a model of ID

A multimodal approach was undertaken to understand the effects of a homozygous *Pdzd8* mutation in mice. Molecular and structural changes, along with neuronal activity and behaviour were probed to get a better understanding of the consequences of mutating *Pdzd8*.

Pdzd8 mice displayed cognitive dysfunction as shown by altered learning and memory on behavioural paradigms. Associative learning was altered in *Pdzd8* mice during both cue- and context-dependent fear conditioning, while long-term memory impairments became apparent during the Barnes maze experiment. The cognitive impairment was supported by structural alterations in brain regions linked to learning and memory. Enlarged hippocampal volume, decreased neurogenesis, and increased hippocampal spine density were found in *Pdzd8* mice. Electrophysiological data also revealed altered synaptic plasticity at the hippocampal level in *Pdzd8* mice (Al-Amri *et al.*, 2022). Together with our collaborators we have identified that *PDZD8* mutation leads to cognitive impairment in humans, mice and flies (Al-Amri *et al.*, 2022).

Pdzd8 mice also displayed stereotypical behaviour. Metabolic cages revealed a hyperactive phenotype in *Pdzd8* mice, which was accompanied by significantly higher levels of wheel running, which is considered a type of repetitive behaviour. The presence of a stereotypical

behaviour was also confirmed by the observation on increased hindlimb repetitive jumping in *Pdzd8* mice. Brain structural changes in the thalamus, basal ganglia, and cerebellum which has been involved in repetitive behaviours support these results, with the thalamus and the pallidum of the basal ganglia having relatively smaller volumes, while the cerebellum displaying an increase in the relative volume in *Pdzd8* mutants (Al-Amri *et al.*, 2022).

Social recognition and discrimination were affected in *Pdzd8* mice. Despite exhibiting no changes in the social interaction with a juvenile mouse or an adult mouse, *Pdzd8* mice showed an inability to differentiate between a familiar mouse and a novel mouse during the three-chamber social approach testing. *Pdzd8* mice also displayed reduced interaction with socially relevant odours during an olfactory habituation and social odour discrimination paradigm, which further supports this social discrimination phenotype. Additionally, structural brain changes in regions previously linked to social interaction, the retrosplenial cortex and olfactory bulbs, were observed. *Pdzd8* mice were characterized by enlarged relative volumes of the retrosplenial cortex and olfactory bulbs, as well as decreased neurogenesis and increased spine density in the olfactory bulb.

Lastly, *Pdzd8* mice displayed altered neuronal activity in the frontal association cortex, a region of the mPFC which is extensively linked to both learning and memory, as well as social interaction. Excitatory spontaneous Ca^{2+} activity was increased during *in vivo* brain imaging experiments in anesthetized *Pdzd8* mice. An increase in the number of spontaneously active neurons found in PDZD8 mutants further supported altered brain activity as a consequence of the *Pdzd8* mutation.

Pdzd8 mutation led to behavioural phenotypes, such as cognitive impairment, dysfunctional social recognition, and stereotypical behaviour, all of which were further supported by brain

structural or functional alterations. The phenotypes observed in *Pdzd8* are representative of mouse models of ID and ASD (Golden, Buxbaum and De Rubeis, 2018; Verma *et al.*, 2019). Therefore, *Pdzd8* mutant mice could constitute a model of ID.

4.2 Future directions

Despite the numerous behavioural, structural and functional alterations observed in *Pdzd8* mice compared to WT controls, there is still a big gap in understanding how all these changes are connected. I propose two distinct avenues to get a better understanding of how *Pdzd8* leads to ID.

Firstly, a molecular approach to gain more knowledge on the mechanisms and pathways involved in Pdzd8. Pdzd8 functions as a tether between the ER and the mitochondria and has been involved in the interaction with multiple organelles, which are essential for normal cellular function, maintenance, and survival (Hirabayashi *et al.*, 2017; Elbaz-Alon *et al.*, 2020; Shirane *et al.*, 2020; Gao *et al.*, 2022). Our qRT-PCR data revealed a multitude of genes upregulated following *Pdzd8* mutation. However, it is impossible to understand what upregulation in genes represents without looking at the full picture. Using RNA sequencing on *Pdzd8* mouse brains would offer a better idea of why some of these genes are upregulated or downregulated, and what mechanisms might be important in Pdzd8 regulation.

Secondly, an *in vivo* brain imaging approach coupled with simultaneous behavioural testing to understand how disruptions in neural activity might be related to learning, memory and social discrimination changes recorded in *Pdzd8* mice. One of the most intriguing aspects in neuroscience research is how brain activity modulations can directly cause changes in behaviour. *Pdzd8* mice displayed both altered neural activity and behaviour. The advent of multiphoton microscopy and development of chronic imaging now allow for examining

neural activity during behavioural paradigms in real time. Neural activity in the frontal association cortex, olfactory bulbs, or even the hippocampus, using deep tissue imaging methods (Streich *et al.*, 2021), could allow for understanding of role these changes observed in neural activity in *Pdzd8* mice play in behavioural output.

4.3 Overall conclusion

This study investigated the effects of a frameshift mutation in *Pdzd8* gene in mice and its role in ID. The cellular function of Pdzd8 has only been elucidated around 5 years ago. Since then, a multitude of papers have been trying to decipher the molecular interactions of Pdzd8. However, together with our collaborators, we are the first to link *PDZD8* dysregulation with a human disease, namely ID (Al-Amri *et al.*, 2022).

My study contributed to gaining a more in depth understanding of the role of *Pdzd8* in the brain and the behavioural consequences of a *Pdzd8* mutation. I have showed that *Pdzd8* mutation leads to ID in mice, along with other symptoms which are characteristic for ID disorders. There are still many questions regarding how Pdzd8 function normally and how its disruption causes ID across species. However, this study brings us a step closer to understanding the complexity of ID and offers new insight into the role of *Pdzd8* in mice.

V. References

Abrous, D. N. and Wojtowicz, J. M. (2015) 'Interaction between neurogenesis and hippocampal memory system: new vistas', *Cold Spring Harbor perspectives in biology,* 7(6), pp. a018952.

Adhikari, A. (2014) 'Distributed circuits underlying anxiety', *Frontiers in behavioral neuroscience,* 8, pp. 112.

Al-Amri, A. H., Armstrong, P., Amici, M., Ligneul, C., Rouse, J., El-Asrag, M. E., Pantiru, A. D., Vancollie, V. E., Ng, H. W., Ogbeta, J. A., Goodchild, K., Ellegood, J., Lelliott, C. J., Mullins, J. G. L., Bretman, A., Al-Ali, R., Beetz, C., Al-Gazali, L., Al Shamsi, A., Lerch, J. P., Mellor, J. R., Al Sayegh, A., Ali, M., Inglehearn, C. F. and Clapcote, S. J. (2022) 'PDZD8 Disruption Causes Cognitive Impairment in Humans, Mice and Fruit Flies', *Biological Psychiatry*.

Alemany-González, M., Gener, T., Nebot, P., Vilademunt, M., Dierssen, M. and Puig, M. V. (2020) 'Prefrontal–hippocampal functional connectivity encodes recognition memory and is impaired in intellectual disability', *Proceedings of the National Academy of Sciences,* 117(21), pp. 11788-11798.

Ali, F., Shao, L.-X., Gerhard, D. M., Sweasy, K., Pothula, S., Pittenger, C., Duman, R. S. and Kwan, A. C. (2021) 'Inhibitory regulation of calcium transients in prefrontal dendritic spines is compromised by a nonsense Shank3 mutation', *Molecular psychiatry,* 26(6), pp. 1945-1966.

Allegra, M., Spalletti, C., Vignoli, B., Azzimondi, S., Busti, I., Billuart, P., Canossa, M. and Caleo, M. (2017) 'Pharmacological rescue of adult hippocampal neurogenesis in a mouse model of X-linked intellectual disability', *Neurobiology of Disease,* 100, pp. 75-86.

Alvarez-Buylla, A. and Garcıa-Verdugo, J. M. (2002) 'Neurogenesis in adult subventricular zone', *Journal of Neuroscience,* 22(3), pp. 629-634.

American Psychiatric Association (2013) *Diagnostic and statistical manual of mental disorders (DSM-5®).* American Psychiatric Pub.

Antoine, M. W., Langberg, T., Schnepel, P. and Feldman, D. E. (2019) 'Increased excitation-inhibition ratio stabilizes synapse and circuit excitability in four autism mouse models', *Neuron,* 101(4), pp. 648-661. e4.

Armario, A. (2021) 'The forced swim test: Historical, conceptual and methodological considerations and its relationship with individual behavioral traits', *Neuroscience & Biobehavioral Reviews,* 128, pp. 74-86.

Bagni, C., Tassone, F., Neri, G. and Hagerman, R. (2012) 'Fragile X syndrome: causes, diagnosis, mechanisms, and therapeutics', *The Journal of clinical investigation,* 122(12), pp. 4314-4322.

Bakken, T. E., Jorstad, N. L., Hu, Q., Lake, B. B., Tian, W., Kalmbach, B. E., Crow, M., Hodge, R. D., Krienen, F. M. and Sorensen, S. A. (2021) 'Comparative cellular analysis of motor cortex in human, marmoset and mouse', *Nature,* 598(7879), pp. 111-119.

Banker, S. M., Gu, X., Schiller, D. and Foss-Feig, J. H. (2021) 'Hippocampal contributions to social and cognitive deficits in autism spectrum disorder', *Trends in neurosciences,* 44(10), pp. 793-807.

Barnes, C. A. (1979) 'Memory deficits associated with senescence: a neurophysiological and behavioral study in the rat', *Journal of comparative and physiological psychology,* 93(1), pp. 74.

Barthas, F. and Kwan, A. C. (2017) 'Secondary motor cortex: where 'sensory'meets 'motor'in the rodent frontal cortex', *Trends in neurosciences,* 40(3), pp. 181-193.

Bear, D. M., Lassance, J.-M., Hoekstra, H. E. and Datta, S. R. (2016) 'The evolving neural and genetic architecture of vertebrate olfaction', *Current Biology,* 26(20), pp. R1039-R1049.

Bekkers, J. M. and Suzuki, N. (2013) 'Neurons and circuits for odor processing in the piriform cortex', *Trends in neurosciences,* 36(7), pp. 429-438.

Bernhard, W. and Rouiller, C. (1956) 'Close topographical relationship between mitochondria and ergastoplasm of liver cells in a definite phase of cellular activity', *J Biophys Biochem Cytol,* 2(4 Suppl), pp. 73-8.

Bodaleo, F., Tapia-Monsalves, C., Cea-Del Rio, C., Gonzalez-Billault, C. and Nunez-Parra, A. (2019) 'Structural and functional abnormalities in the olfactory system of fragile X syndrome models', *Frontiers in Molecular Neuroscience,* 12, pp. 135.

Bourin, M. and Hascoët, M. (2003) 'The mouse light/dark box test', *European journal of pharmacology,* 463(1-3), pp. 55-65.

Burnette, W. N. (1981) '"Western blotting": electrophoretic transfer of proteins from sodium dodecyl sulfate-polyacrylamide gels to unmodified nitrocellulose and radiographic detection with antibody and radioiodinated protein A', *Analytical biochemistry,* 112(2), pp. 195-203.

Caglayan, A. O., Comu, S., Baranoski, J. F., Parman, Y., Kaymakçalan, H., Akgumus, G. T., Caglar, C., Dolen, D., Erson-Omay, E. Z. and Harmanci, A. S. (2015) 'NGLY1 mutation causes neuromotor impairment, intellectual disability, and neuropathy', *European journal of medical genetics,* 58(1), pp. 39-43.

Caldeira, G., Inácio, A., Beltrão, N., Barreto, C., Rodrigues, M., Rondão, T., Macedo, R., Gouveia, R., Edfawy, M. and Guedes, J. (2022) 'Aberrant hippocampal transmission and

behavior in mice with a stargazin mutation linked to intellectual disability', *Molecular Psychiatry*, pp. 1-13.

Can, A., Dao, D. T., Arad, M., Terrillion, C. E., Piantadosi, S. C. and Gould, T. D. (2012) 'The mouse forced swim test', *JoVE (Journal of Visualized Experiments),* (59), pp. e3638.

Canitano, R. and Palumbi, R. (2021) 'Excitation/inhibition modulators in autism spectrum disorder: Current clinical research', *Frontiers in Neuroscience,* 15.

Cardanho-Ramos, C., Faria-Pereira, A. and Morais, V. A. (2020) 'Orchestrating mitochondria in neurons: Cytoskeleton as the conductor', *Cytoskeleton,* 77(3-4), pp. 65-75.

Castillon, C., Gonzalez, L., Domenichini, F., Guyon, S., Da Silva, K., Durand, C., Lestaevel, P., Vaillend, C., Laroche, S. and Barnier, J.-V. (2020) 'The intellectual disability PAK3 R67C mutation impacts cognitive functions and adult hippocampal neurogenesis', *Human Molecular Genetics,* 29(12), pp. 1950-1968.

Castillon, C., Lunion, S., Desvignes, N., Hanauer, A., Laroche, S. and Poirier, R. (2018) 'Selective alteration of adult hippocampal neurogenesis and impaired spatial pattern separation performance in the RSK2-deficient mouse model of Coffin-Lowry syndrome', *Neurobiology of disease,* 115, pp. 69-81.

Chen, P. and Hong, W. (2018) 'Neural circuit mechanisms of social behavior', *Neuron,* 98(1), pp. 16-30.

Chen, T., Lu, J.-S., Song, Q., Liu, M.-G., Koga, K., Descalzi, G., Li, Y.-Q. and Zhuo, M. (2014) 'Pharmacological rescue of cortical synaptic and network potentiation in a mouse model for fragile X syndrome', *Neuropsychopharmacology,* 39(8), pp. 1955-1967.

Chiurazzi, P., Kiani, A. K., Miertus, J., Barati, S., Manara, E., Paolacci, S., Stuppia, L., Gurrieri, F. and Bertelli, M. (2020) 'Genetic analysis of intellectual disability and autism', *Acta Bio Medica: Atenei Parmensis,* 91(Suppl 13).

Cockerham, R. E., Margolis, F. L. and Munger, S. D. (2009) 'Afferent activity to necklace glomeruli is dependent on external stimuli', *BMC research notes,* 2(1), pp. 1-5.

Coe, B. P., Witherspoon, K., Rosenfeld, J. A., Van Bon, B. W., Vulto-van Silfhout, A. T., Bosco, P., Friend, K. L., Baker, C., Buono, S. and Vissers, L. E. (2014) 'Refining analyses of copy number variation identifies specific genes associated with developmental delay', *Nature genetics,* 46(10), pp. 1063-1071.

Corbit, V. L., Manning, E. E., Gittis, A. H. and Ahmari, S. E. (2019) 'Strengthened inputs from secondary motor cortex to striatum in a mouse model of compulsive behavior', *Journal of Neuroscience,* 39(15), pp. 2965-2975.

Cox, W. H. (1891) 'Imprägnation des centralen Nervensystems mit Quecksilbersalzen', *Archiv für mikroskopische Anatomie,* 37(1), pp. 16-21.

Crawley, J. N. (2007) 'Mouse behavioral assays relevant to the symptoms of autism', *Brain pathology,* 17(4), pp. 448-459.

D'Angelo, D., Lebon, S., Chen, Q., Martin-Brevet, S., Snyder, L. G., Hippolyte, L., Hanson, E., Maillard, A. M., Faucett, W. A. and Macé, A. (2016) 'Defining the effect of the 16p11. 2 duplication on cognition, behavior, and medical comorbidities', *JAMA psychiatry,* 73(1), pp. 20-30.

Dana, H., Chen, T.-W., Hu, A., Shields, B. C., Guo, C., Looger, L. L., Kim, D. S. and Svoboda, K. (2014) 'Thy1-GCaMP6 transgenic mice for neuronal population imaging in vivo', *PloS one,* 9(9), pp. e108697.

Díaz, F. C., Caffino, L. and Fumagalli, F. (2021) 'Bidirectional role of dopamine in learning and memory-active forgetting', *Neuroscience & Biobehavioral Reviews,* 131, pp. 953-963.

Dixit, P. V., Sahu, R. and Mishra, D. K. (2020) 'Marble-burying behavior test as a murine model of compulsive-like behavior', *Journal of Pharmacological and Toxicological Methods,* 102, pp. 106676.

Dixsaut, L. and Gräff, J. (2021) 'The Medial Prefrontal Cortex and Fear Memory: Dynamics, Connectivity, and Engrams', *International Journal of Molecular Sciences,* 22(22), pp. 12113.

Dobyns, W. B. and Mirzaa, G. M. 'Megalencephaly syndromes associated with mutations of core components of the PI3K-AKT–MTOR pathway: PIK3CA, PIK3R2, AKT3, and MTOR'. *American journal of medical genetics part C: Seminars in medical genetics*: Wiley Online Library, 582-590.

Dölen, G., Osterweil, E., Rao, B. S., Smith, G. B., Auerbach, B. D., Chattarji, S. and Bear, M. F. (2007) 'Correction of fragile X syndrome in mice', *Neuron,* 56(6), pp. 955-962.

Duvarci, S. and Pare, D. (2014) 'Amygdala microcircuits controlling learned fear', *Neuron,* 82(5), pp. 966-980.

Elbaz-Alon, Y., Guo, Y., Segev, N., Harel, M., Quinnell, D. E., Geiger, T., Avinoam, O., Li, D. and Nunnari, J. (2020) 'PDZD8 interacts with Protrudin and Rab7 at ER-late endosome membrane contact sites associated with mitochondria', *Nature communications,* 11(1), pp. 1-14.

Felix-Ortiz, A. C., Burgos-Robles, A., Bhagat, N. D., Leppla, C. A. and Tye, K. M. (2016) 'Bidirectional modulation of anxiety-related and social behaviors by amygdala projections to the medial prefrontal cortex', *Neuroscience,* 321, pp. 197-209.

Fernández, M., Mollinedo-Gajate, I. and Peñagarikano, O. (2018) 'Neural circuits for social cognition: implications for autism', *Neuroscience,* 370, pp. 148-162.

Ferri, S. L., Abel, T. and Brodkin, E. S. (2018) 'Sex differences in autism spectrum disorder: a review', *Current psychiatry reports,* 20(2), pp. 1-17.

Fiala, J. C., Feinberg, M., Popov, V. and Harris, K. M. (1998) 'Synaptogenesis via dendritic filopodia in developing hippocampal area CA1', *Journal of Neuroscience,* 18(21), pp. 8900-8911.

Figueiredo, T., Mendes, A. P., Moreira, D. P., Goulart, E., Oliveira, D., Kobayashi, G. S., Stern, S., Kok, F., Marchetto, M. C. and Santos, R. (2021) 'Inositol monophosphatase 1 (IMPA1) mutation in intellectual disability patients impairs neurogenesis but not gliogenesis', *Molecular Psychiatry,* 26(7), pp. 3558-3571.

Gage, F. H. (2000) 'Mammalian neural stem cells', *Science,* 287(5457), pp. 1433-1438.

Gandhi, T. and Lee, C. C. (2021) 'Neural mechanisms underlying repetitive behaviors in rodent models of autism spectrum disorders', *Frontiers in Cellular Neuroscience*, pp. 463.

Gangopadhyay, P., Chawla, M., Dal Monte, O. and Chang, S. W. (2021) 'Prefrontal–amygdala circuits in social decision-making', *Nature neuroscience,* 24(1), pp. 5-18.

Gao, Y., Xiong, J., Chu, Q.-Z. and Ji, W.-K. (2022) 'PDZD8-mediated lipid transfer at contacts between the ER and late endosomes/lysosomes is required for neurite outgrowth', *Journal of cell science,* 135(5), pp. jcs255026.

Garrido, D., Beretta, S., Grabrucker, S., Bauer, H. F., Bayer, D., Sala, C., Verpelli, C., Roselli, F., Bockmann, J. and Proepper, C. (2022) 'Shank2/3 double knockout-based screening of cortical subregions links the retrosplenial area to the loss of social memory in autism spectrum disorders', *Molecular Psychiatry*, pp. 1-13.

George, H., Bashir, Z. I. and Hussain, S. (2022) 'Impaired hippocampal NMDAR-LTP in a transgenic model of NSUN2-deficiency', *Neurobiology of disease,* 163, pp. 105597.

Giacomello, M., Pyakurel, A., Glytsou, C. and Scorrano, L. (2020) 'The cell biology of mitochondrial membrane dynamics', *Nature reviews Molecular cell biology,* 21(4), pp. 204-224.

Golden, C. E., Buxbaum, J. D. and De Rubeis, S. (2018) 'Disrupted circuits in mouse models of autism spectrum disorder and intellectual disability', *Current opinion in neurobiology,* 48, pp. 106-112.

Goldenthal, M. J., Damle, S., Sheth, S., Shah, N., Melvin, J., Jethva, R., Hardison, H., Marks, H. and Legido, A. (2015) 'Mitochondrial enzyme dysfunction in autism spectrum disorders; a novel biomarker revealed from buccal swab analysis', *Biomarkers in medicine,* 9(10), pp. 957-965.

Golgi, C. (1873) 'Sulla sostanza grigia del cervello', *Gazetta Medica Italiana,* 33, pp. 244-246.

Greenberg, D. S., Houweling, A. R. and Kerr, J. N. (2008) 'Population imaging of ongoing neuronal activity in the visual cortex of awake rats', *Nature neuroscience,* 11(7), pp. 749-751.

Guillén-Samander, A., Bian, X. and De Camilli, P. (2019) 'PDZD8 mediates a Rab7-dependent interaction of the ER with late endosomes and lysosomes', *Proceedings of the National Academy of Sciences,* 116(45), pp. 22619-22623.

Guo, X., Hamilton, P. J., Reish, N. J., Sweatt, J. D., Miller, C. A. and Rumbaugh, G. (2009) 'Reduced expression of the NMDA receptor-interacting protein SynGAP causes behavioral

abnormalities that model symptoms of Schizophrenia', *Neuropsychopharmacology,* 34(7), pp. 1659-1672.

Han, C., O'Tuathaigh, C. M., van Trigt, L., Quinn, J. J., Fanselow, M. S., Mongeau, R., Koch, C. and Anderson, D. J. (2003) 'Trace but not delay fear conditioning requires attention and the anterior cingulate cortex', *Proceedings of the National Academy of Sciences,* 100(22), pp. 13087-13092.

Helverschou, S. B. and Martinsen, H. (2011) 'Anxiety in people diagnosed with autism and intellectual disability: Recognition and phenomenology', *Research in Autism Spectrum Disorders,* 5(1), pp. 377-387.

Hewitt, V. L., Miller-Fleming, L., Andreazza, S., Mattedi, F., Prudent, J., Polleux, F., Vagnoni, A. and Whitworth, A. J. (2020) 'Decreasing pdzd8-mediated mitochondrial-ER contacts in neurons improves fitness by increasing mitophagy', *bioRxiv*.

Hirabayashi, Y., Kwon, S.-K., Paek, H., Pernice, W. M., Paul, M. A., Lee, J., Erfani, P., Raczkowski, A., Petrey, D. S. and Pon, L. A. (2017) 'ER-mitochondria tethering by PDZD8 regulates Ca2+ dynamics in mammalian neurons', *Science,* 358(6363), pp. 623-630.

Hisaoka, T., Komori, T., Kitamura, T. and Morikawa, Y. (2018) 'Abnormal behaviours relevant to neurodevelopmental disorders in Kirrel3-knockout mice', *Scientific reports,* 8(1), pp. 1-12.

Ho, V. M., Lee, J.-A. and Martin, K. C. (2011) 'The cell biology of synaptic plasticity', *Science,* 334(6056), pp. 623-628.

Holtmaat, A., Bonhoeffer, T., Chow, D. K., Chuckowree, J., De Paola, V., Hofer, S. B., Hübener, M., Keck, T., Knott, G. and Lee, W.-C. A. (2009) 'Long-term, high-resolution

imaging in the mouse neocortex through a chronic cranial window', *Nature protocols,* 4(8), pp. 1128-1144.

Honeycutt, A., Dunlap, L., Chen, H. and Homsi, G. (2004) 'Economic costs associated with mental retardation, cerebral palsy, hearing loss, and vision impairment-United States, 2003', *MMWR: Morbidity & Mortality Weekly Report,* 53(3), pp. 57-57.

Houlden, H., King, R. H., Muddle, J. R., Warner, T. T., Reilly, M. M., Orrell, R. W. and Ginsberg, L. (2004) 'A novel RAB7 mutation associated with ulcero-mutilating neuropathy', *Annals of Neurology: Official Journal of the American Neurological Association and the Child Neurology Society,* 56(4), pp. 586-590.

Hruska, M., Henderson, N., Le Marchand, S. J., Jafri, H. and Dalva, M. B. (2018) 'Synaptic nanomodules underlie the organization and plasticity of spine synapses', *Nat Neurosci,* 21(5), pp. 671-682.

Illouz, T., Madar, R., Clague, C., Griffioen, K. J., Louzoun, Y. and Okun, E. (2016) 'Unbiased classification of spatial strategies in the Barnes maze', *Bioinformatics,* 32(21), pp. 3314-3320.

Ishikawa, A. and Nakamura, S. (2006) 'Ventral hippocampal neurons project axons simultaneously to the medial prefrontal cortex and amygdala in the rat', *Journal of neurophysiology,* 96(4), pp. 2134-2138.

Izquierdo, A. and Jentsch, J. D. (2012) 'Reversal learning as a measure of impulsive and compulsive behavior in addictions', *Psychopharmacology,* 219(2), pp. 607-620.

Jennings, J. H., Kim, C. K., Marshel, J. H., Raffiee, M., Ye, L., Quirin, S., Pak, S., Ramakrishnan, C. and Deisseroth, K. (2019) 'Interacting neural ensembles in orbitofrontal cortex for social and feeding behaviour', *Nature,* 565(7741), pp. 645-649.

Jeyabalan, N. and Clement, J. P. (2016) 'SYNGAP1: mind the gap', *Frontiers in Cellular Neuroscience,* 10, pp. 32.

Jeyasimman, D., Ercan, B., Dharmawan, D., Naito, T., Sun, J. and Saheki, Y. (2021) 'PDZD-8 and TEX-2 regulate endosomal PI (4, 5) P2 homeostasis via lipid transport to promote embryogenesis in C. elegans', *Nature Communications,* 12(1), pp. 1-21.

Jiang, M., Polepalli, J., Chen, L. Y., Zhang, B., Südhof, T. C. and Malenka, R. C. (2017) 'Conditional ablation of neuroligin-1 in CA1 pyramidal neurons blocks LTP by a cell-autonomous NMDA receptor-independent mechanism', *Molecular psychiatry,* 22(3), pp. 375-383.

Joshi, M. and Deshpande, J. (2010) 'Polymerase chain reaction: methods, principles and application', *International Journal of Biomedical Research,* 2(1), pp. 81-97.

Kalish, H. I. (1954) 'Strength of fear as a function of the number of acquisition and extinction trials', *Journal of experimental psychology,* 47(1), pp. 1.

Karvat, G. and Kimchi, T. (2012) 'Systematic autistic-like behavioral phenotyping of 4 mouse strains using a novel wheel-running assay', *Behavioural brain research,* 233(2), pp. 405-414.

Kasai, H., Ziv, N. E., Okazaki, H., Yagishita, S. and Toyoizumi, T. (2021) 'Spine dynamics in the brain, mental disorders and artificial neural networks', *Nature Reviews Neuroscience,* 22(7), pp. 407-422.

Kaufmann, W. E. and Moser, H. W. (2000) 'Dendritic anomalies in disorders associated with mental retardation', *Cerebral cortex,* 10(10), pp. 981-991.

Khan, H., Chen, L., Tan, L. and Im, Y. J. (2021) 'Structural basis of human PDZD8–Rab7 interaction for the ER-late endosome tethering', *Scientific reports,* 11(1), pp. 1-9.

Kim, H., Lim, C.-S. and Kaang, B.-K. (2016) 'Neuronal mechanisms and circuits underlying repetitive behaviors in mouse models of autism spectrum disorder', *Behavioral and Brain Functions,* 12(1), pp. 1-13.

Kim, W. B. and Cho, J.-H. (2017) 'Synaptic targeting of double-projecting ventral CA1 hippocampal neurons to the medial prefrontal cortex and basal amygdala', *Journal of Neuroscience,* 37(19), pp. 4868-4882.

Kingsbury, L., Huang, S., Wang, J., Gu, K., Golshani, P., Wu, Y. E. and Hong, W. (2019) 'Correlated neural activity and encoding of behavior across brains of socially interacting animals', *Cell,* 178(2), pp. 429-446. e16.

Kitamura, T., Ogawa, S. K., Roy, D. S., Okuyama, T., Morrissey, M. D., Smith, L. M., Redondo, R. L. and Tonegawa, S. (2017) 'Engrams and circuits crucial for systems consolidation of a memory', *Science,* 356(6333), pp. 73-78.

Kleele, T., Rey, T., Winter, J., Zaganelli, S., Mahecic, D., Perreten Lambert, H., Ruberto, F. P., Nemir, M., Wai, T. and Pedrazzini, T. (2021) 'Distinct fission signatures predict mitochondrial degradation or biogenesis', *Nature,* 593(7859), pp. 435-439.

Klein, I.-L., van de Loo, K. F., Smeitink, J. A., Janssen, M. C., Kessels, R. P., van Karnebeek, C. D., van der Veer, E., Custers, J. A. and Verhaak, C. M. (2021) 'Cognitive functioning and mental health in mitochondrial disease: A systematic scoping review', *Neuroscience & Biobehavioral Reviews,* 125, pp. 57-77.

Kochinke, K., Zweier, C., Nijhof, B., Fenckova, M., Cizek, P., Honti, F., Keerthikumar, S., Oortveld, M. A., Kleefstra, T. and Kramer, J. M. (2016) 'Systematic phenomics analysis deconvolutes genes mutated in intellectual disability into biologically coherent modules', *The American Journal of Human Genetics,* 98(1), pp. 149-164.

Kol, A., Adamsky, A., Groysman, M., Kreisel, T., London, M. and Goshen, I. (2020) 'Astrocytes contribute to remote memory formation by modulating hippocampal–cortical communication during learning', *Nature neuroscience,* 23(10), pp. 1229-1239.

Kouskou, M., Thomson, D. M., Brett, R. R., Wheeler, L., Tate, R. J., Pratt, J. A. and Chamberlain, L. H. (2018) 'Disruption of the Zdhhc9 intellectual disability gene leads to behavioural abnormalities in a mouse model', *Experimental neurology,* 308, pp. 35-46.

Lacagnina, A. F., Brockway, E. T., Crovetti, C. R., Shue, F., McCarty, M. J., Sattler, K. P., Lim, S. C., Santos, S. L., Denny, C. A. and Drew, M. R. (2019) 'Distinct hippocampal engrams control extinction and relapse of fear memory', *Nat Neurosci,* 22(5), pp. 753-761.

Lai, C. S., Franke, T. F. and Gan, W. B. (2012) 'Opposite effects of fear conditioning and extinction on dendritic spine remodelling', *Nature,* 483(7387), pp. 87-91.

Leal-Galicia, P., Chávez-Hernández, M. E., Mata, F., Mata-Luévanos, J., Rodríguez-Serrano, L. M., Tapia-de-Jesús, A. and Buenrostro-Jáuregui, M. H. (2021) 'Adult neurogenesis: A story ranging from controversial new neurogenic areas and human adult neurogenesis to molecular regulation', *International journal of molecular sciences,* 22(21), pp. 11489.

Leblond, C. S., Nava, C., Polge, A., Gauthier, J., Huguet, G., Lumbroso, S., Giuliano, F., Stordeur, C., Depienne, C. and Mouzat, K. (2014) 'Meta-analysis of SHANK mutations in autism spectrum disorders: a gradient of severity in cognitive impairments', *PLoS genetics,* 10(9), pp. e1004580.

Lee, E., Rhim, I., Lee, J. W., Ghim, J.-W., Lee, S., Kim, E. and Jung, M. W. (2016) 'Enhanced neuronal activity in the medial prefrontal cortex during social approach behavior', *Journal of Neuroscience,* 36(26), pp. 6926-6936.

Lendvai, B., Stern, E. A., Chen, B. and Svoboda, K. (2000) 'Experience-dependent plasticity of dendritic spines in the developing rat barrel cortex in vivo', *Nature,* 404(6780), pp. 876-881.

Li, J., Jiang, R. Y., Arendt, K. L., Hsu, Y.-T., Zhai, S. R. and Chen, L. (2020) 'Defective memory engram reactivation underlies impaired fear memory recall in Fragile X syndrome', *Elife,* 9, pp. e61882.

Li, M., Long, C. and Yang, L. (2015) 'Hippocampal-prefrontal circuit and disrupted functional connectivity in psychiatric and neurodegenerative disorders', *BioMed research international,* 2015.

Liang, J., Xu, W., Hsu, Y., Yee, A., Chen, L. and Südhof, T. (2015) 'Conditional neuroligin-2 knockout in adult medial prefrontal cortex links chronic changes in synaptic inhibition to cognitive impairments', *Molecular psychiatry,* 20(7), pp. 850-859.

Liu, X., Salokas, K., Tamene, F., Jiu, Y., Weldatsadik, R. G., Öhman, T. and Varjosalo, M. (2018) 'An AP-MS-and BioID-compatible MAC-tag enables comprehensive mapping of protein interactions and subcellular localizations', *Nature communications,* 9(1), pp. 1-16.

Llamosas, N., Michaelson, S. D., Vaissiere, T., Rojas, C., Miller, C. A. and Rumbaugh, G. (2021) 'Syngap1 regulates experience-dependent cortical ensemble plasticity by promoting in vivo excitatory synapse strengthening', *Proceedings of the National Academy of Sciences,* 118(34).

Lombardi, L. M., Baker, S. A. and Zoghbi, H. Y. (2015) 'MECP2 disorders: from the clinic to mice and back', *The Journal of clinical investigation,* 125(8), pp. 2914-2923.

Lotta, L., Conrad, K., Cory-Slechta, D. and Schor, N. (2014) 'Cerebellar Purkinje cell p75 neurotrophin receptor and autistic behavior', *Translational psychiatry,* 4(7), pp. e416-e416.

Lu, Y., Fujioka, H., Joshi, D., Li, Q., Sangwung, P., Hsieh, P., Zhu, J., Torio, J., Sweet, D. and Wang, L. (2018) 'Mitophagy is required for brown adipose tissue mitochondrial homeostasis during cold challenge', *Scientific reports,* 8(1), pp. 1-13.

Mahmood, T. and Yang, P.-C. (2012) 'Western blot: technique, theory, and trouble shooting', *North American journal of medical sciences,* 4(9), pp. 429.

Mannan, A. U., Krawen, P., Sauter, S. M., Boehm, J., Chronowska, A., Paulus, W., Neesen, J. and Engel, W. (2006) 'ZFYVE27 (SPG33), a novel spastin-binding protein, is mutated in hereditary spastic paraplegia', *The American Journal of Human Genetics,* 79(2), pp. 351-357.

Maren, S. and Fanselow, M. S. (1996) 'The amygdala and fear conditioning: has the nut been cracked?', *Neuron,* 16(2), pp. 237-240.

Martin, H. G., Lassalle, O., Brown, J. T. and Manzoni, O. J. (2016) 'Age-dependent long-term potentiation deficits in the prefrontal cortex of the Fmr1 knockout mouse model of fragile X syndrome', *Cerebral cortex,* 26(5), pp. 2084-2092.

Matikainen-Ankney, B. A., Garmendia-Cedillos, M., Ali, M., Krynitsky, J., Salem, G., Miyazaki, N. L., Pohida, T. and Kravitz, A. V. (2019) 'Rodent activity detector (RAD), an open source device for measuring activity in rodent home cages', *Eneuro,* 6(4).

Mattson, M. P. (2010) 'Perspective: does brown fat protect against diseases of aging?', *Ageing research reviews,* 9(1), pp. 69-76.

Mignogna, M. L., Musardo, S., Ranieri, G., Gelmini, S., Espinosa, P., Marra, P., Belloli, S., Murtaj, V., Moresco, R. M. and Bellone, C. (2021) 'RAB39B-mediated trafficking of the GluA2-AMPAR subunit controls dendritic spine maturation and intellectual disability-related behaviour', *Molecular Psychiatry*, pp. 1-19.

Ming, G.-l. and Song, H. (2011) 'Adult neurogenesis in the mammalian brain: significant answers and significant questions', *Neuron,* 70(4), pp. 687-702.

Moltedo, O., Remondelli, P. and Amodio, G. (2019) 'The mitochondria–endoplasmic reticulum contacts and their critical role in aging and age-associated diseases', *Frontiers in cell and developmental biology,* 7, pp. 172.

Moreno-Jiménez, E. P., Flor-García, M., Terreros-Roncal, J., Rábano, A., Cafini, F., Pallas-Bazarra, N., Ávila, J. and Llorens-Martín, M. (2019) 'Adult hippocampal neurogenesis is abundant in neurologically healthy subjects and drops sharply in patients with Alzheimer's disease', *Nature medicine,* 25(4), pp. 554-560.

Mossa, A., Pagano, J., Ponzoni, L., Tozzi, A., Vezzoli, E., Sciaccaluga, M., Costa, C., Beretta, S., Francolini, M. and Sala, M. (2021) 'Developmental impaired Akt signaling in the Shank1 and Shank3 double knock-out mice', *Molecular psychiatry,* 26(6), pp. 1928-1944.

Muellerleile, J., Vnencak, M., Ippolito, A., Krueger-Burg, D., Jungenitz, T., Schwarzacher, S. W. and Jedlicka, P. (2022) 'Neuroligin-3 Regulates Excitatory Synaptic Transmission and EPSP-Spike Coupling in the Dentate Gyrus In Vivo', *Molecular neurobiology,* 59(2), pp. 1098-1111.

Nazari-Serenjeh, F., Rezayof, A. and Zarrindast, M.-R. (2011) 'Functional correlation between GABAergic and dopaminergic systems of dorsal hippocampus and ventral tegmental area in passive avoidance learning in rats', *Neuroscience,* 196, pp. 104-114.

Nelson, S. B. and Valakh, V. (2015) 'Excitatory/inhibitory balance and circuit homeostasis in autism spectrum disorders', *Neuron,* 87(4), pp. 684-698.

O'Hare, J. K., Hirabayashi, Y., Hewitt, V. L., Blockus, H., Szoboszlay, M., Rolotti, S. V., Geiller, T. C., Negrean, A., Chelur, V. and Losonczy, A. (2021) 'Compartment-specific tuning of hippocampal dendritic feature selectivity by intracellular Ca2+ release', *bioRxiv*.

O'Leary, C., Leonard, H., Bourke, J., D'ANTOINE, H., Bartu, A. and Bower, C. (2013) 'Intellectual disability: population-based estimates of the proportion attributable to maternal alcohol use disorder during pregnancy', *Developmental Medicine & Child Neurology,* 55(3), pp. 271-277.

Oláhová, M., Peter, B., Szilagyi, Z., Diaz-Maldonado, H., Singh, M., Sommerville, E. W., Blakely, E. L., Collier, J. J., Hoberg, E. and Stránecký, V. (2021) 'POLRMT mutations impair mitochondrial transcription causing neurological disease', *Nature communications,* 12(1), pp. 1-13.

Pachitariu, M., Stringer, C., Dipoppa, M., Schröder, S., Rossi, L. F., Dalgleish, H., Carandini, M. and Harris, K. D. (2017) 'Suite2p: beyond 10,000 neurons with standard two-photon microscopy', *BioRxiv*, pp. 061507.

Paolicelli, R. C., Bolasco, G., Pagani, F., Maggi, L., Scianni, M., Panzanelli, P., Giustetto, M., Ferreira, T. A., Guiducci, E. and Dumas, L. (2011) 'Synaptic pruning by microglia is necessary for normal brain development', *science,* 333(6048), pp. 1456-1458.

Pashkovski, S. L., Iurilli, G., Brann, D., Chicharro, D., Drummey, K., Franks, K. M., Panzeri, S. and Datta, S. R. (2020) 'Structure and flexibility in cortical representations of odour space', *Nature,* 583(7815), pp. 253-258.

Porsolt, R. D., Anton, G., Blavet, N. and Jalfre, M. (1978) 'Behavioural despair in rats: a new model sensitive to antidepressant treatments', *European journal of pharmacology,* 47(4), pp. 379-391.

Port, R. G., Oberman, L. M. and Roberts, T. P. (2019) 'Revisiting the excitation/inhibition imbalance hypothesis of ASD through a clinical lens', *The British journal of radiology,* 92(1101), pp. 20180944.

Qiu, Q., Scott, A., Scheerer, H., Sapkota, N., Lee, D. K., Ma, L. and Yu, C. R. (2014) 'Automated analyses of innate olfactory behaviors in rodents', *PLoS One,* 9(4), pp. e93468.

Rahman, M. T., Uddin, M. S., Sultana, R., Moue, A. and Setu, M. (2013) 'Polymerase chain reaction (PCR): a short review', *Anwer Khan Modern Medical College Journal,* 4(1), pp. 30-36.

Raiborg, C., Wenzel, E. M. and Stenmark, H. (2015) 'ER–endosome contact sites: molecular compositions and functions', *The EMBO journal,* 34(14), pp. 1848-1858.

Rajasethupathy, P., Sankaran, S., Marshel, J. H., Kim, C. K., Ferenczi, E., Lee, S. Y., Berndt, A., Ramakrishnan, C., Jaffe, A. and Lo, M. (2015) 'Projections from neocortex mediate top-down control of memory retrieval', *Nature,* 526(7575), pp. 653-659.

Ramanathan, K. R., Jin, J., Giustino, T. F., Payne, M. R. and Maren, S. (2018) 'Prefrontal projections to the thalamic nucleus reuniens mediate fear extinction', *Nature communications,* 9(1), pp. 1-12.

Rao, M. S. and Shetty, A. K. (2004) 'Efficacy of doublecortin as a marker to analyse the absolute number anddendritic growth of newly generated neurons in the adult dentate gyrus', *European Journal of Neuroscience,* 19(2), pp. 234-246.

Reh, R. K., Dias, B. G., Nelson III, C. A., Kaufer, D., Werker, J. F., Kolb, B., Levine, J. D. and Hensch, T. K. (2020) 'Critical period regulation across multiple timescales', *Proceedings of the National Academy of Sciences,* 117(38), pp. 23242-23251.

Reijnders, M. R., Kousi, M., Van Woerden, G., Klein, M., Bralten, J., Mancini, G., van Essen, T., Proietti-Onori, M., Smeets, E. E. and Van Gastel, M. (2017) 'Variation in a range of mTOR-related genes associates with intracranial volume and intellectual disability', *Nature communications,* 8(1), pp. 1-12.

Rein, B. and Yan, Z. (2020) '16p11. 2 copy number variations and neurodevelopmental disorders', *Trends in Neurosciences,* 43(11), pp. 886-901.

Rubenstein, J. and Merzenich, M. M. (2003) 'Model of autism: increased ratio of excitation/inhibition in key neural systems', *Genes, Brain and Behavior,* 2(5), pp. 255-267.

Ryan, B. C., Young, N. B., Moy, S. S. and Crawley, J. N. (2008) 'Olfactory cues are sufficient to elicit social approach behaviors but not social transmission of food preference in C57BL/6J mice', *Behavioural brain research,* 193(2), pp. 235-242.

Salic, A. and Mitchison, T. J. (2008) 'A chemical method for fast and sensitive detection of DNA synthesis in vivo', *Proceedings of the National Academy of Sciences,* 105(7), pp. 2415-2420.

Schroeder, L. K., Barentine, A. E., Merta, H., Schweighofer, S., Zhang, Y., Baddeley, D., Bewersdorf, J. and Bahmanyar, S. (2019) 'Dynamic nanoscale morphology of the ER surveyed by STED microscopy', *Journal of Cell Biology,* 218(1), pp. 83-96.

Schwarz, D. S. and Blower, M. D. (2016) 'The endoplasmic reticulum: structure, function and response to cellular signaling', *Cellular and molecular life sciences,* 73(1), pp. 79-94.

Shirane, M., Wada, M., Morita, K., Hayashi, N., Kunimatsu, R., Matsumoto, Y., Matsuzaki, F., Nakatsumi, H., Ohta, K. and Tamura, Y. (2020) 'Protrudin and PDZD8 contribute to neuronal integrity by promoting lipid extraction required for endosome maturation', *Nature communications,* 11(1), pp. 1-19.

Sigurdsson, T. and Duvarci, S. (2016) 'Hippocampal-prefrontal interactions in cognition, behavior and psychiatric disease', *Frontiers in systems neuroscience,* 9, pp. 190.

Silverman, J. L., Yang, M., Lord, C. and Crawley, J. N. (2010) 'Behavioural phenotyping assays for mouse models of autism', *Nature Reviews Neuroscience,* 11(7), pp. 490-502.

Skopkova, M., Hennig, F., Shin, B. S., Turner, C. E., Stanikova, D., Brennerova, K., Stanik, J., Fischer, U., Henden, L. and Müller, U. (2017) 'EIF2S3 mutations associated with severe X-linked intellectual disability syndrome MEHMO', *Human mutation,* 38(4), pp. 409-425.

Song, S., Pursell, Z. F., Copeland, W. C., Longley, M. J., Kunkel, T. A. and Mathews, C. K. (2005) 'DNA precursor asymmetries in mammalian tissue mitochondria and possible contribution to mutagenesis through reduced replication fidelity', *Proceedings of the National Academy of Sciences,* 102(14), pp. 4990-4995.

Southwell, D. G., Seifikar, H., Malik, R., Lavi, K., Vogt, D., Rubenstein, J. L. and Sohal, V. S. (2020) 'Interneuron transplantation rescues social behavior deficits without restoring wild-type physiology in a mouse model of autism with excessive synaptic inhibition', *Journal of Neuroscience,* 40(11), pp. 2215-2227.

Srivastava, A. K. and Schwartz, C. E. (2014) 'Intellectual disability and autism spectrum disorders: causal genes and molecular mechanisms', *Neuroscience & Biobehavioral Reviews,* 46, pp. 161-174.

Stoodley, C. J. (2016) 'The cerebellum and neurodevelopmental disorders', *The Cerebellum,* 15(1), pp. 34-37.

Streich, L., Boffi, J. C., Wang, L., Alhalaseh, K., Barbieri, M., Rehm, R., Deivasigamani, S., Gross, C. T., Agarwal, A. and Prevedel, R. (2021) 'High-resolution structural and functional

deep brain imaging using adaptive optics three-photon microscopy', *Nature methods,* 18(10), pp. 1253-1258.

Stringer, C. and Pachitariu, M. (2022) 'Cellpose 2.0: how to train your own model', *bioRxiv*.

Supek, F., Lehner, B. and Lindeboom, R. G. H. (2021) 'To NMD or Not To NMD: Nonsense-Mediated mRNA Decay in Cancer and Other Genetic Diseases', *Trends Genet,* 37(7), pp. 657-668.

Svoboda, K. and Yasuda, R. (2006) 'Principles of two-photon excitation microscopy and its applications to neuroscience', *Neuron,* 50(6), pp. 823-839.

Takechi, H., Eilers, J. and Konnerth, A. (1998) 'A new class of synaptic response involving calcium release in dendritic spines', *Nature,* 396(6713), pp. 757-760.

Thomas, A., Burant, A., Bui, N., Graham, D., Yuva-Paylor, L. A. and Paylor, R. (2009) 'Marble burying reflects a repetitive and perseverative behavior more than novelty-induced anxiety', *Psychopharmacology,* 204(2), pp. 361-373.

Tian, Y., Yang, C., Shang, S., Cai, Y., Deng, X., Zhang, J., Shao, F., Zhu, D., Liu, Y. and Chen, G. (2017) 'Loss of FMRP impaired hippocampal long-term plasticity and spatial learning in rats', *Frontiers in molecular neuroscience,* 10, pp. 269.

Towbin, H., Staehelin, T. and Gordon, J. (1979) 'Electrophoretic transfer of proteins from polyacrylamide gels to nitrocellulose sheets: procedure and some applications', *Proceedings of the national academy of sciences,* 76(9), pp. 4350-4354.

Uchino, S. and Waga, C. (2013) 'SHANK3 as an autism spectrum disorder-associated gene', *Brain and Development,* 35(2), pp. 106-110.

'UniProt', (2021) *Nucleic Acids Research,* 49(D1), pp. D480-D489.

Valenti, D., de Bari, L., De Filippis, B., Henrion-Caude, A. and Vacca, R. A. (2014) 'Mitochondrial dysfunction as a central actor in intellectual disability-related diseases: an overview of Down syndrome, autism, Fragile X and Rett syndrome', *Neuroscience & Biobehavioral Reviews,* 46, pp. 202-217.

Verhoeven, K., De Jonghe, P., Coen, K., Verpoorten, N., Auer-Grumbach, M., Kwon, J. M., FitzPatrick, D., Schmedding, E., De Vriendt, E. and Jacobs, A. (2003) 'Mutations in the small GTP-ase late endosomal protein RAB7 cause Charcot-Marie-Tooth type 2B neuropathy', *The American Journal of Human Genetics,* 72(3), pp. 722-727.

Verma, V., Paul, A., Amrapali Vishwanath, A., Vaidya, B. and Clement, J. P. (2019) 'Understanding intellectual disability and autism spectrum disorders from common mouse models: synapses to behaviour', *Open biology,* 9(6), pp. 180265.

Vicari, S., Costanzo, F. and Menghini, D. (2016) 'Memory and learning in intellectual disability', *International review of research in developmental disabilities*: Elsevier, pp. 119-148.

Vissers, L. E., Gilissen, C. and Veltman, J. A. (2016) 'Genetic studies in intellectual disability and related disorders', *Nature Reviews Genetics,* 17(1), pp. 9-18.

Walsh, R. N. and Cummins, R. A. (1976) 'The open-field test: a critical review', *Psychological bulletin,* 83(3), pp. 482.

Wang, P. Y., Boboila, C., Chin, M., Higashi-Howard, A., Shamash, P., Wu, Z., Stein, N. P., Abbott, L. and Axel, R. (2020) 'Transient and persistent representations of odor value in prefrontal cortex', *Neuron,* 108(1), pp. 209-224. e6.

Wang, W., Rein, B., Zhang, F., Tan, T., Zhong, P., Qin, L. and Yan, Z. (2018) 'Chemogenetic activation of prefrontal cortex rescues synaptic and behavioral deficits in a mouse model of 16p11. 2 deletion syndrome', *Journal of Neuroscience,* 38(26), pp. 5939-5948.

Wang, X., Bey, A. L., Katz, B. M., Badea, A., Kim, N., David, L. K., Duffney, L. J., Kumar, S., Mague, S. D. and Hulbert, S. W. (2016) 'Altered mGluR5-Homer scaffolds and corticostriatal connectivity in a Shank3 complete knockout model of autism', *Nature communications,* 7(1), pp. 1-18.

Wei, D., Talwar, V. and Lin, D. (2021) 'Neural circuits of social behaviors: innate yet flexible', *Neuron,* 109(10), pp. 1600-1620.

Wesson, D. W., Donahou, T. N., Johnson, M. O. and Wachowiak, M. (2008) 'Sniffing behavior of mice during performance in odor-guided tasks', *Chemical senses,* 33(7), pp. 581-596.

Wideman, J. G., Balacco, D. L., Fieblinger, T. and Richards, T. A. (2018) 'PDZD8 is not the ‘functional ortholog’of Mmm1, it is a paralog', *F1000Research,* 7.

Wilkes, B. and Lewis, M. (2018) 'The neural circuitry of restricted repetitive behavior: Magnetic resonance imaging in neurodevelopmental disorders and animal models', *Neuroscience & Biobehavioral Reviews,* 92, pp. 152-171.

Wilson, B. C., Boehme, L., Annibali, A., Hodgkinson, A., Carroll, T. S., Oakey, R. J. and Seitan, V. C. (2020) 'Intellectual disability-associated factor Zbtb11 cooperates with NRF-2/GABP to control mitochondrial function', *Nature communications,* 11(1), pp. 1-20.

Wilson, E. L. and Metzakopian, E. (2021) 'ER-mitochondria contact sites in neurodegeneration: genetic screening approaches to investigate novel disease mechanisms', *Cell Death & Differentiation,* 28(6), pp. 1804-1821.

Won, H., Lee, H.-R., Gee, H. Y., Mah, W., Kim, J.-I., Lee, J., Ha, S., Chung, C., Jung, E. S. and Cho, Y. S. (2012) 'Autistic-like social behaviour in Shank2-mutant mice improved by restoring NMDA receptor function', *Nature,* 486(7402), pp. 261-265.

Wong, Y. C., Ysselstein, D. and Krainc, D. (2018) 'Mitochondria–lysosome contacts regulate mitochondrial fission via RAB7 GTP hydrolysis', *Nature,* 554(7692), pp. 382-386.

World Health Organization (1992) *The ICD-10 classification of mental and behavioural disorders: clinical descriptions and diagnostic guidelines.* World Health Organization.

Wu, H., Carvalho, P. and Voeltz, G. K. (2018) 'Here, there, and everywhere: The importance of ER membrane contact sites', *Science,* 361(6401).

Wu, X., Morishita, W. K., Riley, A. M., Hale, W. D., Südhof, T. C. and Malenka, R. C. (2019) 'Neuroligin-1 signaling controls LTP and NMDA receptors by distinct molecular pathways', *Neuron,* 102(3), pp. 621-635. e3.

Yang, H. K., Sundholm-Peters, N. L., Goings, G. E., Walker, A. S., Hyland, K. and Szele, F. G. (2004) 'Distribution of doublecortin expressing cells near the lateral ventricles in the adult mouse brain', *Journal of neuroscience research,* 76(3), pp. 282-295.

Yang, M., Bozdagi, O., Scattoni, M. L., Wöhr, M., Roullet, F. I., Katz, A. M., Abrams, D. N., Kalikhman, D., Simon, H. and Woldeyohannes, L. (2012) 'Reduced excitatory neurotransmission and mild autism-relevant phenotypes in adolescent Shank3 null mutant mice', *Journal of Neuroscience,* 32(19), pp. 6525-6541.

Yardeni, T., Cristancho, A. G., McCoy, A. J., Schaefer, P. M., McManus, M. J., Marsh, E. D. and Wallace, D. C. (2021) 'An mtDNA mutant mouse demonstrates that mitochondrial deficiency can result in autism endophenotypes', *Proceedings of the National Academy of Sciences,* 118(6), pp. e2021429118.

Yasin, H., Gibson, W. T., Langlois, S., Stowe, R. M., Tsang, E. S., Lee, L., Poon, J., Tran, G., Tyson, C. and Wong, C. K. (2019) 'A distinct neurodevelopmental syndrome with intellectual disability, autism spectrum disorder, characteristic facies, and macrocephaly is caused by defects in CHD8', *Journal of human genetics,* 64(4), pp. 271-280.

Yavas, E., Gonzalez, S. and Fanselow, M. S. (2019) 'Interactions between the hippocampus, prefrontal cortex, and amygdala support complex learning and memory', *F1000Research,* 8.

Yizhar, O., Fenno, L. E., Prigge, M., Schneider, F., Davidson, T. J., O'shea, D. J., Sohal, V. S., Goshen, I., Finkelstein, J. and Paz, J. T. (2011) 'Neocortical excitation/inhibition balance in information processing and social dysfunction', *Nature,* 477(7363), pp. 171-178.

Zaqout, S. and Kaindl, A. M. (2016) 'Golgi-Cox staining step by step', *Frontiers in neuroanatomy,* 10, pp. 38.

Zhang, C.-L., Houbaert, X., Lepleux, M., Deshors, M., Normand, E., Gambino, F., Herzog, E. and Humeau, Y. (2015) 'The hippocampo-amygdala control of contextual fear expression is affected in a model of intellectual disability', *Brain Structure and Function,* 220(6), pp. 3673-3682.

Zhang, W., Ma, L., Yang, M., Shao, Q., Xu, J., Lu, Z., Zhao, Z., Chen, R., Chai, Y. and Chen, J.-F. (2020) 'Cerebral organoid and mouse models reveal a RAB39b–PI3K–mTOR pathway-dependent dysregulation of cortical development leading to macrocephaly/autism phenotypes', *Genes & development,* 34(7-8), pp. 580-597.

Zieger, H. L. and Choquet, D. (2021) 'Nanoscale synapse organization and dysfunction in neurodevelopmental disorders', *Neurobiology of Disease,* 158, pp. 105453.